Methodological developments in imaging and new physico-chemical understanding of archaeological flax-based textiles from the ancient East (3rd and 2nd millennium BC)

Jiayi Li

NNT : 2019SACLV031

Thèse de doctorat

Methodological developments in imaging and new physico-chemical understanding of archaeological flax-based textiles from the ancient East (3rd and 2nd mill. BC)

Thèse de doctorat de l'Université Paris-Saclay
préparée à l'Université de Versailles-Saint-Quentin-en-Yvelines

Ecole doctorale n°573 en Sciences des Matériaux (INTERFACES)
Spécialité de doctorat : Les matériaux innovants et leurs applications

JIAYI LI

Catherine Breniquet Professeur, Université Clermont-Auvergne	Président et rapporteur
Dominique Bernard Directeur de Recherche, CNRS	Rapporteur
Lucile Beck Ingénieur-Chercheur, CEA	Examinateur
Benoît Mille Ingénieur d'études, Ministère de la Culture	Examinateur
Loïc Bertrand Assimilé Directeur de Recherche, IPANEMA CNRS	Directeur de thèse
Alain Lusson Chargé de Recherche, CNRS	Co-directeur de thèse
Ariane Thomas Conservateur, musée du Louvre	Invité

université PARIS-SACLAY
ÉCOLE DOCTORALE
INTERFACES
Approches Interdisciplinaires : Fondements, Applications et Innovation

Titre : Développements méthodologiques en imagerie et nouvelle appréhension physico-chimique de textiles archéologiques en lin de l'Orient ancien (3^{e} et 2^{e} millénaire av. J.-C.)

Mots clés : Matériaux archéologiques, Textiles cellulosiques anciens, Minéralisation, Corrosion, Cuivre, Tomographie de rayons X

Résumé : Les résidus textiles archéologiques de l'Orient ancien sont rares. En Mésopotamie, la plupart des connaissances sur les textiles proviennent de textes cunéiformes. Fabriqués à partir de fibres animales ou végétales, les textiles sont périssables dans la plupart des environnements archéologiques. Un des principaux processus de préservation exceptionnelle de fibres archéologiques implique le contact avec un artefact métallique, ce phénomène est appelé « minéralisation ». Très peu de travaux ont été consacrés à l'étude approfondie des processus de minéralisation des textiles cellulosiques. Ce travail de doctorat a consisté à étudier à multi-échelles l'interaction entre substrat métallique à base cuivre et textile ancien, à partir d'échantillons provenant des sites archéologiques de Gonur-Depe, de Nausharo et de Tello (3^{e} et 2^{e} millénaire av. J.-C.). Le travail a permis de mettre en place une nouvelle méthodologie d'imagerie par microtomographie synchrotron de rayons X semi-quantitative afin de décrire la composition de ces systèmes complexes, hétérogènes et réactifs en 3D. Ces développements nous ont permis d'approfondir la description archéologique de ces textiles et de leur contexte d'enfouissement, en relation avec la question de leur production et de leur usage passés. Nous avons enfin abordé la description du système hybride fibres-produits de corrosion et la présence de signatures organiques dans ces systèmes hybrides altérés en vue de décrire les mécanismes à l'origine de leur préservation exceptionnelle.

Title : Methodological developments in imaging and new physico-chemical understanding of archaeological flax-based textiles from the ancient East (3rd and 2nd mill. BC)

Keywords : Archaeological materials, Ancient cellulosic textiles, Mineralization, Corrosion, Copper, X-ray tomography

Abstract : Archaeological textile remains from the ancient East are rare. In Mesopotamia, most of the knowledge about textiles comes from cuneiform texts. Made from animal or vegetable fibres, textiles are perishable in most archaeological environments. One of the main processes of exceptional preservation of archaeological fibres involves contact with a metal artefact, this phenomenon is called "mineralization". Very little work has been done on the in-depth study of the mineralization processes of cellulosic textiles. This PhD work consisted of a multi-scale study of the interaction between copper-base substrate and ancient textiles, based on samples from the archaeological sites of Gonur-Depe, Nausharo and Tello (3rd and 2nd millennium BC). The work made it possible to implement a new imaging methodology using synchrotron-based semi-quantitative X-ray microtomography to describe the composition of these complicated, heterogeneous and reactive systems in 3D. These developments have allowed us to deepen the archaeological description of these textiles and their burial contexts in relation to the question of their production and use in past times. Finally, we discussed the description of the hybrid system of fibre-corrosion products and the presence of organic signatures in these altered hybrid systems in order to describe the mechanisms underlying their exceptional preservation.

Université Paris-Saclay
Espace Technologique / Immeuble Discovery
Route de l'Orme aux Merisiers RD 128 / 91190 Saint-Aubin, France

Remerciements

Le document que vous tenez actuellement entre vos mains ou que vous consultez sur un écran d'ordinateur, est issu d'un travail d'équipe. Il n'aurait ainsi pas pu voir le jour sans l'aide de plusieurs personnes. À ce titre, je profite de la présence de cette section afin de remercier ces différents contributeurs.

J'adresse mes premiers remerciements aux membres de mon jury. Je remercie mes rapporteurs **Dominique Bernard** et **Catherine Breniquet** d'avoir accepté de lire mon manuscrit et évalué ce travail. Je remercie également **Lucile Beck** et **Benoît Mille** d'avoir accepté d'être examinateur de ce travail.

J'aimerais exprimer toute ma gratitude à mes directeurs et ma co-encadrante de thèse : **Loïc Bertrand**, **Alain Lusson** et **Ariane Thomas**, pour votre accompagnement pendant cette thèse et votre confiance en me proposant ce sujet, pour les choix des artefacts étudiés depuis les collections du **musée du Louvre**, pour votre disponibilité lors des expériences au laboratoire et au Synchrotron Soleil, pour les discussion et les conseils autour de textiles minéralisés, de corrosion du cuivre et de diverses méthodes utilisées, pour les relectures du manuscrit et enfin pour avoir participé activement à la réussite de cette thèse de doctorat. Mes sincères remerciements sont également dédiés à la mémoire de mon précédent co-directeur de thèse, le professeur **Pierre Galtier**.

Toute ma thèse s'est déroulée au sein des laboratoires **IPANEMA** et **GEMaC** dans une excellente ambiance et je tiens à remercier tous les collègues des laboratoires, aussi

bien les anciens que les nouveaux, sans lesquels l'aboutissement de ce travail n'aurait pas été possible. Je vous remercie sincèrement pour votre soutien, pour les discussions scientifiques (mais également les autres) celles-ci et l'intérêt que vous avez porté à ce travail ayant mené à de précieux conseils qui m'ont permis d'avancer. L'atmosphère conviviale et amicale au laboratoire m'a permis de toujours venir avec enthousiasme. Merci **Mathieu Thoury** et **Pierre Guériau**, pour votre aide et vos encouragements de chaque instant pendant mes travaux de thèse ! Merci **Regina Oprandi** pour toute l'aide logistique, ta disponibilité et ta gentillesse au cours de ces trois ans et demi ! Merci **Serge Cohen** pour tes conseils sur le traitement des données. Merci **Jérémy Hénin**, **Cécile Fossé** et **Maëva L'Héronde** pour le travail que nous avons mené ensemble sur la préparation des échantillons. Merci **Patricio Guerrero** pour l'aide sur l'utilisation de R et de Latex. Merci **Giulia Franceschin**, **Selwin Hageraats** et **Mathilde Renouard**, mes collègues de bureau, avec qui j'ai partagé de très bons moments. Merci **Tulin Okbinoglu** pour tes relectures du manuscrit. À **Rafaella Georgiou**, qui m'a assuré de finir sa thèse dans un an, j'attends de voir :). À **Marie Godet** de tes conseils très utiles pour ma présentation de thèse, tu es la seule avec qui je peux parler chinois dans le bureau. Merci **Victoria Beltran** pour ton aide sur les expériences d'infrarouge. Merci **Marta Bellato** d'avoir partagé les résultats de ton stage sur ce même sujet et ton aide lors des expériences synchrotron. Merci **Sophie David**, **Bénédicte Charbonnel**, **Anne-Fleur Barfuss** et **Fanny Dubray** pour votre aide sur la diffusion de mon travail via le site web d'IPANEMA et sur les réseaux socio-professionnel. Merci **Corentin Reynaud** de poursuivre une partie des travaux de cette thèse. Merci **Sebastian Schoeder** et **Alice Gimat** pour votre gentillesse. À **Gaëlle Amiri** de votre aide sur les expériences de diffraction. Merci **Yves Dumont** de votre attention et aide sur toutes les procédures de l'école doctorale.

Je souhaiterais également remercier la **Fondation des Sciences du Patrimoine** pour le financement de ce sujet de thèse. Merci **Emmanuel Poirault** et **Anne-Julie**

Etter de votre aide pendant mon travail et pour les formations doctorales très intéressantes que vous avez organisées.

J'exprime également toute ma reconnaissance envers les différentes collaborations qui ont permis la richesse de ces résultats. Ce travail n'aurait pu voir le jour sans la contribution de toutes ces personnes.

Tout d'abord, je remercie tout particulièrement **Christophe Moulhérat** du musée du Quai Branly - Jacques Chirac pour votre aide sur le choix du corpus d'échantillon ainsi que pour votre accueil chaleureux et votre expertise sur les textiles archéologiques. Je remercie également **Aurore Didier** pour l'autorisation d'étudier des artefacts conservés au laboratoire ArScAn.

Je remercie également **Luc Robbiola** de TRACES pour toutes les discussions sur les artéfacts archéologiques à base cuivre corrodé, pour votre regard expert et votre enthousiasme pour ce projet. Je vous remercie d'avoir partagé votre connaissance sur les mécanismes de corrosion, les interprétations archéologiques et la métallurgie, toujours dans la bonne humeur.

Merci à toutes les collaborations SOLEIL, tout d'abord **Andrew King** de PSICHE sans lequel le développement de micro-tomographie inclus dans ce sujet n'aurait pas pu être mené, **Solenn Réguer** de DIFFABS pour les mesures de XAS, XRF et XRD, **Matthieu Refregiers** de DISCO pour les expériences de photoluminescence, **Mario Scheel** et **Tim Weitkamp** d'ANATOMIX pour les mesures de micro-tomographie de haute résolution, **François Nicolas** pour l'utilisation de microscopie 3D au laboratoire de surface, **Christophe Sandt** de SMIS pour le Raman, **Karine Chaouchi** pour la diffraction au laboratoire de chimie. J'adresse également mes remerciements à **Cristian Mocuta**, à **Camille Rivard**, à **Félisa Berenguer**, à **Frédéric Jamme**, à **Jonathan Perrin**, à **Jean-Paul Itié** et à **Nicolas Jaouen** pour votre aide lors de mes expériences synchrotron.

Merci à toutes les personnes ayant participé à l'obtention des résultats présentés dans

ce manuscrit, **Alexandre Dazzi** et **Ariane Deniset** du LCP pour les mesures d'AFM-IR, **Alain Schmitt** d'Institut Cochin pour votre conseil sur la préparation des échantillons, **Thibault Brulé** d'Horiba France pour les expériences de Raman, **Gaël Latour** d'IMNC et **Arnaud Proietti** de Centre de MicroCaractérisation Raimond Castaing pour votre aide respectivement lors des expériences de SHG et de SEM-EXD/EBSD, **Anne-Laurence Dupont** du CRCC et **Annick Texier** du LRMH pour vos conseils scientifiques lors des réunions annuelles du déroulement de thèse.

Merci aussi à toutes les personnes d'administration de l'UVSQ et de l'école doctorale 573 INTERFACES.

最后，我希望向我的亲朋好友表达最诚挚的谢意。感谢我的父母，李平和党秦绣，以及我的爷爷奶奶，李宪如和王秀兰，感谢你们在我的博士工作中的支持以及在我的生活里无微不至的关怀，你们的肯定和鼓励是我前行的坚实力量和可靠后盾。我也要感谢我的姑姑李伟，感谢你在我对未来的学习方向感到迷茫时给予我有效的建议，让我从理论化学的道路上出发，慢慢走向了考古研究的新天地。此外，我真诚地感谢我的表姐，党明子，如果没有你在我初来乍到时的陪伴，那些晦暗艰难的时光，一定会非常难熬。

我同样要感谢我的好朋友们，张露，王霁雯，周婧文，汤娜，岳宜坤以及阎雯青，在我被淹没于工作中而感到失意疲惫时，是你们的鼓励和开导让我舒心畅怀！

余谨以至诚，感父母之爱，铭师长之育，谢朋友之助！

Contents

List of abbreviations

ABI	Analyzer based imaging
AD-XRD	Angle-dispersive X-ray diffraction
BC	Before Christ
BF	Bright field
CCD	Charged-coupled device
µCT	Micro-computed tomography
DF	Dark field
DP	Degree of polymerization
EBSD	Electron backscatter diffraction
ED-XRD	Energy-dispersive X-ray diffraction
EDS	Energy-dispersive spectroscopy
Eh	Reduction potential
EXAFS	Extended X-ray absorption fine structure
FBP	Filtered backprojection
FOV	Field of view
FPA	Focal-plane array
FT-IR	Fourier-Transform Infrared Spectroscopy
GBI	Grating based imaging
GV	Gray value

IR	Iterative reconstruction
IRUG	Infrared & Raman User Group
MCT	Mercury cadmium telluride
NA	Numeric aperture
NIST	National Institute of Standards and Technology
PBI	Propagation based imaging
RH	Relative humidity
ROI	Region-of-interest
SEM	Scanning electron microscopy
SR	Synchrotron radiation
UV	Ultraviolet
XANES	X-ray absorption near-edge structure
XAS	X-ray absorption spectroscopy
XRD	X-ray diffraction
XRF	X-ray fluorescence

Summary

The present PhD project was developed in the framework of the multidisciplinary program ETAM++ "Etude physico-chimique de Textiles Archéologiques Minéralisés". It is co-directed by the IPANEMA (Institut Photonique d'Analyse Non-destruc-tive Européen des Matériaux Ancients, CNRS, Ministère de la culture, USR 3461, UVSQ, Université Paris-Saclay) and GEMaC (CNRS, UVSQ, UMR 8635, Université Paris-Saclay) laboratories and is co-supervised by musée du Louvre. This PhD thesis involved a collaboration between the TRACES (CNRS, Ministère de la culture, UMR 5608, Université Jean-Jaurès) and ArScAn (CNRS, Ministère de la culture, UMR 7041, Université Paris Ouest Nanterre la Défense, Université Paris I Panthéon Sorbonne) laboratories as well as the musée du Quai Branly-Jacques Chirac. ETAM++ is funded by the PATRIMA LabEx and has received a thesis award from Fondation des sciences du patrimoine.

Textiles made of animal or vegetable fibres are highly perishable materials in burial contexts, leading to a scarce archaeological record compared to pottery or metal artefacts. Nevertheless, textiles can survive over millennia in particular contexts, such as in close contact with metal artefacts. The later enables the morphological preservation of textiles, under a phenomenon referred to as "mineralization". Mineralization of archaeological textiles was studied in a limited number of works [1, 2, 3, 4]. The geological term "pseudomorph" was used to describe the preservation of ancient textiles, implying that the organic fraction of the fibres have totally been degraded and replaced by inorganic

phases due to metal corrosion [5]. Yet, the preservation of organic remnants in archaeological textiles has been revealed, indicating that not only the morphological features but also the chemical composition of textiles can at least be partly preserved [1]. Mineralization processes rely on the diffusion of inorganic ions produced by metal corrosion into the fibres and the deposition of minerals on the surface of fibres [6]. These studies were performed on individual fibres or single yarns. However, although indispensable and clearly involved in the mineralization processes, the role of the metal artefacts undergoing corrosion and the associated formation of various corrosion products have only received little attention. Moreover, the paleo-environmental conditions at the archaeological sites, which played a central role on textiles mineralization and metal corrosion, have not been discussed. This is largely due to the fact that conventional techniques are insufficient to obtain information at multi scales on complex and heterogeneous archaeological artefacts such as fibre-soil-metal systems.

In this thesis, I carried out studies on mineralized flax-based textiles exceptionally preserved on the surfaces of very ancient copper-base artefacts dating from ca. 3000–1800 BC found in three archaeological sites, Tello (current Iraq), Nausharo (current Pakistan) and Gonur-Depe (current Turkmenistan). They represent a unique record of Mesopotamian textiles manufacturing in ancient civilizations, otherwise only known from cuneiform texts. My thesis aims to: (1) develop a methodology including cutting-edge synchrotron-based 3D and 2D micro-imaging approaches (e.g. µCT, UV/Visible photoluminescence, etc.) and conventional techniques (e.g. FT-IR, SEM-EDS, etc.) at multiple spatial resolution, (2) study the physical-chemical properties of the carefully selected coherent corpus of mineralized textiles and their corroded metal substrates, i.e. the identification of organic remnants and inorganic ions mineralized textiles, the characterization of corrosion products, and the investigation of environmental information in archaeological burial contexts. (3) better describe mineralization mechanisms related to textile degradation and copper corrosion using techniques at high spatial resolution

and discuss the role of environmental factors involved in mineralization processes.

This manuscript contains 6 chapters.

Chapter 1 outlines the historical and artistic values of textiles, which constitute an important material record of ancient human activities. It provides a short description of the use and significance of textiles as well as the development of textile technology in the regions of Mesopotamia and Indus Valley, respectively. It presents some of the physico-chemical characteristics of plant fibres (particularly flax fibres) of relevance to our work and their mode of production during Antiquity.

Chapter 2 reviews the current status of physico-chemical studies performed on mineralized textiles and corroded metal supports. It discusses the different degradation pathways of natural plant fibres and presents a brief overview of exceptional preservation processes of archaeological textiles. Current literature and analytical methods used in the study of mineralization mechanisms and influencing environmental factors involved are introduced. Related corrosion mechanisms of copper-base artefacts are also reviewed.

Chapter 3 describes the corpus of artefacts and fragments studied, and their excavation contexts, as well as information on environmental conditions to our knowledge prevailing at the archaeological sites. A set of selected analytical methods used in this thesis is described, together with their respective experimental setups and data processing procedures.

Chapter 4 proposes the use of high-resolution synchrotron X-ray µCT for a fine non-invasive 3D description of the distribution of both internal and external mineral phases in copper-base objects. This approach provides essential clues on long-term corrosion processes. Major and minor phases are identified through semi-quantitative evaluation of attenuation coefficients using polychromatic X-ray illumination. Evidence is found for initially unidentified phases through statistical processing of images. Interpretation of the distribution of these phases is discussed. A good correlation between the corrosion

phases identified by µCT and by invasive BSE-SEM is demonstrated. Additionally to the stratigraphy of the copper corrosion compounds, the variations observed in the attenuation coefficients of Cu(I) phases are examined and discussed. Evidence for the non-invasive observation of phases rapidly altered upon preparation of real cross-sections is provided. The method can be applied when cross-sectioning even of minute fragments is impossible.

Chapter 5 examines the corpus of mineralized flax textiles using a set of complementary laboratory and synchrotron-based analytical methods. The presence of organic remnants, even in highly transformed fibres, in a yet undetermined molecular form, is demonstrated and discussed. Inorganic elements present in mineralized fibres are identified and the characterization of corrosion products formed in metal substrates is performed.

Chapter 6 discusses the data acquired on the artefacts and samples in Chapter 5, which allow them to be presented in their socio-historical context and to study the exceptional preservation of organic remnants in the fibres. The relationship between substrate corrosion and mineralization is further interrogated. Additional insight on the relationship between local taphonomy and the local environmental information is provided for the three archaeological sites.

A conclusion of this PhD work and perspectives for future research is provided at the end of the thesis in 6.4. The manuscript comprise two appendices that present the additional technique used (complementary to Chapter 3) in Appendix A and my scientific productions in this thesis (articles, conferences, etc.) in Appendix B.

Resumé

Ce projet de thèse a été réalisé dans le cadre du programme multidisciplinaire ETAM++ (Étude physico-chimique des Textiles Archéologiques Minéralisés). Il est codirigé par les laboratoires IPANEMA (Institut Photonique d'Analyse Européen des Matériaux Anciens, CNRS, Ministère de la Culture, USR 3461, UVSQ, Université Paris-Saclay) et GEMaC (CNRS, UVSQ, UMR 8635, Université Paris-Saclay) et co-encadré par le musée du Louvre. Cette thèse est mené en collaboration avec les laboratoires TRACES (CNRS, Ministère de la culture, UMR 5608, Université Jean-Jaurès) et ArScAn (CNRS, Ministère de la culture, UMR 7041, Université Paris Ouest Nanterre la Défense, Université Paris I Panthéon Sorbonne) ainsi que le musée du Quai Branly-Jacques Chirac. ETAM++ est financé par le LabEx PATRIMA et a reçu un prix de thèse depuis la Fondation des sciences du patrimoine.

Les textiles fabriqués à partir de fibres animales ou végétales sont des matériaux très périssables, qui ne sont donc que très rarement retrouvés en contexte archéologique par rapport aux découvertes beaucoup plus fréquentes de poterie ou d'objets métalliques. Néanmoins, les textiles peuvent survivre pendant des millénaires dans des contextes particuliers, comme par exemple en contact avec des objets métalliques, permettant de préserver la morphologie physique des textiles par « minéralisation ». Cette minéralisation des textiles archéologiques n'a que très peu été étudiée [1, 2, 3, 4]. Le terme géologique « pseudomorphe » est utilisé pour décrire la préservation des textiles anciens,

impliquant que les fractions organiques des fibres ont été totalement dégradées et remplacées par des phases inorganiques due à la corrosion des métaux [5]. La préservation de restes organiques dans des textiles archéologiques a été confirmée, révélant qu'outre les caractéristiques morphologiques des textiles leur composition chimique pouvait également être au moins partiellement préservée [1]. Les processus de minéralisation sont dus à la diffusion des ions inorganiques produits par la corrosion des métaux dans les fibres et au dépôt des minéraux à la surface des fibres [6]. Ces études ont été réalisées sur des fibres ou des fils individuels. En revanche, bien qu'indispensable et clairement impliqués dans les processus de minéralisation, le rôle des artefacts métalliques corrodés et la formation des divers produits de corrosion associés n'ont attiré que très peu d'attention. Les informations environnementales relatives aux sites archéologiques, qui ont une influence sur la minéralisation des fibres et la corrosion des métaux, n'ont pas fait l'objet d' études. Cela s'explique en grande partie par le fait que les techniques classiques ne suffisent pas pour obtenir des informations à multi-échelles sur des artefacts archéologiques complexes et hétérogènes tels que les systèmes fibre-sol-métal.

Dans cette thèse, j'ai réalisé des études sur des textiles de lin minéralisés exceptionnellement préservés à la surface d'artefacts très anciens à base de cuivre datant d'environ 3000–1800 avant J.-C. découverts dans trois sites archéologiques, Tello (Irak actuel), Nausharo (Pakistan actuel) et Gonur-Depe (Turkménistan actuel). Ils représentent un témoignage unique de la fabrication des textiles Mésopotamiens dans les civilisations antiques, presque seulement connu par les textes cunéiformes. Ma thèse vise à : (1) developper une méthodologie comprenant des approches de micro-imagerie 3D et 2D utilisant le rayonnement synchrotron (e.g. µCT, photoluminescence UV/Visible, etc.) et des techniques conventionnelles (e.g. FT-IR, SEM-EDS, etc.) à résolution spatiale multiple, (2) étudier les propriétés physico-chimiques du corpus cohérent soigneusement sélectionné de textiles minéralisés et de leurs substrats métalliques corrodés, c'est-à-dire l'identification des restes organiques et des ions inorganiques dans les textiles minéralisés,

la caractérisation des produits de corrosion et l'étude des informations environnementales dans des contextes d'enfouissement archéologique. (3) décrire mieux les mécanismes de minéralisation liés à la dégradation des textiles et à la corrosion du cuivre en utilisant des techniques à haute résolution spatiale et discuter du rôle des facteurs environnementaux impliqués dans les processus de minéralisation.

Ce manuscrit de thèse contient 6 chapitres.

Le chapitre 1 décrit les textiles qui, en plus de leur valeurs historiques et artistiques, constituent un témoin unique des activités humaines. Une brève introduction à l'histoire et à l'utilisation, ainsi qu'à l'importance, des textiles dans les région de la Mésopotamie et de la vallée de l'Indus est présentée. Certaines caractéristiques physico-chimiques des fibres végétales (fibres de lin en particulier) pertinentes pour notre travail et leur chaîne de production pendant l'Antiquité sont également décrites.

Le chapitre 2 est une revue de la littérature portant sur les études physico-chimiques réalisées sur les textiles minéralisés et les supports métalliques corrodés. Les différents processus de dégradation des fibres végétales sont discutés. Un aperçu bref des processus à l'origine de la préservation exceptionnelle des textiles archéologiques est présenté. Les méthodes d'analyse utilisées pour l'étude des mécanismes de minéralisation et les facteurs environnementaux en jeu sont introduits. Les mécanismes de corrosion associés aux artefacts à base de cuivre sont également expliqués.

Le chapitre 3 décrit le corpus d'artefacts et de fragments étudiés et leurs contextes de fouilles, ainsi que les informations sur les conditions environnementales à notre connaissance prévalant sur les sites archéologiques correspondants. Les méthodes analytiques utilisées dans cette thèse sont décrites, ainsi que les conditions expérimentales et les traitements de données appliqués.

Le chapitre 4 décrit l'utilisation de la microtomographie à rayons X synchrotron haute résolution pour une description fine, en 3D et non-invasive de la distribution des phases minérales à l'extérieur et à l'intérieur d'objets à base de cuivre. Cette approche

fournit des indices essentiels sur les processus de corrosion à long terme. Les phases majeures et mineures sont identifiées par une évaluation semi-quantitative des coefficients d'atténuation en utilisant un faisceau de rayons X polychromatique. Des phases initialement non observées sont identifiées grâce au traitement statistique des images. L' interprétation de la distribution de ces phases est discutée. Une bonne corrélation entre les phases de corrosion identifiées par µCT et par MEB-EDS (invasif) est démontrée. Outre la stratigraphie des composés de corrosion du cuivre, les variations observées dans les coefficients d'atténuation des phases Cu(I) sont examinées et discutées. Des preuves pour l'observation non-invasive de phases rapidement modifiées lors de la préparation de coupes transversales sont fournies. Cette méthode peut être appliquée lorsque la préparation de coupe transversale, même de fragments minuscules, est impossible.

Le chapitre 5 examine le corpus de textiles minéralisés en lin préservé en utilisant une série des méthodes analytiques complémentaires en laboratoire et au synchrotron. La relation entre les scénarios de minéralisation possibles et les mécanismes de corrosion des substrats à base de cuivre est remise en question. La présence de restes organiques, même dans des fibres hautement transformées, sous une forme moléculaire encore indéterminée, est démontrée et discutée. Les éléments inorganiques présents dans les fibres minéralisées sont identifiés et la caractérisation des produits de corrosion formés dans les substrats métalliques est effectuée.

Le chapitre 6 traite des données acquises sur les artefacts et les échantillons au chapitre 5, ce qui permet de les présenter dans leur contexte socio-historique et d'étudier la conservation exceptionnelle des restes organiques des fibres. La relation entre la corrosion du substrat et la minéralisation est examinée plus en détail. Pour les trois sites archéologiques, des informations supplémentaires sur la relation entre la taphonomie locale et les informations environnementales locales sont fournies pour les trois sites archéologiques.

Une conclusion sur ces travaux de thèse et les perspectives pour de futures recherches

autour de ce projet sont présentés à la fin de cette thèse dans 6.4. Le manuscrit comprend deux annexes qui présentent la technique additionnelle utilisée (complémentaire au Chapter 3) en Annexe A et mes productions scientifiques dans cette thèse (articles, conférences, etc.) en Annexe B.

"Textiles are a fundamental part of our material culture. They serve a wide range of purposes, functional and symbolic. Making them demands skill and raw materials, and is so time-consuming that advances in textile technology have had a major impact in economic and social changes."

——L. BENDER JØRGENSEN, "The World According to Textiles", 2007.

1

Introduction

This chapter outlines the historical and artistic values of textiles, which constitute an important material record of ancient human activities. It provides a short description of the use and significance of textiles as well as the development of textile technology in the regions of Mesopotamia and Indus Valley, respectively. It presents some of the physico-chemical characteristics of plant fibres (particularly flax fibres) of relevance to our work and their mode of production during Antiquity.

Contents

1.1 A brief summary of ancient textiles

Metals, ceramics and cut or polished stones are major testimonies of the knowledge of the life of Protohistoric populations. These archaeological artefacts can provide material records that are longer than the history of written text because they are less likely to disappear due to alteration processes [7]. They are physical remains but are also the results of people's requirements, capabilities and desires. As significant part of archaeological evidence, ancient textiles have remained an under researched field [1]. Archaeological textiles contain critical information on social, political and cultural life in different civilizations, such as clothing manufacture and funerary practices [8]. In this project, we focused on textiles from plant fibres, in particular flax.

1.1.1 Flexible and variety of uses of textiles

Originating from the Latin word *texere*, the term "textile" refers to a flexible material that is formed by a network of fibres (natural or artificial) [9, 10]. This broad term describes any material consisting of interlacing fibres. The words "fabric" and "cloth" are often used in textile industry and trade as synonyms for textile. Fabric has a narrower sense and describes a material achieved from fibres (or yarns) by weaving or knitting to produce further product (e.g. garment) [11, 12], whereas cloth refers to processed fabric for wearing purpose [13, 14]. Raw fibres from animal (wool, silk, etc.) or vegetable (flax, cotton, etc.) sources are spun together after treatment to obtain yarns or threads [10], which are used to produce textile in subsequent steps (weaving, dyeing, etc., see section 1.4).

The history of textiles can be dated to the beginning of human civilization when animal skins were probably used as cloth for warmth. Then, people learned to use plant fibres and to transform them into textiles [15].

The role of the textiles in human society is considerable from the past to nowadays,

since they are involved in many moments of social, political, and cultural life [17]. The two main uses of textiles are for clothing and for container. They can also be used in other fields such as for industry purposes (e.g. automotive applications) [18, 19], for medical materials (e.g. implants) [20] and for scientific processes (e.g. filtering) [21]. Textiles often indicate how dress allowed individual or collective differentiation in terms of sex or social status. They also express a value that is both ostentatious and symbolic for the social elite, they are signs of opulence and prosperity and can stir up the sense of awe among people [3]. For example, in ancient China under the different imperial dynasties, official dress were used to identify the status and authority of those who wore them in the hierarchy of the court. In ancient and traditional societies, ornamented artefacts like textiles were produced not only for decorative use, they were also often offered as gifts for diplomatic purposes in order to attract and retain the loyalty of other rulers or governments [22]. They could be used as a bargaining chip to pay the army or personnel attracted to the governmental authority [23].

1.1.2 A rare and precious material record

Archaeological textile remains are one of the significant sources of study of ancient civilizations for which the use of writing is not established or for which transcription deciphering is still uncertain [7]. They can contribute to the understanding of the technical level reached for their production, the different stages of the production chain (see Section 1.4), their various uses and of the people who manufactured them [3].

A wide variety of information can be obtained from the studies of ancient textile remains, including:

- Materials selected and transformed to be used. The choice of textile as raw materials was various in ancient times [24]. Originating from the plants, the use of bast fibres (flax, hemp, jute, etc.) and leaves (sisal) as well as seed pod fibres (cotton and kapok) was relatively common [25]. Concerning animal fibres, the wool and

silk were the common sources [3].

- Techniques developed to produce simple or complex textiles. Each culture had its own textile production craft according to its different needs, such as back-strap loom and horizontal / vertical loom [26].

The careful studies of ancient textile residues collected from different archaeological sites also make it possible to understand their importance in funerary practices. However, textiles are degraded rapidly when buried underground due to their organic composition and unfavourable environmental conditions. Archaeological textile remains are relatively rare, several indirect sources testifying to the presence of textiles in Antiquity are therefore also important and can help to build the history of textiles.

1.1.3 Existing texts and representations of ancient textiles

The knowledge of textile production in ancient times relies on indirect sources which mostly include:

- Written records. Formal official archives and public or private documents are considered to be the most common sources to understand textile history [22]. For example, the use of linen represents an extreme high social status at Tell Abraq (United Arab Emirates) around 3000 BC as recorded in contemporary cuneiform sources [27]. However, due to the differences between old description based on cuneiform texts (terms, metaphors, etc.) and current archaeological practices, archaeologists may encounter difficulties when reading documents, so that a complete and more accurate translation of cuneiform texts and comparison with other related sources is often necessary [3] (Figure 1.4).

- Iconography. The knowledge of textile production in ancient times can also be traced from images depicted in art works (seals, vases, etc.) that sometimes show

the act of twisting or weaving [22, 17]. The types of fibres cannot be easily determined and should be compared with other document sources in detail to speculate their origin. For example, for the famous so-called *Mesopotamian kaunakes* dated from ca. 2000 BC, the material displayed on the sculpture seems to be made both by flax (first inner layer) and by wool (second outer layer), but the confirmation is difficult even with close observation [28] (Figure 1.1).

- Processing tools. The presence of spindle-whorl, looms and needles can indicate technical condition in which textiles were made [29]. However, the identification of fibre types cannot be achieved based only on the spindle or loom used, as these tools are often incomplete when excavated from archaeological sites and because of the possibility that different textiles may be woven on the same loom (Figure 1.6A and 1.10A) [3].

- Other available sources (such as textile impressions observed on figurines and stone seals, etc.). The structure of these impressions, tight or loose fitting, may sometimes provides clues on the types of fibres used concerning the origin (plant or animal) (Figure 1.12C and D) [3].

Examples of each source from which showing uses of textiles will be detailed in next sections. A general review about the early textiles in Mesopotamia and Indus Valley is described, in a chronological sequence from Palaeolithic to late Chalcolithic period according to available archaeological data.

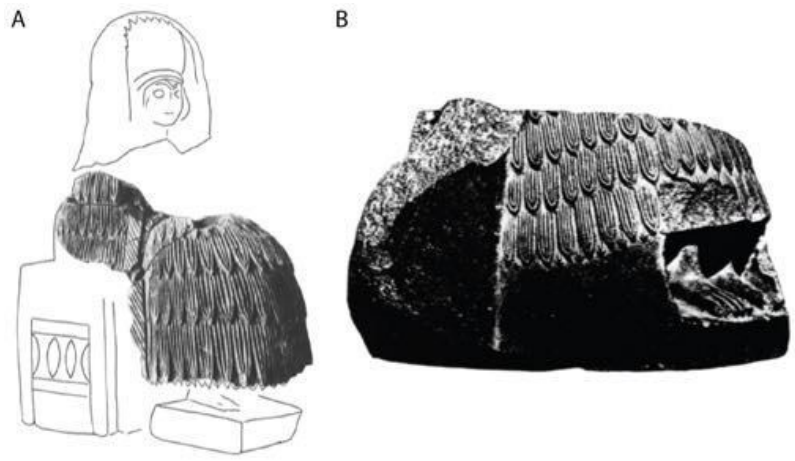

Figure 1.1: Sculptures showing common clothing style with unknown woven material in ancient Mesopotamia. A, Part of the statue *la dame au polos, Mari* (reused from C. Breniquet 2016 [28]). B, Fragment of a seated statue discovered at Tello (reused from E. de Sarzec et al., 1912 [30]).

1.2 Archaeological textile remains from the Mesopotamian and the Indus areas

1.2.1 Early textile remains from Mesopotamia

In the Ancient Near East, a vast region extending from Anatolia to Iran and Arabian Gulf in Kurdistan, the appearance of textile was concomitant with agricultural and livestock development and dates back from about 9000 BC (Figure 1.2) [17].

As an important part of the Fertile Crescent, the Mesopotamian Plain gave rise to several famous civilisations like the Sumer, Akkad and Babylon kingdoms [32]. The continuity in culture and technology is well established despite the economical and political changes. The textile industry through these ancient times can be explored thanks to the history recorded in cuneiform script on a number of clay tablets [33]. Evidence for textile has been found in these contexts in various common aspects like political, ritual and practical uses. Textiles were also possibly used in the role of monetary circulation

Figure 1.2: The map of Ancient Near East (reused from L. Seton 1961 [31]).

and in kin relationships [22].

In ancient Mesopotamia, two main types of natural fibres can be distinguished: vegetable and animal fibres (Figure 1.3) [17]. Considering the available documentation, these two types probably imply flax linen and sheep wool, respectively. The existence of other fibres (e.g. cotton, hemp, jute, etc.) cannot be excluded while their uses were very limited and poorly documented within the chronological records [22]. A global summary of the textile industry is difficult to construct due to the few concrete textile remains (i.e. in a non-mineralized form, see subsection 2.2.1) found in excavated contexts (probably due to the unfavourable preservation conditions in Mesopotamia) [17]. The main sources for the textile production rely on indirect details such as clothing styles on figurines and depictions on seals (Figure 1.4) [26].

The identification of flax within archaeological contexts relies mainly on palaeobotanical data. With the collaboration of several Orientalists, studies on the use of flax in ancient Mesopotamia has been pioneered by the palaeobotanist H. Helbaek [35]. Based

Dates BC	Periods	North Mesopotamia /Syria	South Mesopotamia	General Evolution	Textile Data
12,000	Neolithic	Natufian	?	Settlements	Twined textiles Bast fibres
		PPNA		Domestication of plants	
8000		PPNB		Domestication of animals	• Wool fibres • Suspended spindle • Weaving on loom
7000	Cultures with ceramic	≠ Hassuna	Ubaid 0–2	Agricultural societies	
		Samarra			
6000		Halaf			First selections of sheep
5000		Ubaid	Ubaid	Complex chiefdoms	Warp weighted loom?
4000	Chalcolithic	Gawra	3–5		↑
		Uruk Colonies	Uruk	Urbanisation	• Development of sheep husbandry • Two-bar loom?
3000	Bronze Age	Niniveh 5		Writing	• First artisans
		Early	Protodynastic I–III	Independant city states	
2340		Djezira	Akkad	Political unification	↑
2000		0–5	Ur III	Centralised states	Manufactures

Figure 1.3: A summary of the textile history in ancient Mesopotamia (modified from M.-L. Nosch et al., 2013 [22]).

Figure 1.4: The use of linen recorded on cuneiform cylinders of the Sumerian ruler Gudea dated to 2000 BC (translation of text by J. Black et al., 1988 [34], photo by Ramessos.)

on the fortuitous discoveries of carbonized seeds and on the observation of seed imprints on some prehistoric sites in the 60s and 70s, he identified flax in Mesopotamia and was probably the first to propose its potential use as a textile plant around the beginning of 6000 BC. He was also the first to identify the presence of domestic flaxseed in the Halaf period (6000–5500 BC) at the site of Arpachiyah, as well as at Tell es-Sawwan and Choga Mami, in which the earliest presence of this plant were confirmed at the time [35]. More recent work has shown unambiguously that flax was one of the first crops grown by man in Mesopotamia, particularly in the regions close to the Tigris and the Euphrates rivers in the Pre-Pottery Neolithic period (8000–5000 BC) [36].

Like many plant products used by man, flax currently exists in two varieties, wild and domestic. The domestic type, *Linum usitatissimum*, unlike wild varieties, is present everywhere in the Near East [26]. H. Helbaek has shown that wild varieties are absent from the Mesopotamian floodplain and surrounding plateaus, they grow in relative abundance in the zone of the foothills where the first traces of their use even of their manipulation can be built [35].

Among the very few textile remains made of linen discovered from Mesopotamian

sites, they mostly originate from wrappings around corroded metal figurines (see details in Subsection 3.1.3). These good-quality tabby plain weaves textiles were used as clothing or bags for the figurines during burial activities [37].

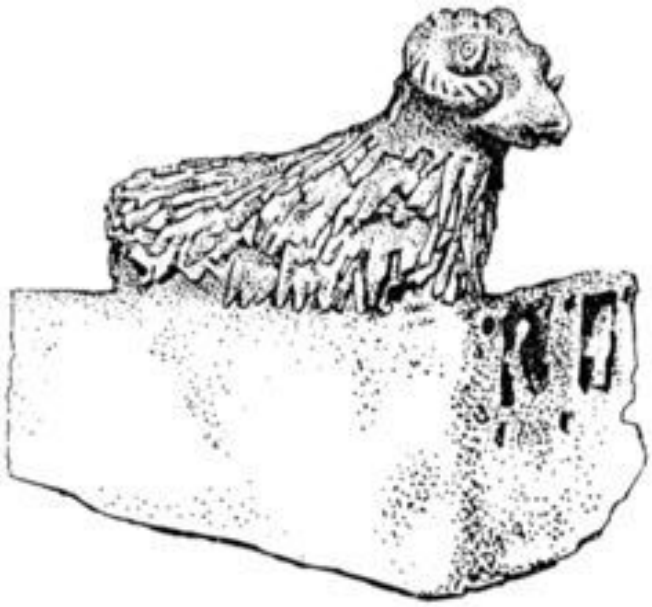

Figure 1.5: Model of a Sumerian sheep with woolly fleece (3000 BC) kept at British Museum (reused from J. David et al., 2003 [17]).

At the beginning of 3000 BC, probably due to the limited available agricultural land and relative high labour cost, the use of linen decreased and was restricted to religious condition and elite clothing [17]. From then on, it is very likely that wool became the main raw materials in textile production. The earliest use of wool, around 9000 BC in an area extending from Iran to Turkey, was first demonstrated by zoo-archaeological studies and verified by genetic data [17]. According to current research, the wool was obtained from distinct types of sheeps (Figure 1.5). In Sumer, according to Archaic texts, the production of wool in standardized quality was gradually established to produce garments and to promote exchanges between city-states [38]. Use of silk and hairs from other animals such as goat and camel has also been found [17].

Except from rare textile remains, indirect evidence demonstrates mature textile pro-

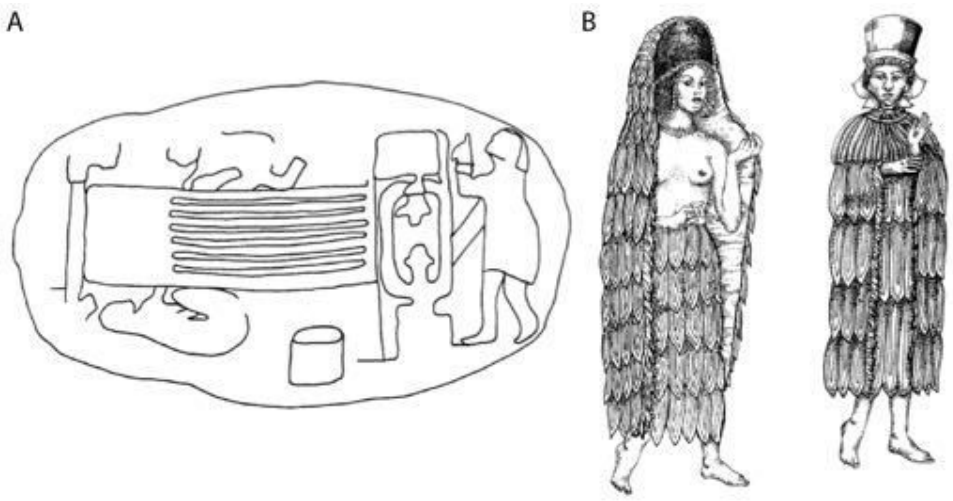

Figure 1.6: Indirect evidences showing textile development in ancient Mesopotamia (reused from J. David et al., 2003 [17]). A, An horizontal ground loom depicted on a seal in Susa (3000 BC). B, Sumerian style clothing for women similar to the so-called *Mesopotamian kaunakes* (see Figure 1.1).

duction and techniques in Mesopotamia. A ground loom of Egyptian-style depicted on a seal found in Susa in Iran (3000 BC) and clothing styles reflected by contemporary art works (Figure 1.6). Other written sources dated from the Bronze Age (3500-1100 BC) suggest that the textile industry was centralised and controlled by temple officials [17]. For example, many weavers (mostly women) worked in the local temples' clothing factory at Lagash to produce textiles using different types of wool as well as dyes, and were paid with food in return [17].

1.2.2 Early textile remains from the Indus valley area

The Indus valley region, extending from current Afghanistan to the India peninsula, covers a large geographical area that is surrounded by the Indus river and its branches, the heartland of this region is located in the modern country of Pakistan [40] (Figure 1.7). Many rich and diverse cultural traditions emerged from the early Stone Age during the Indus Civilisation which have been reconstructed based on material excavated from four main settlements, including Harappa, Mohenjo-daro, Lothal and Kalibangan, the first

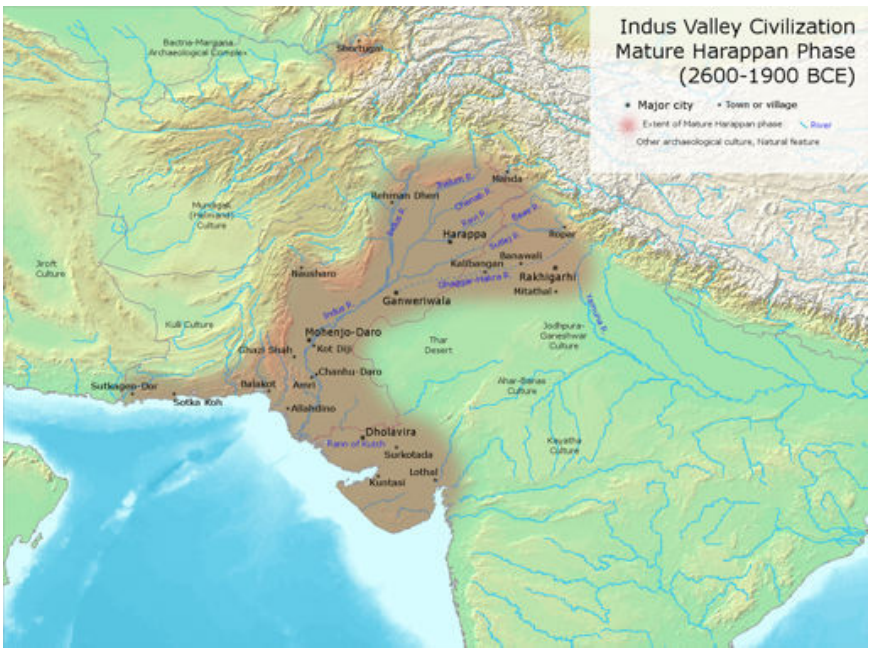

Figure 1.7: Map of the Indus valley region and its main archaeological sites (reused from J. McIntosh 2008 [39]).

two are in Pakistan and the last two are in western India [41].

During the Palaeolithic (or Stone Age) period, it is inferred that animal skins and hairs (e.g. from sheep) were considered as the main potential source of clothing for early nomads in the Indus area [43]. Moreover, it is very likely that the plant fibres from different plants, "bast fibres", were also used for braiding and netting in order to meet daily life needs. Simple twisting and weaving from animal or plant fibres may have existed at that time but cannot be confirmed due to the lack of supporting archaeological remains [44, 43]. Until the end of the Palaeolithic and at the beginning of the Neolithic period, the settlers began to gather and small-scale communities were formed. Their textile traditions can be traced to the activities and overseas trades of farmers and herders along land connections, the evidence which is based on the excavation works conducted at Mehrgarh, one of the important archaeological sites, located between the Kachi Plain and the highland plateaus of current Baluchistan [40, 41]. Mehrgarh is well

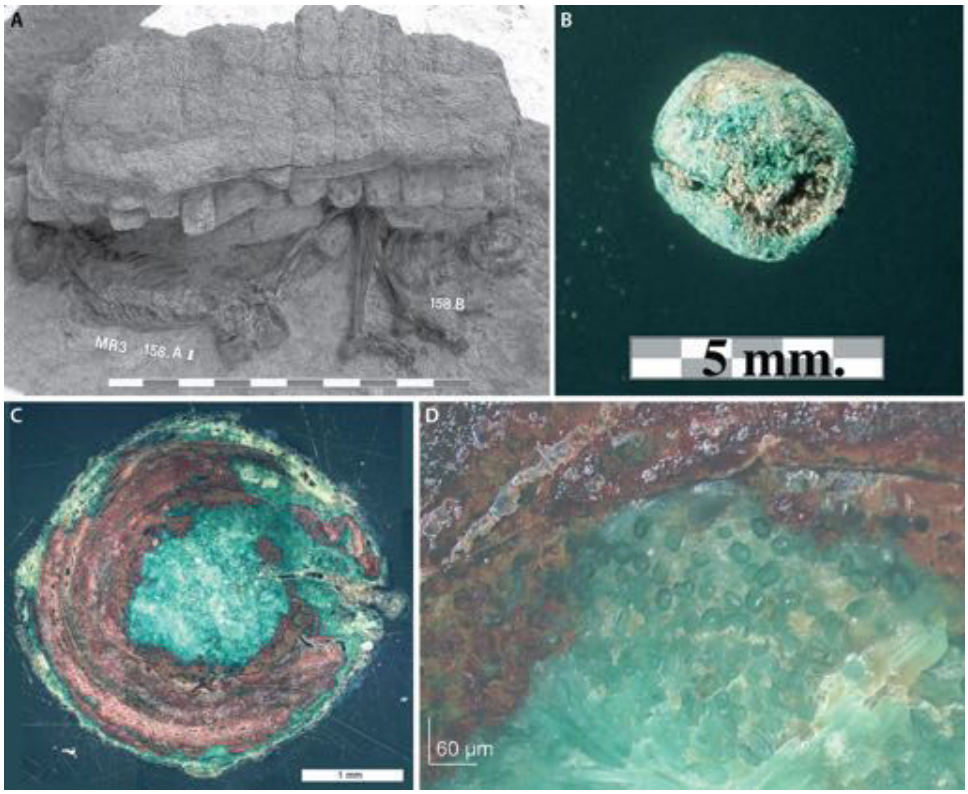

Figure 1.8: Cotton residue dated from 6000 BC (reused from C. Moulhérat et al., 2002 [42]). A, A mud brick tomb found at Mehrgarh. B, A corroded copper bead excavated in the tomb. C, Section of the bead under microscope. D, The characteristic of preserved cotton fibre remains.

identified as a major place of innovation (see M. Thoury et al. 2016 [45]). Although no physical textile remains were identified, probably due to environmental condition during burial, other excavated objects in several burials, such as elaborate woven baskets covered by bitumen and wide stripes composed of micro-beads [46], showed that it is not unlikely that the people knew the technology of weaving fabrics. Contemporaneous woven textiles made of bast fibres discovered at other Ancient Near East sites may suggest that the presence of early textiles in the Indus valley [47].

Figure 1.9: Other objects showing indirect evidences of woven textiles (reused from J.-F. Jarrige et al., 1980 [48]). A, A typical polychrome vase (5500 BC) on which painted design can probably be used for textile production and decoration. B, Two terracotta figurines revealing elaborate cloth styles for men (turban) and women (headdress).

Later, with the improvement of various craft technologies like pottery making and ornament design, urban development in the fertile soil of the rich alluvial plains brought great progress on textile manufacture among different classes of people over the next thousand years (so-called Regionalization Era, 6000-3000 BC) [43]. Archaeological discoveries suggest that the main cash crop yielded at that time were wheat and barley as well as cotton (*Gossypium* sp.) [50]. The metallurgical analysis of a copper bead

Figure 1.10: The presence of spindle-whorl at the site of Harappa (reused from J. M. Kenoyer et al., 1997 [49]). A, An object with painted spindle showing a scene of twisting. B, Excavated whorls in different sizes probably used for wool and cotton.

excavated from a mud brick tomb (dated to ca. 6000 BC) in Mehrgarh revealed several preserved plant fibres inside (Figure 1.8). They have been identified as cotton but could not be attributed to an already domesticated species with certainty [42]. Charred seed remains of cotton (5000 BC) [50] and flax (4000 BC) [51] found respectively at Mehrgarh and Miri Qalat based on archaeobotanical studies confirmed the use of plant fibre at early date.

Additional artefacts like painted pottery and terracotta figurines present further evidence of woven textiles concerning patterns of fine design and various clothing styles for men and women in ancient social stratas [48] (Figure 1.9). The depiction in several painted patterns suggest the use of dye for decorative purposes on textiles [52, 53]. Identification at the site of Harappa of spindle-whorls has shown that textile production was well-established. These spindle-whorls were in different sizes most likely to satisfy the needs of thick or fine threads when twisting and weaving using animal (e.g. wool) or plant (cotton) fibres (Figure 1.10) [49].

During the Harappan period (3000-1900 BC), the growth of textile production was related to the development of important craft traditions like metallurgy and pottery [43]. Several corroded copper fragments have been found covered by textile remains on both sides (3000 BC) at the archaeological site of Nausharo and they are studied in this

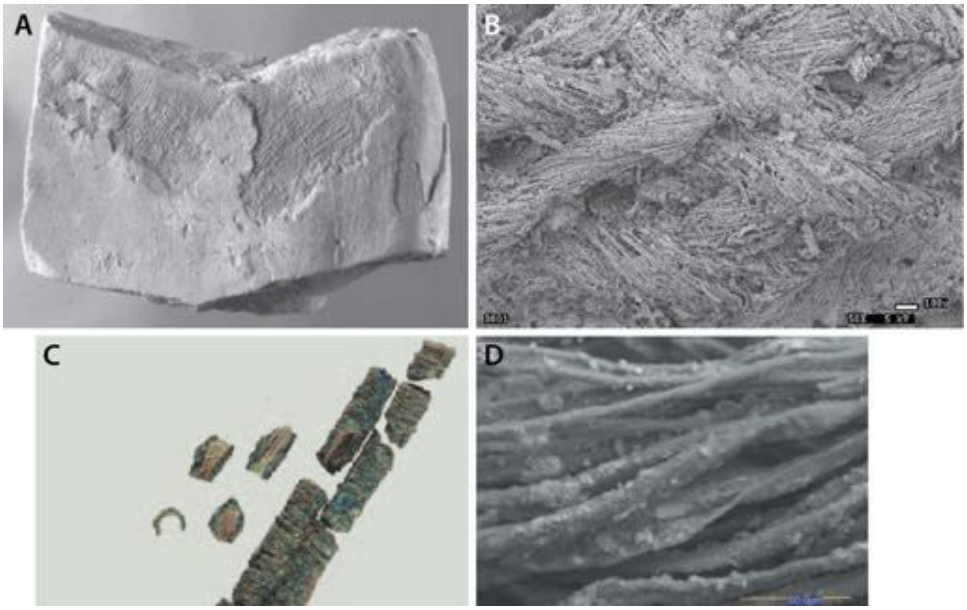

Figure 1.11: Vegetable and animal fibres collected from the site of Harappa. A, Jute remains attached to a ceramic artefact (reused from R. P. Wright et al., 2012 [54]). B, SEM image of jute fibres (reused from R. P. Wright et al., 2012 [54]). C, Silk remains in contact with copper-base alloy artefact (reused from I. L. Good et al., 2009 [55]). D, SEM image of silk fibres (reused from I. L. Good et al., 2009 [55]).

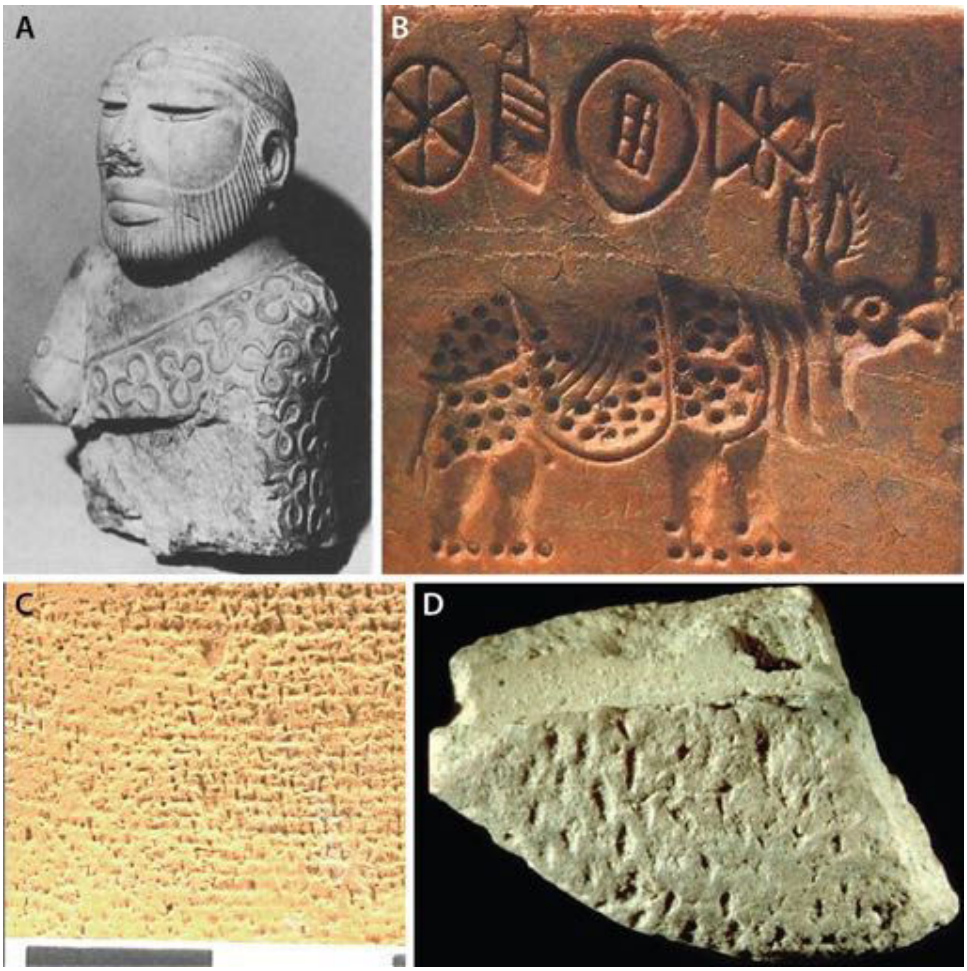

Figure 1.12: Indirect evidence showing the presence of woven textiles during the Harappan period. A, The figurine of "Priest-king" wearing a cloak decorated with trefoils (reused from S. L. Huntington et al., 1985 [56]). B, A rhino depicted with covering on a stone seal (reused from J. M. Kenoyer et al., 2004 [43]). C, Textile impression on a toy bed showing a fairly tightly woven normal weave (reused from J. M. Kenoyer et al., 2004 [43]). D, Irregular form of textile impression on a stone seal (reused from J. M. Kenoyer et al., 2004 [43]).

project (see Subsection 3.1.2) [57]. Jute fibres were identified on a ceramic artefact (2200-1900 BC) (Figure 1.11A and B) [54] and cotton fibres were observed imprinted on a corroded silver jar [43] at Harappa. Presence of animal fibres of wool and silk (Figure 1.11C and D) attached to different copper-alloy artefacts dating from ca. 2000 BC collected from the same site have been demonstrated [43, 55]. Indirect evidence for the development of textile industry has also been identified. As shown from many figurines, the clothing style became subtler with different types of looms used, illustrating the role of textile as an indispensable element for cultural and social identity. One of the famous depictions of clothing, the so-called "Priest-king" discovered at the site of Mohenjo-Daro, suggests a typical patterning still commonly used in modern India (Figure 1.12A) [56]. Animal depictions found on several stone seals also suggest the use of textiles or decorated leather as covering (used as cushion) (Figure 1.12B) [43]. Fabric impressions have been observed on a wide variety of artefacts such as a small toy bed and ceramic vessels as well as bricks (Figure 1.12C and D). Although the type of fibres cannot be identified for certain through the impressions, the twist and weave may provide clues for the quality of textiles and their origin. An impression of uniformly spun threads could indicate fine cotton (or wool) while an irregular form most likely results from bast fibres (e.g. flax or jute) [43, 58].

At the end of Harappan period from about 1900 BC, new cultures emerged and the fabrication of textiles becomes complex and more mature, resulting from the fusion of different technologies and diverse cultural styles [43].

As a conclusion, from the Palaeolithic to the end of the Harappan period, textile remains found in Indus valley region are not common, possibly owing to the influence of the deposition context [43]. These archaeological fibres were mostly attached to corroded metal artefacts, in particular, copper. The use of plant and animal fibres have both been confirmed. Indirect evidence such as those from fabric impressions are fundamental to document the history of textiles in the Indus area.

1.3 Physico-chemistry of cellulosic textiles: bast fibres

Natural fibres are generally classified into two types: animal fibres and plant-based fibres (Figure 1.13) [59].

Produced by many insects and spider species, animal fibres (e.g. silk) are composed of protein materials [59]. They are formed by anti-parallel sheets of the fibrous protein fibroin (e.g. keratin) [60]. Apart from natural animal fibres, artificial regenerated protein fibres, derived from agricultural materials, are also considered as sustainable and eco-friendly materials regarding their good qualities (soft, high moisture absorbency) [61].

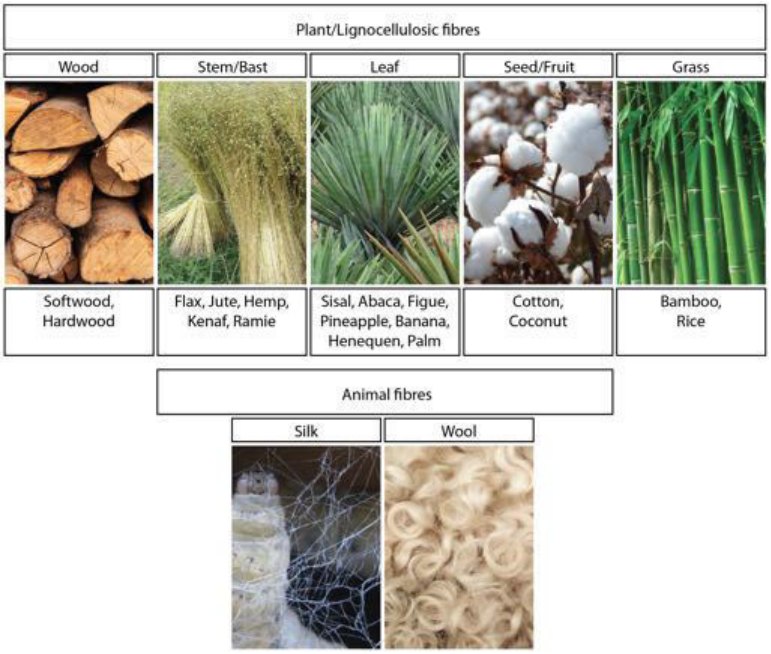

Figure 1.13: Main classification of natural plant-based and animal fibres (modified from D. Chandramohan et al., 2011 [59]).

Plant fibres are derived from different parts of plants, in particular bast, leaf and seed/fruit fibres [59]. A bast centre is a wood core that is surrounded by a stem where a large number of fibre bundles presents, made of single fibre cells or filaments, for example ramie (*Urtica*), hemp (*Cannabis*), flax (*Linum*) and jute (*Malvaceae*). Leaf fibres such

as sisal (*Agave*), abaca (*Banana*) and henequen (*Agave*) are coarser than bast fibres [62]. Today, cotton is the most commonly used seed fibres [59]. Some agricultural residues, such as sunflower seed hulls and bagasse, can also serve as a source of lignocellulosic materials [63] (Figure 1.13).

Considered as the principal source of cellulose, natural plant fibres can be used in many ways as raw materials thanks to their specific properties of high strength, wide availability and sustainability (attracting a renewed interest) as well its density (lighter than most synthetic fibres) [59, 62].

1.3.1 Multi-scale structure and mechanical properties

Extracted from the phloem, a part of the plant vascular system, bast fibres grow in bundles in the inner bark of stems encircling the vascular cylinders [64, 63]. The bundles generally contain an aggregate of 10 to 25 elementary fibres, each with a length of 2–5 mm and a diameter of 10–50 µm.

Plant elementary fibre consists of an internal lumen and cell walls. The lumen is responsible for water transport and surrounded by several cell walls with the appearance of microscopic tubes [62]. The fibre's cell walls are composed of oriented reinforcing semi-crystalline cellulose microfibrils (diameter around 10–30 nm) that connect together in a hemicellulose-lignin matrix. Each microfibril is formed by 30–100 cellulose molecules, in an extended chain conformation which provides the mechanical strength to the fibre (Figure 1.14A). The cementing matrix consists of mainly two compounds: hemicellulose molecules connected by hydrogen bonds forming a cellulose/hemicellulose network and hydrophobic lignin that makes the network more rigid (Figure 1.14B) [62].

There are generally two parts inside fibre cell walls, the primary and secondary walls [62]. The primary wall is composed of closely packed cellulose microfibrils with an irregular loose network. The secondary wall contains three separate layers (outer, middle and inner layer), the thickest middle layer is the most important and could determine the

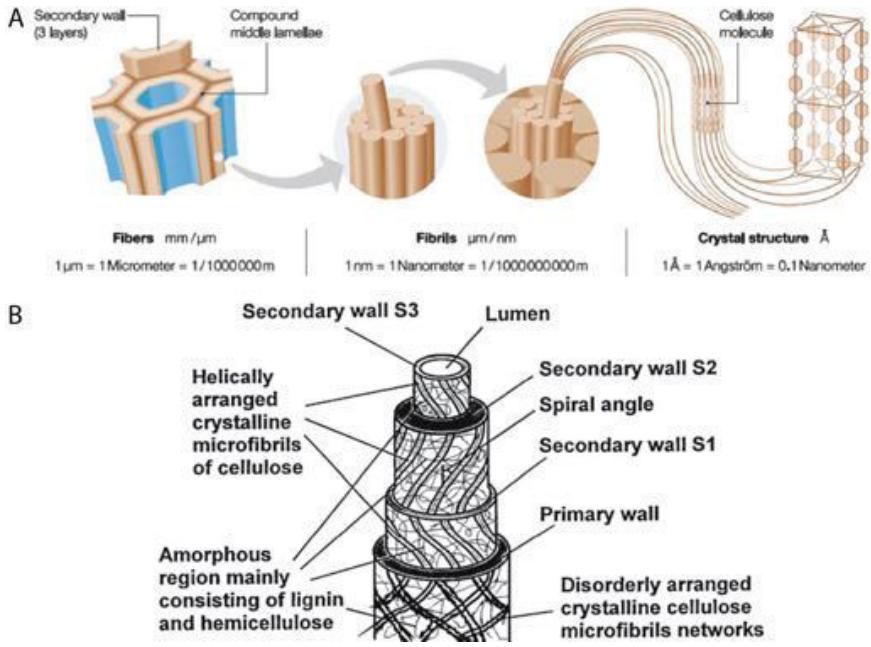

Figure 1.14: Physical organization inside fibres (reused from S. Kalia et al., 2011 [62]). A, Microfibrils and cellulose in elementary fibre. B, Structural composition of one elementary fibre cell.

Table 1.1: Mechanical properties of different fibres. Details refer to S. Kalia et al. 2011 (reused from S. Kalia et al., 2011 [62]).

Fiber	Density	Young's modulus (GPa)	Tensile strength (MPa)	Elongation at break (%)
Flax	1.54	27.5–85	345–2000	1–4
Ramie	1.5–1.56	27–128	400–1000	1.2–3.8
Hemp	1.47	17–70	368–800	1.6
Jute	1.44	10–30	393–773	1.5–1.8
Sisal	1.45–1.5	9–22	350–700	2–7
Coconut	1.15	4–6	131–175	15–40
Cotton	1.5–1.6	5.5–12.6	287–597	7–8
Nettle	1.51	24.5–87	560–1600	2.1–2.5
Kenaf	1.2	14–53	240–930	1.6
Bamboo	0.6–1.1	11–17	140–230	–
E-glass	2.5	70	2000–3500	2.5
Carbone	1.4	230–240	4000	1.4–1.8

mechanical properties of fibres (Figure 1.14B). The fibre diameter, structure, degree of polymerization, source (derived from bast, leaf or seed/fruit), and the growing condition, etc. could all have a great influence on fibre properties. Fibres show a great tensile strength with a combination of higher cellulose content, degree of polymerization (DP) and a lower micro fibrillar angle (the angle made by cellulose fibrils with respect to the axis of the fibre). The composition of these fibre's cell walls vary mainly according to the orientation and spiral angle of cellulose microfibrils, as well as the ratio between cellulose and lignin–hemicellulose matrix (Table 1.1) [62].

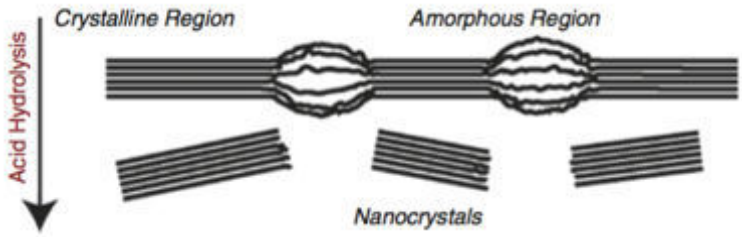

Figure 1.15: crystalline and less-ordered region inside fibre (reused from S. Kalia et al., 2011 [62]).

Cellulosic fibres contain both crystalline and less-ordered regions (Figure 1.15). Different plant materials show various rates of crystallinity. Natural plant fibres have a high degree of crystallinity (65–70%). Whiskers (elongated crystalline rod-like nanofibres) can be formed with the increasing crystallinity of fibrils resulting from the gradual elimination of amorphous regions (e.g. during alkali and bleaching treatments) [62, 65].

Flax is an annual plant whose straight and cylindrical stem is between 0.8 and 1.2 m high with an average diameter of 1 to 3 mm. Flax is grown in humid temperate climates. Planting takes place after spring frosts. Harvesting is done 3.5 to 4 months after sowing when the plants are fully mature. The flax peels off and does not mow down like wheat. Without bundling together, flax fibres tend to dissociate from each other, as the middle lamella contains little lignin (Figure 1.16A) [3].

- In longitudinal view, flax fibres appear as regular cylinders with X-shaped bends

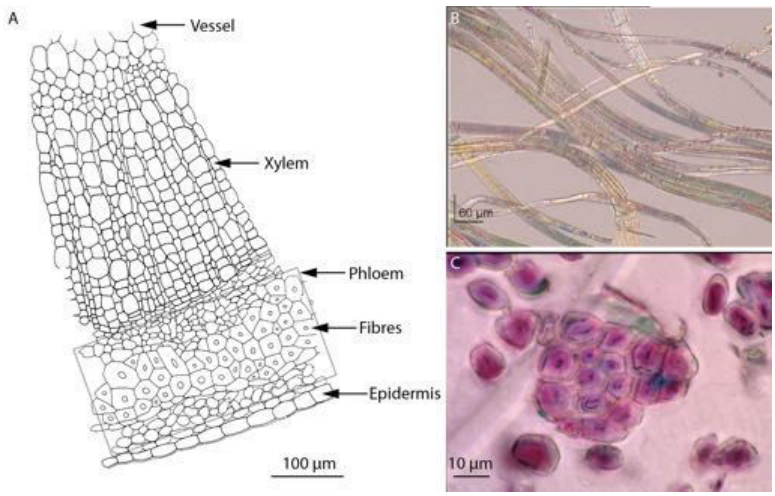

Figure 1.16: The physical structure of flax fibres (modified from C. Moulhérat 2001 [3]). A, Location and characteristic of flax fibres. B, Longitudinal view under optical microscope in polarized light. C, Cross sectional view under optical microscope.

(called *knees*), these particularities are visible in polarized light. When observed, one can see that their extremities either terminate abruptly with a pointed (or clubbed) end or round off. The length of a fibre varies even within a single stem from 2 to 90 mm and the average length is about 22 mm. The natural colour depends especially on the retting process (to facilitate separation of the fibres from the stem): yellowish-grey, bluish-grey (for flax retted in pit), grey-brown (for flax retted on the ground) (Figure 1.16B).

- In cross sectional view, the section is polygonal with rather rounded edges and a small and fine lumen. The diameter of an elementary fibre varies from 5 to 25 µm and the average is mostly around 15 µm (Figure 1.16C).

1.3.2 Chemical composition and reactivity

There are five main compounds forming natural plant fibres: cellulose, hemicellulose, lignin, pectins and waxes (Figure 1.17). The chemical composition of fibres is complicated and differs from plant types. Flax fibres contain about 60–70% celluloses, 17%

hemicelluloses, ca. 10% pectins and 2–3% lignin as well as 2% waxes [63].

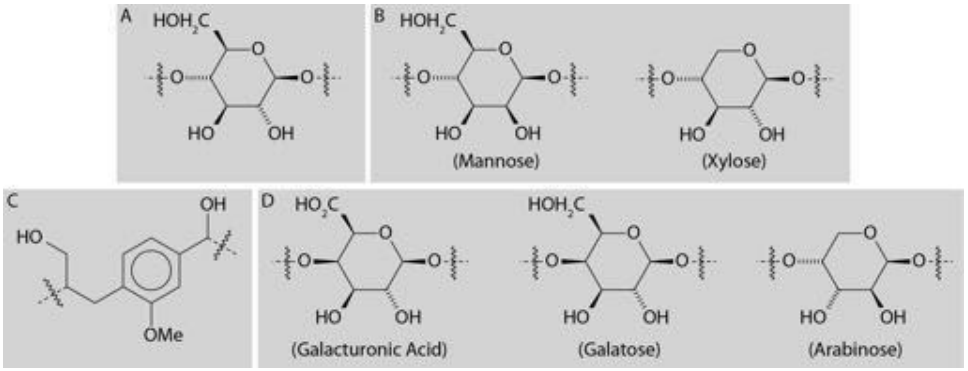

Figure 1.17: Main compounds inside natural plant fibre (modified from P. Garside et al., 2003 [66]). A, Cellulose. B-D, Typical monomers for hemicellulose, lignin and pectins, respectively.

Cellulose

As a basic compound of all plant fibres, cellulose is a linear polysaccharide chain consisting of 7,000-15,000 monomer units of α-D-glucose (Figure 1.17A). Glucose units are connected by the β-glycosidic valence bonds between C_1 and C_4 carbon atoms of adjacent monomer units (Figure 1.18). The repeating unit in cellulose is cellobiose that consists of two α-D-anhydrocopyranose. The number of units per cellulose molecule is considered as half of the degree of polymerization (DP) [67]. Glucose units can alternately rotate 180° because of the C_1-O-C_4 linkage of the pyranose rings (Figure 1.18) [1]. Each unit has three hydroxyls (C_2, C_3, C_6) that can interact with other hydroxyls (or oxygens) groups forming intra- and inter-molecular hydrogen bonds. Long cellulose chains can be formed by two intramolecular linkages: the connection between the hydroxyl group on C_3 and the neighbouring pyranose ring oxygen O_5, and another between the hydroxyls on C_6 and C_2 of neighbouring glucose unit (Figure 1.18A) [1]. Intermolecular linkage can occur by two hydrogen bonds enabling long cellulose chains to form a lateral array in a polymer sheet. Linkage occurs between the hydroxyls on C_6 and C_3 carbon

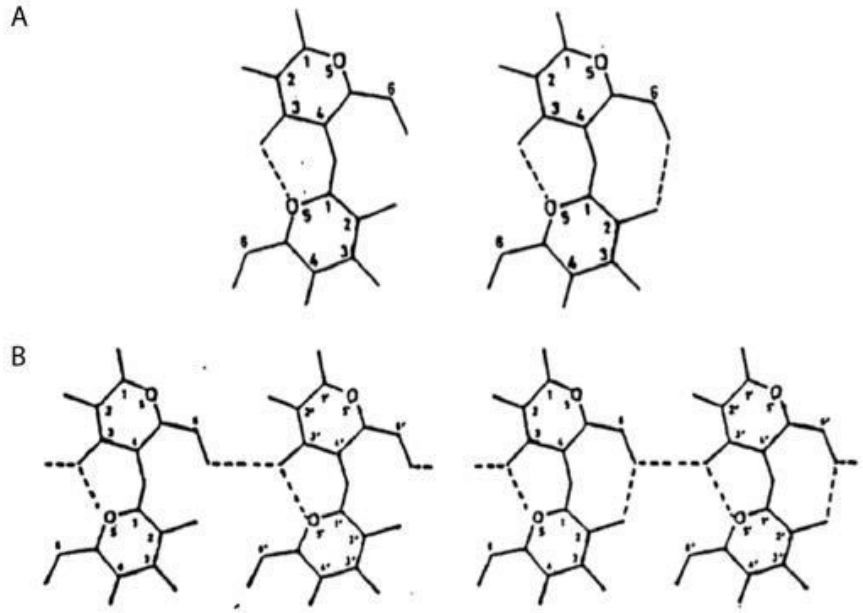

Figure 1.18: Possible linkages between hydroxy groups in cellulose (reused from H. L. Chen 1995 [1]). A, Intramolecular hydrogen bondings. B, Intermolecular hydrogen bondings.)

atoms; another occurs between the hydroxyls on C_3 and the ring oxygen O_5, as well as between the hydroxyls on C_2 and C_6 of the neighbouring units (Figure 1.18B). Finally, a 3D network by long molecular chain sheets held together through weak Van der Waals forces, when all the cellulose hydroxyls groups are occupied in linkages [68]. Cellulose is hydrolysed by acid to water-soluble sugars but relatively resistant to alkali condition and oxidising agents [69, 70].

Hemicellulose

The composition of hemicellulose can vary strongly depending on the different plants [70]. It consists of a group of polysaccharides (except pectin) containing different types of amorphous sugars with 500-3000 monomer units such as xylose, mannose etc (Figure 1.17B). Compared with cellulose, hemicellulose shows a certain degree of chain branching and has short chains as well as a lower DP. Hemicellulose can combine with

cellulose after the removal of lignin. In diluted alkalis, hemicellulose is readily dissolved [70].

Lignin

Formed from hydrocarbon polymers, lignin contains both aliphatic and aromatic compounds like p-hydroxyphenyl (H) and guaiacyl (G) (Figure 1.17C). With lower mechanical strength than cellulose, lignin shows a completely amorphous structure and makes plants rigid. Lignin cannot be hydrolysed by acids but it can react with hot alkali and oxidising agents, and is readily to be condensed with phenol [62].

Pectins and waxes

Pectins are formed of polygalacturonic acid which is a group of hetero-polysaccharides (Figure 1.17D). Pectin gives plants flexibility, it can be neutralized in alkali environments and then becomes soluble in water [62].

Waxes have a complex composition, they are mixtures of long-chain hydrocarbons with a number of substituted long chain compounds, such as fatty acids, primary and secondary long chain alcohols, ketones and aldehydes, esters of fatty acids and long chain alcohols. They are normally present in a minimum percentage in the fibres and they are insoluble in water and in certain acids [71, 72].

The reactivity of fibres depends on the available hydroxyl groups at the surface and in the bulk inside cellulose as discussed above [68, 69, 70]. These hydroxyl groups can interact with water via hydrogen bonding. In less-ordered regions, all the hydroxyl groups are able to interact with water, while in crystalline zones, a small number of surface interactions are observed. The amount of water absorbed in fibres is determined by the relative humidity (RH), atmosphere, cellulose purity as well as the degree of crystallinity [1].

The physical structure (external morphology, internal cross-section, shape, etc.) and

chemical composition can have significant influence on the physico-chemical properties of natural fibres [59, 62].

1.4 Production of cellulosic textiles

As a complicated and time-consuming process, textile production in ancient times, from raw material to final product, required particular know-how and several specific tools. Composed of bone, clay or stone, these tools were sometimes found in archaeological sites during excavations and considered as an important source for the study of ancient textiles. According to the stage of the chain of operation, different tools were used for the preparation of raw materials, the production of thread and textile (twisting and weaving), dyeing, and textile finishing (Figure 1.24) [29]. The exchange and trade of textile are beyond the scope of this section.

The complexity of the procedure stresses the relevance of archaeological textiles as records of ancient human craftsmanship. The way that fibres were selected and textiles were processed are important indications of the knowledge and technological skills reached by a civilization. For example, mineralized flax textiles attached to foundation pegs held in the Louvre Museum collections show a high-level of technology which is substantiated by the yarns fineness (see Subsection 3.1.3). These characteristics suggest that the whole process for fibre treatment was faultlessly mastered [73].

1.4.1 Extraction of fibres from plant

The great majority of textiles that have come down to us from ancient Egypt were made of flax, which was also used throughout the Eastern Mediterranean and Western Asia [74, 3]. According to depictions, ancient Egyptian flax seems to have grown to about waist height and was harvested by pulling from the ground, often when they were still green. Afterwards, they were likely soaked in water several times to separate the fibres from the

woody part to facilitate their extraction. This process is still known in modern industry as “retting”, which includes biological, mechanical, chemical and physical fibre separation (Figure 1.19) [62]. Among these various retting methods, microbial/enzymatic retting (belong to biological or physical retting), is an effective technique to extract cellulosic fibres in good quality from natural plants such as flax, hemp, and jute. With the help of appropriate fungi which remove the pectin link among fibre bundles, and improve the separation of cellulosic fibres from fibre bundles through enzymes produced by fungus. The separation and extraction process of fibres is very important to fibre yield and to its final quality, as well as its properties, colours, structure and chemical composition.

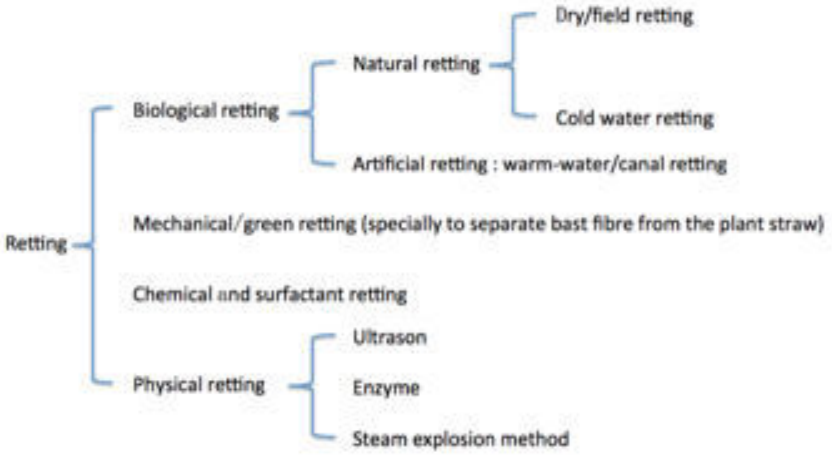

Figure 1.19: Different retting methods for extracting fibres.

Retting was completed by air drying. Drying was essential for ensuring the efficacy of the successive steps. In modern industry, drying is carried out with warm air (50-60°C in furnace) or by infrared radiation [75].

After retting, the second step consisted of “breaking” the dried materials. This process improves the separation of the bast fibres from the xylem (i.e. the wood tissue). The flax stems were beaten along their entire length, either manually or with a wooden break-machine, until the stalks became soft (Figure 1.20).

The third step, “scutching”, consisted of eliminating the pith (a tissue in the stem)

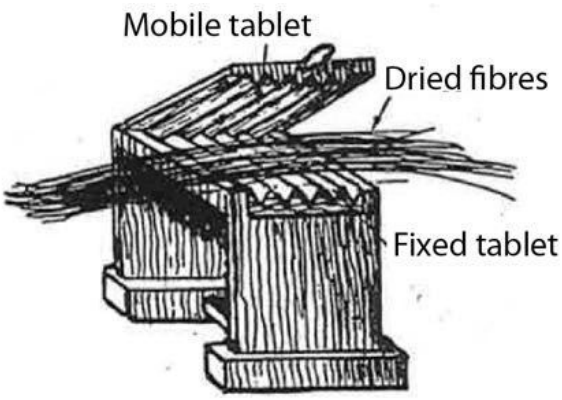

Figure 1.20: Wooden break-machine during beating process for dried fibres (modified from Le Fustec 1964 [75]).

fragments from the beaten fibres. A wooden board was placed vertically and the fibres were hung from its top. A scutching knife was then scraped along the fibres until all the stem fragments were removed.

In order to obtain individual fibres, the fourth step consisted of "combing" the processed flax from previous steps. The processed flax was combed to separate the long fibres from the short and broken fibres that made up the tow. After combing, the fibres were soft to handle, becoming smooth with a fairly shiny appearance. Then, they were ready for further operations required to produce threads ("twisting"), and to fabricate textiles ("weaving") [75, 63].

1.4.2 Twisting

The fibres are twisted into yarns or threads during twisting. The tool used for this process is the spindle-whorl, which could lead to a number of twisting methods [3].

Several combed filaments are pulled and gathered on the drill, which would next be rolled to create thread by torsion. Then the thread could be rolled into a ball or skein. Yarn can also be spun with two hands or rolled on the thigh, without using spindle. However, this time-consuming primitive twisting method was not effective because the

thread would be easily come undone and would be irregular. To overcome this, a piece of finished thread can be strengthened by using a little stick, on which a slit can help to fix the thread. This useful stick can be considered a proto-spindle which no longer relies on the spinners hands. The addition of a weight at the base was necessary to hold the moving spindle when producing thread by turning, leading to the fabrication of spindle-whorl. In this way, the resulting thread was strengthened and became more regular [3, 26]. These twisting tools were usually found along habitats. For example, the spindle was often made of hazel tree or viburnum and the spindle whorl of a found piece of broken ceramic, or a stone, or more commonly, a piece of wood in ancient Bologna (Italy). (Figure 1.21)

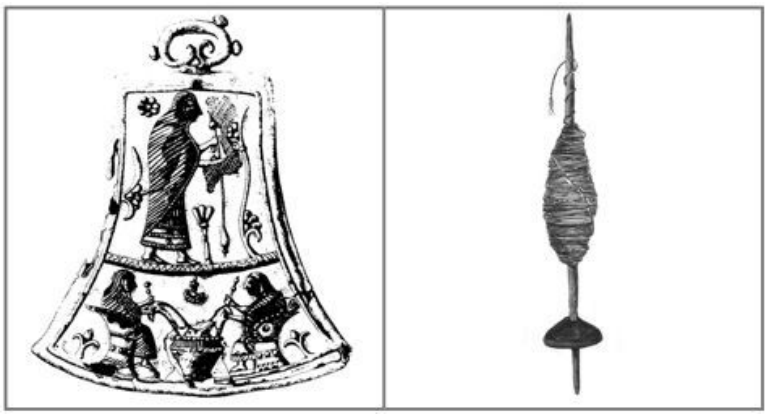

Figure 1.21: Scene of twisting depicted on a bronze bell discovered in a tomb at Bologna in Italy (left) and representation of spindle-whorl (right) (reused from C. Moulhérat 2001 [3]).

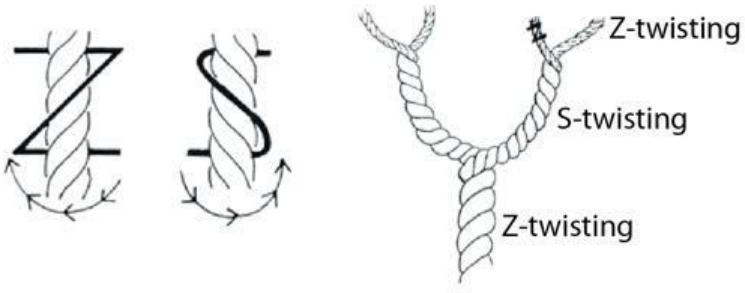

Figure 1.22: Twisting modes of fibre and õr thread (reused from C. Breniquet 2008 [26]).

The twisting mode of thread follow an S or Z torsion (Figure 1.22) depending on the rotation direction given by the spindle. Flax fibres have a natural S-twist after drying due to the fibrillar orientation [76]. When a Z-twist is observed in archaeological linen textiles, it means that the twisting was carried out in the opposite direction with respect to the natural one. This is often attributed to right handedness of the spinner [77].

One can create a more solid thread by twisting two simple threads to create a twisted yarn. These two threads can be spun in opposite directions to their original twisting mode to obtain a durable thread (2s : Z or 2z : S) (Figure 1.22) [26].

1.4.3 Weaving

Weaving involves placing threads on a loom and turning them into fabric or cloth. Depending on the kind of crossing, different weaving patterns may be obtained, such as a plain tabby in which one warp crosses each weft yarn (Figure 1.23A and B).

In general, looms fall into two main categories: horizontal and vertical (Figure 1.23C). The warp yarn was generally fixed in a horizontal loom, as shown by the tablets found at the archaeological site of Susa [77]. When using a vertical loom, the warp was fixed to two poles and kept stretched with weights, usually stones, in order to weave from top to down.

1.4.4 Dyeing

The range of dyes used in Antiquity is wide [78]. Each culture had its own dyeing traditions and materials that related to the nature of its flora and fauna. The presence of coloured elements in a textile fragment can come from:

- the natural colour of fibres, such as sheep wool that has been used in a variety of colours from creamy white to deep brown;
- dyes that can have various origins like plants (e.g. red from safflower, blue from

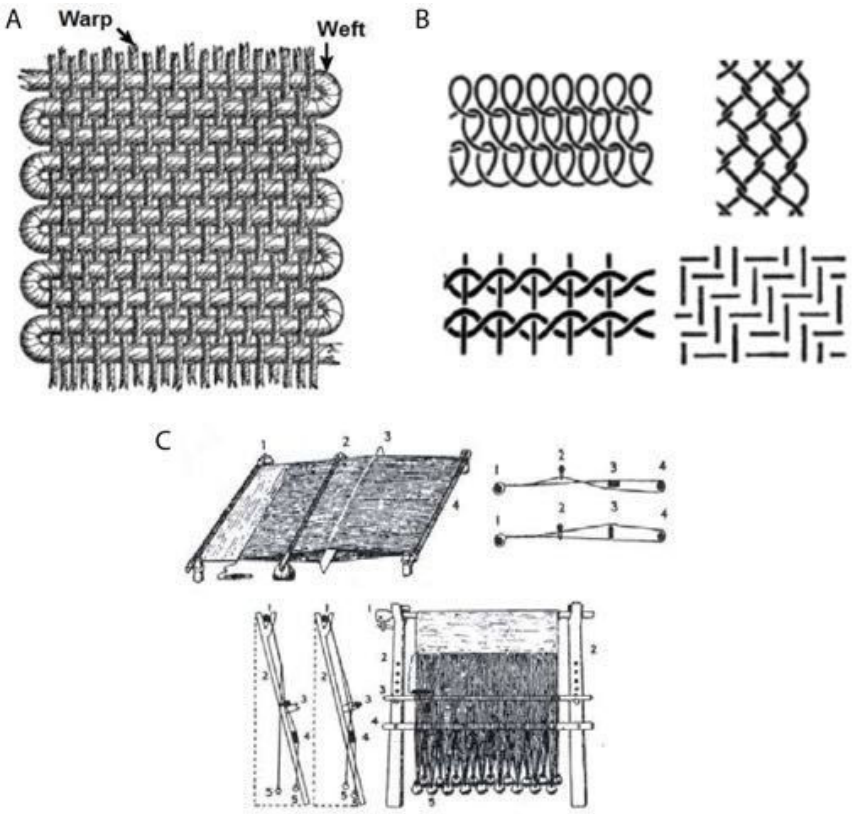

Figure 1.23: Weaving modes and tool. A, Tabby plain weave mode (reused from G.-V. Agnès 2008 [77]). B, Other weaving modes: knitting (top left), sprang (top right), code (bottom left) and twill (bottom right) (modified from C. Breniquet 2016 [28]). C, Representation of horizontal (up) and vertical (bottom) loom (reused from C. Breniquet 2008 [26]).

woad, etc.) and animals (e.g. purple from seashell, red from kermes, etc.) as well as some natural minerals (e.g. green from malachite)

Two main dyeing techniques were used in ancient times, including [79]:

- direct dyeing by simply macerating or boiling certain plants in water. This gives a dyeing bath in which fibres can be immersed. Bath temperatures vary depending on the nature of fibres and dyes.

- mordant dye. Most of the dye molecules that humans have learned to extract from plants and animals cannot bind firmly to textile fibres. However, a large number of dye molecules can combine with various metal salts because the structures of dye molecules have one or more chelating sites (term introduced by chemist G. Morgan and H. Drew in 1920 to characterize the complexation between a dye and a metal). Ancient dyeing took advantage of this property very early to fix these dyes on the fibre. It was thought that the metals adhere to the fibre on which they attracted in turn the dyes. In addition, the nature and concentration of mordants greatly affect the tone and saturation of the dyeing obtained.

In practice, the stage at which dyeing occurs, with mordant if necessary, varies according to the textile fibres used and the desired effects [80]:

- dyeing before twisting or dyeing on fleece mainly concerns wool and animal hair;

- yarn dyeing is widely used for all types of fibres. It requires that skeins are carefully attached to each other.

- piece dyeing requires large containers in which the pieces of textiles can be stretched in the dyeing baths with the help of a lathe in order to avoid irregular dyeing.

1.4.5 Finishing and embellishment

After weaving, the textile would undergo several final treatments in specific workshops for use, including cleaning, softening and drying. A special press could also be used by fullers to produce pleats as seen in some ancient depictions. Other tools, such as a wide range of needles of various sizes were available for decoration purpose if necessary, like embroidery, coloured stripes, and fringes [3].

The following figure schematically illustrates the "life" of archaeological textiles (Figure 1.24). It contains the stages of their preparation, finishing, use, abandonment and excavation. The preservation of textiles is based on many factors introduced from preparation to abandonment.

The processes of textile production nowadays are still very similar to those in ancient times. The developed twisting or weaving techniques coupled with the complexities of the finishing and colouration steps result to a more efficient conversion of fibre into a wide range of final textile product.

1.5 Conclusion

Acting as one piece of significant archaeological evidence, textiles can reveal clothing style and are helpful to identify social status. They were used for decoration, diplomatic and exchange purposes. Textiles also provide clues on raw materials used and related techniques. Knowledge of ancient textiles can be supported by different sources like written records and excavated tools.

Dominant textile in ancient Mesopotamia were mainly made by flax and wools, their uses can be deduced from several depictions due to the rarity of real textile remains. The existence and use of textiles in the Indus region were also shown through indirect evidence like twisting-weaving tools and figurine depiction. In addition, some textile residues were discovered attached on several artefacts of different nature (ceramic and

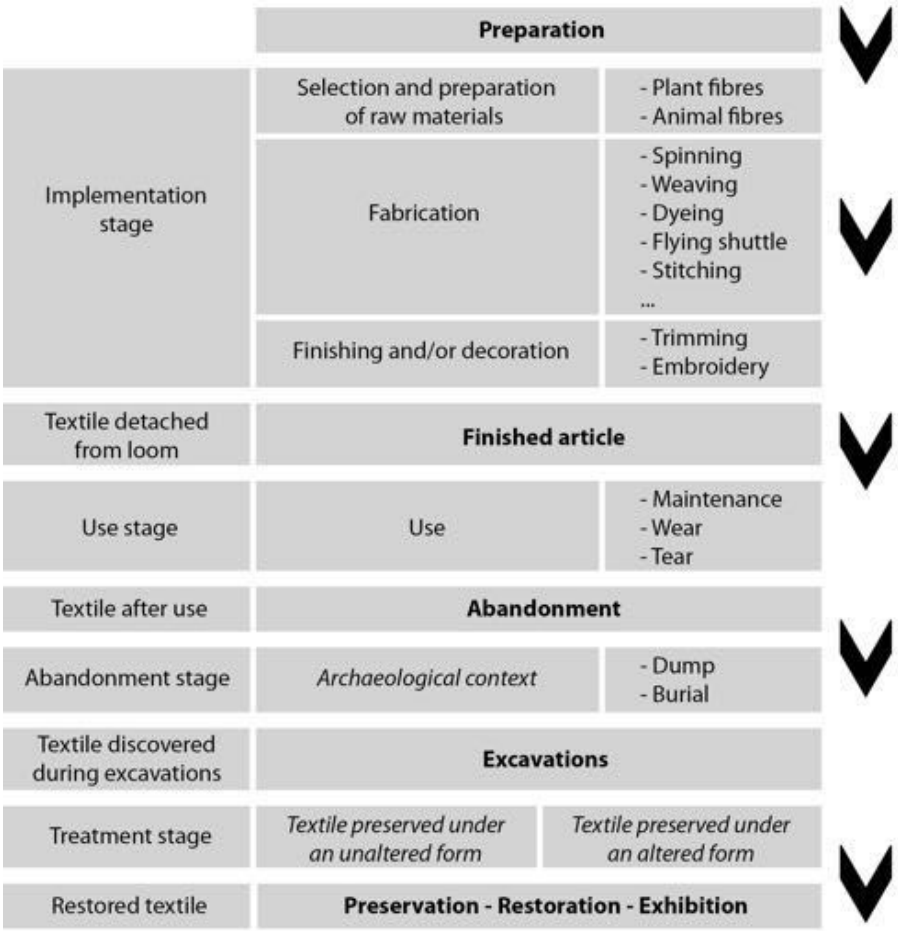

Figure 1.24: Different stages composing the "life" of archaeological textiles (modified from C. Moulhérat 2001) [3].

metal, etc.).

As the raw material of textile, plant fibres possess multiple cell walls structure and good mechanical properties. The main components of cell walls are cellulose and a cementing matrix consisting of hemicellulose and lignin. The hydroxyls in cellulose can form intra- and inter-molecular hydrogen bondings, those existing in amorphous regions reacting first. The production of textiles in ancient times includes many steps beginning with the preparation of raw fibres from plants ending with textile finishing and decoration.

The following chapters present a review of the literature on the study of mineralized textiles in archaeological contexts and provide a summary of the main physical and chemical mechanisms of the degradation of textiles.

2

Taphonomy of archaeological cellulosic textiles

This chapter reviews the current status of physico-chemical studies performed on mineralized textiles and corroded metal supports. It discusses the different degradation pathways of natural plant fibres and presents a brief overview of exceptional preservation processes of archaeological textiles. Current literature and analytical methods used in the study of mineralization mechanisms and influencing environmental factors involved are introduced. Related corrosion mechanisms of copper-base artefacts are also reviewed.

Contents

2.1 Degradation of cellulosic fibres

The chemical stability of a cellulosic fibre depends on several factors such as relative humidity, heat, light, atmospheric gases, acids and pH [59]. The degradation processes of fibres are irreversible, leading to the deterioration of their mechanical properties and poor organoleptic characteristics (senses experienced by an individual) like colour and odour [81]. In addition, biological and mechanical attacks play a role in the degradation of fibre, particularly in a burial environment [82].

In plant fibres, organic constituents (chemical composition refers to the Subsection 1.3.2) have different responses to environmental factors during fibre degradation processes [83]. Hemicellulose is prone to thermal degradation due to its low resistance to heat. Lignin is proved to be more thermally stable, whereas its presence can result in photochemical degradation under UV light when fibre is exposed outside [83]. Since cellulose is the main component of plant fibres, special focus is given here to its degradation. The main chemical processes of degradation of cellulose include hydrolytic, oxidative and microbiological degradation.

2.1.1 Hydrolytic degradation

Cellulose is resistant to the attack of alkaline solutions at low concentrations and it is insoluble in water and many organic solvents (alcohol, benzene, ethyl ether, carbon tetrachloride) mainly due to its linear and rigid structure [84]. As a polyhydric alcohol, cellulose can react with acids. It is soluble in concentrated mineral acids such as hydrochloric acid, hydrobromic acid, nitric acid, sulfuric acid and phosphoric acid. Among the organic acids, only trifluoroacetic acid appears to have sufficient solvating power to dissolve cellulose [84]. This dissolution is generally accompanied by a strong degradation of the cellulose molecule via hydrolysis in two steps [8, 85]:

- the separation of the polymeric sheets through breakage of the intra- and inter-

molecular hydrogen bonds forming hydrocellulose.

- the breakage of the molecular chains at the 1,4 β-glycosidic link, resulting in a shortening of the polysaccharidic chains and the subsequent formation of cellobiose (a disaccharide $C_{12}H_{22}O_{11}$).

The breakage of the cellulose molecular chains with the presence of acids is shown in Figure 2.1 [86]. This process occurs for both amorphous and crystalline regions, with the latter more resistant than the former. Cellulose still retains some fibrous character during decomposition [86].

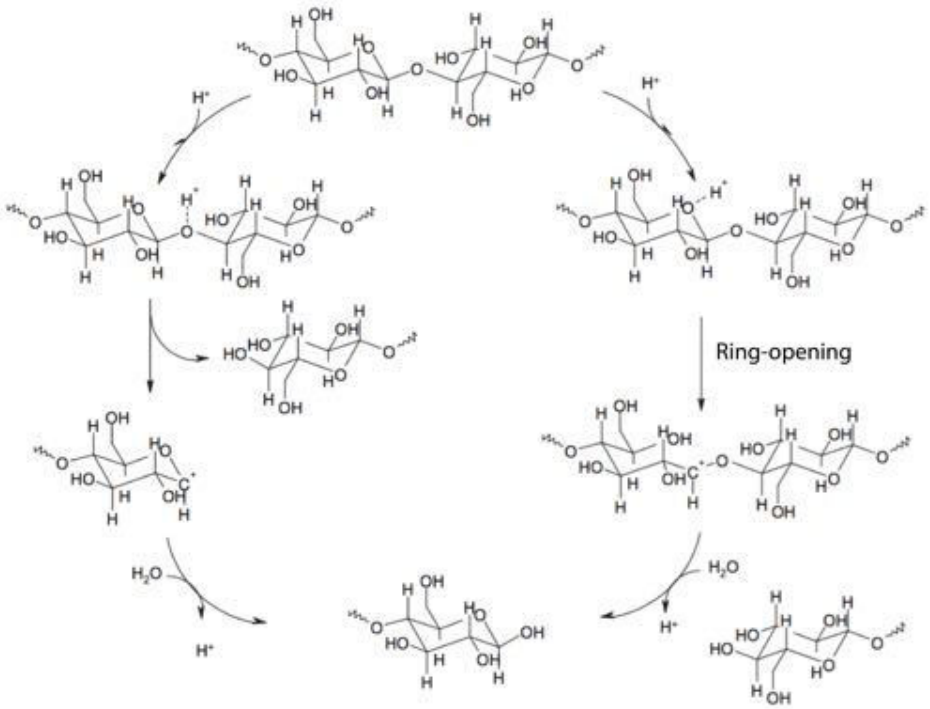

Figure 2.1: Purposed mechanism for the acid hydrolysis of cellulose (reused from L. Fan et al. 1987 [86]).

2.1.2 Oxidative degradation

The degradation of cellulose through oxidation happens when there are oxygen-based chemical agents present in a surrounding *warm* environment [86]. This process occurs readily in basic conditions [87], leading to the production of oxycellulose [88, 89].

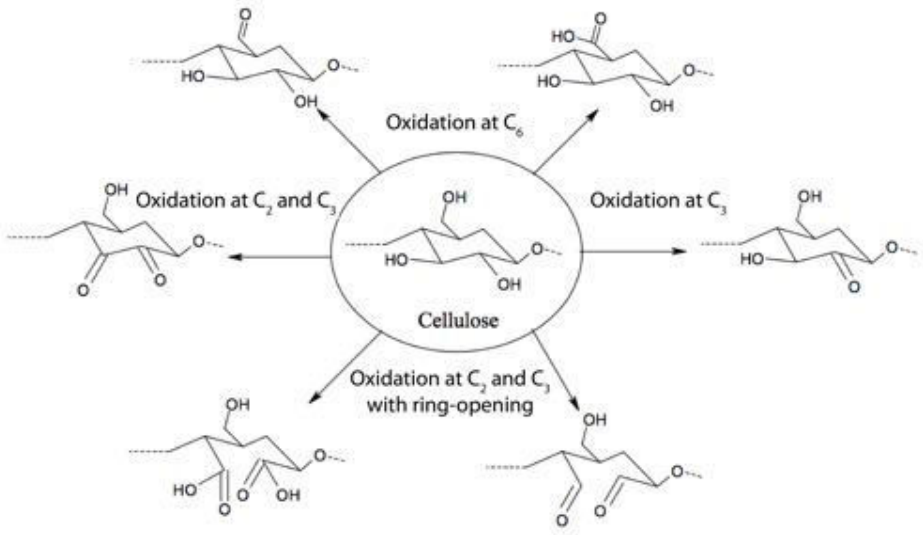

Figure 2.2: The oxidation process of cellulose (modified from J. Le Roux 2003 [90]).

During the oxidation process, pyranose rings are broken and the hydroxyl groups are oxidised into aldehyde, carboxylic acid or carbonyl groups [70] (Figure 2.2). The latter functional groups may then ease glycosidic bond breakage. However, the products of the oxidation are generally determined by the nature of the oxidising agents and the conditions in which the reaction takes place, the key influencing factors are particularly pH and the reduction potential (Eh) of the system.

Under alkaline conditions, the process can cause the fibre to swell and thus increase the internal surface area, which becomes more accessible, with a subsequent decrease in crystallinity and a relaxation of the structural bonds between lignin and carbohydrates [70].

Transition metals like copper and iron can also cause the oxidation of cellulose if one

considers their corresponding oxidation/reduction potentials [91]. Acting as a catalytic agent, their existence can result to an increased production of hydroxyl groups during the chain scission of cellulose. Moreover, studies on chemiluminescence of metal-containing cellulose during its oxidation process have shown that copper is more catalytically active than other transition metals as the amount of hydroperoxides (unstable species in cellulose) decreases [92].

2.1.3 Microbiological degradation

In the presence of microorganisms, the biodegradation of fibres can be divided in three categories, each of which is the successive step of the previous one [93, 94]:

1. Biodeterioration. Direct contact between microorganisms and the surface of fibres leads to several combined effects such as thermal and mechanical degradation.

2. Biofragmentation. Due to the enzymes and free radicals secreted by microorganisms, biofragmentation allows the degradation of polymer chains in fibres into monomers.

3. Assimilation. This process leads to the complete decomposition of monomers into simple products (gaseous molecules and salts).

Biodegradation mechanisms can be divided into two main types, aerobic and anaerobic, that is, in the presence of oxygen or without oxygen [95]. The complete biodegradation of organic compounds ultimately leads to formation of carbon dioxide and water as well as other naturally occurring minerals (e.g. HNO_3, H_3PO_4) [93].

The rate of biodegradation of materials could generally be affected by their own chemical properties, on the one hand, and by environmental factors such as the population quantities of soil microorganism, temperature and water and oxygen content, on the other hand [96, 97]. Specially for cellulosic fibres, the degradation rate depends on three main aspects:

- The type of microorganisms [96]. Microorganisms are present both in the atmosphere and in the soil, with a greater abundance and variety of microorganisms in the soil. Bacteria and fungi are the most common microorganisms. They can break the chemical bonds of the polysaccharide chains of cellulose to produce glucose [98]. Germination (the process of growth of microorganisms) occurs when bacteria and fungi come in contact with the fibres in a moist environment at an appropriate temperature. First, digestion of the non-cellulosic outer layer (cuticle) takes place. Then, the cellulosic walls are attacked by bacteria or fungi. Bacteria develop into small spots and cannot penetrate the fibres, they agglomerate in the outer cellulosic layer and flow. In the case of fungi, they develop into long filaments and can diffuse from the secondary wall of the cellulose into the light. Both bacteria and fungi can cause a decrease in the degree of polymerization of the fibers, which destroys their internal structure and resistance.

- The structural properties of the fibres, such as the degree of crystallinity of cellulose and the compactness of the polymeric/molecular chains [99]. Less-ordered regions were found to be more readily degraded than the crystalline regions (see Subsection 1.3).

- Environmental conditions [88]. For example, high salinity can decrease the rate of biodegradation. Acidic conditions promote hydrolytic degradation, whereas alkalinity contributes to cellulose degradation by oxidation in aerobic conditions further favouring microorganism growth.

- The presence of non-cellulosic constituents in fibres and the degree of orientation of cellulose crystallites (see Subsection 1.3.2). For example, jute fibre is less sensitive to biodegradation than cotton due to the high amount of lignin in jute fibre [100].

Minor constituents of fibres like hemicellulose and pectin are also susceptible to be decomposed by microorganisms and may promote the activities of specific invading

microorganisms in textiles [101].

When buried underground (direct contact with soil, i.e. a typical archaeological context), the main cause of disintegration of fibres has been reported to be the activities of microorganisms [82]. Other degradation pathways like photolytic and photoxidative effects caused by ultraviolet [83] are unlikely for textiles that are not exposed to light [88]. As described in the work of K. Arshad et al (Figure 2.3) [95], due to the natural rigidity of flax fibres, a looser woven structure than with other raw fibres is often obtained after twisting and weaving (see Section 1.4). Biodegradation of linen is therefore more severe than other plant fibres. This can lead to difficult separation between fibres and soil only after two weeks. When textiles are only exposed to soil (i.e. one side of the textiles contacts with the soil), biodegradation is slower due to the limited penetration of microorganisms into the textile fibres.

2.2 The preservation of archaeological textiles in different contexts

Compared to objects made of metal, stone, pottery or glass, ancient textiles are uncommonly excavated materials due to their organic nature [1]. They begin to deteriorate from the moment they are made and used [3]. There are, however, some specific contexts leading to the preservation of textiles [3]. In these contexts, the precious discoveries of ancient textile remains make it possible to explore aspects still little documented such as the selection of raw material, the costume, the textile machinery or the funerary practices from Prehistory to Antiquity (see Subsection 1.1.2) [102]. The study of archaeological textiles is intrinsically linked with their modes of preservation [3].

Depending on the circumstances, textiles can be preserved in various forms: charred, dehydrated, soft or mineralized as described below [3]. Moisture, cold, dryness, soil composition and physical characteristics, contact with metal and clay constitute most

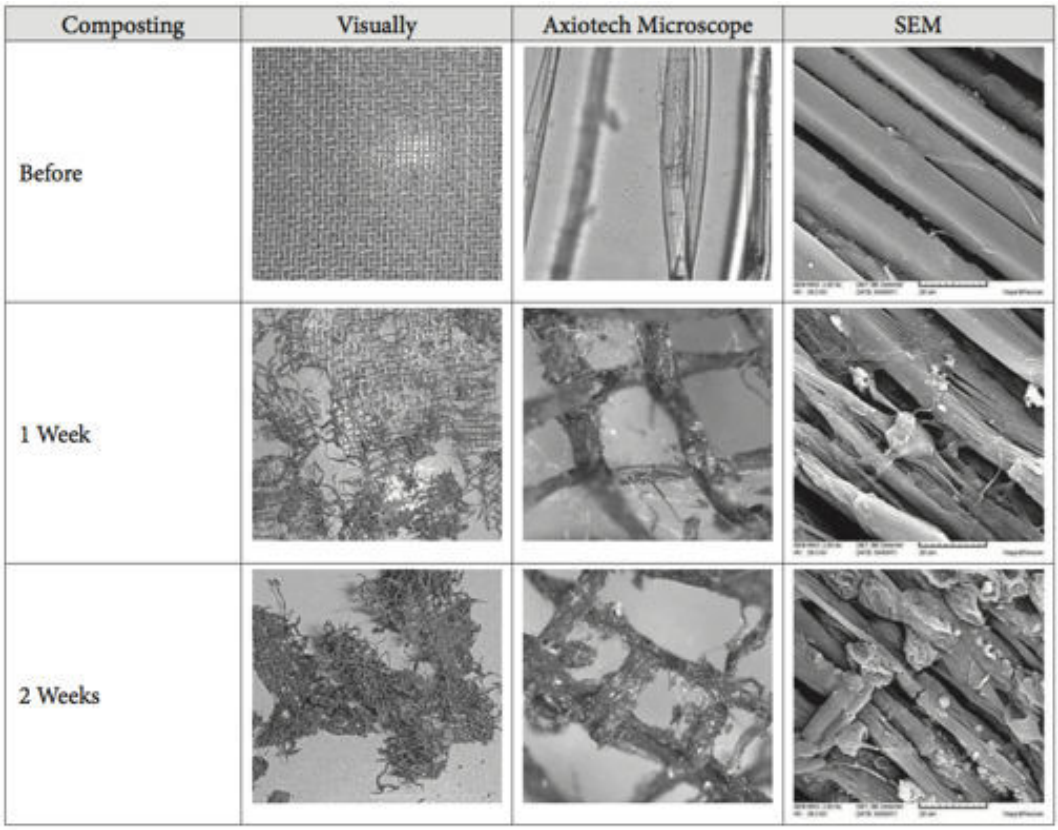

Figure 2.3: Biodegradation of linen buried in soil (reused from K. Arshad et al. 2014 [95]).

favourable environment for the preservation of organic materials like textiles [1].

2.2.1 Textiles preserved in extreme and specific contexts

Textiles preserved under extreme conditions

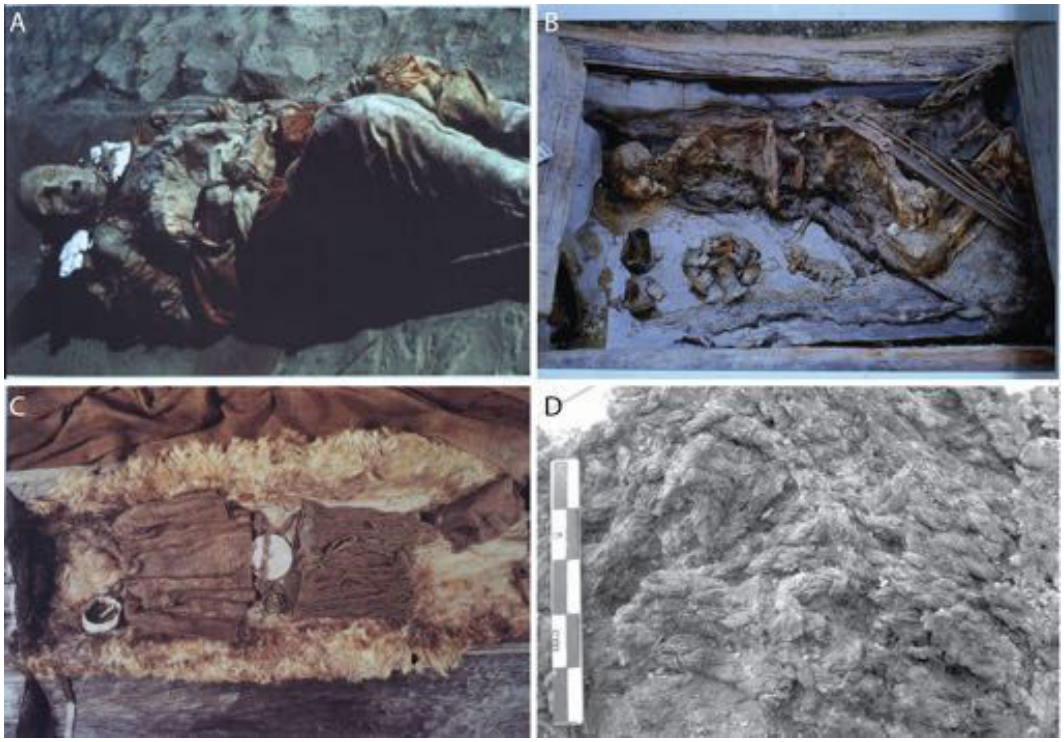

Figure 2.4: Exceptional preservation of textiles in different extreme conditions. A, Chinese mummy and organic tools (birch bark boxes, wood bow, etc.) found in the Taklamakan Desert in Xinjiang (China) and dated between the 8th and the 5th century BC (reused from C. Moulhérat 2001 [103]). B, Frozen burial discovered in southern Siberia (2nd century BC) (reused from C. Moulhérat 2001 [3]). C, Excavation of a deceased placed in an hollow tree trunk under a mound at Egtveg in Denmark (middle of the 2000 BC) (reused from C. Moulhérat 2001 [3]). D, A carbonised net (4000 BC) made by the leaves of a local palm species found at Shahi-Tump (Pakistan) (reused from R. Thomas et al., 2012 [104]).

- Extreme drought. Drought is at the origin of spectacular discoveries where little damaged tissues have kept their suppleness and original colours (Figure 2.4A) [103,

3, 105]. These finds are usually located in arid areas such as desert. These contexts are generally stable and do not contribute to bacterial activity.

- Extreme cold. Cold climatic contexts also include magnificent discoveries from deposits buried in permafrost, such as burials in Mongolia (Figure 2.4B) [3]. Cold can act as an anti-bacterial agent that prevents chemical reactions in aqueous solution [106, 107, 108]. The difficulty lies in the stability of post-excavation conservation conditions for discovered artefacts.

- Extreme humidity. Wetlands, lake shores, rivers, peatlands and swamps are environments conducive to the preservation of organic materials including textiles, wood, leather, bone, skin, hair, etc. Such medium can provide an almost anoxic environment (Figure 2.4C) [3]. The lack of oxygen protects organic materials from bacterial activities which, in other circumstances, destroys them. Sheltered from air, the lime mud of the lakes constitutes an alkaline environment favourable to the preservation of materials of vegetable origin as cellulose is resistant to the attack of alkaline solutions [109] (see Subsection 2.1.1). In the same way, peatlands, considered as an acid environment, are very favourable to the preservation of materials of animal origin because of the relative stability of proteins in this context [110, 111]. The concomitant action of an acid medium and moisture in the lack of oxygen causes a kind of natural mummification (i.e. a process in which the skin and organs of a corpse have been preserved [112]).

- Extreme heat. Increases in temperature (fire, oven, etc.) are an important factor in the morphological preservation of textile fibres. In Figure 2.4D, a carbonized skeleton of the original textile is legible and identifiable [104]. When textile fragments are buried as funerary objects in the tomb sheltered from air, they carbonize slowly due to the incomplete combustion of funeral pyre (firewood used in cremation) caused by the ambient humidity, leading to the preservation of their mor-

phology [113, 114]. The shape of fibres is often sufficient to determine their nature based on the observation using optical microscopy and SEM. However, the diameter of fibres can decrease after carbonization, resulting in a difficult identification of their origin [3]. Strong pressure inside the burial chamber can produce, like in a charcoal kiln, calcination of burial objects [115]. Textiles can also be calcinated if they are exposed to high heat in a rarefied atmosphere where the content of oxygen is very low [104].

Textiles preserved through close or direct contact with other artefacts

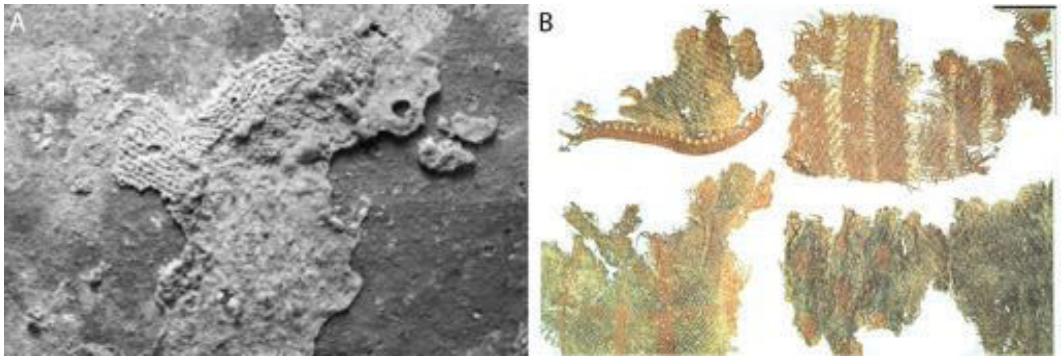

Figure 2.5: Exceptional preservation of textiles through close or direct contact with other artefacts. A, Calcified textiles attached to a clay urn (Tuscania-Tarquinia, 2nd-1st century BC) (reused from M. Gleba et al., 2005 [116]). B, Several well preserved wool fragments found in the salt mines of Hallstatt, Austria (8th century BC) (reused from C. Moulhérat 2001 [3])

.

Most excavated textile remains have been preserved through close or direct contact with minerals. For example, close contact with clay artefacts allows preservation of textile remains through calcification [116]. As shown in Figure 2.5A, textile fragments were used as containers for the urn in which bones ashes were found, the textiles are thus considered as “clothing” of deceased persons [117]. Other mineral salts (e.g. rock salts and corrosion products of metal artefacts) can also contribute to the preservation of textile remains as detailed below (Figure 2.5B).

2.2.2 Textile impressions, textile pseudomorph or mineralized textile?

Interest in archaeological textile remnants which are still attached to copper-base artefacts dates back at least to around 1880, according to the excavation works carried out by E. de Sarzec in Tello (current Iraq) [30]. He noticed the presence of "imprint of a textile [l'empreinte d'un tissu]" on the surfaces of some corroded copper figurines and hypothesized they were previously wrapped. H. de Genouillac, during subsequent excavations in Tello, found "traces of adhering textile [traces de tissu adhérent]" attached to different copper artefacts (e.g. figurine, vase) [118]. He hypothesized these woven textiles were of good quality either made by linen or wool. M. L. Lecaisne described in 1912 "textiles covering copper axes [les tissus recouvrant des hâches de cuivre]" based on artefacts excavated from Susa (current Iran) [119]. His first study was completed by R. Pfister in 1943 [120]. The study of these textiles or impressions were limited to general morphological observations and their usage as wrapping material at that time, without any detailed research on physical structure or chemical composition.

In the works of V. Sylwan from 1930, she identified some textile fragments of silk preserved by a corroded bronze axe from the Yin Dynasty (early Shang Dynasty, 1675-1092 BC) in ancient China [121]. Then, during her studies on the finds excavated from the site of Aurel Stein in Central Asia, she also noted the presence of silk fabrics covered with corrosion products on Chinese bronzes of Shang (1500-1000 BC) and Han (206 BC-220 AD) periods. To describe these fabrics, she used the terms "textile remains", "textile traces" or "textile tracks". The choice of these generic terms do not give a precise idea of the state of conservation of textiles. This is likely because she thought that these textiles are only covered with a layer of corrosion products under which the fibres are still preserved [122].

Around the same period, in 1941 A. C. Whitford studied pieces of fabric wrapped around copper sheets. They were found in Ohio (USA) and belonged to the Hopewell

culture (400-200 BC). Since the main objective of this work was to identify fibres of different species, instead of paying close intention to the preservation states, the author only described these fabrics as “copper stained rope” or “fibres adhering to copper sheet” [123]. Further studies forty years later concerning the mineralized textiles excavated from Ohio Hopewell sites were also focused on better understanding of the culture and society, than on preserved textiles themselves [124].

The real starting point for the studies of mineralized fibres began around the early 1960 with L. Biek’s work. In his publication he used several geological terms, including “pseudomorph” and “petrification”, to depict archaeological textiles found in association with metal artefacts in burial environments, which preserve their morphology due to mineral formation [5]. Biek describes pseudomorphism as a “replacement [that] can take place literally molecule for molecule”. From this work, other British researchers have extended the study to all organic materials, such as the identification of textile fibres and the technical study of tissues performed by H. M. Appleyard [60]. However, their interests were mainly focused on the information involved in the metallic gangue (formed by corrosion products) and not on the mechanisms related to the phenomenon of mineralization of fibres.

Meanwhile, an American researcher, D. L. Carroll, also continued L. Biek’s work. She found the presence of textile impressions on the underside of an Etruscan bronze bowl (500-400 BC) in Vei. In her publication, she used the term “impressions” and “fossil textile”, the term “pseudomorph” was also mentioned but not used systematically. Even though the organic structure were not preserved, the weave pattern and microscopic characteristics of these fibres were useful to explore the technology and development of textile during Etruscan culture [125].

Shortly after, J. Vollmer studied the physical structure of bast and silk fibre pseudomorphs found on Chinese bronzes of Shang and Han periods (1500 BC-220 AD) being held at the Royal Ontario Museum. He began to reflect on the terms being used to

describe these fabrics and refused most of the terms previously used. He considered only the term "pseudomorph" the most appropriate to define archaeological textiles that have been completely replaced by inorganic minerals. In addition, he suggested two preservation states from the remains of silk fibres attached on copper-base alloys [126]:

- "Negative pseudomorphs" where the minerals wrap the fibres and form an impression.
- "Positive pseudomorphs" which indicate that organic fibres are replaced by minerals.

In 1978 M. E. King published work concerning the identification of the structure of archaeological fibres in contact with metal artefacts. She described them as "impressions" and "metallized textile fragments". Her hypothesis was that it was difficult to determine the structure of original fibres due to their superimposed layers in a metal cast [105].

R. Janaway in England studied issues of mineralization of textiles and reported his results in 1983. At first, he preferred the description "fibre preserved by corrosion products" than the term "pseudomorph" [127, 128]. He subsequently adopted "pseudomorph" and even "organic pseudomorph" in his publications. However, the latter term was thought to be meaningless according to the terminology of J. Vollmer since fibres are either organic or preserved in a pseudomorphous form and not both at the same time [129, 130]. R. Janaway used J. Vollmer's nomenclature and refined it based on SEM observations on mineralized textile remains from medieval times. He proposed to classify these textiles into four categories:

- Textiles preserved by metal ions. Fibres retain most of their integrity through the effect of metal ions that act against microorganisms.
- Textiles preserved by corrosion products forming a negative impression. The corro-

sion products cover the fibres before their decomposition and the interior of fibres fills with sediment (case 1 of J. Vollmer).

- Textiles replaced by corrosion products. The organic fibre has disappeared to make way for a "positive replica" of corrosion products (case 2 of J. Vollmer).

- A combination of the negative impression of textiles and the replacing metal. Fibres are represented by the impression they leave in the corrosion and remnants from original fibres.

R. Janaway's observations are currently the most relevant. He investigated the remnants of fibres of different types on copper and iron alloys. He also conducted several experiments in which the burial conditions were reproduced.

American researchers K. A. Jakes and L. R. Sibley as well as J. H. Howard III also used the term "pseudomorph", which seemed appropriate for them to indicate a complete replacement of organic matter by metallic salts [131]. They focused above all on the understanding of the mechanisms of mineralization of silk fibres covered by Chinese bronzes. They used different methods like XRD and SEM to determine the chemical composition of fibres and their structure [132]. They proposed a model of pseudomorph process and considered several influencing environmental factors during the replacement of fibres by minerals [2, 111, 133]. Their works on mineralized fibres found at the Etowah Mound site were useful in understanding cultural contexts at that time [134, 135, 136].

From 1990 onwards, with increasing use and development of FTIR spectroscopy, papers were published either in UK by R. D. Gillard and S. M. Hardman [137, 138] and in America by H. L. Chen and his collaborators [1, 139, 6]. These studies indicated the presence of organic remains in some mineralized fibres and emphasized the potential of FTIR spectroscopy as a powerful tool for the detection and identification of preserved organic residues.

C. Moulhérat has studied from 1997 a large number of archaeological textiles mainly excavated in France and Mongolia. He discussed the use of terms “pseudomorph” and “mineralization”based on references and listed the four states of mineralization (see next Section) [3]. L. Bertrand has discussed “mineralization” of archaeological keratinized fibres and the role of environment involved in this process in his work from 2002 [140, 141]. A. Thomas and her colleagues have described archaeological flax textile preserved in “mineralized” form on some foundation pegs excavated at Tello [37, 73].

Based on what has been described above, the term “pseudomorph” describes complete replacement of one mineral by another one without any internal and external change on its original morphological form [142]. In the case of preserved archaeological fibres, this means that mineral compounds completely replace the original organic compounds in fibres but their physical shapes are retained. This term only explains one particular situation of physico-chemical states of preserved fibres. Thus, “pseudomorph” is not the most appropriate term for describing all types of archaeological textiles preserved. As a result, it is preferred to use the term “mineralization”, which can better account for the observed partial substitution of organic compounds by minerals [1, 6, 3]. This term was once used to describe the physical shapes of wood fibres replaced by iron-base minerals at a macromolecular level [143]. In the studies of H. L. Chen and his colleagues, this phenomenon was considered a process at the molecular level occurring between fibres and copper substrate [1, 139, 144, 6]. They discussed the penetration of metal ions into partially degraded fibres, as detailed in the next section.

This thesis is focused on the preservation of archaeological cellulosic fibres under a mineralized form and is restricted to the study of the mineralization of fibres via close contact with copper corrosion products.

2.3 Mineralization of cellulosic fibres in contact with copper-base artefacts

2.3.1 The different states of mineralization

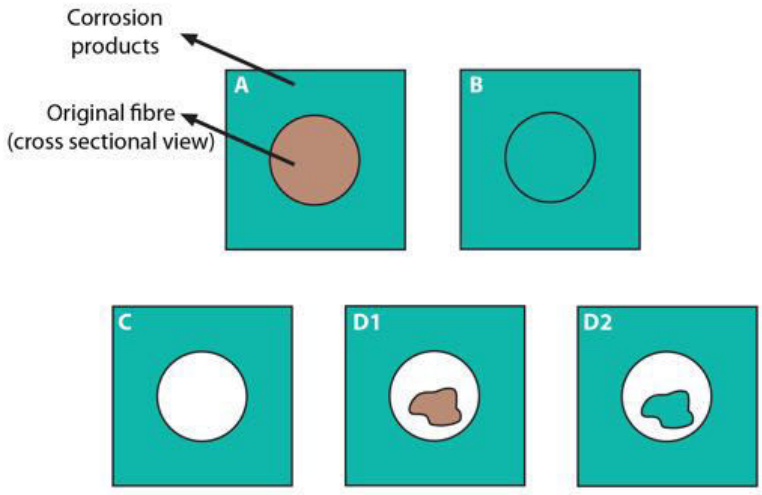

Figure 2.6: Simplified illustrations of cross sectional view of four mineralization states of archaeological fibres (modified from C. Moulhérat 2001 [3]). A, Superficial mineralization. Preservation of the chemical composition of the fibres and formation of corrosion products as encrustation. B, Positive mineralization. Complete substitution of the chemical composition of the fibres by corrosion products (pseudomorphism). C, Negative mineralization. Complete degradation of the fibres (cast or imprint). D1 and D2, Partial mineralization. Partial degradation of the fibres (D1) and partial substitution of the fibres by corrosion products (D2).

Four states of mineralized fibres related to corrosion products on metal supports can be determined through optical and electron microscopies: superficial, negative, positive and partial mineralization (Figure 2.6).

- Superficial mineralization [3, 126]

  The corrosion products enclose the fibres, preserving not only their physical morphology but also the chemical integrity. These corrosion products can encase fibres

by forming an encrustation around them, resulting in the protection of fibres from microorganism activity.

- Positive mineralization [1, 6]

  This mineralization state is similar to the "pseudomorphism" in geology. It indicates a total replacement of organic materials in original fibres by corrosion products. Corrosion layers are rapidly deposited enclosing fibres and metal ions penetrate fibres. In this case, only the morphological characteristics of fibres are preserved.

- Negative mineralization [1, 6]

  This process consists of deposition of corrosion products around fibres followed by complete decomposition of fibres. This results in an external imprint of fibres in a mineral-based matrix. The imprint can reflect the external morphological features (e.g. size) of the degraded fibres.

- Partial mineralization [3, 1]

  This state corresponds to an intermediate situation between positive and negative mineralization. The chemical composition of the fibres is partially preserved. Degraded areas in the fibres can lead to substitution by minerals (Figure 2.7).

Fibres are rarely identifiable when their decomposition occurs before the formation of corrosion products. Various mineralization states mentioned above can be observed in the same archaeological textile fragment [3, 1]. Mineralization depends on the nature of fibres (linen, silk, wool, etc.), the attached metal support (copper, iron, etc.), and the burial environment [3].

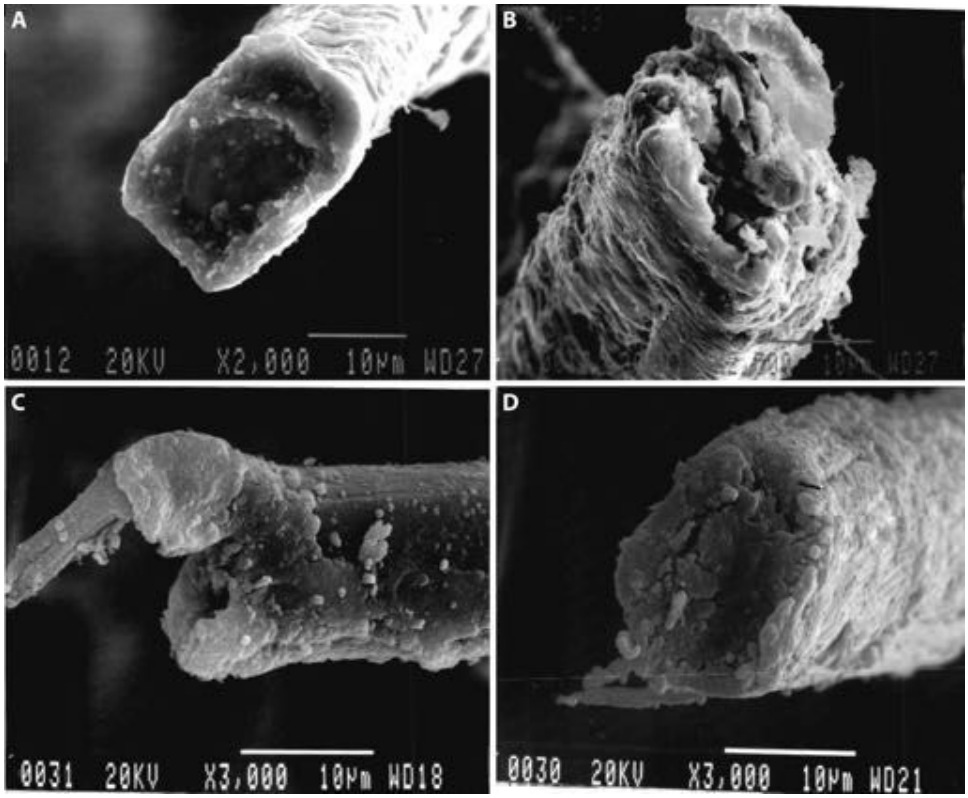

Figure 2.7: Cross sectional views of partially mineralized bast fibres observed with SEM showing various lumens diameters (reused from H. L. Chen 1995 [1]). A, Large lumen opening. B, Small lumen opening. C, Tiny lumen opening. D, Lumen filled with copper corrosion products (completely closed lumen).

2.3.2 Physico-chemical mechanisms of mineralization

The mechanism of mineralization of fibres was once considered as the formation of a pseudomorph, which is comparable to the petrification process [5]. In a geological context, a fossil preserves both the substituted compounds and its original morphological form. The development of a plant fossil can be explained by three processes: petrification, cast and mould (impression), the latter ones are followed by complete disintegration of plant tissue [145]. In the case of petrification, the original cell structure of the fossil can be preserved due to the gradual replacement of original material by other substances like minerals from the environment [146]. Most plant fossils display cast or mould showing only an impression of their external outline without the preservation of their internal composition, i.e. complete degradation of plant tissue leading to empty spaces inside. However, it should be noted that the formation of plant fossils can take millions of years, which is much longer than the formation of pseudomorph or mineralization over thousands of years.

In the work of K. A. Jakes et al, a possible model of fibre pseudomorph attached to corroding copper artefact was proposed (Figure 2.8) [133]:

1. Since fibres are in close contact with the corroded metal substrate, dissolved copper ions can penetrate fibres in the presence of water and swell the fibres.

2. The copper ions bind, forming minerals in the amorphous regions of the fibre structure. Fibres degradation continue, crystalline areas are dilated by water and the strength between polymer chains of cellulose is weakened, resulting in the formation of copper minerals in these areas.

3. With the accumulation of copper minerals, the structure of fibres is replaced by minerals while the physical shapes of fibres are preserved.

The type of minerals formed due to the metal corrosion can provide information

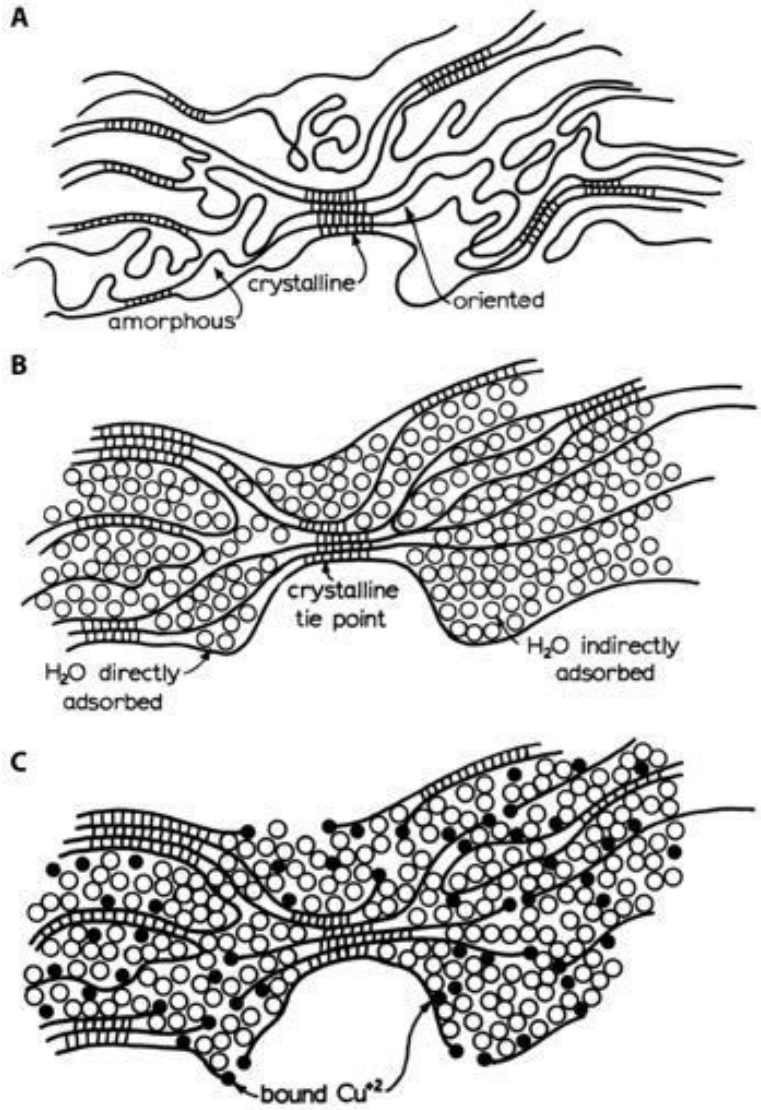

Figure 2.8: The formation of fibre pseudomorph proposed by K. A. Jakes et al., 1986 (reused from K. A. Jakes et al., 1986 [133]). A, The internal structure of fibres containing crystalline and amorphous regions. B, The swelling of fibres due to water absorption. C, The penetration of copper ions into fibres resulting to a combination between ions and polymer chains of fibres.

about the surrounding burial environment, which may in turn facilitate the formation of a specific type of mineral [133].

Several experiments simulating the mineralization process of fibres were conducted in the laboratory by R. Janaway and R.D. Gillard in the 1980's, in order to obtain a better understanding of the mechanism [129, 137]. They showed that the preservation of fibres in association with metal artefacts generally depends upon two decay rates: (I) the rate of fibre degradation at molecular level (see later) and (II) that of metal corrosion related to the diffusion and deposition of metal ions onto and into fibres. The influencing factors on the two rates consist mainly in [3]:

- The nature of the fibres leads to distinct resistance to degradation process. For example, cellulosic fibres are readily preserved in alkaline condition [102].
- The nature of the metal substrate showing varied susceptibility to corrosion attack. In the case of copper, a corrosion-resistant layer (passivation) can form quickly avoiding further attack.
- The environmental conditions (temperature, humidity, etc.) and the type of burial (inhumation or incineration) [129].

The two rates lead to different mineralization states (Figure 2.9), for example fibres attached to copper artefacts are found mostly in positive mineralization state [129, 137, 138, 3] However, the structure of fibres cannot be preserved if rate (I) is faster than rate (II) [129].

H. L. Chen and his collaborators proposed a more detailed mechanism of mineralization involving degradation of fibres [1, 6], which can be summarized in several stages (Figure 2.10):

- First, the copper begins to oxidise in the presence of water in an acidic environment, resulting in the release of copper ions (Cu^{2+}) and their subsequent penetration into

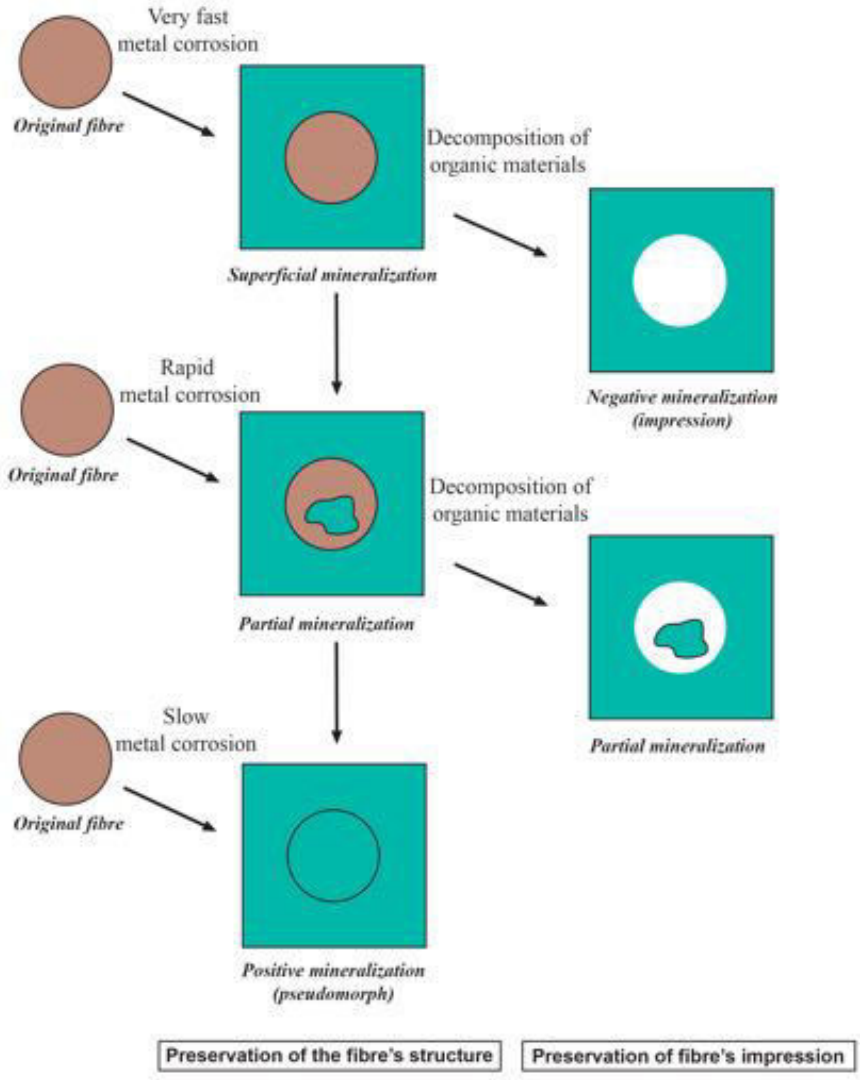

Figure 2.9: Formation of different mineralization states related to metal corrosion process (modified from C. Moulhérat 2001 [3]).

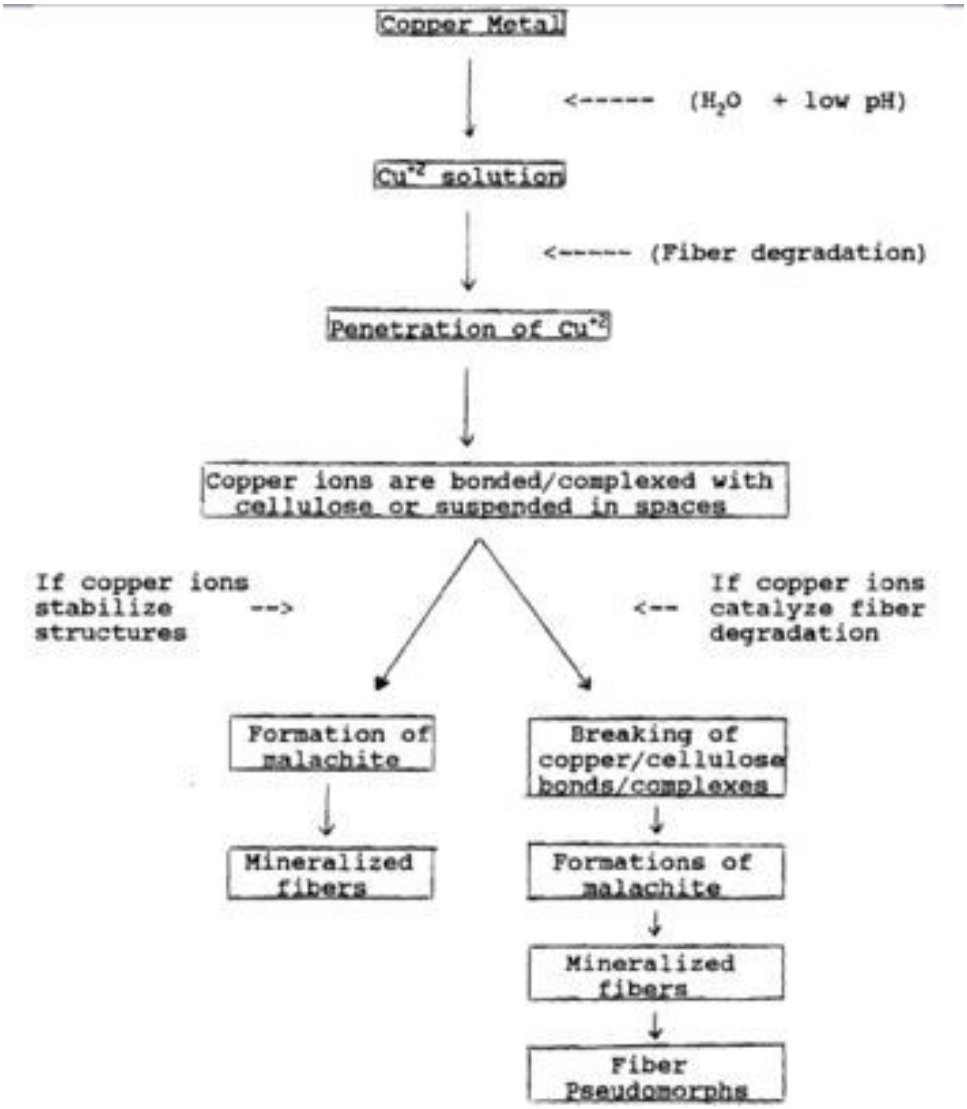

Figure 2.10: Mechanism of mineralization in related to copper corrosion (reused from H. L. Chen 1995 [1]).

fibres.

- Due to the bacterial activities originating from the burial environment, the degradation of fibre takes place in amorphous areas and proceeds to crystalline ones (Figure 2.11). Small-scale decomposition of organic material can lead to empty space in fibre structure, allowing easier penetration of copper ions into fibres and inhibition of microbial degradation.

- Copper ions in fibres may bind with partially degraded polymer chains. In addition, copper ions at the surface of fibres can aggregate as encrustations forming a mineral gangue (e.g. copper carbonate).

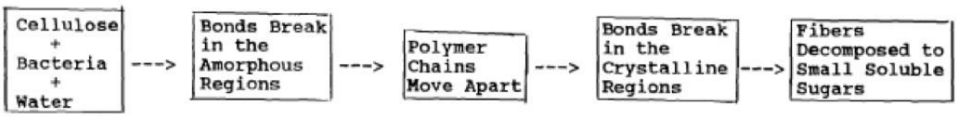

Figure 2.11: Structural degradation of fibres(reused from H. L. Chen 1995 [1]).

According to the proposed mineralization process, preservation of organic remnants can be explained by the formation of complexes between cellulose and copper ions. Once all available active sites of cellulose molecules are occupied, gradual deposition of copper ions in fibres can occur.

However, the precise process of the formation of new chemical bonds between cellulose and copper corrosion products, and the nature of these neo-formed bonds is not clearly known.

The process of dyeing cellulosic fibres can be compared to the mineralization mechanism [147, 6]. Due to the degradation of fibres, several hydroxyl groups become available, particularly those at active sites on C_2, C_3 and C_6 (see Subsection 1.3.2). Cellulose can ionize providing cellulosate anions (2.1) [148]:

$$\text{Cellulose}-\text{OH} + \text{OH}^- \rightleftharpoons \text{Cellulose}-\text{O}^- + \text{H}_2\text{O} \tag{2.1}$$

This reaction occurs in a dilute alkaline environment, as when positive copper ions are present due to corrosion. The cellulosate can then react with dyes forming dye-fibre bonds. Similarly, in the case of mineralisation, Cellulose$-O^-$ may react with Cu^{2+} forming a metallic complexe (2.2).

$$2\text{Cellulose}-O^- + Cu^{2+} \rightarrow (\text{Cellulose}-O)_2Cu \tag{2.2}$$

The role of copper ions as catalyst to the degradation of fibres has been shown [1, 6, 92]. Complete decomposition of organic compounds in fibres may take place over time with the simultaneous formation of copper corrosion products replacing the original structure of fibres [1]. In this case, a fibre's pseudomorph would be observed (Figure 2.10).

2.3.3 Corrosion process of copper-base artefacts

The use of copper and copper-base alloys can date back to 4th mill. BC for decorative and functional purposes as well as burial practices [149, 150]. When copper and copper alloys are exposed to a moist environment, corrosion would take place as a result of chemical action of water and oxygen.

The knowledge of the corrosion process of archaeological copper artefacts is mostly based on ancient bronzes, in which copper oxidation induces the formation of a common structure encountered in most of natural environments either in atmosphere or soil. This proposed structure is often described as made of a bi-layer [151]: an internal reddish-brown layer of cuprous oxide (Cu_2O) and an external green-blue layer of hydroxyl cupric species. This structure needs to be refined according to the different corrosion contexts as described later. The following overview focuses on the corrosion of copper, which can be divided into three categories based on the surrounding environment: atmospheric, burial/soil and marine corrosion.

Atmospheric corrosion

When exposed to outdoor humid atmosphere where appropriate conditions of redox potential Eh (measurement of the tendency of a chemical species to acquire electrons and therefore be reduced [152]) and pH are present, the oxidation of copper generally occurs first due to the presence of oxygen (Figure 2.12A) [153]. On the copper surface, in most corrosive contexts, a (thin) water layer is present as an electrolyte, in which the dissolved oxygen is reduced, initiating the cathodic reaction (2.3) [154]:

$$O_2 + 2H_2O + 4e^- \rightarrow 4OH^- \tag{2.3}$$

Through anodic reactions (i.e. a half reaction of oxidation that release electrons), the metal starts to dissolve producing Cu^+ and Cu^{2+} ions (2.4 and 2.5):

$$Cu \rightarrow Cu^+ + e^- \tag{2.4}$$

$$Cu^+ \rightarrow Cu^{2+} + e^- \tag{2.5}$$

Cuprite (cuprous oxide) Cu_2O is a dominant corrosion product that can indicate the original shape of an artefact [156]. This compound is commonly of a red-brown colour while other colours are also possible according to the impurities and particle size. The characteristic p-type (the positive charge of a hole) semi-conductivity (i.e. compound tending to accept electron) enables the cuprite layer to act as a transport medium for both cuprous ions towards the external environment and anions (mostly O^{2-} but in some cases Cl^-) in the opposite direction [157]. Tenorite (cupric oxide) CuO is a rare product due to its instability, which exhibit a black colour among naturally formed patinas [151].

Other elements present in the atmosphere can play a significant role in the corrosion process. Sulfur (e.g. from sulfur dioxide SO_2) can dissolve in water generating sulfide

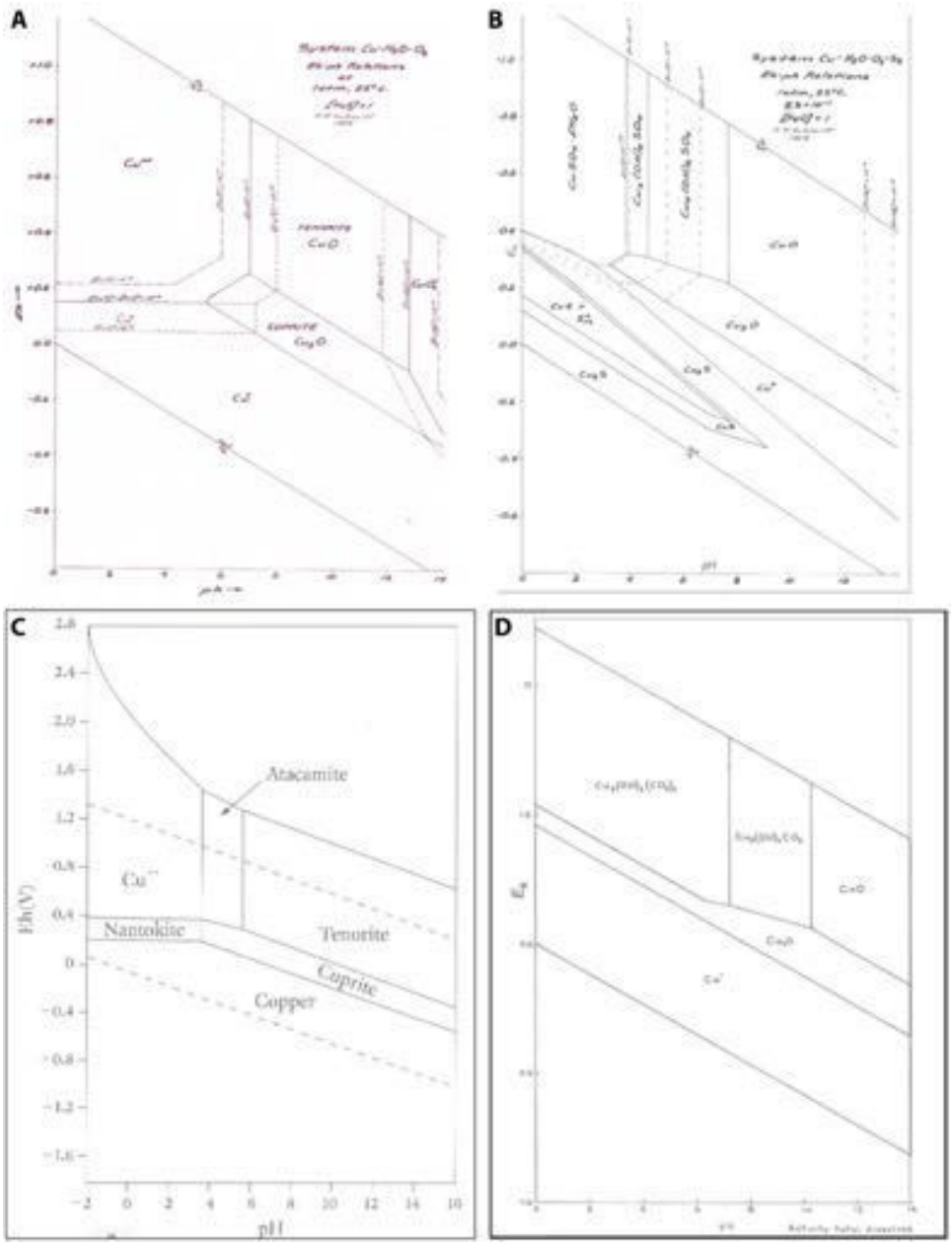

Figure 2.12: The Eh-pH diagrams for different systems (reused from M. Pourbaix 1974 [152] and H. Schmitt 1962 [155]). A, Cu–O system. B, Cu–S–H_2O system. C, Cu–Cl–H_2O system. D, Cu–CO_3–H_2O system.

(S^{2-}) and sulfate (SO_4^{2-}) ions. Sulfide ions can be observed in high concentration in atmospheric environment in close contact with archaeological media rich in bacteria and in reducing environment, such as in pits, dave or latrina, resulting to the formation of copper sulfide (e.g. chalcocite Cu_2S). Sulfate ions can produce many copper hydroxy sulfates according to the environmental conditions, such as langite $Cu_4(OH)_6SO_4 \cdot 2H_2O$ in ambient moist and posnjakite $Cu_4(OH)_6SO_4 \cdot H_2O$ in relative dry climate (Figure 2.12B and 2.13) [151, 158].

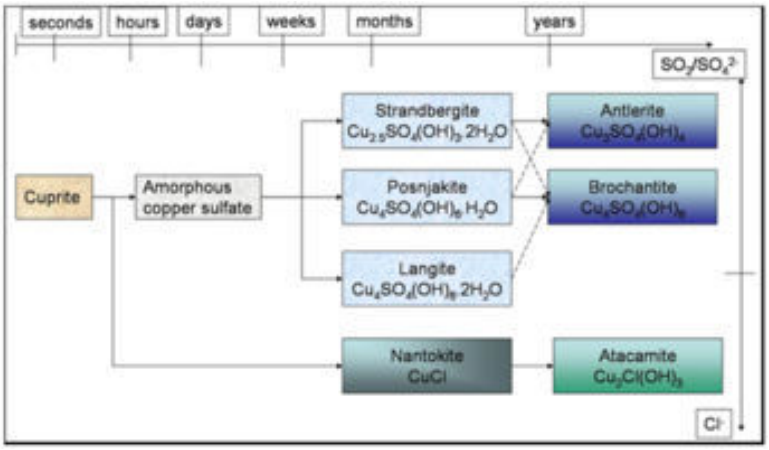

Figure 2.13: Formation sequences of copper corrosion products in presence of sulfur and chlorine in different concentrations (reused from C. Leygraf et al., 2016 [158]).

The oxidizing anion Cl^- derived from aerosol particles and the dissolution of Cl_2 in water can react with cuprous ions Cu^+ to form nantokite CuCl. With the presence of oxygen in humid atmosphere, this compound is considered as a seed crystal for the formation of the polymorphs of copper trihydroxy chloride $Cu_2(OH)_3Cl$ (Figure 2.12C and 2.13): atacamite, clinoatacamite or botallackite [151]. The layer of nantokite is often invisible from the exterior since it is located under the cuprite layer. Nantokite is a source of the so-called "bronze disease" due to its conversion into copper trihydroxy chlorides. This conversion leads to volume expansion and subsequent physical stress inside the artefact, which likely resulted in cracks and even fragmentation [159].

The presence of the CO_2 in atmosphere can lead to formation of carbonate ions

CO_3^{2-}, which results in the formation of green malachite $Cu_2(OH)_2CO_3$ and blue azurite $Cu_3(OH)_2(CO_3)_2$ (Figure 2.12D) [151, 160].

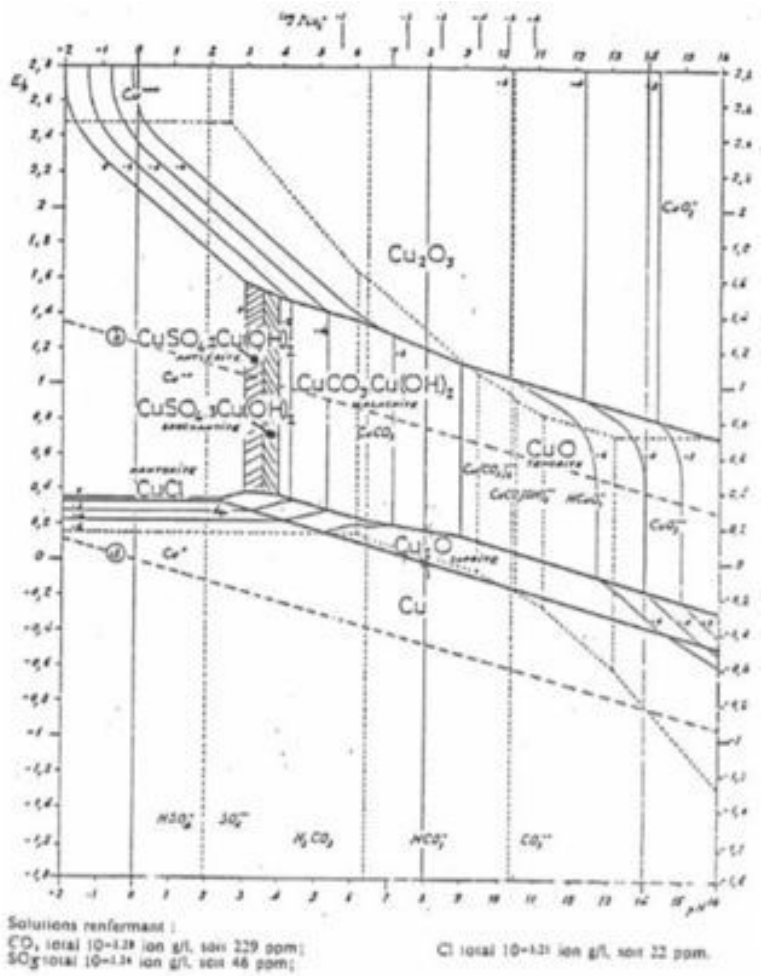

Figure 2.14: Stability diagram Eh-pH of a quinary system Cu–CO_3–SO_3–Cl–H_2O at 25°C (reused from M. Billiau et al., 1983 [161]).

According to the pH of the aqueous solution and the redox potential of the corrosive environment, Pourbaix diagrams (Figure 2.12A) can be used to determine the thermodynamic stability of these corrosion products [151]. For the species mentioned above, a quinary system (a numeral system with five elements as the base) can help to investigate the formation of corrosion products in a multi-elemental environment (Figure 2.14).

The location and orientation of the artefact in its environment can be an important

factor in the corrosion process in atmosphere [162, 158]. For example, in a Cl^- dominated condition, the formation of chloride-containing corrosion products is slower on exposed surfaces than on the sheltered surfaces due to the effect of wind and rain.

Burial corrosion

Soil is a complex mixture of organic compounds and inorganic ions. Two soils are never alike due to distinct content in microorganisms and diversity in moisture and pH, etc. Various corrosion structures can be observed in different soils.

According to analysis at different scales, two main categories of corrosion structures of copper-base alloys can be observed when buried. The principal difference between the two types is based on the presence or absence of the original surfaces that allow identifying the original shape of the artefact (Figure 2.15) [163, 164, 165]. The presence of original surfaces allows defining the initial shape of artefact. The identification of an original surface of archaeological artefact is based on macroscopic and microscopic examinations. Usually observed on a cross-sectional view of the corrosion stratigraphy, the remnant original surface is marked by a regular limit of layers with respect to the more irregular corrosion layers. It corresponds to the limit under which only the elements of metallic alloy are present, whereas above them, corrosion products combined with soil elements (such as Si, Al, etc.) are detected. This repartition of the elements is identifiable when corrosion compounds from the copper ions all deposit onto the external surfaces, i.e. there is no leaching of ions that ensure complete deposition of corrosion products formed [166].

In a *Type I* structure (Figure 2.15A), the original surface is generally well identifiable and can be directly observed due to the interface between external deposits or encrustations and internal corrosion layers. Its preservation allows to identify the original shape of artefact. The corrosion process induces a dissolution of the copper from the artefact itself to outside, then a diffusion of ionic species occurs. However, in this case, the

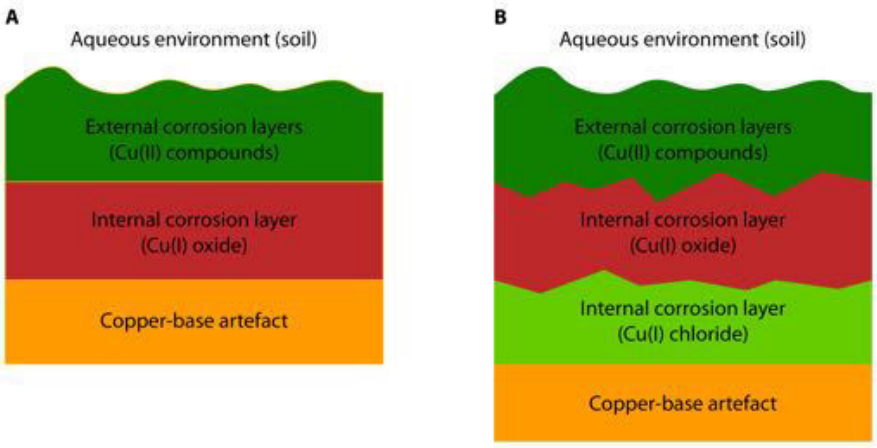

Figure 2.15: The schematic representation of two corrosion processes. A, *Type I*. The original surface is revealed by the interface between external and internal corrosion layers. B, *Type II*. The original surface is severely damaged through the interface between external and internal corrosion layers.

change in volume is minimal and two corrosion layers can be observed: an outer layer of different colours from grey to blue and also green based on attached soil elements; an inner layer of red-brown colour. The thickness of these two layers varies and can range up to several millimetres after a relatively short period (around two decades) and the corrosion rate is faster in more humid environment [167, 164, 165, 168]. This porous corrosion structure is also known as "noble patina", because it was demonstrated that it has very good corrosion resistance properties [169].

In a *Type II* structure (Figure 2.15B), the corrosion structure is commonly rough and non-uniform. Pits, crevices and lamellar corrosion features can be observed from the high dissolution rate during the corrosion process. The original surface has been destroyed or damaged due to severe corrosive attacks. The corrosion layers appear thicker and more complicated than those of the *Type I*. Three layers can be reported: an external layer in dark or olive green and a fragmented red-brown middle layer, as well as an internal layer often showing metallic "ghost" structures. This tri-layer structure can be formed during the early stages of corrosion, whereas corrosion can continue intermittently up to

the present [167, 164, 165, 168].

Table 2.1: Common copper corrosion products (modified from L. Robbiola 1990 [170]). **aq**: aqueous or humid milieu. **atm**: atmospheric milieu. **sea**: marine milieu. +++: very frequent. ++: frequent. +: less frequent. **r.**: rare. **s**: soluble. **i**: insoluble. **w**: water. **a**: strong acid.

Compound	Formula	Natural mineral	Milieu			colour	Solubility	Crystalline system
			aq	atm	sea			
OXIDES								
Copper (I) oxide	Cu_2O	Cuprite	+++	+++	+++	red-brown, dark red	iw, sa	cubic
Copper (II) oxide	CuO	Tenorite	r.	r.	r.	grey, black	iw, sa	monoclinic
CARBONATES								
Basic copper (II) carbonate	$Cu_2(CO_3)(OH)_2$	Malachite	+++	++	+	green, emerald-green	iw, sa	monocline
Basic copper (II) carbonate	$Cu_3(CO_3)_2(OH)_2$	Azurite	+	+	-	azure blu	iw, sa	monoclinic
CHLORIDES								
Copper (I) chloride	CuCl	Nantokite	+	+	+	coloureless, white	iw, sa	cubic
Basic copper (II) chloride	$Cu_2(OH)_3Cl$	Atacamite	++	++	++	olive-green	iw, sa	orthorhombic
Basic copper (II) chloride	$Cu_2(OH)_3Cl$	Clinoatacamite	++	++	++	olive-green	iw, sa	monocline
SULPHIDES								
Copper (I) sulphide	Cu_2S	Chalcolite	r.	-	++	grey	iw, sa	orthorhombic
Copper (I) sulphide	CuS	Covellite	r.	-	++	dark blue, indigo	iw, sa	hexagonal
SULPHATES								
Basic copper (II) sulphates	$Cu_4(SO_4)(OH)_6$	Brochantite	r.	+++	-	dark-green	iw, sa	monoclinic
PHOSPHATES								
Basic copper (II) phosphate	$Cu_2PO_4(OH)$	Libethenite	r.	-	-	olive-green	iw, sa	orthorhombic
Basic copper (II) phosphate hydrated	$Cu_3(PO_4)_2(OH)_4$	Pseudo-malachite	r.	-	-	dark-green	iw, sa	monoclinic
SILICATES								
Hydrate copper silicate	$CuSiO_3 \cdot H_2O$	Dioptase	r.	-	-	green, blue green	iw, sa	trigonal

The external layers in the two corrosion types consist mainly of cupric compounds (Figure 2.15). This layer usually combines with elements from soil such as Si, Al and Ca, which are helpful to distinguish different soil types (e.g. calcareous, sandy, clayey, etc.) [165]. Hydrated corrosion products of copper (II) such as hydroxy-silicates,

-phosphates or -sulphates can often be identified. Ranging from gray to green and even to blue, the colour of this layer depends mostly on the incorporated soil materials and their amounts. Occasionally, a layer including copper cations forms, which might be defined as the "alteration" of the soil due to the presence of the metallic object. Emerald green compounds in this layer generally imply the presence of copper (II) hydroxy-carbonates, such as malachite (Table 2.1). The red-brown internal layer in contact with the metal core of the artefact is typically composed of copper (I) oxide, corresponding to the stoichiometric mineral cuprite Cu_2O (Figure 2.15). In addition, another internal Cl-containing layer (nantokite CuCl) is usually identified in *Type II* corrosion at the interface of corrosion products / artefact (Figure 2.15B).

Marine corrosion

Since the artefact studied in this thesis do not come from marine contexts, this category of corrosion is limited to a very brief introduction. When buried in seawater, dissolved gases (e.g. O_2 and CO_2) and many ions (e.g. Cl^-, SO_4^{2-}, etc.) can contribute to the corrosion of copper, leading to the formation of a wide range of corrosion products (e.g. usually cuprite, nantokite, copper trihydroxy chlorides, etc.). In addition, biological organisms (e.g. algae and coral) can produce hydrogen sulfide (H_2S) during decay, leading to the common identification of copper sulfides (Cu_2S) in copper-base artefacts recovered from seawater [151].

Identification of corrosion products

The composition of corrosion products formed are typically identified from sampling or on prepared cross-sections of artefacts using SEM-EDS, powder XRD, IR and Raman spectroscopy (Figure 2.16 and Table 2.1) [45, 171, 172, 151, 173, 174, 175, 176, 177, 164, 178, 165, 168, 179].

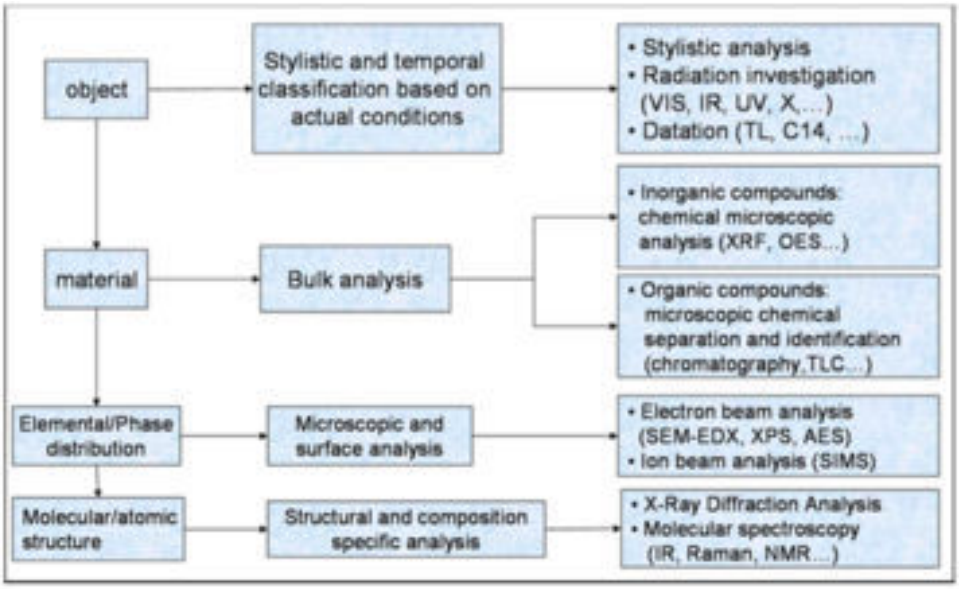

Figure 2.16: Analysis of an archaeological copper-base artefact by combining various methods at different scale (reused from M. Schreiner et al., 1985 [180]).

2.3.4 Factors influencing mineralization and corrosion processes

The mineralization process of a given copper–fibre system and the preserved state of fibres both depend on the surrounding environment. According to the mineralization mechanism described in Section 2.3.2, several specific conditions are reported as indispensable [1, 137, 3]:

- A relative stagnant environment (not leaching).
- Close contact between copper artefact and fibres (i.e. direct contact or in the immediate vicinity).
- The presence of water and oxygen leading to metal corrosion and facilitating the diffusion of metal ions within fibres.

These conditions can all be present in archaeological burial contexts. The burial type (e.g. inhumation or cremation) can also influence the mineralization process. In case of

inhumation, the metal corrosion and bacterial activities can both be enhanced through decay of the body. In the case of cremation, textiles are often used to wrap a metallic urn or to contain bone ashes inside an urn, compared to inhumation, no particular additional effect such as increasing bacterial activities is correlated to mineralization-corrosion processes (Figure 2.17) [129, 3].

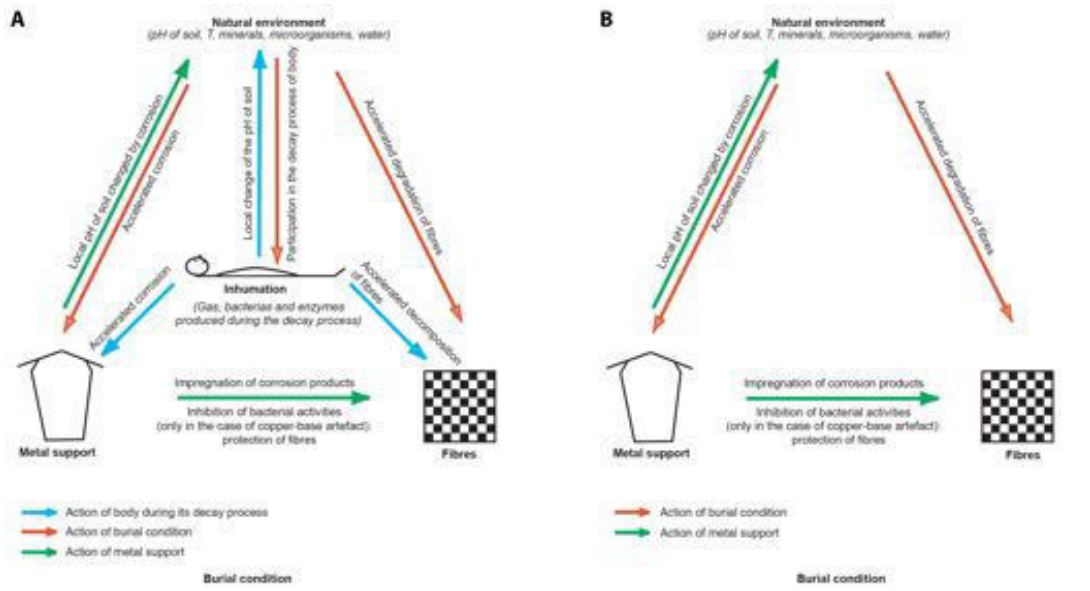

Figure 2.17: Burial types influencing mineralization processes (modified from C. Moulhérat 2001 [3]). A, Inhumation. B, Cremation.

2.4 Review of analytical approaches to study archaeological mineralized cellulosic textile

Few studies have been conducted in the past on the preservation of archaeological cellulosic fibres and the corresponding mechanisms. Some works provide information to establish hypothesis on the mineralization of system copper–cellulosic fibres, particularly those of H. L. Chen and his collaborators as detailed in this section. Synchrotron-based techniques were firstly used on mineralized keratinized fibres by L. Bertrand [140].

2.4.1 Morphology

Conventional light microscopy allows detailed observation on morphological characteristics of mineralized fibres. Twisting mode of fibres and / or threads can be determined (Figure 2.18A and B) [37, 73]. In transversal view, the cross-sectional shape of an individual fibre gives information on types of fibres. In the studies of A. Thomas et al., 2015 [73]), they suggested that the preserved fibres are derived from flax because the shape of sections is polygonal with rather rounded angles. They also found that most fibres are isolated and not assembled together like other bast fibres (hemp, jute, etc.), corresponding to flax fibres that tend to dissociate from each other (Figure 2.18C). The use of polarized light can be helpful to observe coloured outlines of microfibrils of cellulose inside fibre [76, 181, 182]. Distinction between even highly mineralized plant and animal fibres can be achieved through chemical staining experiments using optical microscopy and polarized light [4].

As a powerful tool for obtaining images in high resolution, SEM was commonly used to observe morphological features of mineralized fibres combined with light microscopy. H. L. Chen has shown various shapes of lumen in mineralized fibres using SEM-SE/BSE (Figure 2.7). The interior of fibres displays some adhering agglomerates and / or small bead-like compounds of varying dimensions. These compounds, which exhibit irregular and rough forms, are similar to what he has observed on the longitudinal surface of fibres (Figure 2.19) [1].

2.4.2 Elemental composition

EDS coupled with SEM is commonly used to determine the elemental composition (mainly inorganic elements) of the mineralized fibres. In the studies of H. L. Chen and his co-workers, they analysed two ancient mineralized fibres, OSU-19 and OSU-20, which were extracted from the interior of corroded copper beads excavated from

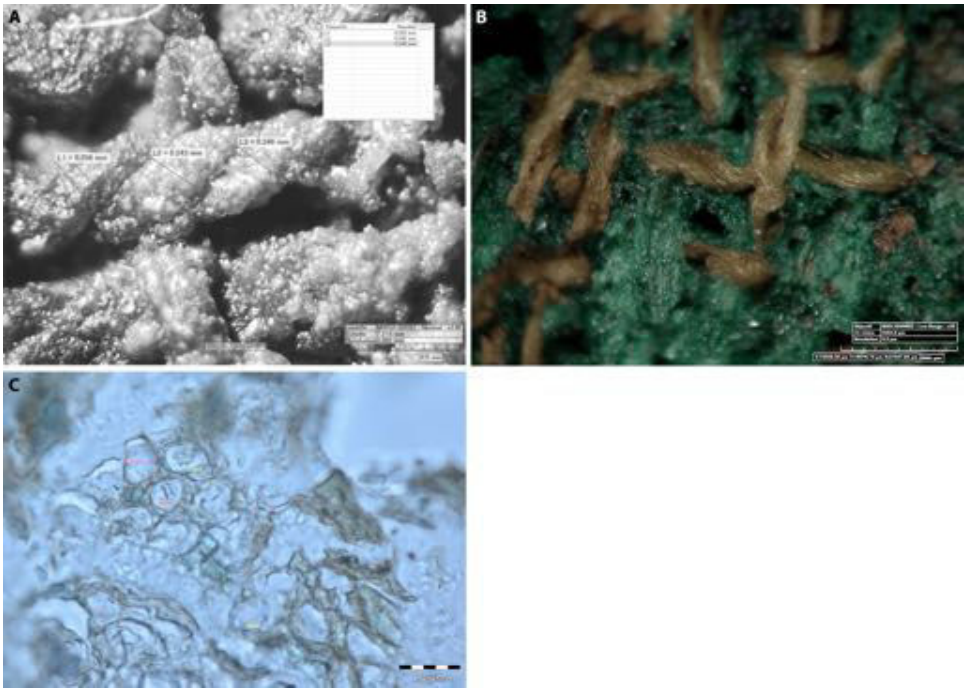

Figure 2.18: Microscopic observation of mineralized fibres on corroded copper foundation pegs (details see Chapter 5). A, Twisting mode S (reused from A. Thomas et al., 2012 [37]). B, Twisting mode Z (reused from A. Thomas et al., 2015 [73]). C, Cross-sectional view of fibres in B (reused from A. Thomas et al., 2015 [73]).

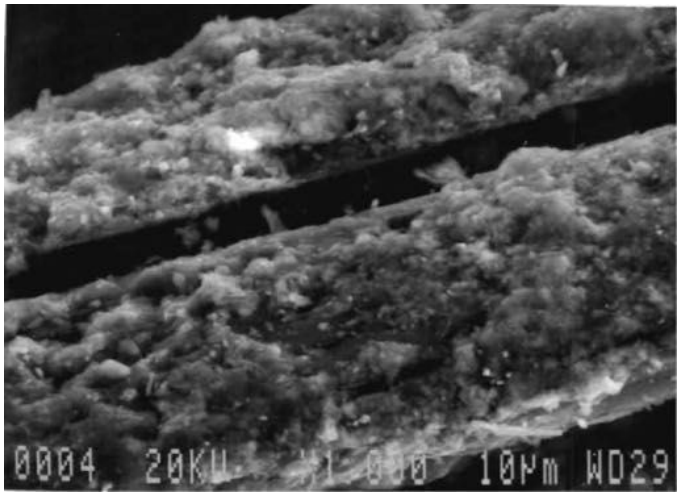

Figure 2.19: SEM observation of longitudinal morphology of mineralized bast fibres showing irregular agglomerates of varied sizes (reused from H. L. Chen 1995 [1]).

the James River burial site (Virginia, 1600 AD). The latter (OSU-20) was partially exposed on the exterior of the bead. EDS experiments were performed on encrusted areas (containing irregular agglomerates and chunky materials) and non-encrusted areas (only consisting of small bead-like structures) of the two fibres in longitudinal view. The result showed that copper and other elements derived from the soil of burial environment are present in both areas, whereas the content of copper is higher than soil elements and the quantity of all detected elements are lower in the non-encrusted areas of both fibres (Table 2.2A). Examination of the lumen wall (inner wall) and interior (containing area between the lumen wall and outer surface) of fibres in cross-sectional view. The amount of copper detected is approximately the same for both areas of the two fibres (Table 2.2B) [1, 139].

Table 2.2: Elemental composition of OSU-19 and OSU-20 using SEM-EDS (reused from H. L. Chen et al., 1996 [139]). A, Results on encrusted and clean areas in longitudinal view of fibres. B, Results on lumen wall and interior in cross-sectional view of fibres.

A	OSU-19		OSU-20	
Element	Encrustation areas	Clean surface	Encrustation areas	Clean surface
O	40.85 ± 3.50	69.39 ± 2.80	50.12 ± 2.92	80.99 ± 2.06
Cu	44.52 ± 2.47	22.09 ± 2.51	38.19 ± 2.16	14.30 ± 0.32
Ca	3.11 ± 1.21	1.58 ± 0.47	1.20 ± 0.33	1.16 ± 0.80
Si	-	-	2.69 ± 0.34	-
P	7.38 ± 2.09	2.02 ± 0.84	3.35 ± 0.51	-

B	OSU-19		OSU-20	
Element	Lumen wall	Fiber interior	Lumen wall	Fiber interior
O	46.31 ± 1.81	47.33 ± 2.63	75.62 ± 2.34	77.78 ± 3.75
Cu	43.25 ± 2.13	43.56 ± 2.61	14.73 ± 3.21	13.37 ± 2.61
Ca	-	-	1.69 ± 0.22	1.30 ± 0.31
Si	-	-	2.69 ± 0.13	1.76 ± 0.20
P	6.86 ± 0.65	4.57 ± 0.87	-	-

Two phenomena can be deduced based on the results: (1) a high content of copper is observed on the encrusted areas of the outer surface and lumen wall of inner surface of fibres, particularly for OSU-19 that was embedded in corroded copper beads. This suggests that copper encrustation were formed on both outer surface and inside lumen surface of fibres. (2) the presence of copper in the non-encrusted area and in the fibres interior indicates a penetration of copper into fibres, leading to an infilling

or a replacement of the internal compounds of fibres by copper-containing compounds (e.g. malachite in these fibres) [1, 139].

2.4.3 Physical microstructures

As a highly crystalline material, cellulosic fibres provide diffraction patterns characteristic of fibrous single crystals which can be measured using XRD. The method is useful to determine the physical microstructures of fibres. In the work of H. L. Chen et al., a powder diffractometer was used to analyse the crystallite size and unit cell parameters as well as the ratio of crystalline component of mineralized fibres OSU-19 and OSU-20. A single crystal diffractometer was also employed to evaluate the crystallite orientation within the same fibres [1, 144, 6].

- Crystallite size

H. L. Chen and his co-workers used Indian Hemp fibre as a reference of modern cellulosic fibre in their experiments. They found three main crystallite reflections derived from cellulose, σ_{101}, $\sigma_{10\bar{1}}$ and σ_{002} (Figure 2.20A). Additional peaks were detected in the diffractograms of mineralized fibres due to the presence of malachite after comparison with the standard compound (Figure 2.20B, C and D) [144].

Compared to the modern fibre, the crystalline size σ_{002} based on the 002 reflection plane (parallel to the long fibre axis) of the mineralized fibres decreases. Since all the hydroxyl groups are occupied to form intra- and intermolecular bonds in mineralized fibres, there are no other available valence bonds between 002 planes thus they are held only by weak Van der Waals forces. This decrease of σ_{002} in the *c*-axial direction (parallel to the long fibre axis) of the crystal might be mainly explained by the separation between the layers of polymeric sheets, due to the breakage of Van der Waals forces following the degradation process of fibres. Moreover, the increase in the crystal size of σ_{101} and $\sigma_{10\bar{1}}$ in the *a*-axial direction (perpendicular to the long fibre direction *b*-axial), compared

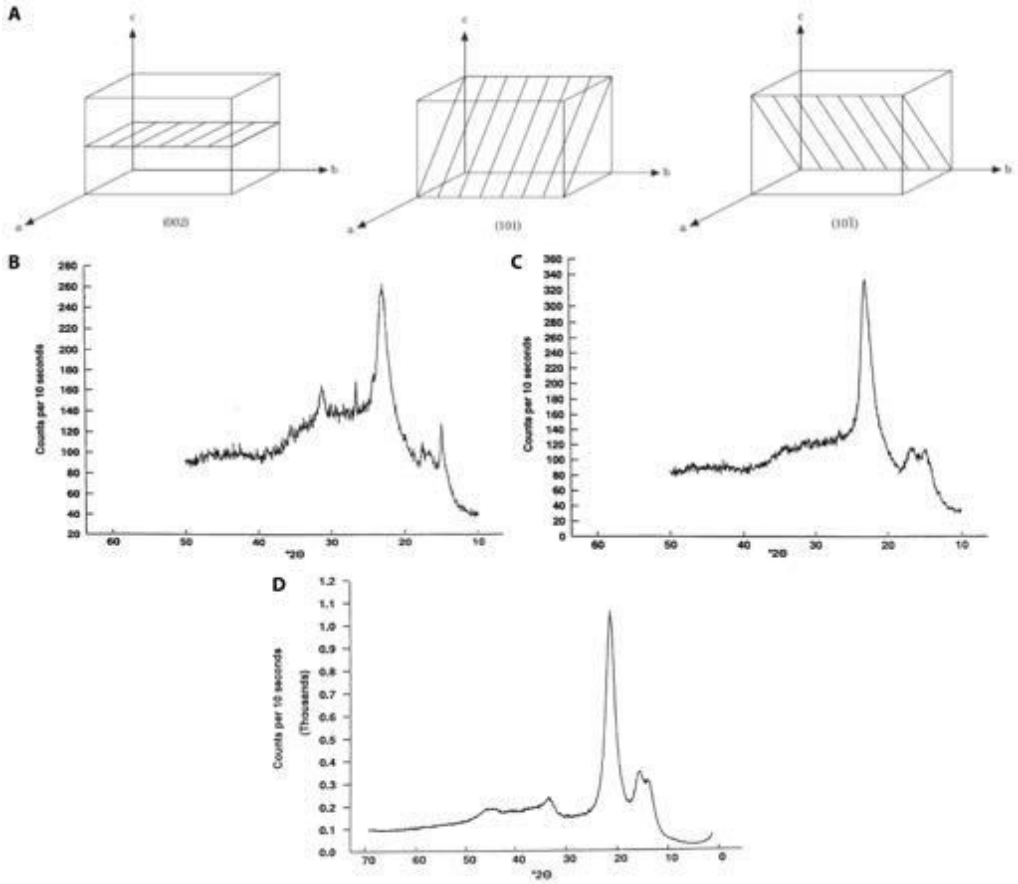

Figure 2.20: The reflection planes of cellulose and diffractograms of mineralized fibres and modern hemp fibre (reused from H. L. Chen et al., 1996 [144]). A, Positions of 002, 101, $10\bar{1}$ reflection planes observed in cellulose. B-D, The diffractograms of OSU-19, OSU-20 and modern hemp fibre.

Table 2.3: Determination of physical microstructures using XRD (reused from H. L. Chen et al., 1996 [144]). A, Crystallite size Å(10^{-10}m) of σ_{101}, $\sigma_{10\bar{1}}$ and σ_{002} of mineralized fibres and modern hemp fibre. B, The measurements of unit cell dimensions in Å(10^{-10}m) and monoclinic angle β. C, The measurements of crystalline percent. D, The measurements of crystallite orientation angle.

A

hkl	*Indian Hemp*	*OSU-19*	*OSU-20*
101	46±3	124±1	90±1
$10\bar{1}$	88±1	128±2	87±1
002	65±2	45±2	58±1

B

	Indian Hemp	*OSU-19*	*OSU-20*
a-axis	8.04±0.05	8.28±0.10	8.12±0.09
b-axis	10.46±0.08	10.51±0.07	10.47±0.04
c-axis	7.94±0.02	7.94±0.01	7.91±0.02
β	84.68±0.50	83.67±0.90	83.46±0.50

C

Sample	*Cellulose*	*Malachite*
Indian Hemp	76.6±1.47	0
OSU-19	42.5±0.35	7.7±0.50
OSU-20	43.2±0.24	4.6±0.30

D

Sample	*Angle*
Indian Hemp	13.2°
OSU-19	27.1°
OSU-20	20.5°

to that of modern fibre, suggests an absorption of water molecules in the amorphous regions of cellulose. This could allow rearrangement of less-ordered areas that are close to the edges of *a*-axial direction and increase in the global crystallite size in this special direction. The changes of crystallite appear different for OSU-19 and OSU-20, this can result from the differences between their surrounding environmental conditions as described previously, in which the concentration of copper ion was high around OSU-19 because it was confined inside a corroded copper bead (Table 2.3A) [144].

- Unit cell dimensions

The measured unit cell dimensions in mineralized fibres are slightly larger than those in modern fibre, particularly in the *a*-axial direction (Table 2.3B). This result is consistent with the larger crystallite size detected in the same direction. The larger *a*-axial unit cell dimension might be another reason for the increase on crystallite size [144].

- Percent crystalline components

Compared to modern hemp fibre, there is a decrease of crystalline components of

cellulose and a presence of malachite in mineralized fibres. The sum of the percent of cellulose and the percent of malachite is not equal to the cellulosic composition in modern fibre. This indicates not only a partial degradation of cellulose but also a loss of organic compounds of original fibre. The content of malachite is high in OSU-19, this result is in accordance with changes in crystalline size of two archaeological samples due to the environmental conditions (Table 2.3C) [144].

- Crystallite orientations

The measured crystallite orientation angles are larger in mineralized samples than in modern ones, suggesting a decrease of crystallite orientation due to the fibre degradation and mineralization (Figure 2.21 and Table 2.3D). The structural rearrangement of molecules in crystalline areas of fibres can lead to a more random distribution of crystallite. The penetration of copper ions into fibres and replacement of their original organic structures may also emphasis the disturbance of the crystallite orientation of cellulose along the fibre's long axis. The larger orientation angle detected in OSU-19 implied a more severe interruption of its physical microstructure and a highly mineralized state [144].

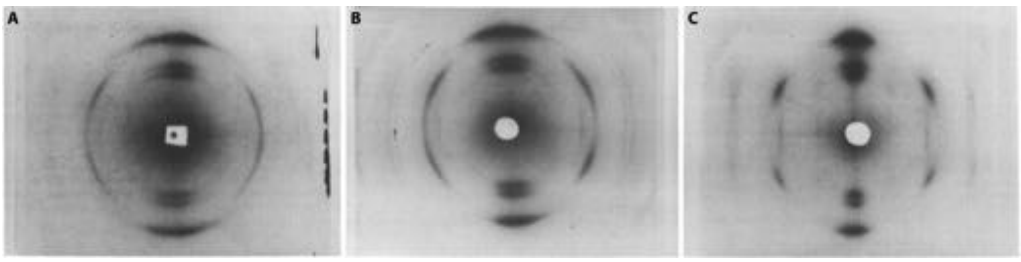

Figure 2.21: The X-ray photographic image of mineralized fibres and modern one (reused from H. L. Chen et al., 1996 [144]). A, OSU-19. B, OSU-20. C, Modern hemp fibre.

2.4.4 Organic remnants

H. L. Chen and colleagues investigated the possible presence of organic remnants in mineralized fibres using FTIR. They compared the FTIR spectra of archaeological mineralized fibres, OSU-19 and OSU-20 (Figure 2.22), to those of two modern fibres (Indian Hemp and Common Milkweed) and a malachite standard (Figure 2.23). Malachite was selected as a reference because it was detected in the XRD experiments and is usually found in fibres that are preserved through contact with copper-base artefacts. From the comparisons of absorption bands, he identified the presence of organic residues and external corrosion products. The analysis also showed a change in the structure of mineralized fibres compared to modern [1, 139].

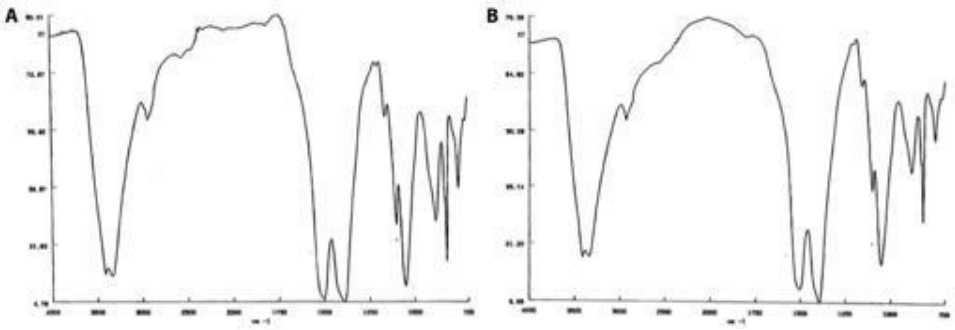

Figure 2.22: The FTIR spectra of mineralized fibres (reused from H. L. Chen et al., 1996 [139]). A, OSU-19. B, OSU-20.

The observed absorption bands include a strong diffuse band around 3400 cm^{-1} due to OH stretching and a weaker band around 2900 cm^{-1} attributed to CH stretching, which are typical of the absorption of cellulose. A water absorption band occurs around 1650 cm^{-1}. In the 1200-1500 cm^{-1} region, sharp absorption bands are observed due to CH_2 vibration and to deformation of the C-O-H valence angles, these absorptions appear to be affected by the amorphous structure of the fibre. The 950-1200 cm^{-1} region contains a broad diffuse absorption due to the C-O and C-C groups stretching vibrations. The 800-950 cm^{-1} region derives from the movements involving the bridge oxygen C_1-

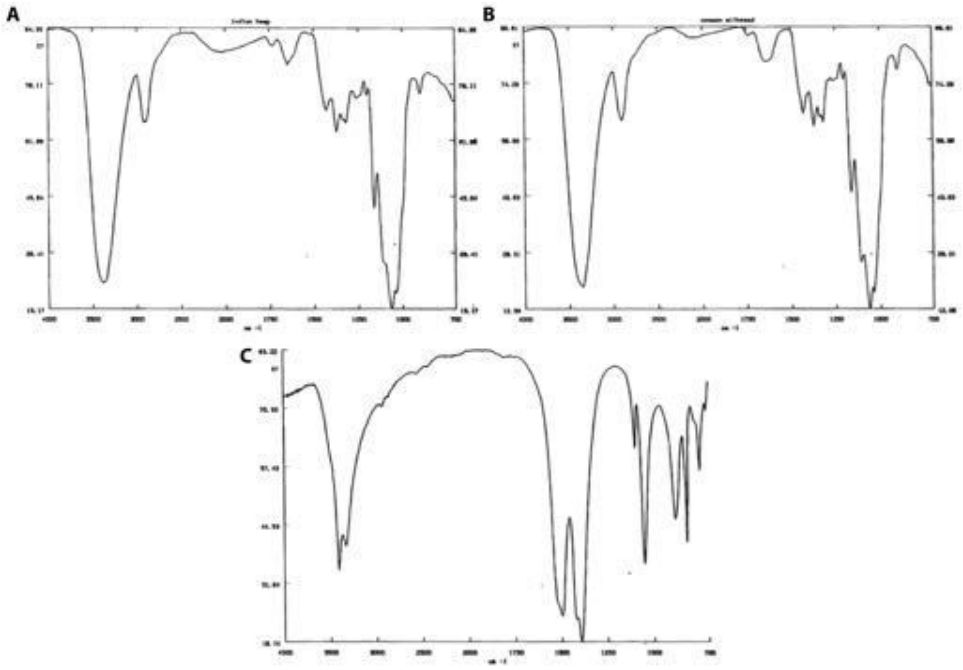

Figure 2.23: The FTIR spectra of modern fibres and standard copper-containing compound (reused from H. L. Chen et al., 1996 [139]). A, Indian Hemp fibre. B, Common Milkweed fibre. C, Malachite.

O-C_4. The typical hemicellulose absorbance bands appear at 1740 cm^{-1} due to C=O vibration in carboxylic acids or esters and at 1240 cm^{-1} due to C-O vibration. For the lignin, the characteristic absorption bands generally occur around 1500 cm^{-1} due to C=O absorption, at 1460 cm^{-1} due to C=C absorption and at 1270 cm^{-1}, 830 cm^{-1} due to the C-O vibration (Figure 2.23A and B) [1, 68].

Malachite ($Cu_2CO_3(OH)_2$) includes covalent bonds of the CO_3^{2-} anion, which is identifiable as a strong broad absorption band in the 1350-1530 cm^{-1} region due to asymmetric stretch. Medium strength sharp bands in the 640-890 cm^{-1} region are due to in-plane bending modes in the carbonate anion and those in the 1040-1120 cm^{-1} region due to symmetric stretching. The medium broad band at 3370-3420 cm^{-1} is due to water vibrational modes (Figure 2.23C) [183].

To confirm the presence of malachite, a spectral subtraction from the mineralized fibres was performed. In addition, absorptions of standard malachite has subtracted from the spectra of mineralized fibres, leaving the spectra with only cellulose absorption bands (Figure 2.24B).

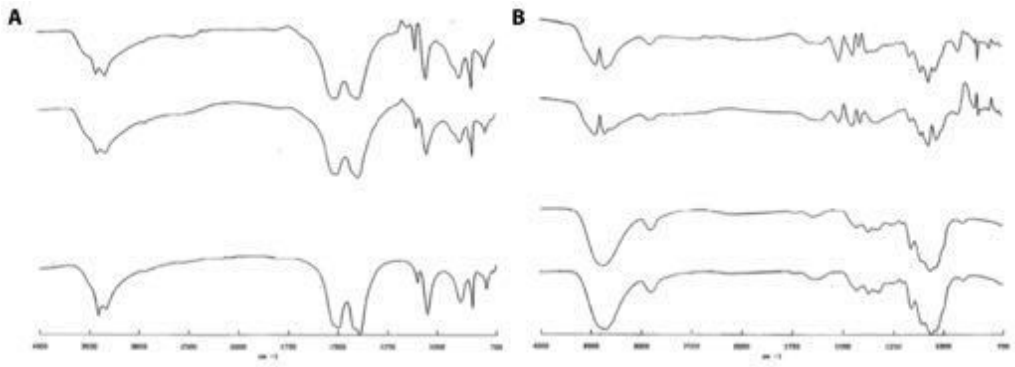

Figure 2.24: The FTIR spectra of mineralized fibres after a subtraction process (reused from H. L. Chen et al., 1996 [139]). A, The spectrum of OSU-19 (top) and OSU-20 (middle) after subtracting that of Indian hemp fibre as well as the spectrum of malachite standard (bottom). B, The spectrum of OSU-19 (top) and OSU-20 (upper middle) after subtracting that of malachite standard as well as the spectrum of Indian hemp fibre (lower middle) and Common Milkweed fibre (bottom).

From the spectra of mineralized fibres, a lack of the absorption band at 1740 cm^{-1} suggests a loss of hemicellulose (Figure 2.22). This could be ascribed to the fibre's degradation and/or a replacement of hemicellulose by copper elements [139]. A difference in absorption intensity is also seen between same bands that could indicate the molecular conformation. Particularly, a lower band intensity at 1163 cm^{-1} in the mineralized fibres versus the modern suggest changes in hydrogen bonding of the oxygen bridge C-O-C of cellulose. This is also confirmed by the intensity at 893 cm^{-1} that occurs when the oxygen in the bridge is released from hydrogen bonding, where the C-O-C is hence free to rotate. The changes in molecular conformation suggest an increase in the amorphous regions of cellulose, implying a decrease of the crystalline content that can be attributed to fibre degradation.

The crystallinity index was also determined in the fibres using FTIR spectroscopy, particularly the ratio between absorbance of 1372 cm^{-1} and 2900 cm^{-1} (Table 2.4). The crystallinity ratio of mineralized fibres appear to be lower than in modern samples, this result is consistent with that obtained from the XRD experiments.

Table 2.4: The measurements of crystallinity ratio between absorption band at 1372 cm^{-1} and 2900 cm^{-1} (reused from H. L. Chen et al., 1996 [144]).

Fiber	Common milkweed	Indian hemp	OSU-19	OSU-20
Ratio	0.73	0.73	0.53	0.55

Moreover, the FTIR measurements show a split of the broad diffuse regions around 3400 cm^{-1}, 1200-1500 cm^{-1} and 1000-1200 cm^{-1} in the spectra of modern fibres into well-defined individual sharp bands in the spectra of mineralized fibre. A slight shift of the entire region at 1200-1500 cm^{-1} toward higher wave numbers was also observed in mineralized fibres. Penetration of copper elements into less-ordered regions of the mineralized fibres may cause new absorption; whether these splits observed are resulted from the presence of new and/or different chemical bonds are still unknown [144].

Thus, FTIR analysis revealed the presence of organic remnants that survived at trace levels even in highly mineralized fibres. Identification of cellulosic fibres is possible even after their long-term burial in soil. The presence of corrosion products of copper attached to mineralized fibres (i.e. malachite in studies of H. L. Chen et al) can be simultaneously shown through FTIR measurements.

2.4.5 Reproduction of fibre mineralization

In order to elucidate the mineralization mechanism, several simulation experiments were performed in laboratory as presented below.

R. D. Gillard and colleagues used natural cellulosic and proteinous fibres after some cleaning and drying treatment. Fibres were placed into different copper-containing solutions and in pure water for comparison. All the containers were kept in a water bath at 50°C in an aerated environment. Fibres were then extracted regularly for characterization using mainly UV, EDS and FTIR [137]. A similar experiment was also conducted by H. L. Chen and his collaborators, where Indian Hemp fibres and copper hydroxide solution were used [6] (Figure 2.25).

Based on their results, the mineralization mechanism depends on kinetic factors related to the formation of mineral product. The organic remnants in mineralized fibres were sufficient to allow an identification between plant and animal fibres, even after a long-term burial. The total replacement of original fibres by corrosion products is rarely achieved, implying that a partial mineralization can be usually observed while a real pseudomorph (positive mineralization state) is uncommon [137].

2.5 Conclusion

A description of previous studies performed on preserved archaeological cellulosic fibres in contact with corroded copper-base artefacts is presented. Natural fibres tend to ir-

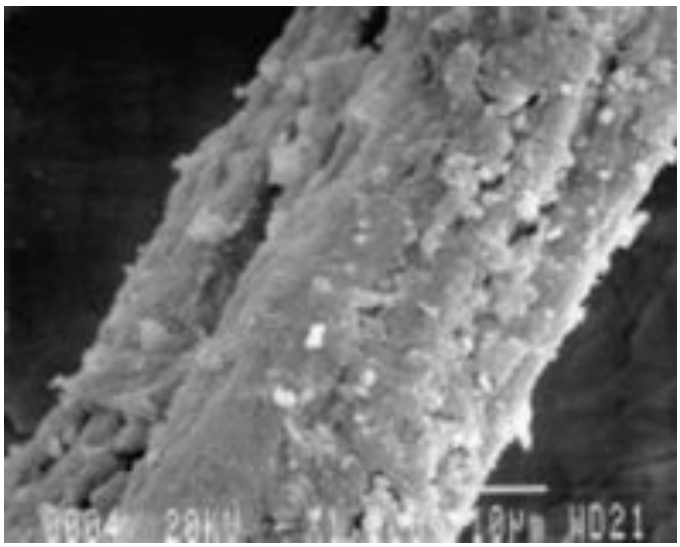

Figure 2.25: Longitudinal surface of mineralized fibre of simulation experiment in laboratory(reused from H. L. Chen et al., 1998 [6]). The formation of copper-containing crystals around fibre are clearly visible.

reversibly degrade due to several physico-chemical factors. As the main component in plant fibres, cellulose can degrade through different processes such as hydrolysis, oxidation and biodegradation, leading to the decomposition of polymer chains into simple monomers and even gaseous molecules. When buried in soil, the degradation of fibres lead to morphological damage and chemical deterioration, which can be mainly influenced by the activity of microorganisms.

Archaeological fibres can "survive" over millennia with the preservation of their physical form due to the extreme environmental conditions like drought and cold. Fibres can also be preserved resulting from contact with corroded metal artefacts. A special focus is given on the preservation of cellulosic fibres attached to corroded copper-base artefact.

According to the previous studies, different terms were used to describe the fibres preserved in contact with corroded copper artefacts including "textile pseudomorph" and "mineralized textile". Term "Textile pseudomorph" indicates only one particular state of preserved fibres. Thus, in this work, "mineralization" is used in accordance with the

definition explained previously, where organic composition is either partially replaced by minerals at the molecular level with micro- even nano-scale yielding mineralized archaeological fibres, or completely replaced by inorganic compounds resulting in textile pseudomorphs. In addition, this term allows for other influencing factors which might be involved (the nature of fibres and metals, the environmental condition). Based on the observation of morphology and chemical composition, four classifications can be made: superficial, positive, negative and partial mineralization state.

Mineralization implies a gradual process through which the original organic materials in fibres are partially/completely replaced by minerals derived from corrosion of attached copper-base support. Several steps are involved in the mineralization process consisting of the diffusion of dissolved copper ions onto fibres, and combination of penetrated copper ions with partially degraded polymer chains inside fibres. These two actions, similar to the dyeing process of fibres, can lead to an encrustations as mineral gangue around fibres and a formation of copper corrosion products within fibres, respectively. Corrosion of copper occurs in aerobic and humid environments. When buried in soil, two types of copper corrosion can be determined depending on the state of original surfaces. The main corrosion products formed contain cuprous oxide, copper (II) carbonates and copper (I/II) chlorides.

As a result, the specific surrounding environmental conditions of a given copper-fibre system play an indispensable role. Metal corrosion and fibre degradation happen concurrently. Due to the complexity of the physico-chemical environment encountered in burial contexts, in-depth understanding of the mineralization mechanism is in an early state and need further study. In addition, as some individual fibres are not in direct contact to the metal support at micro-metric scales, the role of water from humidity or seepage is thought to be essential to transport metal ions from the corroding slab to the textile. When does it occur? Is it possible that diffusion and percolation pathways can influence the morphology and presence of the distinct copper-containing phases?

Significant physico-chemical questions remain to be answered.

The analytical methods used on the investigation of mineralized fibres contain SEM-EDS and XRD as well as FTIR, which allow not only the characterization of physical structures of fibres but also an evaluation of their chemical composition. As precious material records of textile technique and production in ancient times, destructive methods should be avoided. New methodology for the study of mineralized fibres is proposed in this thesis to extract information at different scales, combining several non-destructive 2D and 3D synchrotron-based micro-imaging techniques (µCT, PL-UV/Vis spectroscopy, etc.) with classical approaches (SEM-EDS, FTIR, etc.). Semi-quantitative analysis is developed based on this methodology, which can also be performed on other precious archaeological samples of small dimension. Each method will be detailed and the corresponding results will be explored in the following chapters.

3

Materials and methods

This chapter describes the corpus of artefacts and fragments studied, and their excavation contexts, as well as information on environmental conditions to our knowledge prevailing at the archaeological sites. A set of selected analytical methods used in this thesis is described, together with their respective experimental setups and data processing procedures.

Contents

3.1 Materials

The artefacts studied in this work are listed in Table 3.1 and archaeological sites are showed in Figure 3.1. Artefacts consist of corroded copper-base fragments with textile remains and textile fragments detached from corroded supports. They date from the Chalcolithic period (3rd to the 2nd mill. BC). Among the very rare findings of ancient textiles remains in these sites, we carefully selected artefacts on which a wealth of archaeological information can be extracted. All the samples pose essential questions in terms of preservation mechanisms of mineralized fibres related to copper corrosion, with visually comparable mineralization states and corrosion features.

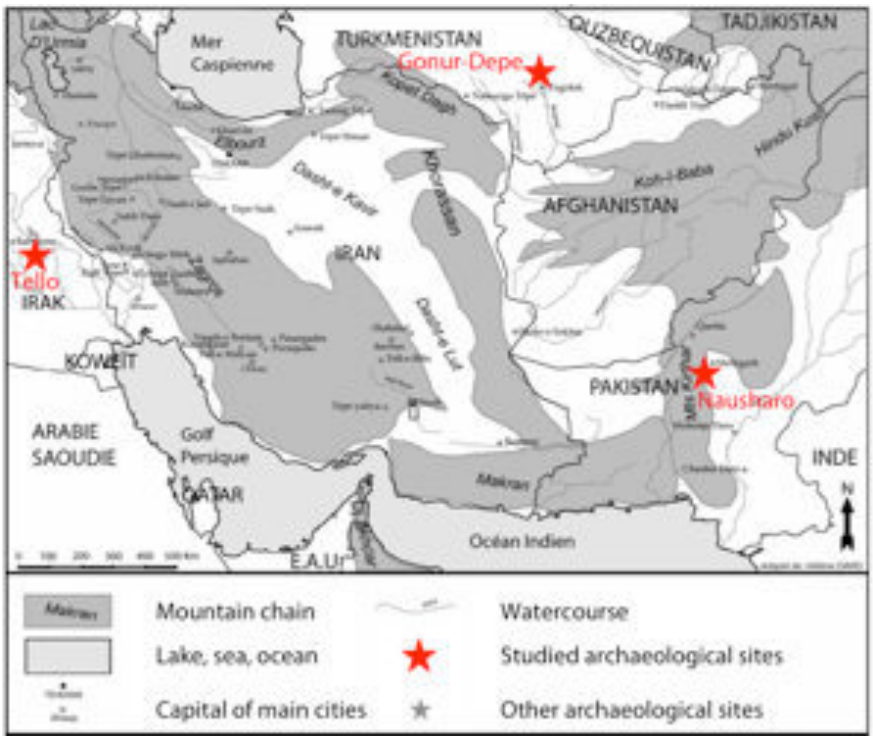

Figure 3.1: Map of the archaeological sites from which the studied artefacts come from (modified from H. David): Gonur-Depe (current Turkmenistan), Nausharo (current Pakistan), Tello (curent Iraq).

Table 3.1: List of main artefacts and samples studied in this work.

Archaeological site	Artefact	Description	Estimated date	Sample
Gonur-Depe (current Turkmenistan)	Gonur 2380	Textile fragment	3rd-2nd mill. BC	Gonur 2380-1 Fibre
Nausharo (current Pakistan)	NS 95015002	Copper plate	3rd mill. BC	NS 95015002-1 NS 95015002-2 NS 95015002-3 NS 95015002-6-1 Fibre
Tello (current Iraq)	AO 27703	Copper axe blade	Early 2nd mill. BC	--
	AO 14506	Copper vase	2nd mill. BC	AO 14506-3 AO 14506-1b Fibre
	AO 77 AO 76	Copper foundation peg	3rd mill. BC	-- --

3.1.1 Material from Gonur-Depe (current Turkmenistan)

The site of Gonur-Depe in southeast Turkmenistan was discovered in the 1950s. As the capital of the ancient Margush (or Margiana) civilization and one of the largest Bronze Age archaeological sites of Central Asia, Gonur-Depe was occupied from the very late 3rd to 2nd mill. BC and consists of numerous graves of varying sizes, from which many funeral artefacts have been unearthed, including ceramics and metal artefacts [184]. The first excavation works at the Gonur-Depe cemetery (about 10 ha) were conducted in the autumn of 1991 by a team of Italian archaeologists led by S. Salvatori (Centro Studi Ricerche Ligabue, Venice, Italy) in collaboration with the Ministry of Culture of the Republic of Turkmenistan (Fig. 3.2A and B) [184]. The graveyard of Gonur-Depe has been investigated by the members of the Margiana Archaeological Expedition (Russia) since 1996, under the direction of V. Sarianidi [184, 185]. The soil at the Gonur-Depe necropolis consists in friable sand with layers of clay, which led to an incomplete preservation of many tombs [186].

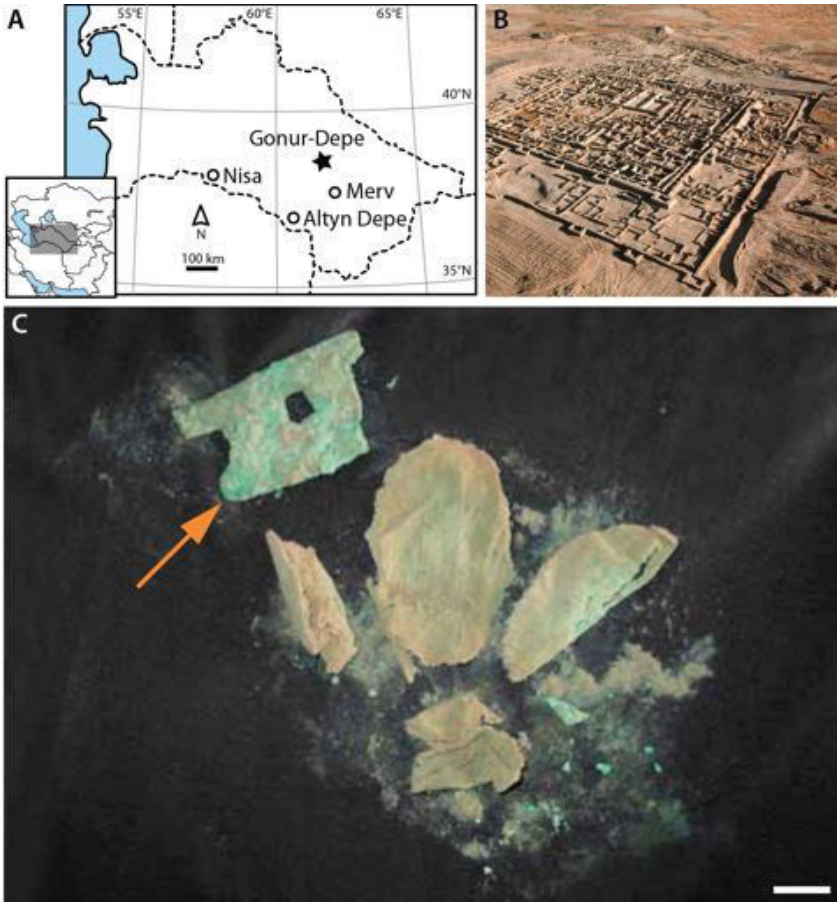

Figure 3.2: A, Location of Gonur-Depe. B, Photo of Gonur-Depe graveyard during excavations (reused from V. Sarianidi 2007 [184]). C, Textile fragment Gonur 2380 (© V. Sarkisian [184]). Scale bar in C: 1 cm.

One artefact from the site was studied under the supervision of C. Moulhérat (Musée du Quai Branly-Jacques Chirac).

Textile fragment (inv. no. Gonur 2380, Fig. 3.2C)

The grave of a warrior with human bones inside, inv. no. Gonur 2380, dated to 2nd mill. BC was excavated in the autumn 2001. Since this tomb has not been illegally robbed, many initial copper-base military objects were preserved and found during the cleaning of the left shin of the buried warrior such as a cylinder goblet and a short sword [184, p. 127]. A corroded copper 'ladder' preserved in poor condition was found (arrow in Fig. 3.2C) which normally indicates the high social position of the owner [187]. Several textile fragments in pale-green and beige were noticed (Fig. 3.2C), which are thought to have originally wrapped the ladder and been folded together several times. Several textile fragments were pre-studied by E. Tsareva (Museum of Anthropology and Ethnography, Russian Academy of Sciences, Saint Petersburg), A. K. Elkina (D. S. Likhachev Russian Scientific-Research Institute of Cultural and Natural Heritage, Russian Academy of Sciences, Moscow) and T. Shangurova (MVI Bashkirien Laboratory of Forensic Examination, Ministry of Justice of the Russian federation, Oufa) [184, p. 335–337]. Other textile fragments are now scientifically studied under the supervision of C. Moulhérat. One sample was selected and studied in this work, Gonur 2380-1 (dimensions ca. $1.2\times1.0\times0.5\,\mathrm{mm}^3$). Individual fibres were extracted from the sample for cross sectional and longitudinal microscopic analysis.

3.1.2 Material from Nausharo (Indus valley, current Baluchistan, current Pakistan)

The site of Nausharo is located in the Kachi-Bolan region in the south-eastern Baluchistan province of Pakistan. Nausharo is an emblematic archaeological site of the Harappan civilization, with more than a thousand years of protohistoric occupation (three main

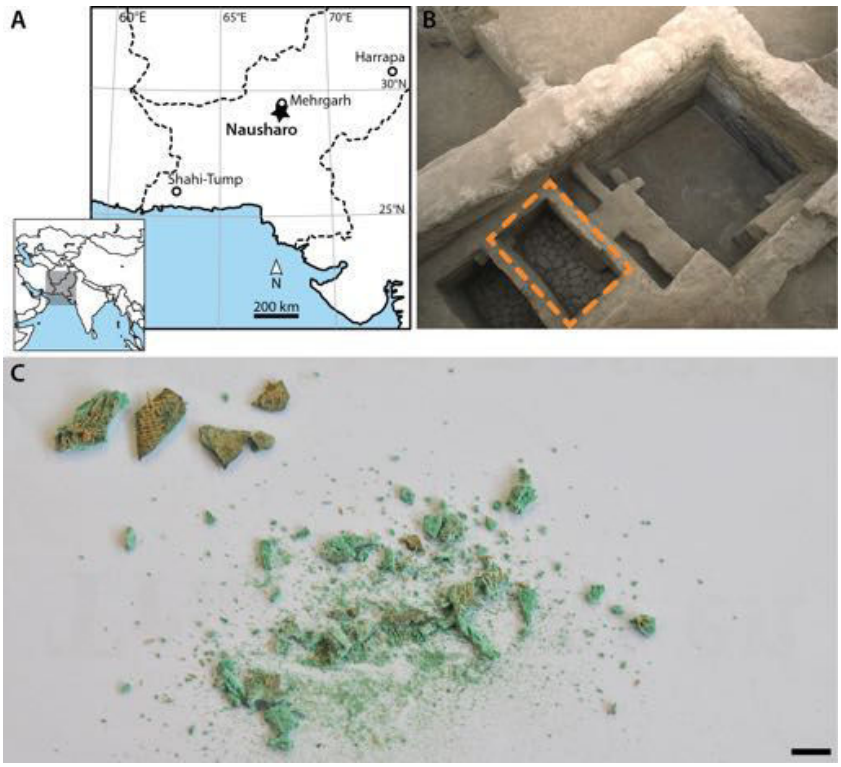

Figure 3.3: Archaeological site and artefact of Nausharo (current Pakistan). A, Location of Nausharo. B, Photo of storage rooms from Nausharo during excavations (© Mission Archéologique de l'Indus, C. Jarrige). C, Artefact NS 95015002 found in the storage room (locus 161) shown with the orange rectangle in B. Scale bar in C: 5 cm.

periods I–III) which extends from the pre-Indus to the late Indus period (3rd–2nd mill. BC), with a transition period during the mid-2nd mill. BC [188, 189, 190]. A team of archaeologists conducted excavation works between 1985 and 1996 under the direction of J.-F. Jarrige, the responsible of the Indus-Balochistan archaeological research centre of CNRS (UPR 316) and the Mission archéologique de l'Indus [191, 57], in collaboration with the Department of Archaeology of Pakistan (Fig. 3.3A). Archaeobotanical studies relying on palynology have indicated that the climate was warmer and dryer than nowadays around the 3rd mill. BC at Nausharo [57]. The site of Nausharo is now made up of two tepes (small hills), one in the north which rises 9 m above the plain and the other in the south which is only slightly less than 6 m high [57]. The present surface area of the

site does not exceed 6 ha, resulting from several erosion episodes of successive agglomerations, whereas the original surface is expected to have been much larger [57]. Excavations show that all the structures, even the platforms more that 11 m wide, disappeared in bevels on the east and west before after being covered by the nearly 3 m-thick new alluvial deposits [57]. Several archaeological artefacts dating from the "pre-civilisation of the Indus" (i.e. period I of Nausharo) were found at the northern tepe of the site. Sherds were found in the deeper archaeological stratigraphic levels of the northern tepe, which are comparable to those found in the early period VII and possibly even the end of the period VI of Mehrgarh [57]. The oldest buildings that were excavated in Nausharo are contemporaneous with the period VIIB of Mehrgarh and belong to the period IB of Nausharo, around 3rd mill. BC. Buildings from period IB in Nausharo were located in an area limited to a little less than 300 m^2. Geologically, Nausharo was characterized by very saline waters, while tertiary limestone was the main soil component in a silty ("marly" [188]) environment of clay and sand.

One artefact from Nausharo was studied under the supervision of A. Didier (laboratory ArScAn) and C. Moulhérat.

Artefact (inv. no. NS 95015002, Fig. 3.3C)

This fragmentary artefact dates from the 3rd mill. BC. During the excavation led by Gonzague Guivron in 1995, corroded copper slabs with textile remains on their surfaces were found in the pre-Indus workshop identified as 'NS 01', located in the northwestern part of the northern tepe. The original shape and function of the object is unknown (Fig. 3.3C). These fragments were collected in one of the rectangular storage rooms, locus 161 (orange rectangle, Fig. 3.3B), which located to the west of a large rectangular room. Several millimetric samples were selected and studied to describe this artefact, numbered NS 95015002-1 (dimensions ca. 2.0×1.5×1.0 mm^3), NS 95015002-2 (ca. 2.5×2.0×0.5 mm^3), NS 95015002-3 (ca. 5.0×3.0×0.5 mm^3), and NS 95015002-6-1 (ca. 4.0×3.5×1.0 mm^3).

Individual fibres were extracted and an individual yarn was embedded in epoxy resin for cross sectional analysis.

3.1.3 Material from Tello (Mesopotamia, current Iraq)

Designated by the Arabs as Tello in modern times, the site is located in the delta plain between the Tigris and Euphrates rivers in Lower Mesopotamia (Fig. 3.4A and B). Tello was occupied at least from the beginning of 5th mill. BC in the so-called Ubaid period to the last 1st mill. BC. Tello is mostly known for its 3rd mill. BC archaeological levels when it belonged to an important Sumerian kingdom ruled by the 1st Lagash Dynasty. Tello was then called Girsu. Submitted, with the other Sumerian kingdoms, in the 24th century BC by the Akkadian kings, the Lagashite kingdom regained independence at the fall of Akkad around 2200 BC. In the last centuries of the 3rd mill. BC, Tello and the other cities of the Lagashite kingdom were ruled by the 2nd Lagash dynasty, whose most famous prince was Gudea. Finally governed by the kings of Ur (close to Girsu), Tello definitely lost its importance after the fall of Ur in 2004 BC. From the 1870's, the French excavations in Tello uncovered the then totally forgotten Sumerian kingdoms. The excavation works in Tello were initiated by E. de Sarzec (1877–1900) and continued by G. Cros (1903–1909), H. de Genouillac (1929–1931) and A. Parrot (1931–1933) for the musée du Louvre [30, 192, 118, 193, 194]. These excavations brought to light the first evidence of ancient Sumerian culture through a large number of archaeological finds (metals, clay products, stone, etc.). The arrival of these excavated artefacts at the musée du Louvre led to the creation in 1881 of a specific department dedicated to the Ancient Near Eastern antiquities (*Département des Antiquités orientales*). The mounds of Tello cover an area of about seven square kilometres that extend along a north-west to south-east axis. From a major mound extends a series of smaller mounds more or less spaced, converging at the front and enclosing between them a vast free space almost circular of about one kilometre in diameter. The other mounds extend

Figure 3.4: Archaeological site and artefacts of Tello (current Iraq). A, Location of Tello. B, Photo of Tello during excavations (reused from E. de Sarzec et al., 1912 [30]). C, Axe blade AO 27703. D, Vase AO 14506 (© Musée du Louvre, A. Thomas). E, Foundation peg AO 77 (© Musée du Louvre, P. Fuzeau). Scale bars in C, D and E: 1 cm.

eastward for several kilometres. The ancient constructions were built of raw square bricks made of a mixture of clay and chopped straw (lateral length about 20 cm and thickness about 10 cm). These bricks, which were tightly compressed and then dried in the sun before installation, offered very strong mechanical resistance. A light layer of mortar was placed between the bricks, guaranteeing the homogeneity and solidity of the construction [30, 194]. In ancient time, since the Neolithic Revolution, the water table was very close to the surface. Cultivation quickly led to salty soils throughout the plain. As the site was located in a marshy landscape, huge areas were unusable for agriculture or very difficult to develop. Human activities such as deforestation and land reclamation have caused imbalances in climate and vegetation, leading to soil erosion and increased aridity [195, 196].

Four artefacts excavated from Tello have been studied as part of this work. It is very likely that they were rapidly rinsed, mechanically cleaned (brushed) and let dried under the sun as is almost systematically the case for an excavation. They are all kept at the musée du Louvre (Département des Antiquités orientales) under the supervision of A. Thomas.

Axe blade (inv. no. AO 27703, Fig. 3.4C)

This artefact is the blade of an axe (dimensions ca. $10.0 \times 4.0 \times 0.5\,\mathrm{cm}^3$, weight: 149 g). It is dated from the early 2nd mill. BC and was found in female grave by H. de Genouillac between 1929 and 1931 [193, p. 92]. Textile remains are present on both sides of the artefact although they were not recorded in the excavation report (Fig. 3.4C). Extraction of individual fibres to observe in detail the microscopic features of the textile could not be attempted due its fragility.

Metal vase (inv. no. AO 14506, Fig. 3.4D)

A corroded copper-base metal belly vase dating from the 2nd mill. BC was collected in a female grave during the excavation carried out by H. de Genouillac between 1929 and 1931 [118]. The vase (weight: 61 g) was originally 62 mm high and with a maximum circumference of 42 mm. Textile remains were observed on the artefact described by H. de Genouillac as "traces de tissu adhérent" [traces of adhering textile] [118, p. 49]. Due to its fineness (fragility), the vase was broken into fragments probably during mechanical cleaning or during transportation (Fig. 3.4D). One of these fragments, AO 14506-3 (dimensions ca. $6.0\times4.0\times1.0\,mm^3$), was selected and studied in detail in this paper. Analysis of another fragment without textile remains, AO 14506-1b (ca. $2.5\times2.5\times1.0\,mm^3$), has been presented as part of a methodological work by Li et al. [197].

Foundation pegs (inv. no. AO 77, in Fig. 3.4E and inv. no. AO 76)

Both artefacts were unearthed among other foundation pegs by E. de Sarzec and then H. de Genouillac between 1884 and 1931. They discovered these pegs buried in brick cubicles under the doors or walls of edifices [30, 37]. Dedicated to Ningirsu, the godfather of Girsu, these artefacts are dated to the reign of prince Gudea during the Second Dynasty of Lagash according to the inscriptions they bear (Neo-Sumerian period, late 3rd mill. BC; AO 77: height 21.2 cm, thickness 7.25 cm, width 3.25 cm, weight 1313 g; AO 76: height 21.8 cm, thickness 7.5 cm, width 4.2 cm, weight 1324 g) [198]. They were restored in a laboratory in Nancy (France) in the 1980s [37, 73]. However, the textiles of these two pegs are well preserved, suggesting very limited mechanical treatment, otherwise textile remains and external corrosion products would all be cleaned as seen on other artefacts. As mentioned in cuneiform texts and represented on a stele fragment (inv. no. AO 4581), foundation pegs were ritually be placed in the foundations of a temple or of an important edifice under construction [37]. Each artefact takes the form of a bearded man, in fact a

god according to the four-row tiara he wears, which characterizes deities (Fig. 3.4E). He is dressed in a short loincloth and a long open dress on his left side [37]. He is crouching with one knee half raised and holds himself a peg between his legs with both hands. Ornaments may have also been added over his head suggested by the presence of a slot at the centre of his tiara. The pegs are made of an unalloyed copper material [37, 199] that were certainly cast in one piece using the lost-wax process invented and developed in Baluchistan [200, 45]. Remnants of textiles are clearly visible on the two pegs, as already mentioned by E. de Sarzec: "plusieurs figurines sur lesquelles le vert-de-gris a conservé aussi l'empreinte d'un tissu dans lequel elles devaient être enveloppées" [several figurines on which the verdigris has also retained the imprint of a textile in which they must have been wrapped] [30, 37, 73, p. 242]. Fibres were extracted for microscopic examination.

3.1.4 Materials from other archaeological sites

Corroded copper-base fragments with textile remains excavated from other archaeological sites are also studied (Figure 3.5). Sample St-Dizier 12-1 was discovered in Saint Dizier (France) and dates back to 14th–15th century of Middle Ages (Figure 3.5A). This sample shows a global blue colour and crossing of mineralized yarns is visible. Another sample Orléans 347-1 was excavated from Orléans (France) and dates back to 5th–7th century of Merovingian period, it is one of the fragments of a broken corroded copper brooch (Figure 3.5B). These samples are conserved in Quai Branly–Jacques Chirac museum under the supervision of Christophe Moulhérat.

3.1.5 Reference flax fibres

Modern flax fibres as reference were provided by Christophe Moulhérat. They were collected from la Haute-Normandie region in France without any chemical treatment (e.g. bleaching) (Figure 3.6).

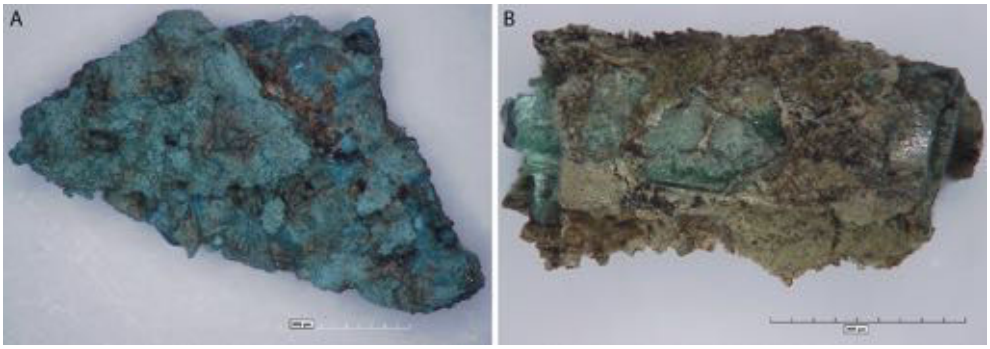

Figure 3.5: Samples from archaeological sites of Saint Dizier and Orléans in France. A, Sample St-Dizier 12-1. B, Sample Orléans 347-1.

Figure 3.6: Reference flax fibres collected from la Haute-Normandie region in France.

3.2 Methods

In order to characterize the organic remnants and inorganic phases of the artefacts (and samples) described above, a dedicated methodology was developed based on complementary non-invasive synchrotron based techniques and classical approaches. It aims at collecting multimodal information at different spatial resolutions (from millimetric to nanometric). Here a brief introduction to synchrotron radiation and several analytical methods as well as the corresponding data processing steps are presented. Additional techniques used which are less significant to this work are described in Appendix B.

3.2.1 Short introduction to synchrotron radiation (SR)

Synchrotron-based methods are increasingly used for the physico-chemical characterization of ancient materials [201, 202].

Synchrotron radiation is an electromagnetic radiation emitted by charged particles for example electrons, that are subjected to transverse acceleration. Electrons are accelerated to high energies and maintained at high energies in a storage ring. Magnetic dipoles (bending magnets) are used to deflect the electrons within the storage ring. In straight sections, insertion devices (wigglers or undulators) consisting of series of alternating magnetic dipoles can be installed in the straight sections between the bending magnets. These deflect the electrons in a sinusoidal trajectory with tangential accelerations. When deflected, the electrons emit photon radiation. For a wiggler, the radiated flux is proportional to the number of dipoles used and is composed of polychromatic photons with a broad and continuous spectrum ranging from hard X-rays to far infrared (Figure 3.7C). In an undulator source, constructive interference of radiation emitted from successive dipoles produces a non-continuous spectrum with harmonic peaks (Figure 3.7C). The emitted radiation is delivered to experimental end stations via different beamlines [203]. Each beamline is equipped with optical elements that are used to gather,

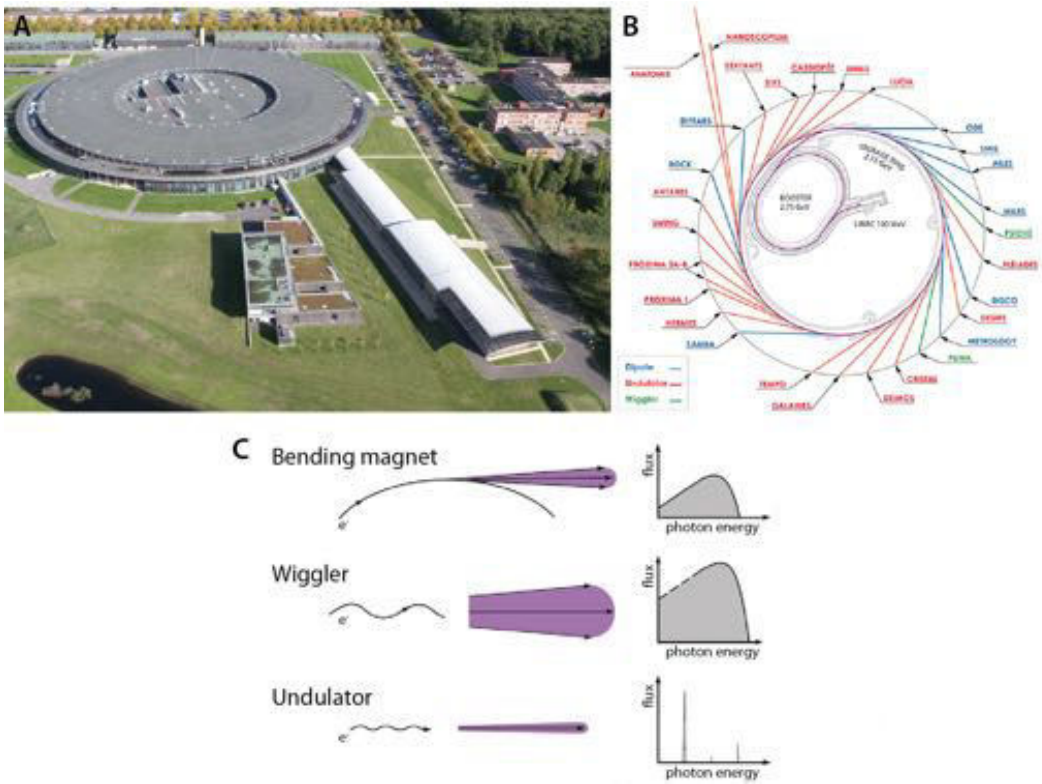

Figure 3.7: Presentation of the synchrotron source of the SOLEIL Synchrotron (Gif-sur-Yvette, France). A, Top view of SOLEIL Synchrotron (*reused from SOLEIL Synchrotron Magazine*). B, Distribution of various beamlines. C, Different synchrotron radiation sources (modified from lectures of D.T. Attwood).

select and focus the synchrotron beam towards samples to be studied (Figure 3.7B).

Considered as a bright artificial source of parallel X-rays, the synchrotron radiation can provide high photon flux, small source size and low divergence, thus making synchrotron-based spectroscopy and imaging techniques more sensitive and suitable for the analysis of archaeological materials, which are usually complex or heterogeneous [201].

Within this PhD project, all synchrotron experiments have been performed at SOLEIL Synchrotron located at Gif-sur-Yvette France (Figure 3.7A). Here, electrons are produced and pre-accelerated in the linear accelerator (Linac, 16 m). Then, they are accelerated again in the booster ring (156 m circumference) to an energy of 2.75 MeV and transported into the storage ring (354 m circumference).

3.2.2 Micro-computed tomography (µCT)

Invented in 1972 by G. N. Hounsfield [204] for medical applications (Figure 3.8), X-ray tomography has developed considerably since then both in the medical field and the industrial field (defect detection and dimensional inspection) [205].

Overview of principle

From a set of two-dimensional X-ray transmission radiographs acquired during the rotation of a bulky artefact, CT provides a reconstruction of its internal structure in three dimensions, a major asset in the field of material characterization [206]. The principle of tomography by X-ray absorption is based on the multidirectional analysis of the interaction between the X-ray beam and the material, and relies on the collection of X-ray radiography at each position of the studied sample with respect to the incoming X-ray beam [207]. The incident X-ray source can be either a cone beam (usually laboratory setup) or a parallel beam (e.g. synchrotron radiation).

The acquisition time during the measurement varies from a fraction of a second to a

Figure 3.8: G. N. Hounsfield with an early version of the CT scanner (reused from G. N. Hounsfield 1973 [204]).

few hours depending on the installation. Data are collected at multi projection angles, of which the number and the step depend on the type of device and the requirement of resolution [208]. Next, using these data, a digital image can be mathematically calculated and reconstructed as an array of voxels (the 3D equivalent of pixels) in different grayvalues [205].

X-ray tomography thus allows access to density variation inside the material to assess the variations of radiological absorption and the differences in composition. It also enables the identification of very fine structure such as heterogeneity, voids or inclusions present in an artefact, and to verify the assembly and positioning of complex mechanical assemblies in industry [205, 206].

Micro-CT (µCT)

Since the geometry, the dimension and the chemical composition of materials composing artefacts can be a limitation regarding the analytical capabilities of existing medical

or industrial devices, and requirements for characterization are becoming increasingly demanding nowadays in terms of resolutions, new specific tomographs thus have been developed to achieve better resolution.

The resolution obtained with conventional tomography devices is at best a fraction of a millimetre [209]. Micro-focus X-ray tube sources can improve the spatial resolution to the sub-micrometre, but at the cost of reduced flux, and hence longer acquisition times. With dedicated X-ray sources such as synchrotron radiation that can provide high spatial coherence and very high brightness, µCT can enable access to small parts with very fine resolution giving essential information for the understanding of structures and certain mechanisms in the medical or industrial field, as well in material science [206].

Contrast mechanisms

Absorption contrast. When a parallel beam of monochromatic X-rays of intensity I, at normal incidence, passes through a quantity of material of infinitesimal thickness dx, the transmitted beam is attenuated by the intensity dI (Figure 3.9) [205].

$$dI = I\mu dx \tag{3.1}$$

This leads to Beer-Lambert's law (or attenuation low) giving the transmitted intensity by a thickness x of matter, with I_0 incident intensity and µ, the linear attenuation coefficient (expressed in cm^{-1}).

$$I_x = I_0 e^{-\mu x} \tag{3.2}$$

In the case of a homogeneous material consisting of n elements with the proportions expressed in atomic densities (number of atoms per unit volume of the material), the coefficient μ can be written as follows, with N_m - atomic density of m^{th} element and σ_m - cross section of m^{th} element [207].

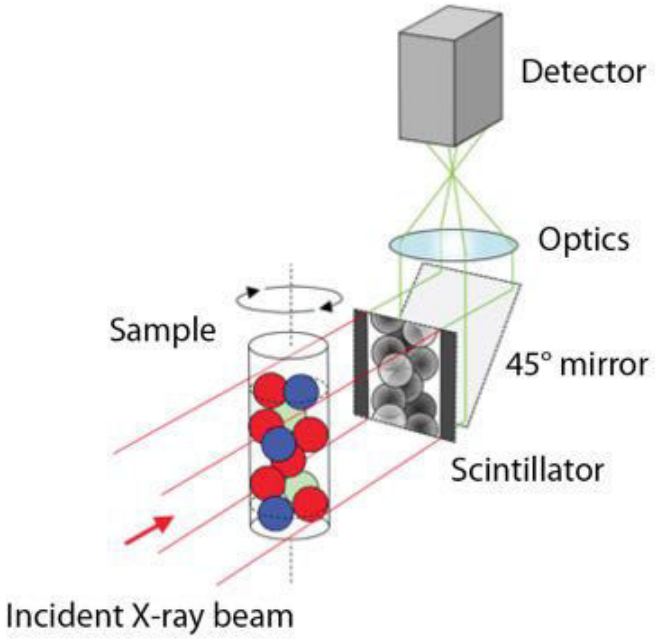

Figure 3.9: Schematic representation of the CT with a parallel incident X-ray beam (© A. King). When sample is irradiated by photons (X-ray beam), the intensity recorded in the detector is a measurement of the integral of the attenuation coefficients along the line perpendicular to the detector and passing through the sample.

$$\mu = \sum_{m=1}^{n} N_m \sigma_m \tag{3.3}$$

The relation (3.2) can explicitly involve the density ρ of the material concerned into the form as:

$$I_x = I_0 e^{-\rho x \frac{\mu}{\rho}} \tag{3.4}$$

in which the $\frac{\mu}{\rho}$ is the mass attenuation coefficient (often expressed in $cm^2 \cdot g$):

$$\frac{\mu}{\rho} = N_A \sum_{m=1}^{n} w_m \sigma_m / A_m \tag{3.5}$$

with N_A - Avogadro constant, A_m - atomic mass of element m and w_m - weight concentration of element m in the material ($w_m = N_m A_m / N_A \rho$).

Absorption tomography allows to obtain a map of μ, the linear attenuation coefficient, based on the equations mentioned above. The amplitude of this term depends on the energy of the incident photon E (therefore on the wavelength of the incident beam), the density ρ, and the atomic number Z of the investigated material.

For X-rays of low energy (less than 100 keV), the dominant mechanism is the absorption of the photon with ejection of a photoelectron, which also explains the jumps of absorption observed when the energy of the photon reaches a value sufficient to eject an electron from a deep atomic level. Beyond 100 keV, the contribution of the Compton effect (inelastic scattering of photon) becomes progressively preponderant until the dominant phenomenon is the interaction of the photon γ (higher than 1MeV) with the electrostatic field of the atomic nucleus, which leads to the absorption of the incident photon and to the creation of an electron-positron pair.

The Figure 3.10 represents the evolution of $\frac{\mu}{\rho}$, the mass attenuation coefficient, as a function of the energy E of the photons for two pure elements, limited to the energy

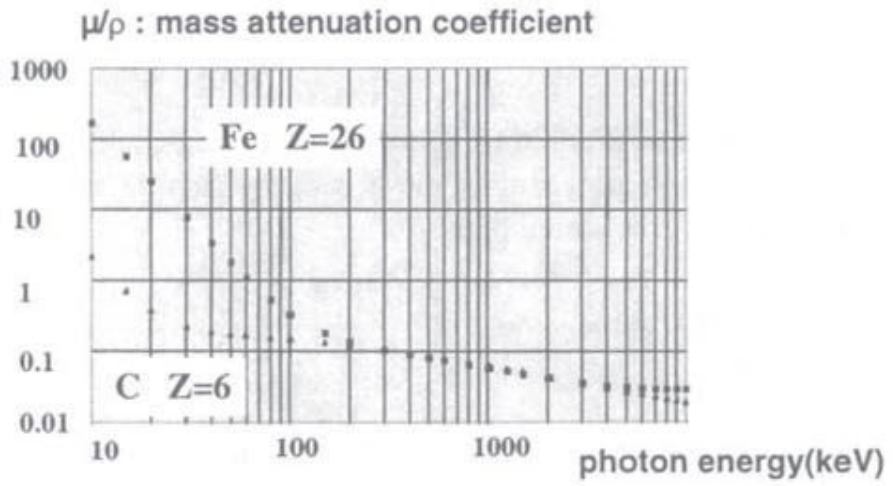

Figure 3.10: Value of the mass attenuation coefficient of Fe and C (reused from J. Baruchel et al., 2000 [205]).

domain of the conventional computerized tomography (E≤1 MeV): in the 1 keV≤E≤100 keV domain, dominated by photoelectric absorption for the two elements, the essential remark concerns the rapid decrease of $\frac{\mu}{\rho}$ when the energy of the photons increases and, for a given photon energy, the very high growth of $\frac{\mu}{\rho}$ as a function of the atomic number of the element concerned [205]. These two behaviours can be summarized by an empirical formula as:

$$\frac{\mu}{\rho} = C \cdot \frac{Z^4}{E^3} \tag{3.6}$$

where C is a constant. According to this equation, μ is proportional to ρ and to Z^4 for a given photon energy. The equation implies that only with the same Z (identical atomic element or chemical composition), is the comparison of ρ between two regions of interest (ROIs) inside an artefact (or between two different artefacts) quantitatively meaningful; a change in ρ between two zones can be counteracted if there is a change of Z in the opposite direction. In that way, if one needs to obtain a clear separation between Z and ρ in the photoelectric absorption domain, the use of two different incident

energies is necessary to perform two tomographic images.

Then in the energy domain above 200keV, e.g. when the phenomenon is dominated by Compton effect, it's seen that the information obtained by tomography is almost proportional to ρ, because of the slow change of μ based on Z and on photon energy. Nevertheless, according to the Beer-Lambert law, it may not be possible to achieve sufficient contrast within the reconstructed image in the case of lower μ at higher photon energies [210].

Phase contrast. When attenuation contrast is low between two components in a sample or, when a sample to be detected mainly consists of weakly absorption materials and structures with low atomic number such as soft tissue, absorption-based CT imaging cannot provide satisfying contrast and spatial resolution [211]. In this case, an additional configuration called "phase contrast (PC)" is applicable [212, 205], the delivered contrast is orders of magnitude better than conventional absorption contrast images [213].

X-ray is a wave that can interfere at the interface between two materials and cause refraction. During propagation through the interface between materials with distinct refraction indexes, the amplitude (intensity) of X-ray is attenuated and the phase is shifted due to refraction [214]. These changes in amplitude and phase can be calculated using the complex index of refraction n (unit-less, 3.7):

$$n = 1 - \delta + i\beta \tag{3.7}$$

In this expression [213], the refractive index decrement δ, originally proportional to the electron density in the material, leading to a phase variation of X-ray compared with its propagation in vacuum (Figure 3.11). The phase shift can also affect the direction of X-ray. The imaginary part β, called absorption index, determining the attenuation of the wave when passing through an artefact and, essentially proportional to the linear attenuation coefficient μ of material.

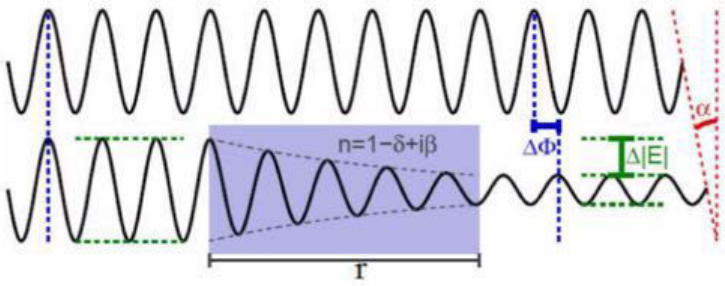

Figure 3.11: Changes in phase and attenuation of a wave when passing through a material (modified from T. Jensen 2010 [213]). The loss in amplitude (intensity) $\Delta|E|$ of wave influenced by β is indicated by green lines. The phase shift $\Delta\Phi$ affected by δ is indicated by blue lines. The change in direction of wave α resulted from the phase shift is indicated by red lines. The thickness of material is represented by r.

The phase shift can be determined through measurements of change in direction of X-ray using several phase contrast imaging methods, such as crystal interferometer (Figure 3.12A) [215, 216, 217], analyzer based imaging (ABI, Figure 3.12B) [218], propagation based imaging (PBI, Figure 3.12C) [219] and grating based imaging (GBI, Figure 3.12D) [220]. Here special focus is given to PC-CT based on PBI, this method is suited for synchrotron use and is particularly good at edge enhancement [221]. Each of the interfaces present in sample (for example the interface between two components, or cracking of one of them) results, on the screen, by the appearance of a diffraction pattern which highlights the discontinuities of the medium. The camera is placed far from the sample (a few centimetres to several metres, depending on pixel size and photon energy) to clearly record these diffraction patterns, which corresponds to the Fresnel regime (radiative near-field diffraction) [205] (Figure 3.13).

Based on PBI-PC-CT imaging, a more quantitative approach, holotomography, was developed [223]. Instead of the reconstruction of linear absorption coefficient in conventional absorption CT, this method allows quantitative reconstruction of the refractive inde.g. The procedure to determine the phase shift is based on obtaining radiographs for several (usually between 2 and 4) distances between sample and detector. At each

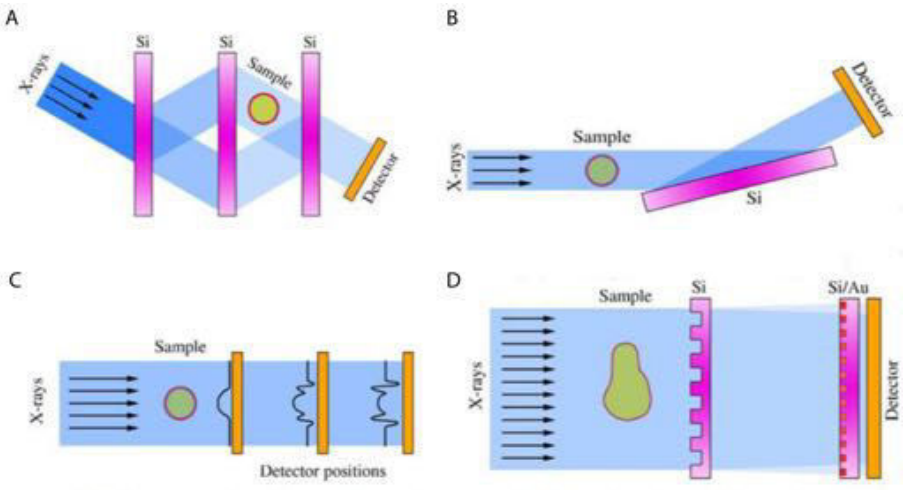

Figure 3.12: Schematic representation of several phase contrast imaging methods (modified from M. Bech 2009 [222]). A, Crystal interferometer. B, Analyzer based imaging (ABI). C, Propagation based imaging (PBI). D, Grating based imaging (GBI).

point of sample, the difference between 1 and local refractive index of the considered voxel can be quantified. This difference is proportional to the electronic or mass density of the material in corresponding voxel [224].

For homogeneous object, an algorithm was developed by David Paganin aiming to enhance the phase contrast effect, under assumption that the object can be described by a single ratio of $\frac{\delta}{\beta}$ and is subjected to illumination by a sufficient monochromatic radiation [225]. In this case, the sample to detector distance is adjusted such that a single Fresnel diffraction fringe is visible. Figure 3.14 shows the algorithm applied to X-ray radiographs to retrieve the projected thickness of a sample.

Local tomography

Experimental constraints usually exist during CT measurements. For example, the field of view (FOV) is limited because of the physical size of the detector. When the dimension of the sample is larger than FOV, a setup called *local tomography* or *region-of-interest (ROI) tomography* can be used (Figure 3.15) [226]. In local tomography, the signals

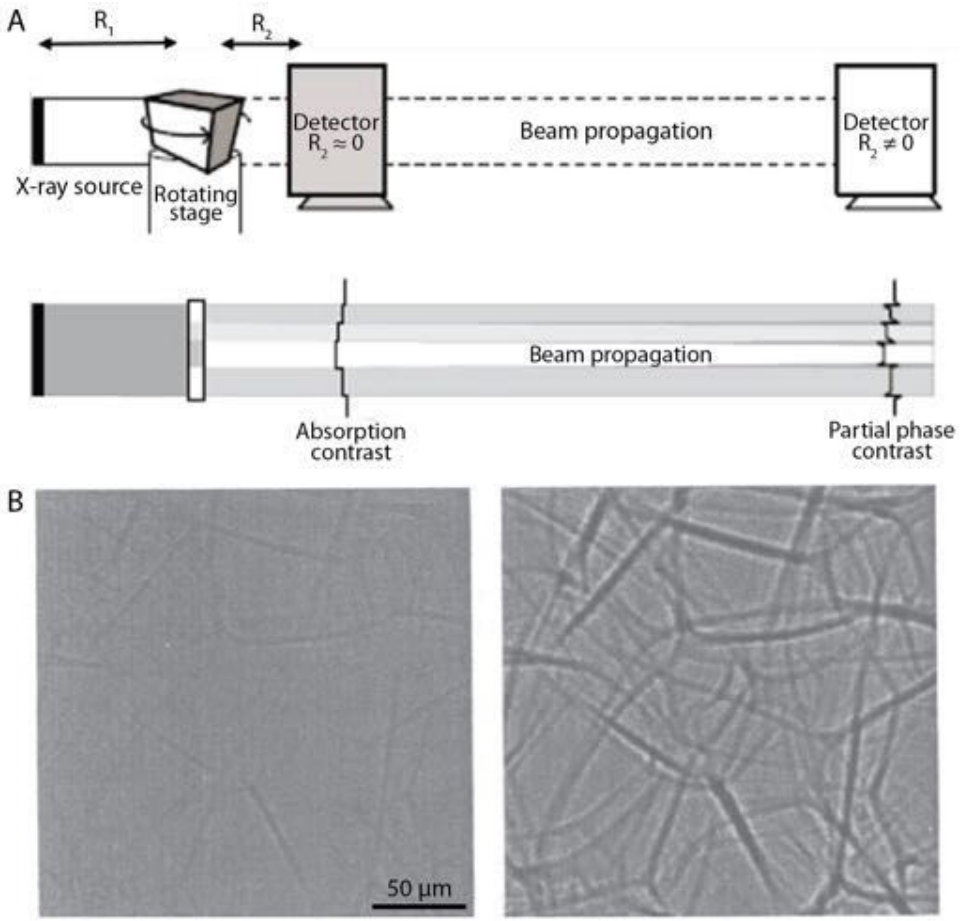

Figure 3.13: Principle of PC-CT based on PBI. A, Comparison between CT in traditional absorption mode and in PBI based phase contrast mode (modified from L. Bertrand et al., 2012 [201]). B, Enhanced edge of polystyrene foam due to the high phase contrast that occurs when R_2 (sample-detector distance) increases from 0.03 m (left) to 0.2 m (right) (reused from J. Baruchel et al., 2000 [205]).

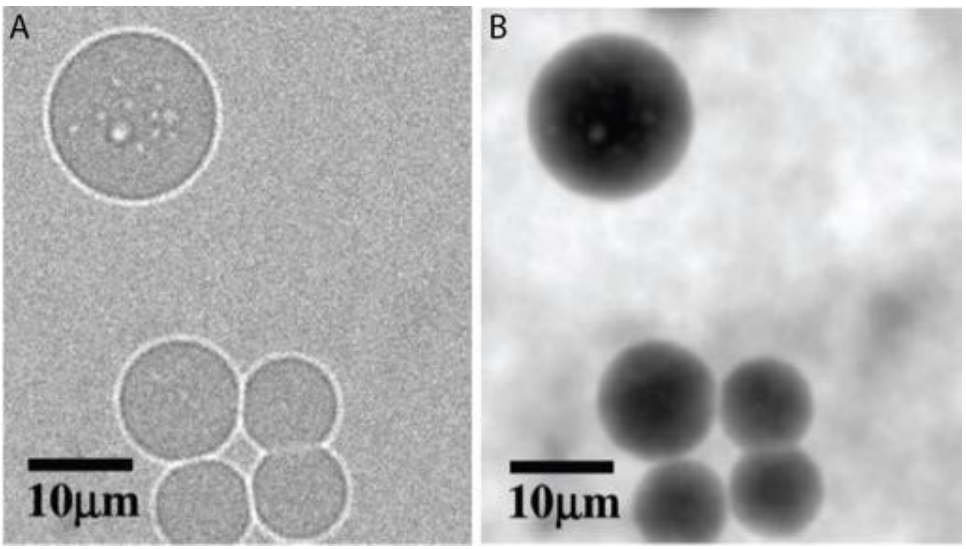

Figure 3.14: µCT imaging of latex spheres (reused from D. Paganin et al., 2002 [225]). A, Phase contrast X-ray image. B, Retrieved projected thickness as obtained from A.

are collected from the imaged ROI and some area around ROI, whereas other areas of external part are not imaged for every angle. Since the data are not complete, several methods aiming to estimate the exterior of the ROI during reconstruction from collected data are available, such as sinogram (the Radon transform data, see later) extrapolation [227]. The quality of reconstruction in local tomography depends on the composition of sample, the position of selected ROI during measurements and, the ratio between ROI and the size of sample. If ROI is well centred during rotation and the sample is generally homogeneous, a satisfactory reconstruction of the sample structure can be obtained [228].

Preprocessing

The acquired raw data (projections) are generally preprocessed by several steps [205, 208, 206]. The first treatments are usually composed of two parts:

- elimination (subtraction) of the averaged false signal, i.e. removal of the detector read-out dark current background measured by the detector in the absence of

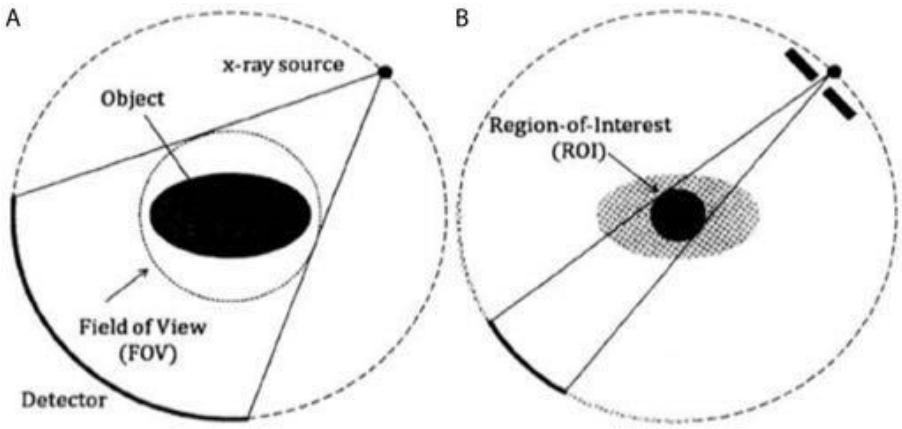

Figure 3.15: Schematic representation of CT setup (reused from E. A. Rashed et al., 2010 [229]). A, Standard CT setup. B, Local CT setup.

beam, which is aim at avoiding the influence by imperfect camera pixel elements and by impurities/defects on the scintillator screen.

- correction by the flat field images, that is, images of beam profile recorded at different moments when no sample was present. The beam spatial non-homogeneity can be thus corrected via dividing each projection by the median flat field image acquired.

Then, the set of projections obtained is rearranged as a sequence of sinograms, one per detector line perpendicular to the rotation axis. The rearrangement is in particular adapted to the parallel geometry case, in which each reconstructed slice is treated by one (and only one) sinogram.

An additional optional pre-treatment step is conducted on the sinograms processing (or after the reconstruction) to correct the often encountered ring artefact, resulting from the remaining error of certain pixels after flat field correction of the data. These errors are visibly parallel to the projection-angle axis in the sinogram, forming thus the concentric rings in the reconstructed slices (Figure 3.16). Three main sources of ring artefact after previous corrections are:

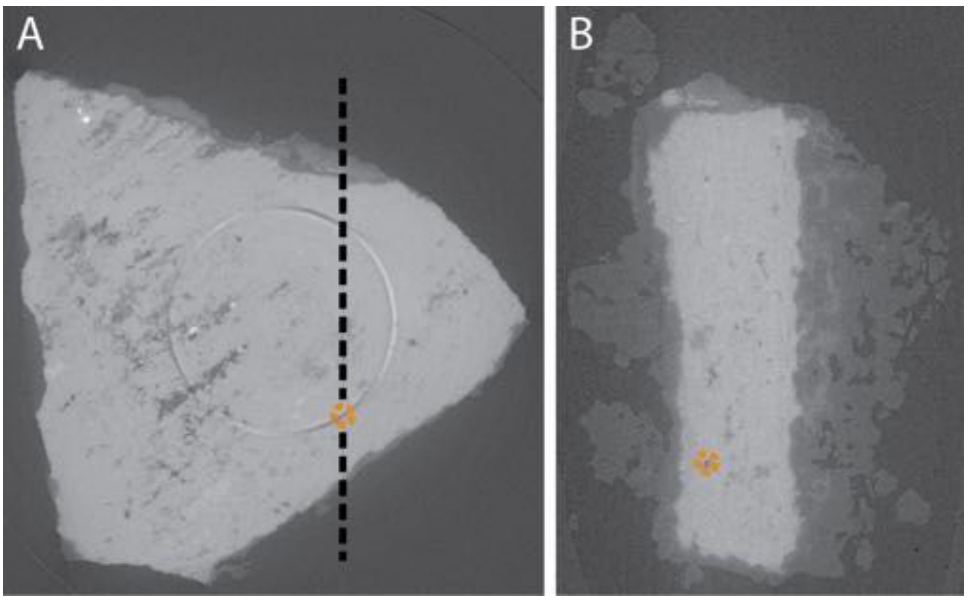

Figure 3.16: An example of ring artefact. A, Ring-artefact observed in one reconstructed tomographic slice of vase fragment AO 14506-1b. B, Another slice at perpendicular plane to A that passes through the dashed line. The black part inside orange cercle in B due to the ring artefact can give a false impression that there is a pore at this position.

- Intensity dependency of the non-uniform sensitivity of the different camera pixels.
- Non-linearity of the non-uniform response of the scintillator screen.
- Timely dependant heterogeneities in the incident X-ray beam.

Since the superimposed ring-artefact affects more or less the grayvalue in the reconstructed images, they cause difficulties for quantitative treatment as well as segmentation. Thus, it's crucial to remove (or reduce) such artefact for a subsequent analysis. Several algorithms are available to reduce the ring artefact, for example three commonly used methods [230]:

- The second treatment, called double flat field correction, intending to deal with the spurious contributions remaining after flat field correction due to imperfections in the detector system (scintillator or camera). After a first flat field correction, all projections are averaged together to produce a single mean image. High frequency

features in this image are assumed to result from artefacts in the detector system, for example dust on the scintillator, or defective pixels. Low frequency features are removed by median filtering the mean image, and subtracting the result. The window size can be adjusted according to the image artefacts. The resulting "defect image" is used to correct the projections.

- High frequency filter: after the sum over the projection-angles transforming all the sinograms to a 1D signal in Fourier space, this optional correction method could be used to reduce the ring artefacts by extracting these errors and next subtracting them from the sinogram. This method works well on the aberrant pixels at the level of detector, whereas the new artefact could be observed because of the so-called Gibbs effect (the overshoots at jump discontinuities) resulted from the Fourier transformation. At the same time, new artefacts could also be generated if the filtered signal involve a zone belonging to the sample itself, i.e. a zone with high X-ray absorption. In this case, the high-absorbed zone can be thresholded in advance in the first reconstructed slice, the signal of this zone can be thus skipped from the treatment by the high frequency filter for the rest of the sample.

- Moving average filter: this efficient algorithm is applicable by sinogram processing during the volume reconstruction to eliminate the ring artefacts. It is aimed at smoothing the whole image to change the grayvelue at the peak positions in the sinogram transformed by all measured projections, thus facilitate the subsequent volume segmentation.

Reconstruction

Before the launch of volume reconstruction, it is important to confirm the position of rotation axis, which is generally at the centre of the FOV for the entire acquisition data but, off-centred at different levels for the half-acquisition (extended FOV [231])

data. The influence of the selection of rotation axis is revealed in the Figure 3.17 of one same reconstructed slice, the semicircle-shaped artefacts, presented particularly at the boundary of artefact (and at the interfaces not shown in the figure) in various orientations are due to the improper rotation axis [207, 232, 233, 234].

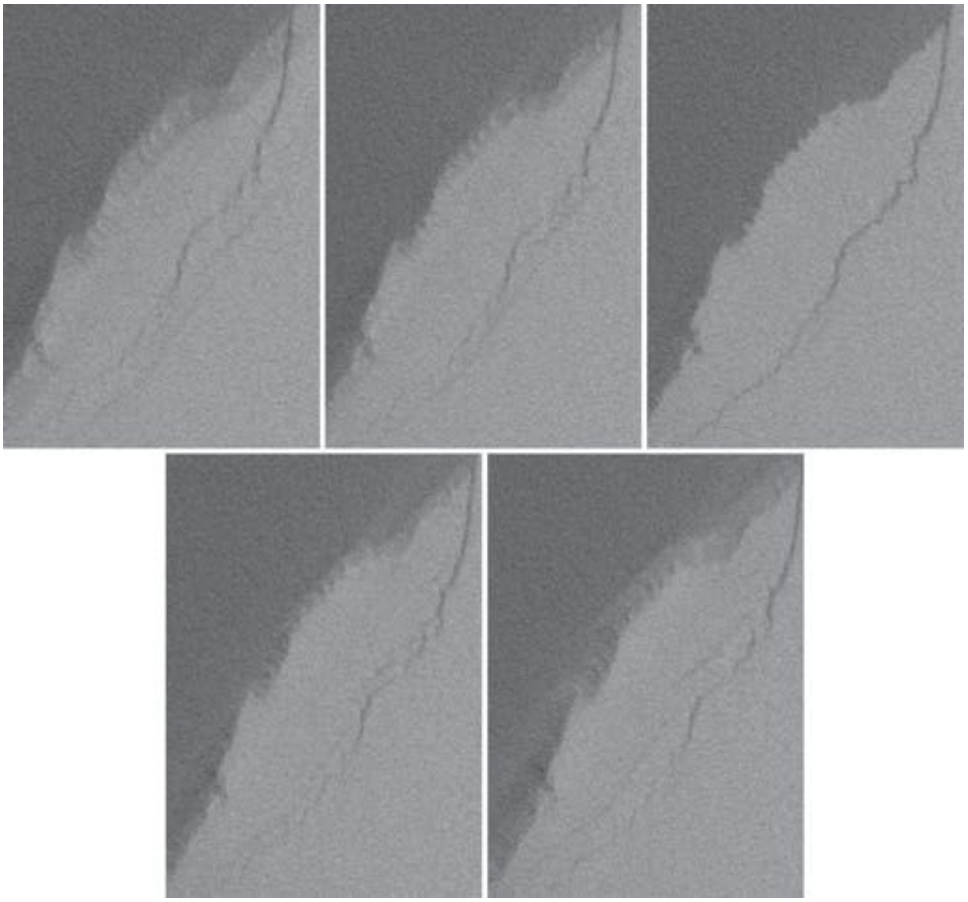

Figure 3.17: Influence of selection of rotation axis during the volume reconstruction of part of one sample (from left to right then top to bottom), the third one is obtained using the correct rotation axis value.

The reconstruction methods can be classified in two categories, analytical reconstruction and iterative reconstruction (IR). Here we focused on the most commonly used analytical reconstruction, the so-called filtered backprojection (FBP).

The image to be reconstructed is composed of m×n points, called pixels (picture

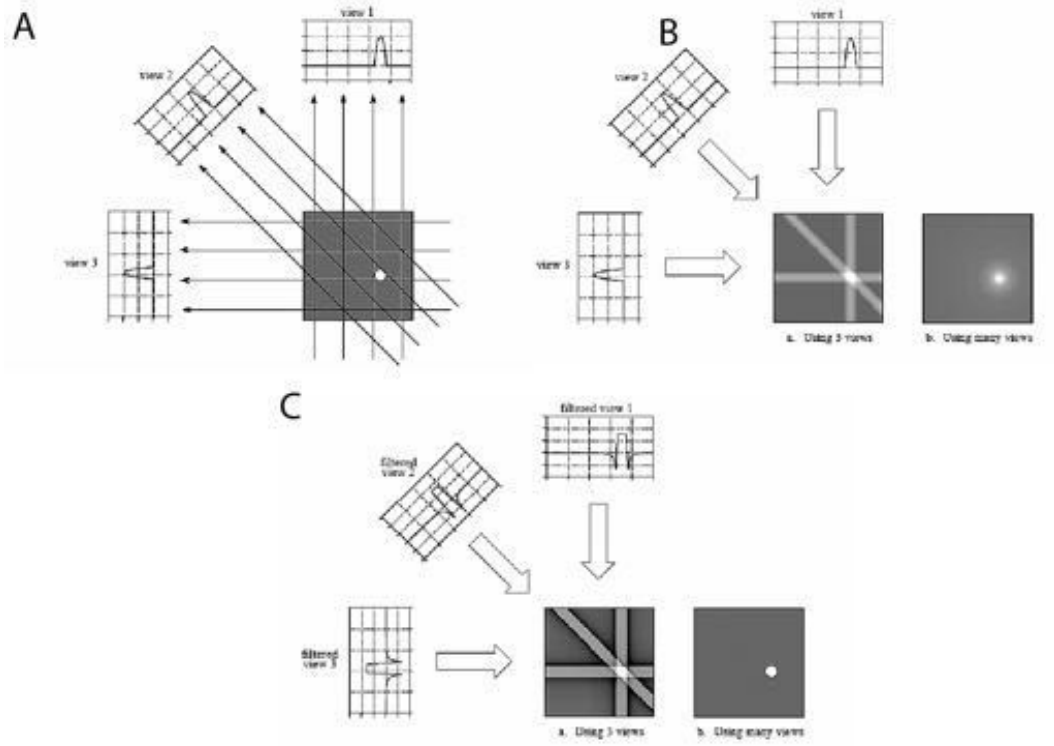

Figure 3.18: Principle of FBP (reused from S. W. Smith et al., 1997 [232]). A, A set of views at slightly different angles are acquired using CT and the corresponding image is reconstructed. The sample in a view is equal to the sum of the image values along the ray that points to the sample. B, An blurry image can be reconstructed using backprojection by taking each view and smearing it along the path that it was initially acquired. C, An clearer image can be reconstructed using filtered backprojection by filtering each view before backprojection. As a most commonly used algorithm for CT reconstruction, filtered backprojection eliminates the blurry effect of image and corresponds to mathematically exact reconstruction of the image.

elements), each of them is assigned to an absorption coefficient μ (or a local density ρ) that should be determined. The intensity measured by the detector at position (i, j) is described as follows (3.8), in which I_0 represents incident intensity.

$$\ln \frac{I_0}{I_{ij}} \propto \mu_{ij} \tag{3.8}$$

The same formula would apply to all successive positions (1 to n) measured during the relative rotations of the artefact with respect to the source-detector pair.

A system of linear equations can be thus established in which the logarithm of the intensities is deduced from the measurements, and the μ_{jl} represents the unknowns to be determined. A matrix inversion should allow, in principle, to express these unknowns as a function of the measured intensities, providing that the system admits a solution which presupposes that the number of measured quantities is equal to the number of unknowns, determining thus the enough distinct angular positions (projections) are needed (usually related to the number of detector pixel). These two matrices projected (intensities and linear absorption coefficients) are correlated between them by the Radon and inverse Radon transforms [205], widely used in tomography, the creation of an image from the acquired projections associated with cross-sectional scans of an artefact.

Assuming that the projection data are available and that the image, in which the Radon transform corresponds to these measurement data is unknown. The next operation to implement is the backprojection. The principe is illustrated schematically in Figure 3.18: by proceeding the same treatment for n profiles obtained under the n different angles, the superposition of the n projections will delimit the artefact and modulate the different rows introducing reinforcements and weakening that reconstruct the internal structure of the initial artefact.

In fact, the reconstruction is not perfect and it is clear that the back projection of a discrete set of n projections is not identical to the initial artefact (the back projection

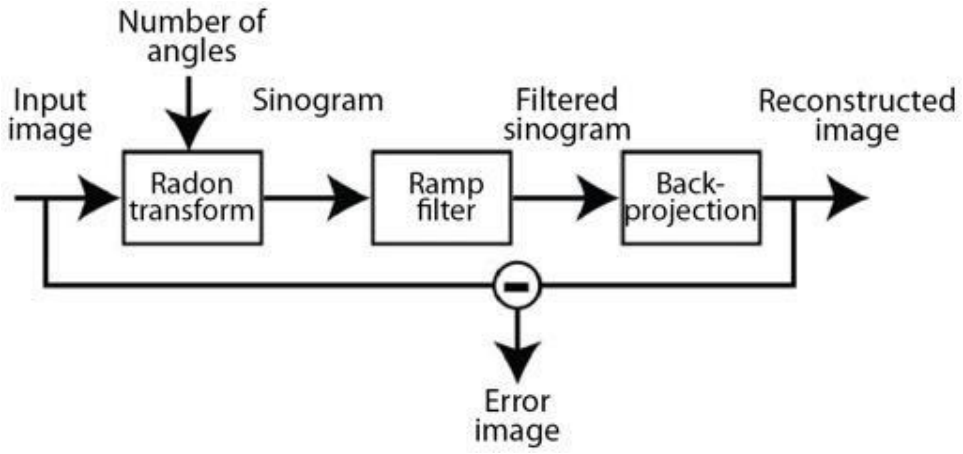

Figure 3.19: The main steps to obtain reconstructed images through filtered backprojection method (reused from M. Liebing [235]).

of a point artefact restores a star with n branches). To improve the method [207], a deconvolution must be performed by the projection function which is a linear function in κ (wave vector). The filtered backprojection method therefore consists in taking the Fourier transform of each profile, then proportionally amplifying the high frequencies (using a ramp filter $|\upsilon|$) and then returning by inverse Fourier transform to the real space before perform back-projection operations [233] (Figure 3.18 and 3.19).

Experimental setup at the PSICHE beamline

PSICHE - Pressure Structure Imagerie par Contraste à Haute Énergie (Pressure Structure Imaging by Contrast at High Energy) – is one of the beamlines in SOLEIL Synchrotron (3^{rd} generation of synchrotron), at Saint-Aubin in France. The principle of synchrotron microtomography at PSICHE is shown in the Figure 3.20A.

Sample mounting. The sample was covered by a polypropylene or kapton film (almost no absorption of X-ray) and laid flat on a plastic screw with a sunken part on the surface to ensure that the sample was immobile during rotation. The screw was next fixed to a metal post, mounted on a kinematic magnetic base (Thorlabs) to allow

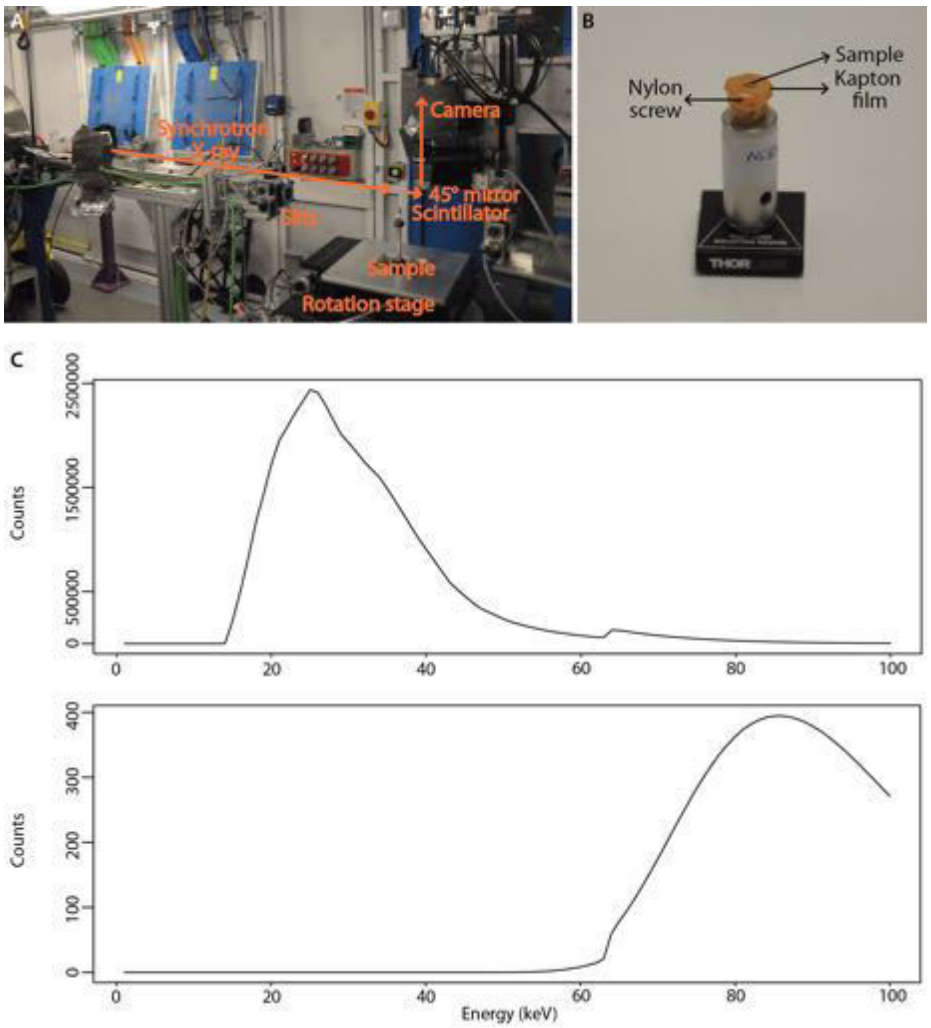

Figure 3.20: A, Setup of the tomography experiment showing the path of the incident and detected beams. B, Fixing of the sample for characterization. C, Incident beam energy profile after passing through a permanent SiC filter and scintillator (top). Energy profile used in this work. The beam is filtered through 6.4 mm of copper to obtain a relatively greater photon flux at higher energy range (bottom).

reproducible positioning on the rotation stage (Figure 3.20B).

Detector parameters. The radiographic projection image of the sample resulting from the absorption of the X-rays by sample is converted into a visible light image by a scintillator screen (LuAG - lutetium $Lu_3Al_5O_{12}$ - 90 and 250 µm thickness respectively for high and low resolution). Then, an image of the scintillator is formed on a camera using visible-light optics, they consist of a mirror at 45° placed behind the scintillator to protect the optical components darkening due to X-ray radiation , and an objective lens (QIOPTIQ Rodagon, Stemmer Imaging) provides 2.7x magnification if in low resolution setup. For the high resolution case, the lens is a 7.5x MITUTOYO long working distance microscope objective. The image is recorded with a sCMOS camera/detector (ORCA Flash 4.2, Hamamatsu: dynamic range 2^7–2^8 bits; pixel size 6.5 mm^2). The obtained pixel/voxel size is 2.4 $µm^3$ for low resolution case and 0.86 $µm^3$ for high resolution.

Beam parameters. The incident white beam (0-100 keV) was first filtered using fixed CVD diamond and silicon carbide filters which removed most photons below 15 keV. For a pink beam operation, other filters were added according to the requirements of the experiment. In our case, a filter consists of several copper sheets was used to have a pink beam between 60 and 100 keV. The thickness of copper filters was set to 6.4 mm (low voxel resolution mode) and 5 mm (high voxel resolution mode). Apart from the relative high photon flux at high energy, the advantage of pink beam used is that it is possible to weaken the phenomena of beam hardening, that is, when the incident radiation X is completely polychromatic or poly-energetic, by passing through a dense structure, the low energy rays are more attenuated than the more energetic rays, which leads to the hardened beam and generates cupping effects and streak artefacts in the reconstructed images [236].

The beam was then defined by adjustable slits to the size of FOV, in our case 5×3 mm^2 and 1.8×1.8 mm^2 respectively for low and high resolution modes. The electron

beam current in the storage ring was 450 mA and the resultant photon flux on the sample was around $2.7\times E^{11}$ ph/mm^2/s (for low resolution mode) and $6.8\times E^{11}$ ph/mm^2/s (for high resolution mode). The propagation distance between sample and detector was fixed to 50 mm to obtain satisfactory phase contrast effect (and 100 mm for higher contrast in low absorbing samples).

Acquisition modes. Three acquisition modes were used during CT measurements at PSICHE beamline, including:

- Simple mode. One image per projection.
- Accumulation mode. Five to ten images per projection averaged together to improve the signal to noise ratio.
- *Spiral mode.* In order to extend the vertical field of view beyond the size of the beam, a series of acquisitions are made while stepping the sample vertically through the beam. This is referred to as "spiral mode" at the PSICHE beamline. The projections are combined to create a single dataset. By ensuring a large overlap (in our case 90% that is equal to 132 pixels-height) from one acquisition to the next, a large number of images are averaged together, improving the signal to noise ratio as for the accumulation mode. In addition, certain image artefacts are reduced.

Acquisition parameters. The number of projections was set to 3000 for entire acquisition and to 5000 for the half-acquisition (or local CT, in case the sample size exceeds the FOV). The time to acquire one image was about 75/100 ms. 31 images were acquired for dark field (DF, with sample but no beam, at the start of analysis), as well as 62 projections for bright field (BF, with beam but no sample, 31 images at the start and other 31 images at the end) for all the samples.

Preprocessing and reconstruction. All the raw data volumes were treated using the PyHST2 software–2nd version of the High Speed Tomography in Python language, developed by Alessandro Mirone of ESRF (European Synchrotron Radiation Facility), including a data pre-processing pipeline and a default FBP reconstruction method. The code used in the software assumes little divergence of the X-ray beam, and on the consideration of kinematic propagation through the sample [230].

Based on what has been mentioned above, individual radiographs were corrected from detector bias and spatial inhomogeneity of the incoming beam intensity by collecting dark and flat field images and applying the following correction to the image intensities: (radiograph – dark field) / (flat field – dark field). Data were next double flat field corrected using a window size of [25,25] (25 was the number of pixels) to remove ring artefacts. After the confirmation of rotation axis, the reconstruction of all data were performed using FBP method. Additional reconstruction using the Paganin method were also performed for each samples.

These 3D volumes were first examined using Fiji software [237]. For the segmentation stage only, the 32-bit float data volumes were converted into unsigned 16 bit integer images in Fiji using a linear transform to reduce memory requirements. Local segmentation and 3D rendering were carried out using Mimics Innovation Suite 19 (Materialise, Leuven, Belgium).

3.2.3 UV/Visible photoluminescence spectroscopy

Photoluminescence is a phenomenon used in many fields such as biology, medicine and materials science [238]. For ancient materials, it has long been restricted as a qualitative tool to observe contrast at the surface of artefacts or artworks revealing restoration or alteration processes. Spectroscopy and more recently, imaging approaches have allowed to retrieve information on materials relative to their composition, stoechiometry and local environment. The principle is described in Appendix A. The UV/Visible photolu-

minescence spectroscopy measurements were performed using synchrotron radiation at DISCO beamline (Dichroism, Imaging and mass Spectrometry for Chemical and biO-logical systems) in SOLEIL Synchrotron.

Experimental setup

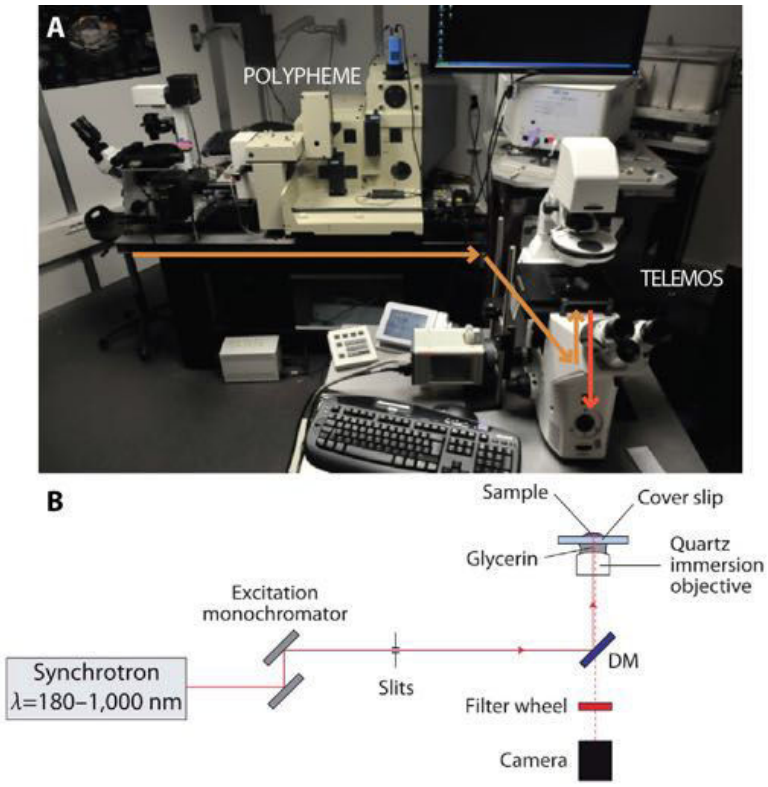

Figure 3.21: Experimental setup at DISCO beamline. A, Two imaging stations: TELEMOS (full-field microscopy) and POLYPHEME (raster-scanning micro-spectroscopy). B, Schematic setup of TELEMOS endstation (modified from Bertrand et al., 2013 [239]).

The imaging station of DISCO beamline consists of two branches, TELEMOS and POLYPH-EME. TELEMOS is a full-field photoluminescence imaging microscope, and POLYPHEME is a microscope allowing raster scanning photoluminescence micro-spectroscopy. In this project, all the experiments were conducted at TELEMOS (Figure 3.21A).

The full-field imaging system is built around an inverted microscope (Axio Observer

Table 3.2: The list of light source, excitation wavelength, dichroic mirror and emission filter used in our studies.

Excitation wavelength λ (nm)	Dichroic mirror	Band-pass interference filter (nm)
240	DM5050	307 - 323
		327 - 353
260		370 - 410
	DM300	412 - 438
280		451 - 486
		499 - 529
330	DM400	535 - 607
		641 - 708
340		850 - 1020

Z1, Zeiss). The incident synchrotron beam is monochromatized and allows to cover a wavelength ranging from 180 nm to 1000 nm (Table 3.2). The excitation optical path is optimized to be transparent in the UV range with quartz optics. Entrance and exit slits were fixed at 0.3 nm and several excitation wavelengths were used. Combined with a 45°dichroic mirror that separates excitation and emission, a quartz immersion artefactive of 100x magnification (numeric aperture = 1.25) was employed with the use of cover-slip. A drop of glycerine is deposited at the surface of the external lens of the objective to ensure the continuity of the optical index between the latter and the cover-slip. The dichroic mirrors of cut-off frequency of 300 nm are positioned in a turret that can hold up to six dichroic cubes. The position of the emission filter inside the dichroic cube is left empty and the spectral selection is performed via a motorized filter wheel holding up to 10 positions offset. Band-pass interference filters (Omega Filter) in the UV–visible range of variable transmission are used in emission according to the detected spectral ranges. The detector is a CCD (charge-coupled device) camera (PIXIS/1024BUV, Princeton Instrument, 1024×1024 pixels, pixel size 13×13 µm^2, 16 bits). Images were collected with the software Micro-Manager with a lateral resolution limited by the size of the pixels of camera. It allows controlling the CCD camera (various acquisition time, shutter speed, reading speed, gain), the filter wheel, the dichroic mirror turret and the motorized XYZ

sample stage. The movement of stage in x and y direction makes it possible to record mosaic of images to extend the field of view up to a few hundred square micrometers (Figure 3.21B).

Sample preparation

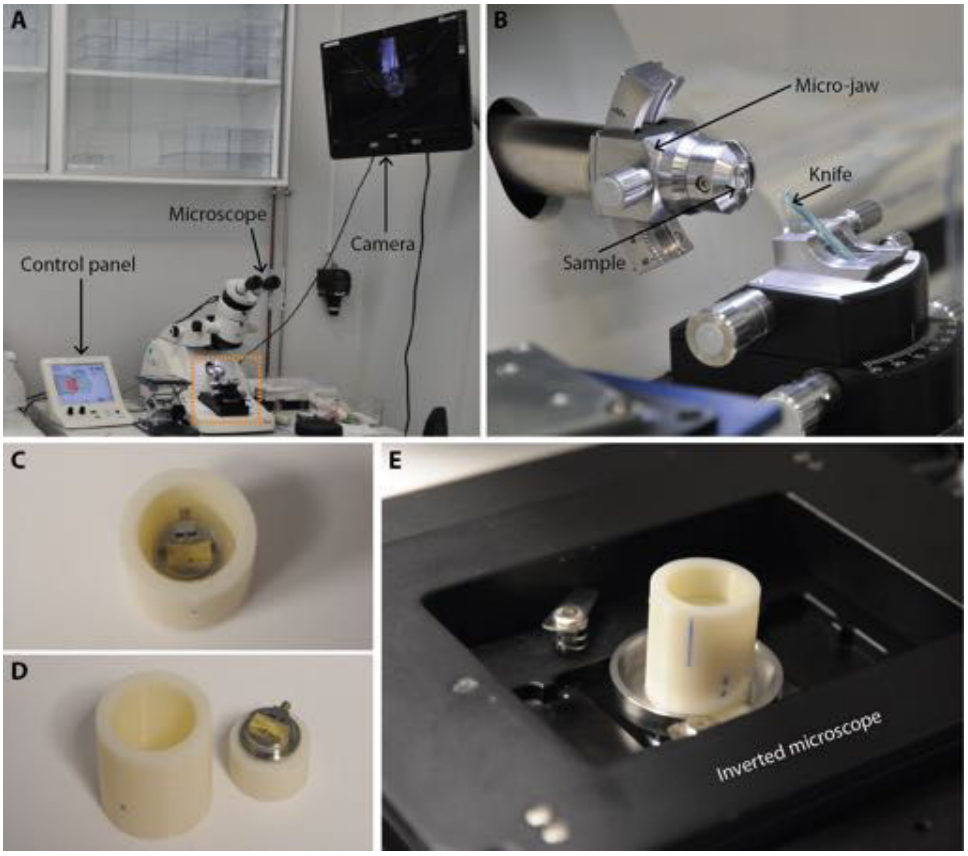

Figure 3.22: Sample preparation and fixing. A and B, Cutting and polishing by ultramicrotome. C and D, Fixing of prepared sample with two plastic cylinders. E, Sample placed on inverted microscope at DISCO beamline.

Two kinds of samples were selected for the UV/Visible imaging, individual mineralized threads and small corroded fragments with attached fibres. The detected areas respectively for the two kinds were phase distribution on cross-sectional view and, interface between fibres and corroded products of copper. In order to obtain a smooth and

flat surface of detected areas for their optimal contact with microscope, samples were embedded in blocks of epoxy resin (Embedding 812 kit), then cut and polished by ultra-microtome (Figure 3.22A and B). The resin block was tightly fixed by a micro jaw that stuck on the surface of one plastic cylinder-formed sample holder by carbon tape. Another bigger hollow plastic cylinder was also used in the periphery to ensure an optimal contact between detected area of samples and the inverted microscope (Figure 3.22C, D and E).

Data processing

The treatment of collected data was mainly conducted with Fiji (ImageJ) software.

In order to correct the images from detection noise, an darkfield image (with sample but no beam) was recorded under the same conditions as the photoluminescence imaging (integration time, stray light sources, detector). The intensity of each pixel of the darkfield image was then subtracted from the that of the photoluminescence of samples.

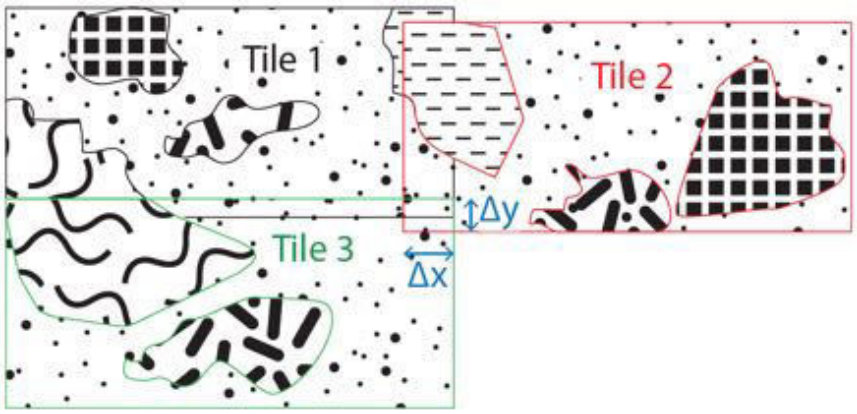

Figure 3.23: Reconstruction of mosaic images by translation (modified from T. Séverin–Fabiani 2016 [240]).

Concerning the images collected from mosaic tiles, a plug-in *Stitching* developed in ImageJ was used for their reconstruction to correct the error of expected repeatability during the movement of sample stage at the same position [241]. This plug-in allows the

reconstruction of the mosaic by simple translation of tiles (Figure 3.23). The translation are parametrized by the dimension of the tile matrix (XY), the incrementation of tiles and the dimension of overlap of the tiles (Δx and Δy). Tile overlap can be set to a maximum of 1% accuracy for the reconstruction using this plug-in. The mosaic formed, after the complete reconstruction, a final image with a wider field of view. The intensity of the pixels in overlapping areas between the tiles is estimated from a linear smoothing of the intensities of two images. Another plug-in *Template Matching* was subsequently used spatially register images corresponding to one tile collected in different spectral range. Images can also be represented as false-colours RGB using corresponding spectral range for comparison.

3.2.4 Fourier transform infrared spectroscopy (FT-IR)

Infrared spectroscopy (IR) is a class of spectroscopy that deals with the infrared region of the electromagnetic spectrum. It covers a wide range of techniques, the most common is the absorption spectroscopy. As with all spectroscopy techniques, it can be used for the identification of compounds or to determine the composition of a sample. The principle is described in Appendix A. The FT-IR measurements were performed in IPANEMA laboratory using either transmission or reflection mode.

Experimental setup

Equipped with MCT (mercury cadmium telluride) and FPA (focal-plane array) detectors, a spectrophotometer (Bruker Vertex 70) coupled with a microscope (Bruker Hyperion 3000 IR) was used to conduct all the FT-IR experiments at IPANEMA laboratory (Figure 3.24). Spectral images for thin fibre sections placed on transparent ZnS support were obtained in transmission mode using a 15× (NA = 0.4) condenser and a 15× (NA = 0.4) artefactive, 4 cm^{-1} of spectral resolution, co-adding 512 scans at scanner velocity of 80 kHz (35 s), in the 4000 to 900 cm-1 mid-Infrared range. Embedded samples are

measured in reflection mode with a 20x artefactive in similar conditions. The measuring area was generally set to 20×20 µm^2 when using MCT detector. The measurement of background was achieved before each experiment.

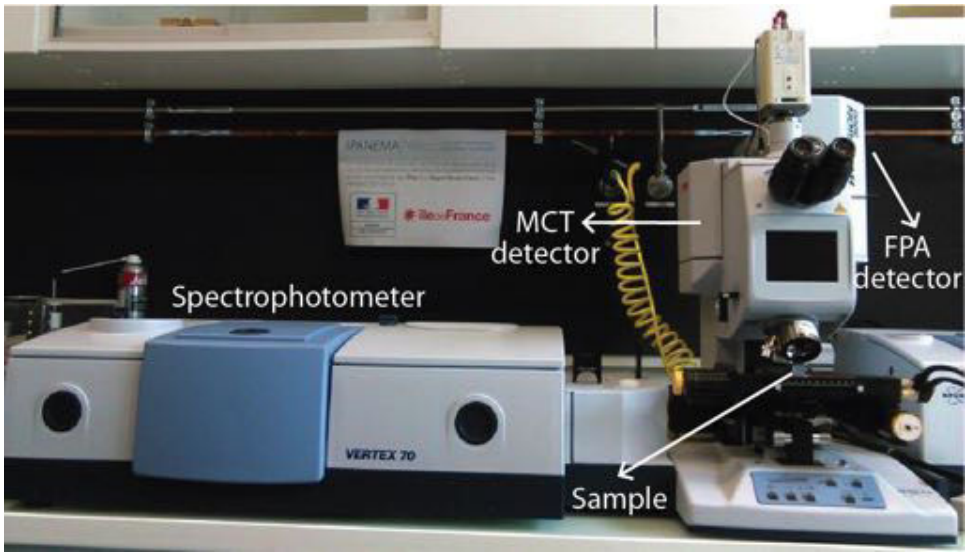

Figure 3.24: Spectrophotometer (Bruker Vertex 70) coupled with an IR microscope (Bruker Hyperion 3000) and equipped with two detectors.

Sample Preparation

Individual fibre or thread were cut by ultra-microtome for 2 µm-thickness for transmission analysis, through a specifically developed procedure to exclude the need of embedding (Figure 3.25). Using extra-fine tip tweezers, the fibre can be carefully lifted and deposited on a bent glass slide. Then two plastic slides were cut using a razor blade with rectangular dimensions of about 2×4 mm^2, they were cleaned with acetone and dried in advance. Put the fibre in "sandwiched"form between them. A drop of transparent nail polish and a micro-jaw were used to fix the assemblage avoiding any contact of chemical product with the sample. The assemblage was next mounted in a micro-mount of ultra-microtome described before. As a preliminary operation, a razor blade was chosen to remove most of the plastic material around the fibre and by forming a frustum of a

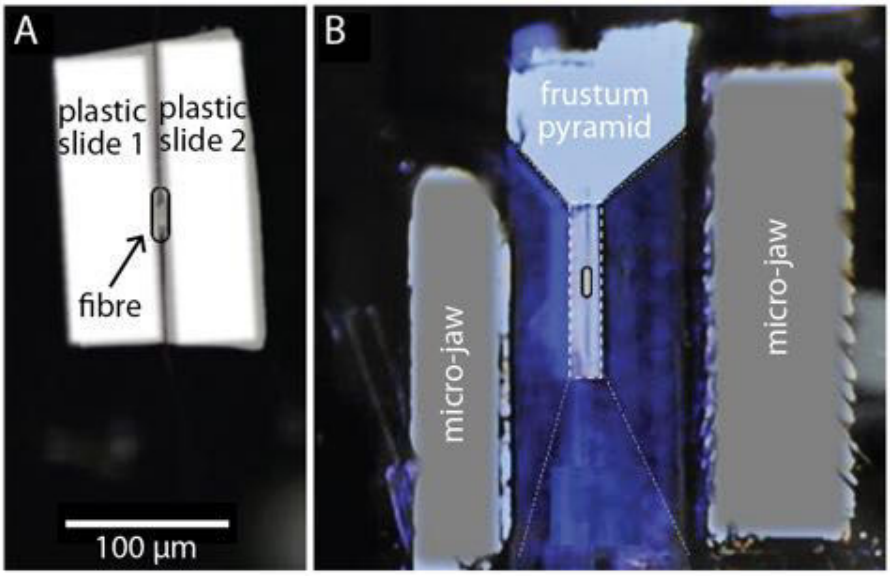

Figure 3.25: Preparation of individual fibre without embedding. A, Rectangular plastic slides (2×4 mm^2) that keep a fibre as a sandwich: "slide-sample-slide" form. B, The frustum of a pyramid obtained by cutting at the ultra-microtome for sections of the sandwich (kept together with a micro-jaw).

pyramid with the cross section of the fibre slightly under the smaller base. Then, using a glass knife cleaned with ethanol, the upper surface of the frustum was leveled by cutting sections 2 µm-thickness until the fibre emerged. Finally, ultra-sectioning was performed in dried conditions using a Cryo 35°diamond knife. The thin cross sections were collected from the knife with an eyelash and directly deposited onto specific supports for IR analysis. Several embedded prepared samples were measured in reflection mode.

Data processing

The spectra were obtained and firstly visualised using OPUS software, the original data can be extracted and re-plot using R computing tool. The identification of organic groups were carried out after comparison with related literature database and with reference spectra published on website IRUG (Infrared and Raman Users Group).

3.2.5 Scanning electron microscopy (SEM)

SEM allows to acquire images at a resolution of few nanometers in specific detection configuration. Chemical information of samples can also be extracted. It was used to observe the distribution of chemical phases on the prepared samples (imaging) and to have a semi-quantitative analysis of the elements present. The principle is described in Appendix A. The SEM-EDS/EBSD measurements were performed in IPANEMA laboratory and Centre de MicroCaractérisation Raimond Castaing (Toulouse).

Experimental setup

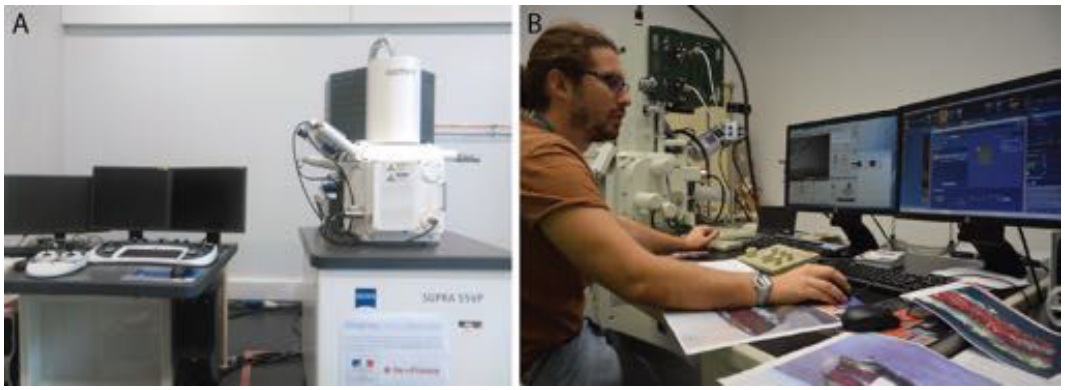

Figure 3.26: Photos of SEM. A, SEM of IPANEMA. B, SEM of Centre de MicroCaractérisation Raimond Castaing.

During the SEM analysis (ZEISS Supra 55 VP) performed at IPANEMA (Figure 3.26A), SE and BSE images were obtained with a voltage of 20 kV and a working distance of 8 mm. Elemental X-rays microanalysis were conducted with an EDS probe (Brucker xFlash 5030). The analytical chamber was maintained in vacuum. At Toulouse, the SEM examination was performed using the environmental FEG SEM (JSM 7100F TTLS LV – EDS/EBSD, JEOL) for EDS analysis and for the acquisition of microstructural information about the crystallographic nature of samples using EBSD technique (Figure 3.26B).

Sample preparation

Samples analysed with SEM (vase fragment AO 14506-1b and NS 95015002-2) are mainly those embedded in epoxy resin (Resineco Green Composites, Barcelona, Spain) (Figure 3.27A), and surfaces were polished using an automatic polisher (Struers S.A.S, Champigny sur Marne, France) with SiC sheets of decreasing particle size at IPANEMA (Figure 3.27C) after cutting by 220 µm-thickness diamond wire saw (Escil, Chassieu, France) (Figure 3.27B). As our samples are mostly composed by corroded copper compounds, the supplementary treatment like metallization on sample surfaces can be avoided. However, a secondary vibrational polishing (BUEHLER VibroMet2, London, UK) at centre de MicroCaractérisation Raimond Castaing (UMS 3623, Toulouse) using 0.05 µm aluminia on sample was carried out for our EBSD analysis because of the high requirement of a very smooth surface (Figure 3.27D).

Data processing

Data processing was achieved by using the Quantax 400 software (Bruker) at IPANEMA and spectra were plotted in the R software (Figure 3.28A). The EBSD data were processed using the Aztec HKL software by A. Proietti (Toulouse) (Figure 3.28B and C).

3.2.6 Raman spectroscopy

Optical spectroscopy techniques make it possible to obtain chemical, electronic and structural information rapidly on solid, liquid or gaseous samples. Among these methods, Raman spectroscopy is particularly developed by its non-destructive aspect and its applicability in many scientific fields such as materials science, biology, art and heritage as well as pharmacology [242]. The principle is described in Appendix A. The Raman measurements were performed in HORIBA France.

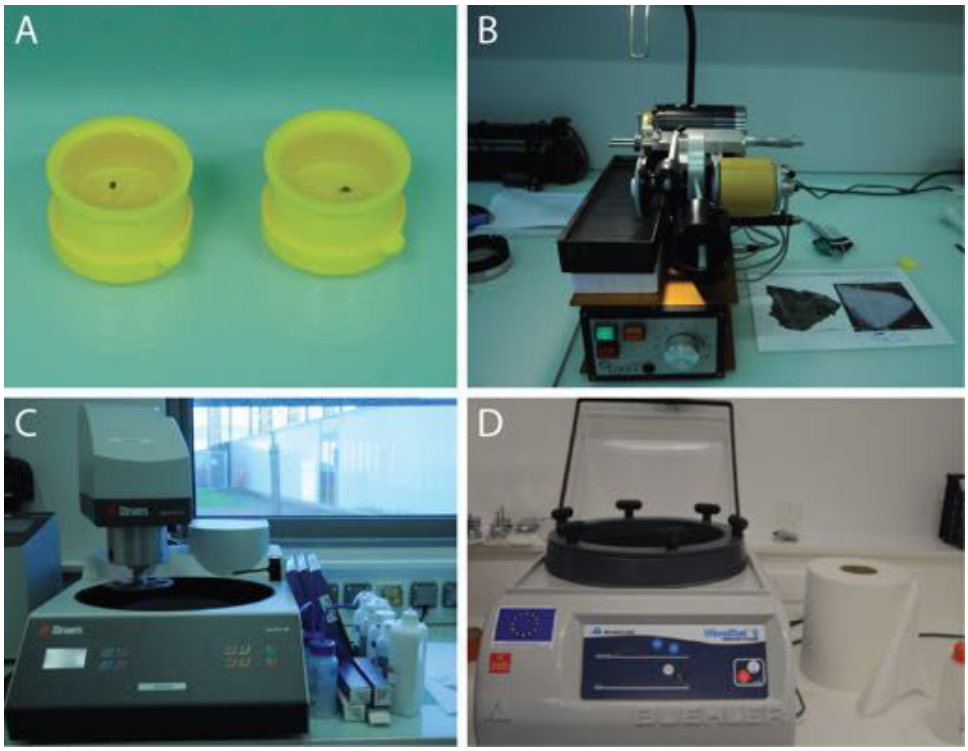

Figure 3.27: Steps of sample preparation for SEM analysis. A, Embedding in epoxy resin. B, Cutting by 220 µm-thickness diamond wire saw. C, Automatic polishing. D, Secondary vibrational polishing at Toulouse.

Figure 3.28: Photos of data processing. A, Treatment of EDS data using the Quantax 400 software. B and C, Treatment of EBSD data using the Aztec HKL software.

Experimental setup

A commercial Raman microspectrometer (LabRam, Jobin-Yvon, Horiba, France) equipped with a 633 nm laser source giving power of 1 mW, a Syncerity CCD detector and a 50×/0.5 numerical aperture objective was used (Figure 3.29). The spectra were obtained with three accumulations of 10 s per point from 2300 to 150 cm^{-1}. A pinhole of 300 µm and 300 lines/ mm grating were used to operate the microspectrometer in non-confocal mode. Measurements were performed on cross sections of samples NS 95015002-2 and vase fragment AO 14506-1b (embedded in epoxy resin).

Data processing

The data were treated using the LabSpec6 (with the help of Thibault Brulé, Horiba France, Palaiseau) and R computing softwares.

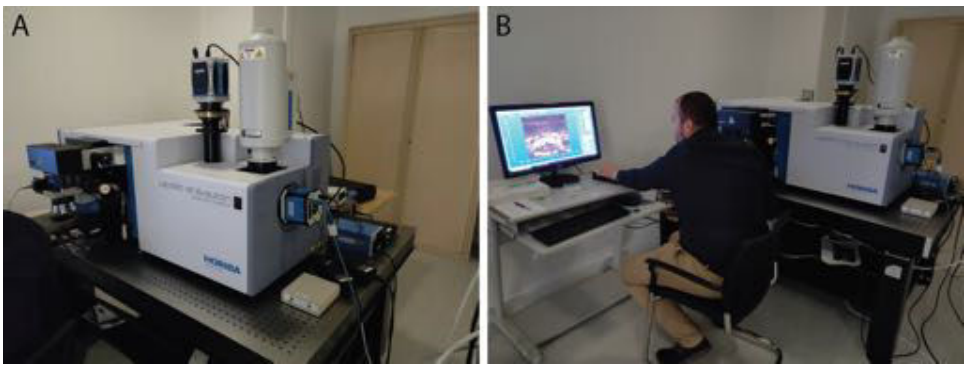

Figure 3.29: Raman measurements performed at Horiba (Palaiseau, France).

3.3 Conclusion

The information of analysed artefacts and the corresponding excavation sites have been described in this chapter. The sample preparation and a variety of selected methods mainly based on synchrotron radiation have been listed. In the following chapter, a study on copper corrosion products that formed almost simultaneously with the mineralization of fibres will be detailed, using mainly µCT.

4

Synchrotron-based phase mapping in corroded metals: insights from early copper-base artefacts

This chapter proposes the use of high-resolution synchrotron X-ray µCT for a fine non-invasive 3D description of the distribution of both internal and external mineral phases in copper-base objects. This approach provides essential clues on long-term corrosion processes. Major and minor phases are identified through semi-quantitative evaluation of attenuation coefficients using polychromatic X-ray illumination. Evidence is found for initially unidentified phases through statistical processing of images. Interpretation of the distribution of these phases is discussed. A good correlation between the corrosion phases identified by µCT and by invasive BSE-SEM is demonstrated. Additionally to the stratigraphy of the copper corrosion compounds, the variations observed in the attenuation coefficients of Cu(I) phases are examined and discussed. Evidence for the non-invasive observation of phases rapidly altered upon preparation of real cross-sections is provided. The method can be applied when cross-sectioning even of minute fragments is impossible.

Contents

4.1 Introduction

Metallic objects including ornaments, dishes, tools and weapons are considered central in archaeology as they bear witness to the state of technological development of a culture, and inform on social and political habits of past human societies. Copper is one of the first metals to be discovered as early as the 9th mill. BC most probably under its native form [149, 150]. Later metallurgical developments allowed the production of copper using smelting from copper minerals, and spread from Anatolia and the Levant across wide parts of Eurasia (ca. 5th mill. BC) [150, 243, 244]. In parallel, contemporary innovations in casting processes such as the lost-wax technique [45] lead to the production of a wider range of artefacts, followed later by the production of As–Cu and Cu–Sn alloys (ca. 4th mill. BC) in this region [171, 172]. Recently, Oudbashi et al. reviewed works, evolution of techniques and archaeological context regarding copper archaeometallurgy in this area of the Middle East [172].

However, ancient metallic artefacts are often marked by corrosion in archaeological contexts, and may have been extensively altered. In burial environments, this phenomenon is directly related to the soil conditions (particularly the presence of water, its pH, and the availability of aqueous electrolytes such as chlorides and sulfates [151, 245]) as well as to the structure and initial surface state of the metal. For Cu-based materials, corrosion most often gives rise to a structure in which layers of Cu(I) and Cu(II) species form, such as red Cu_2O (cuprous oxide) and green $Cu_2Cl(OH)_3$ phases (clinoatacamite or atacamite) [151, 173]. According to the timescale and the conditions of the burial environment, a wide range of structural modifications can be observed, from large periodic corrosion structures to less severe attacks in more compact layers, leading to highly heterogeneous and complex morphologies, that extend from deeply stratified [246, 174, 175, 176] to fully intermixed [45]. Nonetheless, the corroded structure carries information about the history of the metallic object, which can be recovered

through the identification of corrosion products [247, 177] and the characterization of the corroded structures [45, 164, 178, 165, 168].

Standard identification of internal corrosion products and metals relies on the preparation of a section through the object under investigation [174, 175, 176, 178, 165, 168], which can then be studied using a range of techniques. The most commonly used characterization analyses are scanning electron microscopy (SEM) coupled to energy-dispersive X-ray spectroscopy (EDS) that allows the elemental composition of the corrosion products to be assessed, X-ray diffraction and more recently Raman spectroscopy, that provide information about their crystal structure, composition and properties [45, 171, 172, 151, 173, 174, 175, 176, 177, 164, 178, 165, 168, 179]. However, these approaches suffer from significant limitations: sample embedding as well as cutting and polishing often affects the object, e.g., by pulling off grains and creating artefactual microcavities, by compressing the object, or by "buttering" (displacing) the embedding resin or mineral grains over the surface. Furthermore, some archaeological samples are so rare or precious that museum curators cannot authorize the use of invasive methods, and must seek strictly non-invasive approaches for the investigation of valuable heritage.

The potential of X-ray micro-computed tomography (µCT) for the study of corroded metals was evaluated. µCT provides non-destructive imaging of the internal structures of an object at sub-micrometric spatial resolution (see Subsection 3.2.2), and is as yet rarely used by archaeologists. µCT generates virtual cross-sections through the whole object (i.e., a 3D volume) based on local contrasts due to the absorption and refraction of X-rays. Although usually not considered in quantitative terms, the grey level contrast of X-ray µCT is based on the electron density of the materials. Data processing of the grey level histograms obtained with a polychromatic synchrotron source is a remarkably efficient means to map and identify different corrosion products. Statistical processing of images reveals the presence of phases not initially evident in the segmentation of two samples.

4.2 Experimental section

The measurements consist in scanning a reference sample and archaeological samples with same experimental setup. From these acquisitions it is possible to obtain µCT slices showing controlled correspondence between attenuation and grey level intensity.

4.2.1 Archaeological samples

Two archaeological samples were studied: vase fragment AO 14506-1b (Figure 4.2A) and NS 95015002-2 (Figure 4.1A), for details refer to Subsections 3.1.3 and 3.1.2).

4.2.2 Production of a standard for calibration of attenuation coefficients

A standard sample was produced to experimentally calibrate attenuation coefficients from the µCT experiment (Figure 4.4A). Ten disks were cut in high-purity metal foils (Ge, Al, Ti, Cr, Mn, Fe, Co, Zn, Cu, Sn; thicknesses from 50 to 250 µm, diam. 2 mm; Table 4.1) using a manually operated punch (Mob Mondelin, Le Chambon-Feugerolles, France). The disks were assembled in a stack using X-ray resistant double-sided Kapton

Table 4.1: Reference data for the metal disks used as calibration standard in the experiment.

Standard	Supplier	Product number	Thickness (µm)	Reference density ($g \cdot cm^{-3}$)
Al	Sigma–Aldrich	326860	130	2.70
Ti	Sigma–Aldrich	348791	127	4.50
Cr	Goodfellow	CR000190/11	50	7.14
Mn	Goodfellow	MN000200/6	50	7.43
Fe	Sigma–Aldrich	356808	100	7.86
Ge	Goodfellow	GE003030/3	250	5.32
Co	Sigma–Aldrich	356867	100	8.90
Zn	Sigma–Aldrich	356018	250	7.13
Cu	Sigma–Aldrich	GF00712437	100	8.94
Sn	Sigma–Aldrich	356948	127	7.31

tape (DuPont^{TM}). The resulting cylinder was fixed to the polished surface of a screw (RS Components, M6×25 mm) made of polyamide (Nylon 66) for easier handling and fixing to the µCT stage. The diameter of the disks was chosen to correspond to the field of view of the tomography measurements. For good reconstruction quality, only those foils allowing an X-ray transmission greater than 20% at 87 keV (33% for copper), based on calculated linear attenuation coefficients [248], were used for the calibration. The Sn foil, in particular, was designed for use at higher energy and was not used in the present calibration. As the Cr and Mn foils showed some degree of cracking and porosity formation, we decided to exclude the corresponding data from the calibration of attenuation coefficients although the induced variation appears negligible. The standard was stored in a dessicator between analyses to prevent oxidation.

4.2.3 Synchrotron X-ray micro-computed tomography and complementary characterization techniques

Experimental setup of µCT and complementary techniques used refer to Section 3.2 in Chapter 3.

4.2.4 Data processing

The pre-processing steps of acquired µCT data refers to Subsection 3.2.2 in Chapter 3.

Densities of pure metals and minerals were obtained from reference data of the National Institute of Standards and Technology (NIST) [249] and of the Mineralogy Database [250], respectively. Theoretical linear attenuation coefficients were calculated using reference data from NIST [251]. While these coefficients are given for monochromatic radiation, our data were collected using a polychromatic incident beam as indicated previously. Monochromatic attenuation coefficients were therefore weighted according to the photon flux and detector efficiency variations throughout the energy range to produce polychromatic attenuation coefficients (μ_{Th}) relevant to our experimental

conditions (Tables 4.4, 4.5, 4.3, and 4.2).

The tomographic reconstruction of the standard sample was used to calibrate the reconstructed gray levels (measured attenuation coefficients). Domains of 2,000 voxels were selected in each pure metal disk in order to evaluate experimental attenuation coefficients μ_{Exp}. Areas affected by ring artefacts and intensity variations attributed to beam hardening were carefully avoided.

In the analysis of the archaeological samples, histograms were produced from the distribution of the measured gray level intensities (I_{GV}) by carefully selecting 2,525 voxels per corrosion product using the Fiji software. Subsequently, histograms based on complete sections were decomposed as sums of Gaussian distributions according to the procedure presented in Results and Discussions. The fits in Figures 4.7 and 4.8 were performed using scripts based on the non-linear regression package NLS [252] in the 'R' computing environment [253]. For the archaeological samples, the resulting values of attenuation coefficients (from the center of the Gaussian distribution), standard deviation, intensity and integrated area were designated as μ_{Fit}, σ_{Fit}, I_{Fit} and $\mathcal{A}_{\mathrm{Fit}} = I_{\mathrm{Fit}} \cdot \sigma_{\mathrm{Fit}} \cdot \sqrt{2\pi}$, respectively.

4.3 Results and discussion

3D datacubes of both archaeological fragments were reconstructed from the synchrotron µCT radiographs. Tomographic slices extracted from the datacubes show the full stratigraphy of the corroded samples from the central to outer corrosion layers. µCT allows a non-invasive selection of slices showing the spatial distribution of the different corrosion phases within the full 3D volume. At the spatial resolution attained and without further processing of the data, the organisation of the different phases is reconstructed with sufficient contrast to provide the main qualitative features in order to understand the long-term corrosion processes that took place in each case.

4.3.1 Description of the 3D morphology

As expected for archaeological corroded copper-base samples, their stratigraphy appears complex and composed of multiple phases. The sample from Nausharo (NS 95015002-2) shows a stratified multilayer system with complex 3D internal morphology. Figure 4.1B shows a reconstructed section through the sample, oriented as Figure 4.1A. In this gray scale tomographic slice, white corresponds to high reconstructed attenuation coefficients (i.e. more dense) and black corresponds to low attenuation coefficients (less dense). Figure 4.1C shows a tomographic section perpendicular to Figure 4.1B, and perpendicular to the corrosion layers. The inside of the sample appears denser than its outer crust. This inner part consists of a highly absorbing flat plate, ca. 350 µm-thick (arrow 1 in Figure 4.1D), which includes two 'zones' (areas with homogeneous gray level intensity) of different lower relative attenuation. From the most absorbing to the least, we can distinguish a zone made up of elongated strips and very irregular patches (arrows 2 and 3), and a typical 80 µm-thick discontinuous layer (up to 200 µm thick depending on the selected section) near to the centre line of the plate (arrow 4). In addition, pores appear as very low attenuation (black) domains that are elongated in the plane of the plate. These pores are irregular in shape and dimensions, with thicknesses ranging from 5 to 40 µm and are primarily located in the center of the sample (e.g., arrow 5). The formation of pores in the internal corrosion structure is frequently observed in extensively corroded copper artefacts, linked to the dissolution of copper ions [166]. It is also found in tin-bronze thin films at nanometric scale that have undergone a decuprification process [254, 255].

The spatial resolution is sufficient to allow the non-invasive observation of two discontinuous 'straight' lines up to ca. 14 µm thick in the cross-sectional planes of each plate (arrow 2). These planes (in 3D) can clearly be attributed to the 'in-place original surfaces' of each artefact, that delineate the boundary between the original artefact and

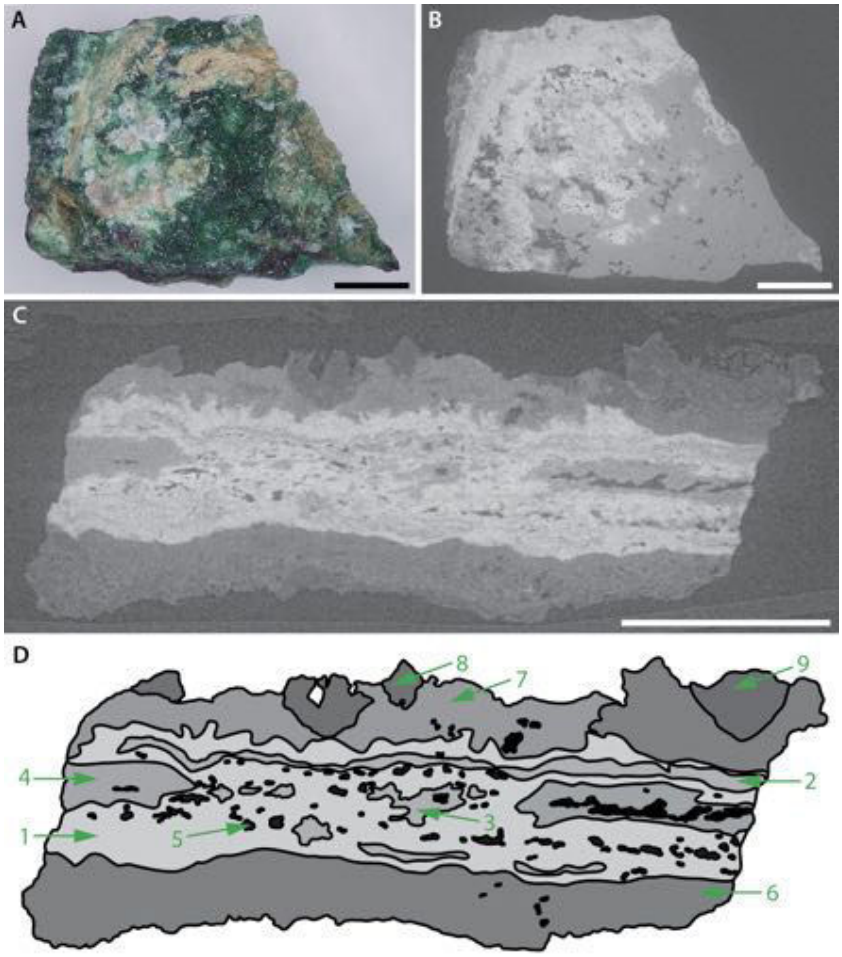

Figure 4.1: Sample NS 95015002-2. A, Digital microscopy reconstruction of the sample surface. B, Tomographic slice of the sample in an inner plane parallel to the sample surface in A. C, Tomographic slice showing the distribution of corrosion products in an inner plane perpendicular to the sample surface shown in A. D, Schematic illustration of the different zones observed in the tomographic slice in C. Scale bars in A, B and C: 500 µm.

the corrosion layers, as are frequently observed in ancient artefacts [256]. The material of greater attenuation that forms the core of the sample extends by typically 60 µm beyond the original surfaces. This zone is associated with a Cu(I) phase, typically cuprous oxide Cu_2O, playing the role of a chloride selective membrane during subsequent corrosion [257, 176, 45]. Beyond this membrane, the corrosion crust appears to be composed from at least two low-attenuation compounds. These likely correspond to less absorbing Cu(II) corrosion products that are formed outside of the sample surface (arrows 6 and 7), as well as possible sedimentary compounds (e.g., arrow 8). Cu(II) compounds are significantly less absorbent to X-rays than both Cu(I) compounds and metallic copper Cu^0 (Table 4.2). Remnants of organic textile fibres enclosed in the corrosion are visible

Table 4.2: Attenuation of common copper compounds formed in archaeological corrosion. Polychromatic μ_{Th} values were calculated according to the process indicated in the Experimental section.

Ox. d°	**Name**	**Primary formula**	**Density** ($g{\cdot}cm^{-3}$)	μ_{Th} (cm^{-1})
0	Copper	Cu	8.94	6.03
1	Cuprite	Cu_2O	6.10	3.78
	Chalcocite	Cu_2S	5.65	3.34
	Nantokite	CuCl	3.93	2.10
2	Paramelachonite	Cu_4O_3	6.11	3.64
	Digenite	Cu_9S_5	5.60	3.27
	Covellite	CuS	4.68	2.52
	Brochantite	$Cu_4(OH)_6SO_4$	3.97	1.86
	Atacamite	$Cu_2(OH)_3Cl$	3.76	1.86
	Antlerite	$Cu_3(SO_4)(OH)_4$	3.90	1.79
	Malachite	$Cu_2(OH)_2CO_3$	3.80	1.79
	Botallackite	$Cu_2(OH)_3Cl$	3.60	1.79
	Azurite	$Cu_3(OH)_2(CO_3)_2$	3.83	1.75
	Tolbachite	$CuCl_2$	3.42	1.58
	Chalcocyanite	$CuSO_4$	3.65	1.44
	Dioptase	$CuSiO_2(OH)_2$	3.31	1.29
	Chrysocolla	$Cu_{1.75}Al_{0.25}H_{1.75}(Si_2O_5)(OH)_4 \cdot 0.25\,(H_2O)$	2.15	0.77
	Chalcanthite	$CuSO_4 \cdot 5\,H_2O$	2.21	0.70

at a low attenuation intensity (arrow 9). Their description is discussed in Chapter 5.

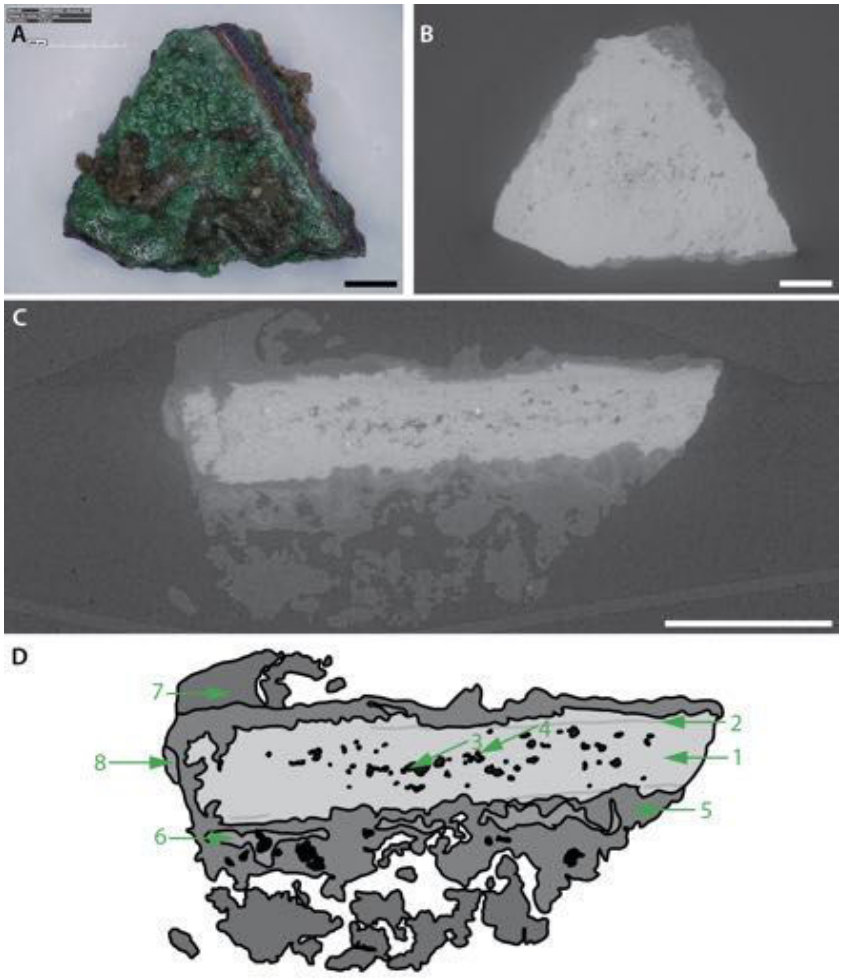

Figure 4.2: Sample AO 14506-1b. A, Digital microscopy reconstruction of the sample surface. B, Tomographic slice of the sample in an inner plane parallel to the sample surface in A. C, Tomographic slice showing the distribution of corrosion products in an inner plane perpendicular to the sample surface shown in A. D, Schematic illustration of the different zones observed in the tomographic slice in C. Scale bars in A, B and C: 500 µm.

As for sample AO 14506-1b, the internal part is mainly composed of highly absorbing zone and holes of varying sizes (arrows 1 and 3 in Figure 4.2D). The two straight lines (arrow 2) that define the inner unit plate are thin and clear, particularly at the right side. The discontinuous layer observed in NS 95015002-2 is not presented in sample AO 14506-1b, but several high-absorbing rounded particles in white, near the holes, are clearly identifiable with a diameter about 10 µm (arrow 4). Two low-absorbing layers (arrows 5 and 6) showing a crossed structure particularly at right side are identified at outer part. The possible sedimentary compounds are located at the sample surfaces (arrow 7). In addition, protuberant material (arrow 8) of similar absorbance as the outside low-absorbing (arrow 6) is present at the left side of the object, measuring about 70×300 µm^2.

The images obtained by non-invasive µCT allow the identification of corrosion products without sectioning the sample with a comparable discrimination as with medium resolution SEM in BSE mode. In the present configuration, the contrast mechanism of µCT is dominated by X-ray attenuation, characterized by the linear attenuation coefficient $\mu(E)$. In the recorded radiographs, the observed photon flux density at the energy E, $I(E)$, decreases exponentially with the thickness of material traversed x, according to the Lambert-Beer law [258]: $I(E) = I_0(E) \times \exp(-\mu(E)\,x)$. The gray value intensities I_{GV} reconstructed in the tomograms are proportional to $\mu(E)$. $\mu(E)$ has a strong dependency on the atomic number Z, close to the Bragg-Pierce law ($\propto Z^4$, except for when close to characteristic absorption edge energies). The origin of the contrast is similar in BSE-SEM, in which the dependence of the backscattered yield I^{BSE} for a flat surface as a function of Z can be expressed as $I^{\mathrm{BSE}}(Z) = -0.0254 + 0.016Z - 1.86\times10^{-4}Z^2 + 8.31\times10^{-7}Z^3$ [259, 260]. It is particularly interesting that the resolution and contrast are sufficient to decipher the main characteristics of the sample morphology even in our potentially less quantitative "pink" beam configuration.

Beyond morphological information, further detail on the chemical composition can be inferred to complement identification of the phases in the stratigraphy of the samples.

4.3.2 Towards semi-quantitative identification of phases

Phase identification was performed step by step according to the differences in gray value intensities I_{GV} in the reconstructed images. Steps are indicated as "Sm": (S1) identification of major phases, (S2) determination of additional main phases from zones identifiable by inspection of the reconstructed volume, (S3 and S4) identification of residual trace phases (Table 4.4).

Step 1: Major phases

A procedure was implemented to attempt to identify the main mineral phases observed in the sample stratigraphy by making a quantitative interpretation of the reconstructed I_{GV}. It relies on first calibrating the I_{GV} using standard materials, and then analyzing the distribution of the I_{GV} values in the reconstructed volumes (Figure 4.4). A multi-material standard was built from ten metal disks (see Experimental Section, Figure 4.4A and B). The diameter of the standard was chosen to be compatible with the field of view of the tomography detector, and similar to the size of the archaeological samples. In a tomographic slice of each (pure) disk (Figure 4.4B and C), the reconstructed intensity is observed to decrease from the edge to the center by ±8% at maximum in the case of the highly absorbing Cu, while this variation is limited to below ±5% for materials that absorb as much as our most absorbing phases. For example, cuprite Cu_2O has an attenuation coefficient close to metallic iron whose signal varies by ±4% (Table 4.3). This "cupping effect" in the reconstructed image results from the differential attenuation of X-ray energies in the polychromatic beam ("beam hardening" [205]). For our calibration, we selected voxels in an area intermediate between the center of rotation and the border of the standard sample where fluctuations are in the percent range or below. We observe

that the distribution of I_{GV} for each of the metal foils can be fitted satisfactorily by a Gaussian distribution as demonstrated using the Shapiro Normality test ($0.068 < p < 0.75$ considering each of the ten reference material independently, see also Figure 4.3). Collected I_{GV} values are linearly correlated to the expected attenuation μ_{Th} ($R^2 \simeq 0.95(1)$, $F(1, 19998) = 3.86 \times 10^5, p < 10^{-15}$, see Figure 4.4D). The standard deviation σ_{Exp} slightly increases with μ_{Exp} (Table 4.3). Our results therefore show promise that, even in far faster 'pink' beam X-ray microtomography, semi-quantitative attenuation data can be retrieved to support phase attribution.

Table 4.3: Determination of attenuation coefficients using the purpose-made standard. μ_{Th}: theoretical attenuation coefficient for each standard material under polychromatic excitation (please refer to the Experimental section). $I_{GV,\,Exp}$: experimental gray value intensity. $I_{GV,\,Fit}$: gray value intensity determined from the Gaussian fit. σ_{Exp}: standard deviation of the experimental distribution. σ_{Fit}: standard deviation determined from the Gaussian fit. N/A: not applicable.

Standard	μ_{Th} cm^{-1}	$I_{GV,\,Exp}$	$I_{GV,\,Fit}$	σ_{Exp} cm^{-1}	σ_{Fit} cm^{-1}
Air	0.00	0.03	0.02	0.37	0.37
Nylon	0.22	0.18	0.17	0.42	0.43
Al	0.54	0.43	0.42	0.37	0.38
Ti	1.69	0.91	0.90	0.42	0.41
Cr	3.19	1.27	1.27	0.44	0.45
Mn	3.57	1.69	1.69	0.53	0.54
Fe	4.21	2.02	2.00	0.49	0.48
Ge	4.50	2.08	2.06	0.46	0.46
Co	5.09	2.40	2.40	0.51	0.51
Zn	5.29	2.62	2.61	0.54	0.55
Cu	6.03	2.77	2.77	0.56	0.56
Sn	17.32	N/A	N/A	N/A	N/A

This calibration was applied to the I_{GV} values measured in the two archaeological samples in order to determine μ_{Exp}. As a starting point, an experimental linear attenuation coefficient was calculated for the major, most dense phase, identified as a "Cu(I)" phase from its location in the sample and morphology. The mean I_{GV} value was calculated from a region of 2,525 voxels in each sample (Figures 4.5 and 4.6). In

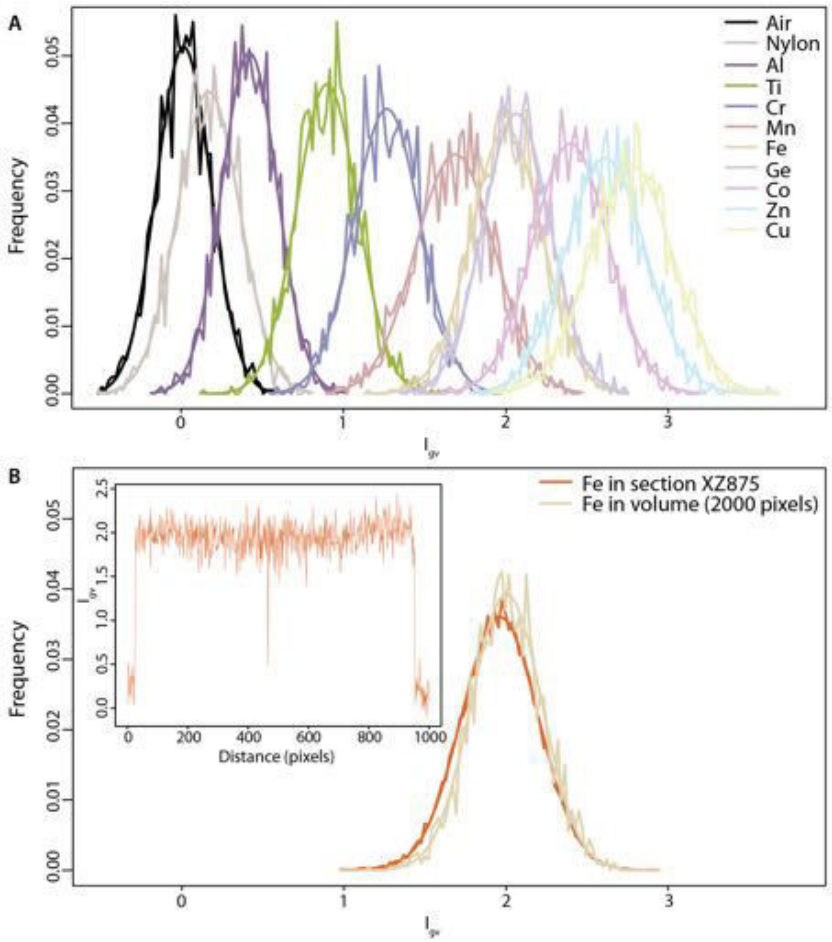

Figure 4.3: Measurement of I_{GV} values for the calibration standard. A, Distributions of I_{GV} values established by selecting voxels in a square of 10×10 voxels^2 through 20 successive slices in the reconstructed data volume (i.e., 2,000 voxels) for each metal disk, the nylon support and air. A Gaussian function is used for the fit. B, Distribution of the I_{GV} of the Fe disk respectively in one full slice across the rotation axis in the reconstructed volume (34,612 voxels) and in the volume used in A (2,000 voxels). The I_{GV} fluctuation of a line through the middle of Fe disk in section XZ875 is showing at top left in B.

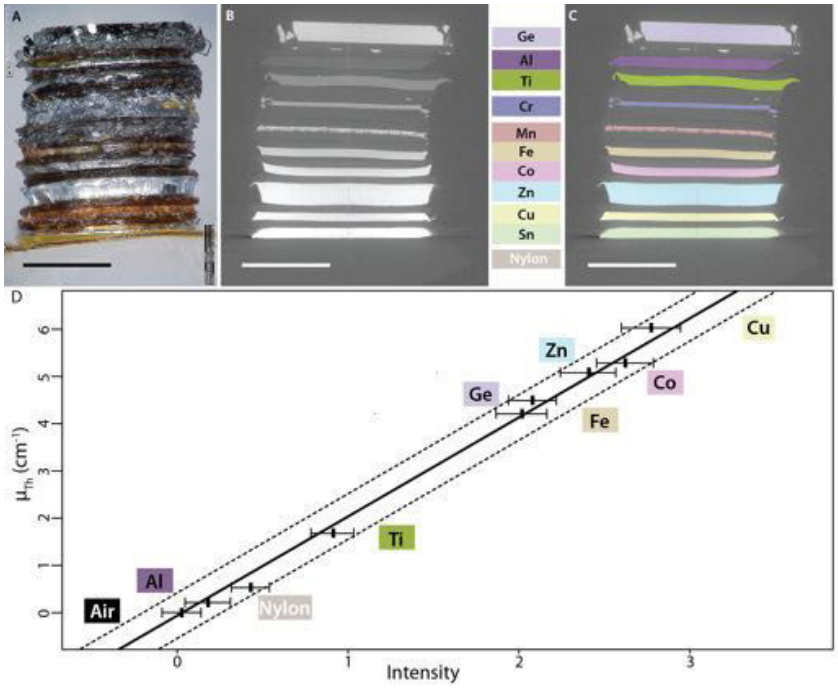

Figure 4.4: Calibration of attenuation coefficients. A, Digital microscopy reconstruction of the standard. B, Tomographic slice in the purpose-made standard consisting of ten metal disks. C, Slice represented in A after manual segmentation of the data. D, Calibration curve of attenuation coefficients based on the measurements of 2,000 voxels per disk (including nylon and air). A correlation is found between the experimental intensity and the corresponding theoretical attenuation μ_{Th}. The whiskers correspond to +/- 1σ. Scale bars in A and B: 1 mm.

sample NS 95015002, the mean attenuation of this "Cu(I)" phase is 3.76±0.34 cm^{-1}. This value is very close to that expected for a pure cuprous oxide phase (Cu_2O): 3.78 cm^{-1}, and in a range where no other common Cu-based phase is present (Supporting Information Table 4.2). Being identified in this first step, Cu_2O is designated as 'S1.1' in Table 4.4. In sample AO 14506-1b, the major "Cu(I)" phase possesses a mean attenuation of 4.12±0.32 cm^{-1}which is slightly greater than the theoretical value of pure Cu_2O (Table 4.5). This is discussed further later.

Table 4.4: Attribution of zones of homogeneous attenuation coefficient in sample NS 95015002-2. μ_{Exp}: mean attenuation coefficient of 2,525 selected voxels per selected zone. μ_{Fit}, σ_{Fit}, I_{Fit}: attenuation coefficient, standard deviation and intensity established from a Gaussian fit of the distribution of calibrated attenuation coefficients in the entire selected slice. μ_{Th}: theoretical attenuation length for each pure compound. $\mathcal{A}_{Fit}$: relative fitted area under the distribution curve of each phase. $\mathcal{A}^{\mathcal{S}}_{Fit}$: in-sample relative fitted area under the distribution curve of each phase. N/A: not applicable. *: values discussed in the main text. Validation using (S)EM-EDX, (E)BSD, (R)aman, (F)T-IR, (ED)-XRD (refer to main text for precision).

Step	μ_{Exp} **cm^{-1}**	μ_{Fit} **cm^{-1}**	σ_{Fit} **cm^{-1}**	I_{Fit}	**Proposed attribution**	μ_{Th} **cm^{-1}**	$\mathcal{A}_{Fit}$ %	$\mathcal{A}^{\mathcal{S}}_{Fit}$ %	**Validation**
N/A	0.00	-0.03	0.31	0.0169	Air	0.00	27.8	0.0	
N/A	0.02	-0.01	0.31	0.0041	Nylon	0.22	6.8	0.0	
N/A	0.30	0.29	0.31	0.0029	Kapton	0.24	4.8	0.0	
S1.1	3.76	3.74	0.40*	0.0094	Cu_2O	3.78	19.6	32.4	S,E,R,F,ED
S2.1	2.33*	2.30*	0.29	0.0029	CuCl	2.10	4.4	7.3	ED
S2.2	1.36	1.33	0.34	0.0092	$CuSiO_2(OH)_2$*	1.29	16.7	27.5	S,F
S2.3	1.91	1.89	0.28	0.0034	$Cu_2(OH)_3Cl$	1.86	5.0	8.2	S,E,R,F,ED
S2.4	0.72	0.71	0.29	0.0046	$CaSO_4 \cdot nH_2O$ (sediment)*	0.52–0.70	7.0	11.6	S,R
S3.1	N/A	3.00	0.33	0.0045	Unknown*	N/A	7.9	13.0	

Step 2: Additional main phases from zones identifiable by inspection

In each sample, several zones homogeneous in I_{GV} are observed from visual inspection of the slices in addition to the previously-discussed "Cu(I)" phase. Indeed each image consists of a limited number of spatial zones rather homogeneous in attenuation with piecewise continuity. We can therefore attempt to identify the chemical identities of these

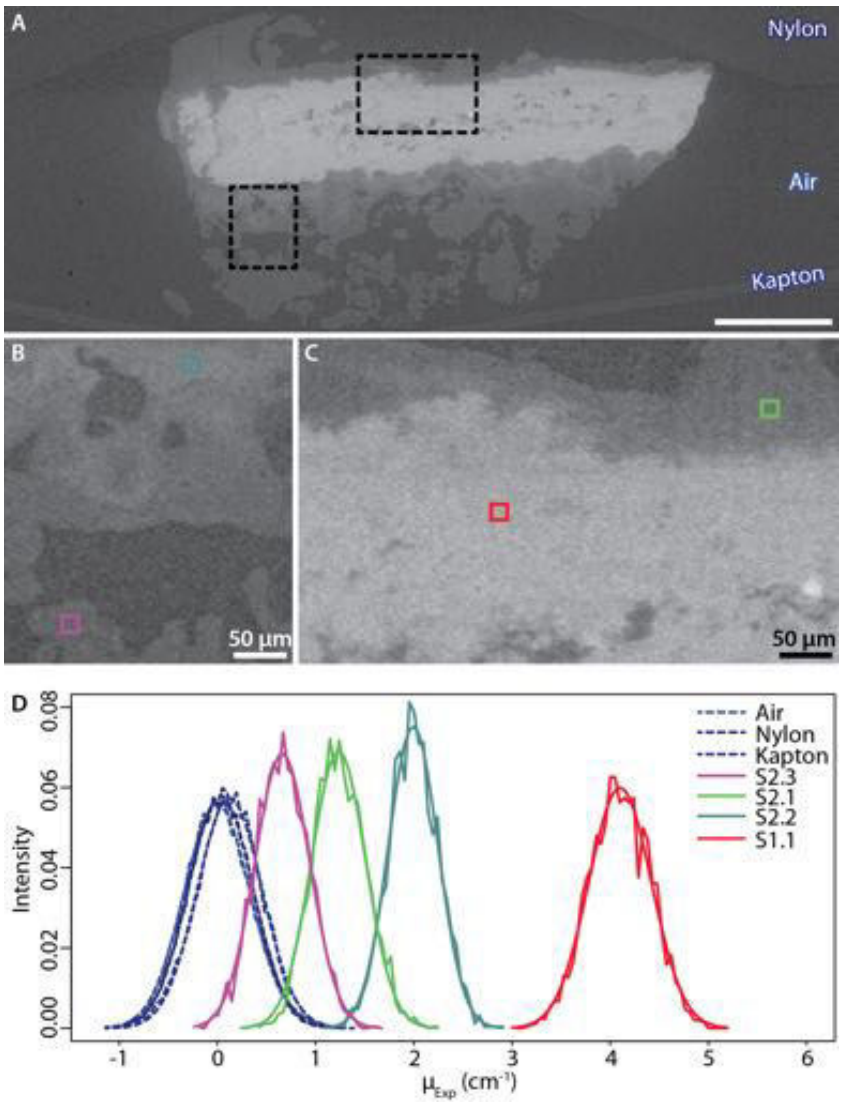

Figure 4.5: Measurement of attenuation coefficients μ_{Exp} from selected zones in sample AO 14506-1b. A, Tomographic slice showing zones where attenuation coefficients were measured. Scale bar: 500 µm. B and C, Close-up of the left and right dotted boxes in A. Scale bar in B and C: 50 µm. D, Distribution of calibrated μ_{Exp} of each selected zone fitted by Gaussian distributions. I_{GV} values were sampled at the locations indicated by a square of 5×5 voxels through 101 successive slices in the reconstructed data volume (2,525 voxels in total).

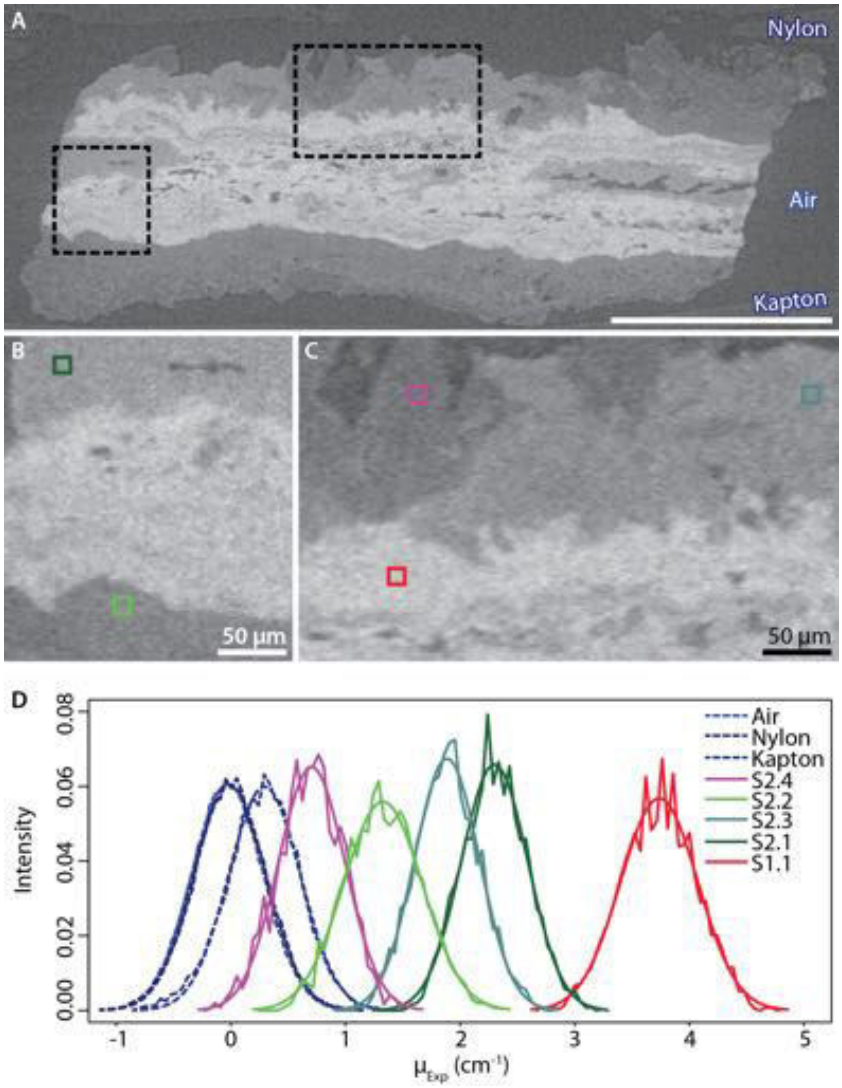

Figure 4.6: Measurement of attenuation coefficients μ_{Exp} from selected zones in sample NS 95015002-2. A, Tomographic slice showing zones where attenuation coefficients were measured. Scale bar: 500 µm. B and C, Close-up of the left and right dotted boxes in A. Scale bar in B and C: 50 µm. D, Distribution of calibrated μ_{Exp} of each selected zone fitted by Gaussian distributions. I_{GV} values were sampled at the locations indicated by a square of 5×5 voxels^2 through 101 successive slices in the reconstructed data volume (2,525 voxels in total).

Table 4.5: Attribution of zones of homogeneous attenuation coefficient in sample AO 14506-1b. μ_{Exp}: mean attenuation coefficient of 2,525 selected voxels per zone. μ_{Fit}, σ_{Fit}, I_{Fit}: attenuation coefficient, standard deviation and intensity established from a Gaussian fit of the distribution of calibrated attenuation coefficients in the entire selected slice. μ_{Th}: theoretical attenuation length for each pure compound. $\mathcal{A}_{\mathrm{Fit}}$: relative fitted area under of each phase. $\mathcal{A}^{\mathcal{S}}_{\mathrm{Fit}}$: in-sample relative fitted area under of each phase. N/A: not applicable. *: values discussed in the main text. Validation using (S)EM-EDX, (E)BSD, (R)aman, (F)T-IR, (ED)-XRD (refer to main text for precision).

Step	$\mu_{\mathbf{Exp}}$ **cm^{-1}**	$\mu_{\mathbf{Fit}}$ **cm^{-1}**	$\sigma_{\mathbf{Fit}}$ **cm^{-1}**	$I_{\mathbf{Fit}}$	**Proposed attribution**	$\mu_{\mathbf{Th}}$ **cm^{-1}**	$\mathcal{A}_{\mathbf{Fit}}$ **%**	$\mathcal{A}^{\mathcal{S}}_{\mathbf{Fit}}$ **%**	**Validation**
N/A	0.04	0.00	0.34	0.0209	Air	0.00	37.2	0.0	
N/A	0.05	0.03	0.33	0.0047	Nylon	0.22	8.0	0.0	
N/A	0.14	0.13	0.33	0.0052	Kapton	0.24	9.0	0.0	
S1.1	4.12	4.12	0.39*	0.0089	Cu_2O	3.78	18.0	39.3	S,E,F
S2.1	1.27	1.23	0.35	0.0067	$CuSiO_2(OH)_2$	1.29	12.3	26.9	S,F
S2.2	2.03*	1.99*	0.30	0.0028	$Cu_2(OH)_3Cl$	1.86	4.4	9.5	S,E,R,F
S2.3	0.69*	0.71*	0.24	0.0059	Al_2SiO_5	0.59	7.4	16.1	S
S3.1	N/A	2.62	0.23	0.0009	Unknown phase 1*	N/A	1.1	2.4	
S3.2	N/A	3.35	0.33	0.0015	Unknown phase 2*	N/A	2.6	5.8	

phases from their I_{GV}. 2,525 intensity values were arbitrarily selected from the zones corresponding to each of these phases in several neighbouring slices. The I_{GV} distribution for each of these 'individual' phases could be fitted as a normal distribution (Figures 4.5D and 4.6D). A putative attribution is proposed by comparison to known phases usually observed in copper-base archaeological artefacts. In sample NS 95015002-2, a phase of medium attenuation, typical of another Cu(I) compound is observed on both sides of sample, in the middle of its thickness (arrow 4 in Figure 4.1D). The measured attenuation μ_{Exp} is 2.33±0.29 cm^{-1}. This falls in a range where no common Cu compound is present except nantokite (CuCl, $\mu_{\mathrm{Th}} = 2.10$ cm^{-1}). Three additional phases are observed at the periphery of the sample. Two of them are typically in the attenuation range expected for Cu(II) compounds. The most abundant has an attenuation μ_{Exp} of 1.36±0.34 cm^{-1}, close to the dioptase mineral (1.29 cm^{-1}). Dioptase is a silicate copper compound ($CuSiO_2(OH)_2$, or $CuSiO_3 \cdot H_2O$). Silicon is very often detected in the corrosion products of archaeological copper-base artefacts [164, 175], while dioptase has occasionally been

directly identified [261]. The mean attenuation of the lesser abundant phase is 1.91±0.28 cm^{-1}. This value is in the higher range of attenuation of Cu(II) compounds observed in archaeological corroded copper artefacts (0.8–1.9 cm^{-1}, see Table 4.2). Here, the likely candidate is atacamite $Cu_2(OH)_3Cl$, as the sulphate brochantite $Cu_4(OH)_6SO_4$ is far less likely in this archaeological soil context. Finally the low-attenuation phase at $\mu_{Exp} \simeq 0.72\pm0.29$ $cm^{-1}$is likely to originate from the sediment. The latter is for instance in good agreement with calcium sulfate minerals $CaSO_4 \cdot nH_2O$.

In sample AO 14506-1b, similarly to the previous sample, three categories of zones of quasi constant attenuation are observed, typical of two Cu(II) phases and a third one located at the surface of the sample at the interface with the burial environment. Here again, the abundant Cu(II) phase of low attenuation has a μ_{Exp} of 1.27±0.35 $cm^{-1}$and is tentatively assigned to dioptase. The phase of greater attenuation ($\mu_{Exp} \simeq 2.03\pm0.30$ cm^{-1}) is attributed to atacamite. The phase at the surface of the sample has a comparatively very low attenuation ($\mu_{Exp} \simeq 0.69\pm0.24$ cm^{-1}) as in sample NS 95015002-2.

These compounds are noted as "S2.n" in Tables 4.4 and 4.5 for the two samples. Several phases could therefore be identified from the 3D reconstructed volumes. However, two main limitations can be induced by this process: (1) remaining "trace" phases could remain unnoticed, and (2) different phases of similar attenuation may be misleadingly identified as a single phase.

4.3.3 Extraction of hidden information through statistical processing

In order to attempt identifying remaining "trace" phases, we decomposed the gray level histograms from both selected slices into linear combinations of distributions corresponding to individual phases.

Step 3: Fitting the gray level histograms

A tomographic slice was selected in each 3D volume that contained the full sample stratigraphy and the diversity of phases observed. We constructed an histogram of the I_{GV} from each slice. These histograms were decomposed into a linear combination of Gaussian distributions with initial mean values and standard deviations (μ_{Exp}, σ_{Exp}) determined from the phases identified thus far. The result of this fit is shown in Figures 4.7 and 4.8 for samples NS 95015002-2 and AO 14506-1b, respectively. We then calculated the residue after subtraction of the fit to the measured distribution at each step.

In sample NS 95015002-2, a residual peak is observed at $\mu_{Fit} \simeq 3.00$ cm^{-1}. The identity of this residual phase is unknown as no commonly found corrosion product of copper has a theoretical attenuation value in this range (Table 4.2). The voxels belonging to the central part of the peak are primarily located at the interface between "Cu(I)" and "Cu(II)" phases and at the periphery of pores. They are also found along the two discontinuous lines that are attributed to the original surfaces (Figure 4.7). A new linear fit was performed using the new set of parameters, in which the peak position and standard deviation value of the Cu_2O phase were allowed to vary. After this fit, the new residue was calculated, which appears unstructured and of mean value close to 0 (9.96×10^{-6}). The number of collected voxels is 282,240 in total while the integral area under the fitted Gaussian distributions (calculated as $\mathcal{A}_{Fit} = I_{Fit} \cdot \sigma_{Fit} \cdot \sqrt{2\pi}$) corresponds to 281,853 voxels (99.86% of the total number of voxels). The model therefore agrees well with the distribution measured even with a limited number of fitting parameters.

In sample AO 14506-1b, two additional unforeseen peaks of medium attenuation are revealed by the spectral residue. The corresponding voxels are mainly distributed at the interface between the phases attributed to cuprite Cu_2O and to dioptase $CuSiO_2(OH)_2$ ($\mu_{Fit} = 2.62$ cm^{-1}) and around internal pores (3.35 cm^{-1}, Figure 4.8). The mean value

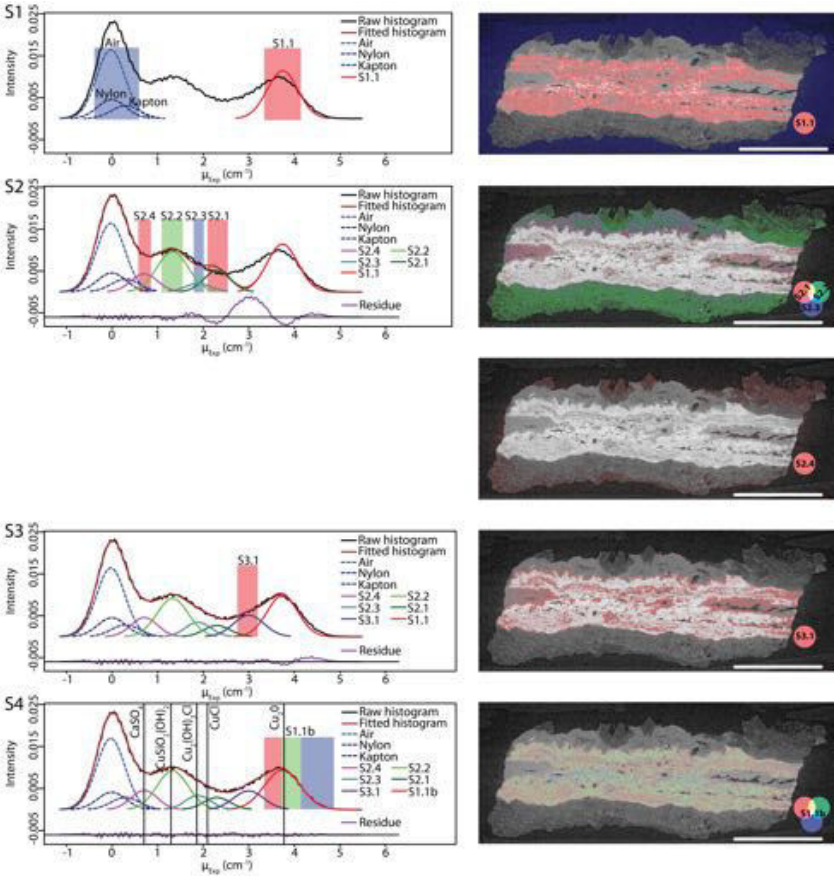

Figure 4.7: Decomposition of the μ_{Exp} histogram and identification of the phases in sample NS 95015002-2. The four steps S1–4 are discussed in detail in the text. For each step, we display the histogram of the calibrated experimental attenuation coefficients μ_{Exp} in the entire selected slice displayed in Figure 4.1C with results from the fits performed (left) and the distribution of the μ_{Exp} corresponding to the color bands superimposed on the histograms (right). S1, identification of the main Cu(I) phase as well as phases from the sample environment. The fit is established on the tested assumption that the distribution is normal. S2, Distribution of μ_{Exp} of additional Cu(II) phases and archaeological sediment which are identified as zones homogeneous in intensity in the same slice, and corresponding fit. The residual of the fit is displayed below the distribution. S3, Identification of a remaining phase resulting from the residue in S2. S4, Optimization of the fit by adjusting the peak position and FWHM of the Cu(I) identified in S1.1, the mean value of the fit residue is now very close to 0. The vertical lines indicate the μ_{Th} defined in Table 4.4 of all pure compounds assumed to be present in the sample. Scale bars: 500 µm.

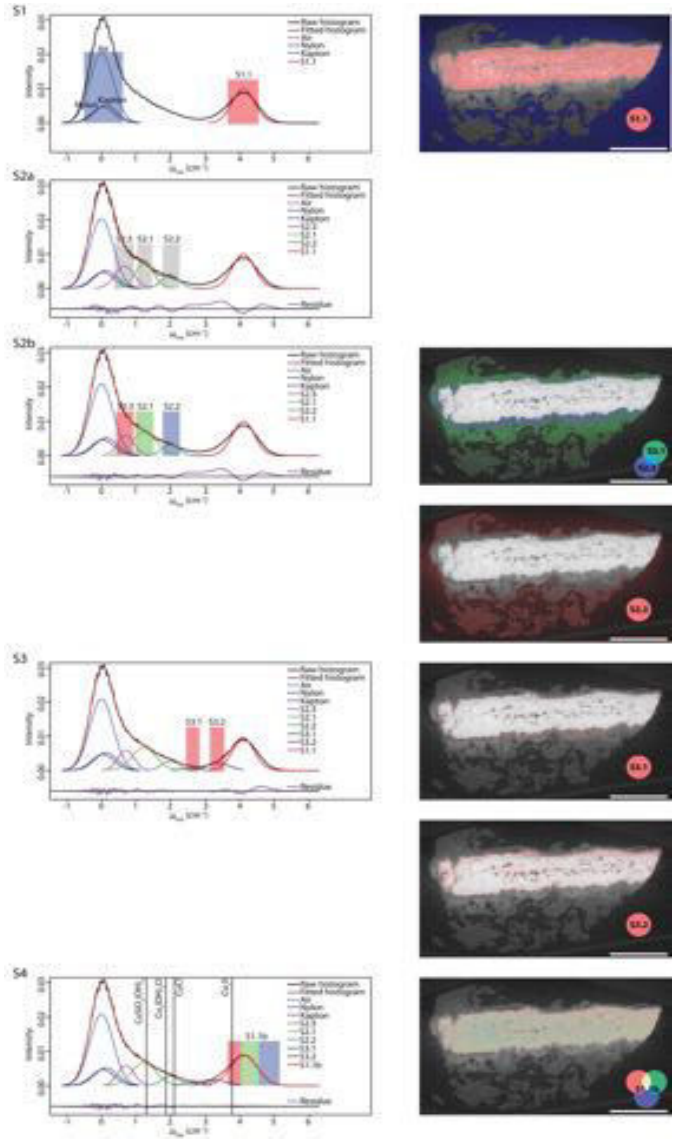

Figure 4.8: Decomposition of the μ_{Exp} histogram and identification of the phases in sample AO 14506-1b. The four steps S1–4 are mentioned in the text. For each step, we display the histogram of the calibrated experimental attenuation coefficients μ_{Exp} in the entire selected slice displayed in Supporting Information Figure 4.2C with results from the fits performed (left) and the distribution of the μ_{Exp} corresponding to the color bands superimposed on the histograms (right). S1, identification of the main Cu(I) phase as well as phases from the atmosphere and sample environment. The fit is established on the tested assumption that the distribution is normal. S2a, Distribution of μ_{Exp} of additional Cu(II) phases and archaeological sediment which are identified as zones homogeneous in intensity in the same slice, and corresponding fit. The residual of the fit is displayed below the distribution. S2b, Improvement of the fit by adjusting the distributions of μ_{Exp} for S2.1 and S2.3 (peak position and FWHM). S3, Identification of two remaining phases resulting from the residue in S2b. S4, Optimization of the fit by adjusting the peak position and FWHM of the Cu(I) identified in S1.1, the mean value of the fit residue is now very close to 0. The vertical lines indicate the μ_{Th} defined in Table 4.5 of all pure compounds assumed to be present in the sample. Scale bars: 500 µm.

of the final residue after adding the two peaks is very close to 0 (1.22×10^{-5}), showing here as well that the model developed is in good agreement with the data. The newly identified phases, indicated as "S3.n"in Table 4.4 for sample NS 95015002-2 and Table 4.5 for sample AO 14506-1b, were added to the model.

For the purpose of the validation of the methodology, real cross sections as close as possible to the tomographic slices were located in each sample by observing their stratigraphy using optical microscopy while polishing the sample. Complementary characterization was performed on both real sections using SEM-BSE, SEM-EDX, EBSD as well as Raman and FT-IR micro-spectroscopy.

In-depth comparison with the corresponding µCT data leads to several observations. In sample NS 95015002-2, the μ_{Exp} of the low-attenuation phase in the corrosion products is in good agreement with a silicate Cu(II) compound, such as dioptase $CuSiO_2(OH)_2$. This attribution is further supported by the atomic ratios of Si and O with respect to Cu at 1.1±0.3 and 3.7±0.7, respectively, determined by SEM-EDS analysis. A band around 1025 $cm^{-1}$is observed for this phase in FT-IR measurements which is consistent with Si–O stretching [183] (Figure 4.9). Additional EBSD measurements performed locally show that this compound is amorphous (Figure 4.10). The intense luminescence of this phase hampers its positive identification in Raman microspectroscopy. Dioptase is a compound of secondary origin commonly associated with secondary copper minerals formed in zones of copper oxidation, yet not originating from direct corrosion.

The Cu(I) phase (S2.1) at the measured attenuation 2.33 cm^{-1}has an attenuation coefficient slightly greater than CuCl (2.10). This phase is present in our object as a layered corrosion structure. The slight positive shift of μ_{Exp} of this phase may thus point to the incorporation of oxygen anions within the CuCl lattice. Indeed, non-invasive ED-XRD coupled to fast µCT was conducted on a bigger fragment (NS 95015002-6, see Chapter 5) of the same artefact NS 95015002 and yielded a positive identification of

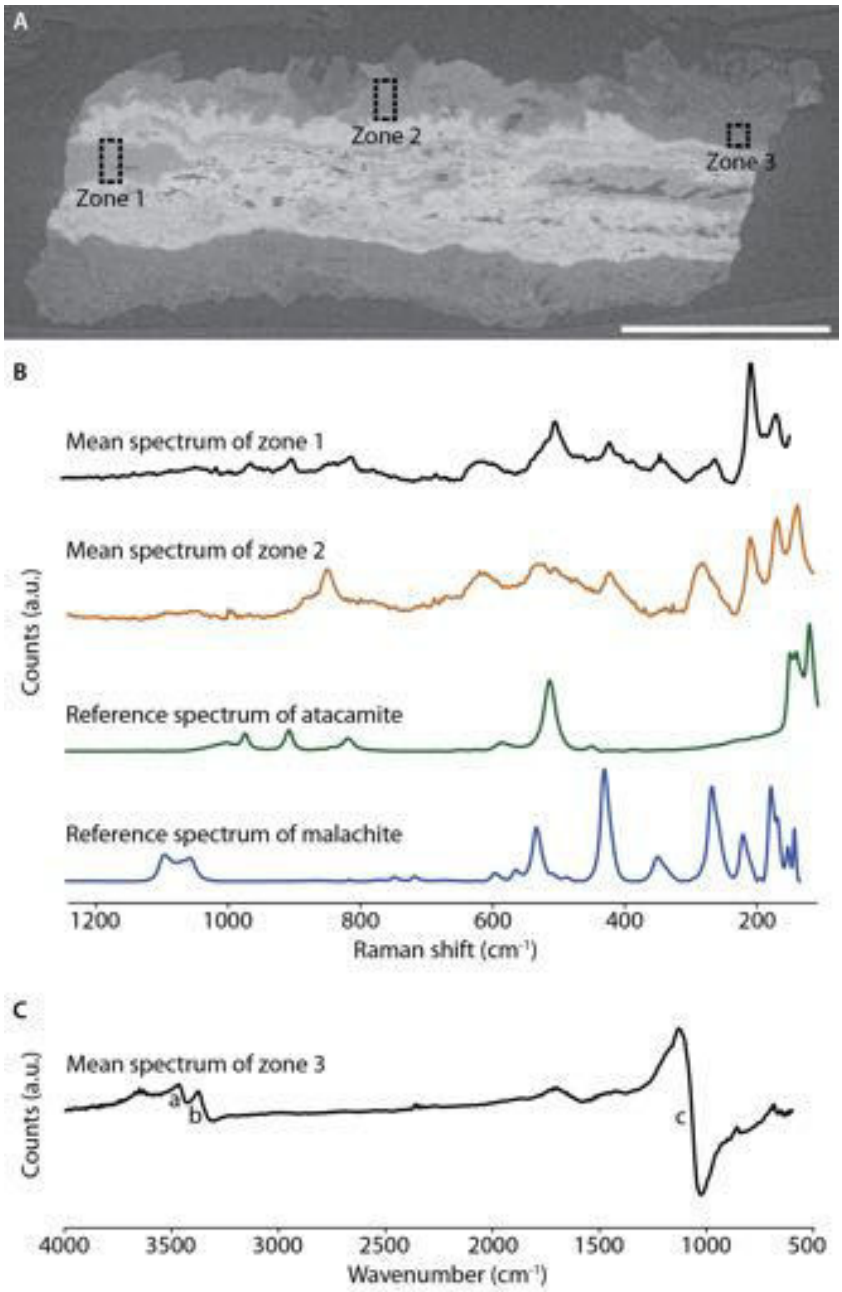

Figure 4.9: Raman and FT-IR spectra of zones including phases S2.1, S2.2 and S2.3 of sample NS 95015002-2. A, Tomographic slice showing zone where Raman and FT-IR analysis were performed. Scale bar: 500 µm. B, Mean Raman spectrum from zones 1 and 2, as well as reference spectra of atacamite $Cu_2(OH)_3Cl$ (RRUFF ID: R050098) and malachite $Cu_2(OH)_2CO_3$ (RRUFF ID: R050508). C, Mean FT-IR spectrum from zone 2. Features a (3428 cm^{-1}) and b (3410 cm^{-1}) are assigned to O–H stretching in green patina [262], feature c (1025 cm^{-1}) is attributed to Si–O stretching in silicates [183].

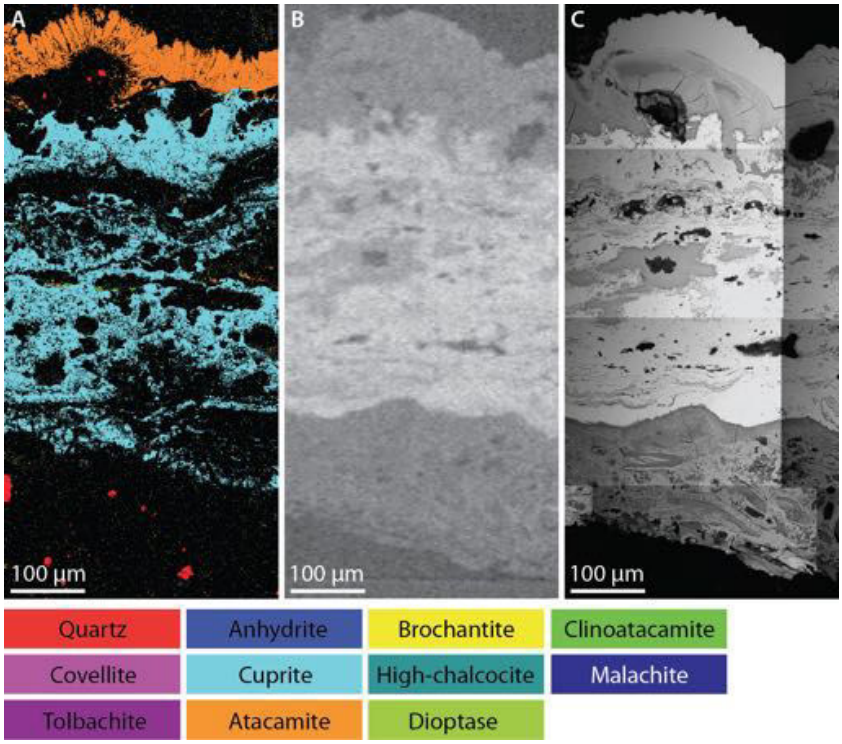

Figure 4.10: EBSD measurements of sample NS 95015002-2. A, EBSD results obtained for selected zone, phases are indicated by colour-scale below. B, The same zone in µCT virtual slice. C, The same zone in SEM-BSE imaging. Scales in A–C: 100 µm.

the CuCl phase. The comparison is considered representative because of the similar composition and history of all broken fragments composing this artefact. In the real cross-section, beyond copper, this phase contains essentially Cl and O anions as revealed by SEM-EDX (Figure 4.13). However, we could not directly identify the presence of CuCl using Raman micro-spectroscopy; atacamite and traces of malachite are found instead (Supporting Information Figure 4.9). The instability of CuCl must have led to its rapid conversion to atacamite upon the preparation of the sample cross section [151, 159]. Both in-situ analysis and the reactivity of the phase with air therefore point to the Cu(I) phase in the archaeological sample being CuCl with incorporated oxygen anions. This phase was noted in the core of many corroded archaeological copper-base artefacts [245, 174, 254, 246, 176, 175, 166]. This corrosion process is usually associated to oxidation under humid aerobic condition in soils [173].

The Gaussian shape of the residual centered at 3.00±0.33 $cm^{-1}$and its standard deviation are comparable in the other phases. This suggests that it should be attributed to a single phase which remained unnoticed in the initial steps of data analysis. However, its estimated attenuation coincide with no previously tabulated phase. Using EDX analysis, we observed a variable content ratio between detected elements (Cu,O,S,As,Al,Cl). No ascription to a precise species could be proposed. Beyond those cases, the chemical identities of all the other phases postulated (e.g., presence of $Cu_2(OH)_3Cl$ and $CaSO_4 \cdot nH_2O$) were confirmed by SEM-EBSD and EDS spectroscopy, as well as Raman and FT-IR micro-analysis. In addition, some malachite $Cu_2(OH)_2CO_3$ was found in association with atacamite $Cu_2(OH)_3Cl$, those two phases being difficult to discriminate on the basis of their attenuation coefficients which differ by only 4%.

Regarding the identities of the two Cu(II) phases in sample AO 14506-1b, EDX mapping is consistent with the presence of both dioptase and atacamite, while EBSD positively identifies atacamite (Figure 4.11, zone 1; Figure 4.12). We analyzed with Raman and FT-IR micro-spectroscopy a zone encompassing both phases S2.1 and S2.2.

Results show the presence of a copper silicate associated with atacamite and traces of malachite. The μ_{Exp} (2.03 cm^{-1}) of S2.2 is larger than the μ_{Th} of pure atacamite (1.86 cm^{-1}). We could not identify its composition, but it could result from the co-existence of CuCl ($\mu_{Th} = 2.10$ cm^{-1}) crystals of subvoxel size. The compound showing a very low attenuation ($\mu_{Exp} = 0.69$ cm^{-1}) at the sample surface consists mainly of Al, Si and O according to the EDX spectra. It could therefore typically be attributed to clays from the burial environment such as Al_2SiO_5 ($\mu_{Th} = 0.59$ cm^{-1}), with Ca and Cu detected as minor impurities. The residual phase at 2.62 $cm^{-1}$is distributed mainly at the interface between "Cu(II)" and "Cu(I)" phases, suggesting some mixing at these boundaries. EDX spectra show that the residual phase at 3.35 cm^{-1}consists of Cu, O and Cl, indicating a potential cupric oxide (or hydroxide) partially substituted by chloride.

Step 4: Discussing intrinsic heterogeneity

SEM-EDX elementary maps show a good correlation in the spatial distributions of Cu and O at the centre of the sample. EDX spectra in this area indicate Cu and O as main elements present, in an atomic ratio close to 2:1. This therefore confirms the significant presence of Cu_2O in the core of sample NS 95015002-2. In addition, SEM-EBSD confirms the overwhelming presence of cuprite Cu_2O (Figure 4.10). However, while it is noticeable that the σ_{Fit} values are comparable for all other phases identified, a good quality of fit could only be obtained for this phase by allowing variations in the standard deviation and the centroid position of the Gaussian. The fit resulted in a greater σ_{Fit} value at 0.40 while the attenuation marginally increased at 3.74 cm^{-1}. Even by correcting for the slow linear increase of σ_{Exp} with μ_{Exp}, σ_{Fit} was not expected to exceed 0.35, very close to the value of 0.34 measured initially at a single spot. Still, a single Gaussian peak is able to explain the whole distribution which makes it less likely that this peak consists of a mixture of two definite compounds. We therefore tried to identify whether a single phase yet of continuously varying density could explain this

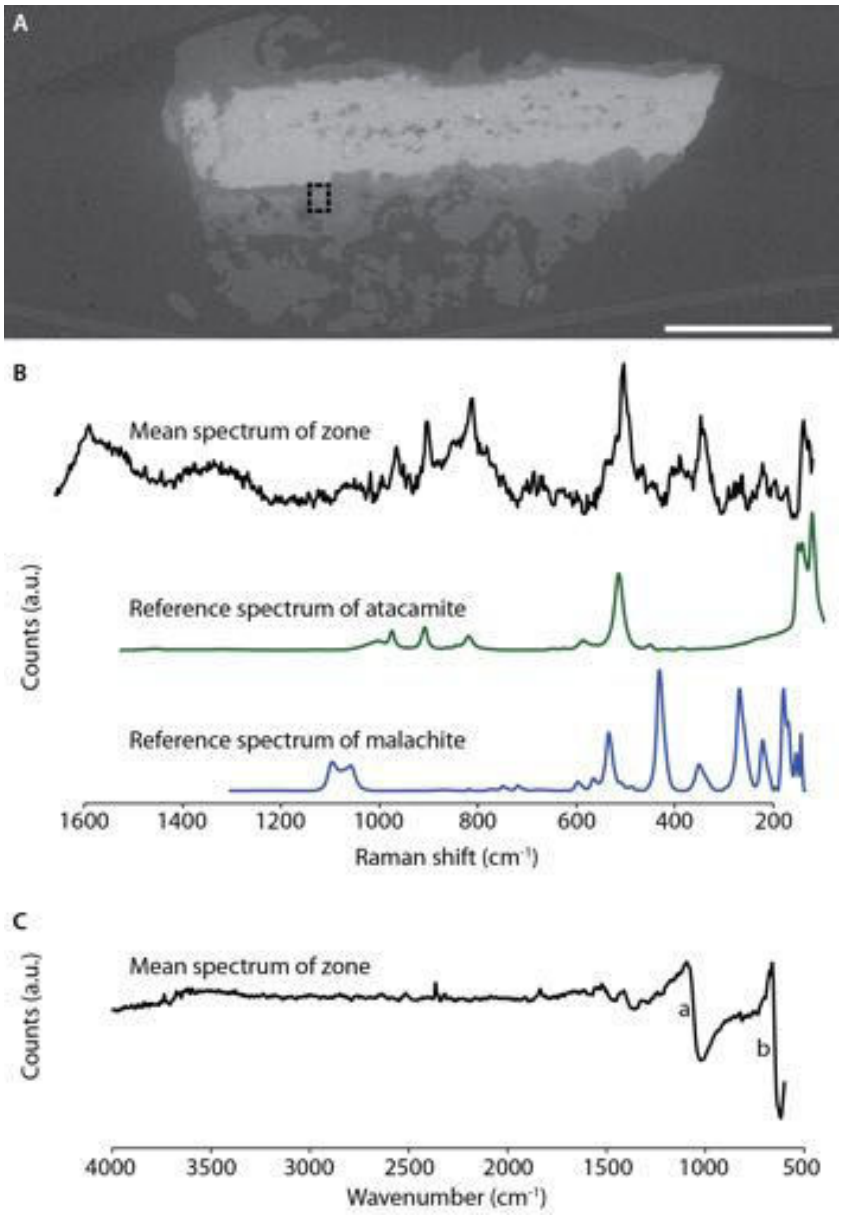

Figure 4.11: Raman and FT-IR spectra of a zone encompassing both phases S2.1 and S2.2 of sample AO 14506-1b. A, Tomographic slice showing the zone where Raman and FT-IR micro-spectroscopy were performed. Scale bar: 500 µm. B, Mean Raman spectrum from selected zone and reference spectra of atacamite $Cu_2(OH)_3Cl$ (RRUFF ID: R050098) and malachite $Cu_2(OH)_2CO_3$ (RRUFF ID: R050508). C, Mean FT-IR spectrum from selected zone. Feature a (1021 cm^{-1}) is assigned to Si–O stretching in silicates [183] and feature b (620 cm^{-1}) is a phonon-related feature attributed to Cu_2O [263].

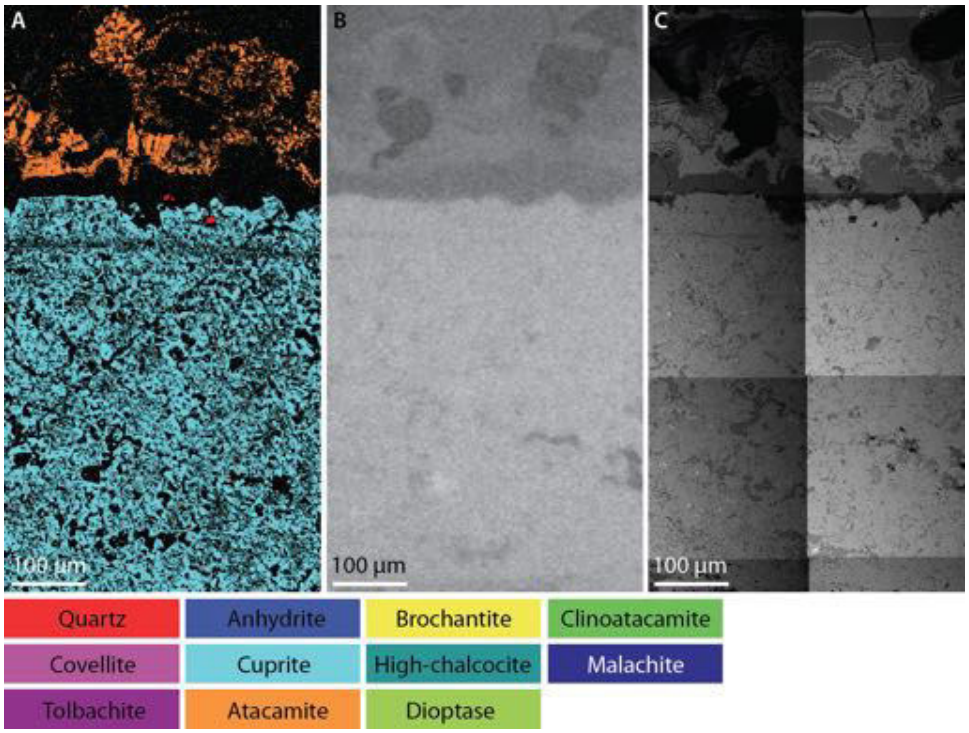

Figure 4.12: EBSD measurements of sample AO 14506-1b. A, EBSD results obtained for selected zone, phases are indicated by colour-scale below. B, The same zone µCT virtual slice. C, The same zone in in SEM-BSE imaging. The scale is for 100 µm.

feature. In order to attempt the deconvolution of different phases of similar attenuation, the spatial distribution of domains in calibrated μ_{Fit} ranges was carefully checked, in particular focusing to cases where discontinuous domains would show similar μ_{Fit} values (this was achieved by extracting integrated intensities along the whole μ_{Exp} domain every 0.2 cm^{-1}The highest μ_{Exp} values in this distribution are located in the core of the sample and could consist of a denser Cu_2O phase and/or a Cu_2O phase with partial substitution of Cu by an alloying element.

In sample AO 14506-1b, the presence of Cu_2O at the core is also confirmed by EDX (Figure 4.14) and EBSD imaging (Figure 4.12) and point analysis. The measured μ_{Exp} for this phase (4.12 cm^{-1}) significantly exceeds the theoretical value (3.78 cm^{-1}). This phase co-localises with residual Ag (e.g., high attenuating grain ca. 20 µm width at the centre of the tomographic slice) and Pb particles (invisible in the slice shown as their sizes are below the limit of resolution attained in our µCT experiment), as detected with EDX. Ag and Pb originate from the ores used for copper elaboration and their presence can explain the increased μ_{Exp}.

4.4 Potentials and limits of the methodology

3D visualization and semi-quantitative identification of the spatial distribution of the different copper compounds provide significant information for these copper-base archaeological materials. The visualization of the entire 3D volume, in a totally non-invasive way, directly informs on the morphology of the objects, their metallurgical state of manufacture and their state of alteration. No metallic copper is identified even at the microscopic scale, in the entire volumes. For these two fragments of sheet metal, initially made of copper, the resolution reached makes it possible to accurately identify the original surfaces [256] and the volume of the artefact. This leads to the conclusion that the sheets used here, in these ancient times, have regular thicknesses in the range of

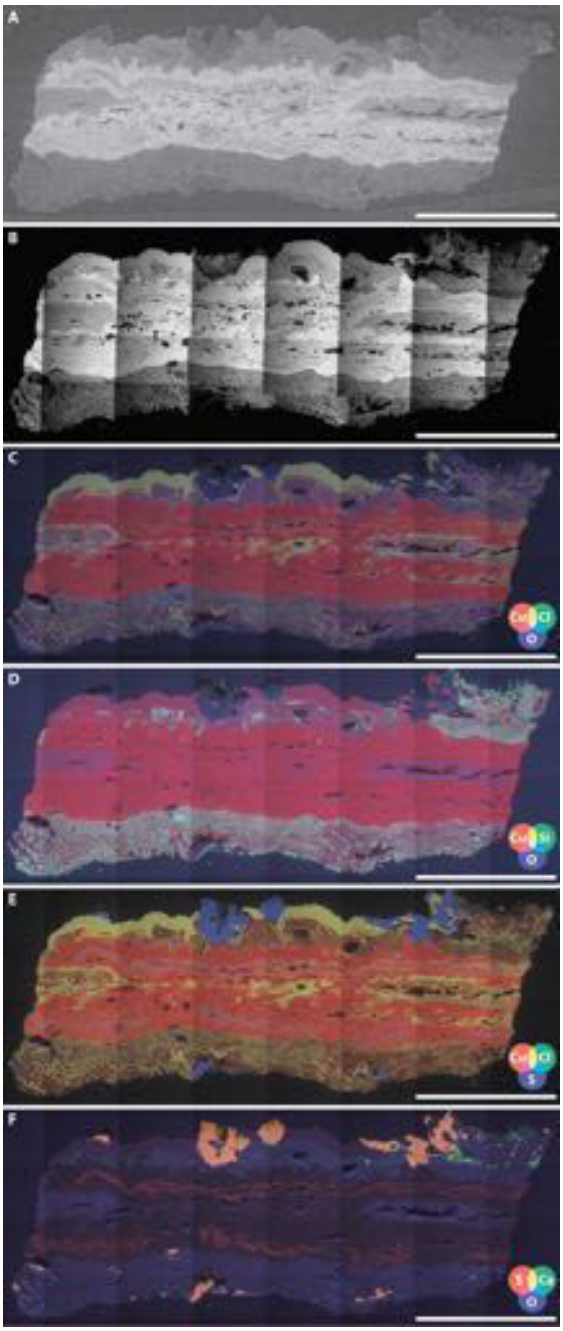

Figure 4.13: Complementary invasive characterization of sample NS 95015002-2. A, Tomographic slice. B, SEM-BSE imaging of a real section similar to the tomographic one. C–F, False color elemental maps of the section in B established from SEM-EDS analysis. Scale bars: 500 µm.

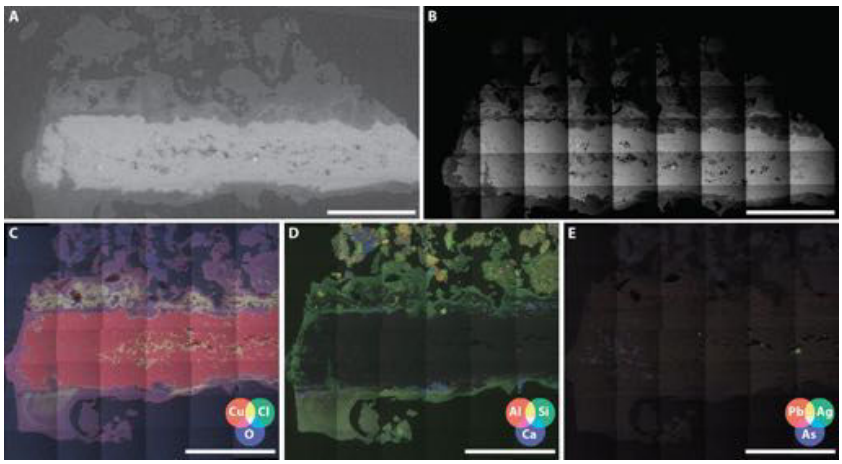

Figure 4.14: Complementary invasive characterization of sample AO 14506-1b. A, Tomographic slice. B, SEM-BSE imaging of a real section similar to the tomographic one. C–E, Elemental maps of the section in B established from SEM-EDS analysis. Scale bars: 500 µm.

200 to 300 µm. Moreover, although these fragments are totally corroded, the anisotropy of the internal structure revealed by the internal banded areas shows that these sheets obtained by hammering have been left in a cold-worked condition. In fact, µCT data on the internal condition of these artefacts, integrally altered, provide direct information on the metallurgical manufacturing process used. Here the results obtained in a non-invasive manner reveal a clear metallurgical quality of these remains from the Ancient Near East, which correspond to very thin sheets (<300 µm) and which have been left in their cold-worked state to ensure the necessary rigidity. With regard to the structure and corrosion phases clearly identified in the volume with this µCT approach, it is also possible to provide precise information on the corrosive environment of the artefact and its evolution over time. The direct 3D semi-quantitative comparison of the initial volume of copper with that of the corrosion products of Cu(I) and Cu(II) can be evaluated with great precision. We were thus able to establish a material balance between the copper initially present at the deposition of the artefact and that present in the current state, after corrosion in these unrestored remains [166]. Here, for NS 95015002-2 and

AO 14506-1b, this ratio between the amount of initial copper and the amount of copper remaining (in the artefact and its corrosion crust) is in the order of 93% and 80%, respectively. These values, close to 100%, indicate that a very low amount of copper has been dissolved in the archaeological environment, extremely little for fragment NS 95015002-2 and a little more for AO 14506-1b. Initially, these artefacts were therefore left or deposited in a closed environment that did not allow copper ions to dissolve in the environment, probably in an atmospheric environment as shown for a Dead Sea scroll copper roll, yet by invasive means [166]. However, the presence of exogenous mineral compounds on the external part of the corrosion crust suggests that the deposition context has changed over time. These compounds (calcium sulphate, silicates, etc.) are characteristic of a contact of the corroded fragment with an archaeological soil [165]. The presence and distribution of chlorinated phases shows the impact of a more saline environment for the NS 95015002-2 sample, compatible with its discovery near an arid site located closer to the sea shore. The methodology developed therefore reveals that the fragments have undergone a complex evolution involving several successive stages, including (1) deposition in an isolated confined space without leaching action from the soil, probably in the open air (confined passivating atmospheric-type conditions), then (2) a direct impact of the archaeological soil following an evolution of the initial archaeological context. Finally, it should be noted that from the point of view of the conservation of these ancient remains, the methodological approach developed here allows the identification and precise location of chlorinated phases that have a direct influence on the long-term stability of copper-base artefacts. This offers a particularly relevant approach to prevent and control active or recurrent corrosion of this type of material, also known as “bronze disease” [151]. The data clearly indicate that sample NS 95015002-2, which contain chlorinated phases internally in the fragment, unlike AO 14506-1b, will have to be stored in a controlled environment to avoid its subsequent alteration in ambient air.

The approach presented here is directly applicable to measurements performed at

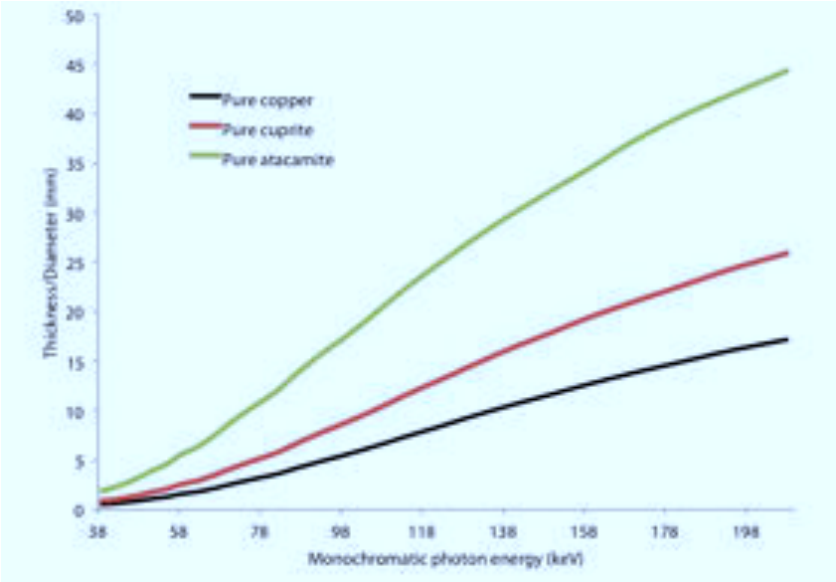

Figure 4.15: Maximum thickness of analyzable samples as a function of the incoming beam energy. In order to obtain a sufficient signal-to-noise ratio, a ratio of 10% of transmitted photons compared to incident ones is used to estimate the maximum sample size. As shown in the figure, if we consider a sample composed by pure copper, cuprite Cu_2O or atacamite $Cu_2(OH)_3Cl$, the transmitted thickness (or the diameter of a cylindrical sample) increases with the energy of monochromatic beam. For example, copper samples of 10 mm thick can be analyzed under the highest energy obtainable at the PSICHE beamline (about 140 keV), while samples up to about 17 mm thick can be analyzed at the European Synchrotron Radiation Facility (ESRF) using an energy of about 200 keV. Thicker samples can be traversed when they contain mainly cuprite or atacamite as in our case. In addition, a detector with a larger number of pixels can increase the field of view for a given pixel size; thus a larger sample can be analyzed with a resolution of a few micrometers. An incident spectrum containing higher energy photons can be produced in several laboratory tomographs, thus allowing even thicker samples to be studied, albeit with lower spatial resolution and signal-to-noise ratio. Local tomography can also be used to study small pre-defined regions of interest inside a bigger sample.

the ca. 70 synchrotron facilities in the world. Using high energy beamlines, with high definition detectors, a comparable resolution of a few micrometers like the one used here could be obtained on samples larger than one centimeter. Further discussion about the maximum sample size is provided in Figure 4.15. In addition, the proposed methodology makes use of a polychromatic beam and should therefore be applicable using conventional laboratory setups making use of X-ray tubes, yet at the expense of a decreased

signal-to-noise ratio. Tomographic investigation is therefore a powerful non-destructive tool for characterizing the conservation state of ancient metals, providing similar information to established techniques. Similarly interpretable gray levels to SEM-BSE are observed. Semi-quantitative analysis combined with morphological observation can be performed over large areas inside the samples without modifying or damaging their original morphology and composition. In particular, the loss or displacement of materials during sample preparation (cutting, polishing) is totally avoided. The rapid chemical alteration of the cross-section exposed to oxygen could be demonstrated and such non-invasive protocol could be particularly interesting to study other unstable phases in corroded metal artefacts [264].

The calibration approach presented allows a semi-quantitative interpretation of the gray values. Semi-quantitative determination of attenuation coefficients proves efficient to complement visual observation of contrasts across the images. It thoroughly contributes to the non-invasive attribution of phases. Most semi-quantitative approaches in µCT were developed for low-absorbing organic systems studied in medicine or pharmacy. For instance, Bossi and Nelson used a calibration standard made of inserts of 10 different cylinder-shaped materials of varying density and atomic number in an acrylic disk [265]. With low energy X-rays (below 1 keV), the CT intensity values poorly correlates to the material density due to the contribution of the photoelectric absorption edges while the correlation between the CT intensity values and material density is linear at high energy even in systems made of various chemical elements since the photoelectric absorption decreases rapidly with increasing photon energy, so that the Compton interaction is preponderant [210]. Similar results were found in the measurements of wood densities in plants [266, 267]. Quantitative density maps produced from low-absorbing pharmaceutical tablets samples were also shown to be approximately proportional to the CT intensity values [268]. In the latter work, the average energy is well above the absorption edges of most common elements but below the regime dominated by Compton scattering, and

so linear attenuation coefficients are generally well described by the Bragg-Pierce law. Here, as our archaeological samples consist primarily in dense corrosion compounds, a polychromatic "white" beam is needed to provide the high-energy photon flux needed to attain sufficient transmission of X-rays at most synchrotron facilities. The decomposition of the histogram of gray value intensities could be performed satisfactorily in these conditions. The attenuation coefficient spread was not significantly degraded compared to works performed using monochromatic radiation on inorganic materials. This suggests that the reconstruction noise is dominated by the detector performance and image statistics, and that the minor systematic error introduced by beam hardening is close to negligible. Efforts will be made to further reduce this effect in future work. Interestingly, the observed spread in calibrated attenuation coefficients is similar to data established with a monochromatized synchrotron source (Si(311) monochromator, $\Delta E/E < 10^{-3}$, varying energy in the 15–35 keV range), employing a calibration making use of single crystals of low-density Si-containing compounds and of metal wires [260].

Small discrepancies to the model such as larger than expected standard deviations or shifts in attenuation proved useful to identify mineralogical specificities in our complex heterogeneous samples. An additional indirect benefit of the process is the ability to precisely evaluate the quantitative volume ratio of phases in the sample from the area under each Gaussian contribution even when overlap is present between individual Gaussian contributions (Tables 4.4 and 4.5). Besides identification of phases supported by the calibration of attenuation coefficients, the decomposition process proposed in this study provides an original way to identify unexpected phases in complex heterogeneous systems. The process is expected to be particularly successful when the studied system consists in an assembly of well-defined phases, with fixed stoichiometry (e.g., no solid solution) and with negligible subvoxel physical heterogeneity (e.g., no submicrometric mineral grains), for which filtered back projection provides a good estimate of the attenuation coefficient. This is the case for long-term copper-based corroded systems

(compared for instance to iron-based) as thermodynamically-controlled copper corrosion mostly leads to phases of known stoichiometry within precise stratigraphies. The limited number of corrosion compounds of copper and the clear difference in attenuation between those phases (Table 4.2) are favourable; phase attribution will work efficiently as long as the elemental composition and the density of the investigated compounds do not excessively deviate from the reference phases. In this regard, it is noticeable that only a limited set of Gaussians is sufficient to explain our full sample dataset. Such analysis of residuals of the fit could further be automated to obtain the complete identification of phases present in a sample in 3D. This could be combined with automatic image segmentation to determine the spatial distributions of phases. Modeling of interface regions could be used to avoid introducing spurious extra phases.

4.5 Conclusion

The synchrotron-based micro-computed tomography methodology employed in this work on copper-based artefacts allowed to assess the suitability of the technique for: (1) exploring corrosion phases without any invasive sample preparation as in traditional techniques, (2) clarifying the corrosion processes that occurred mostly under atmospheric conditions, (3) investigating the reactivity of the artefact with the external environment defined by the presence of the original surface, (4) defining missing phases, and (5) avoiding the effects of the rapid alteration of the cross-section upon exposure to the atmosphere. Altogether, such semi-quantitative phase identification through synchrotron-based µCT appears as a promising approach for the non-destructive investigation of corroded archaeological artefacts. It could also be applied to a wider range of three-dimensionally preserved archaeological or fossil materials. Beyond ancient systems, the proposed methodology is applicable to most heterogeneous multiphasic materials.

5

Advanced physico-chemical description of mineralized flax textiles

This chapter examines the corpus of flax textiles using a set of complementary laboratory and synchrotron-based analytical methods. The presence of organic remnants, even in highly transformed fibres, in a yet undetermined molecular form, is demonstrated and discussed. Inorganic elements present in mineralized fibres are identified and the characterization of corrosion products formed in metal substrates is performed.

Contents

5.1 Introduction

The study of ancient textiles is arguably less advanced than that of many other archaeological materials, probably for two principal reasons [269]: (1) Textiles are perishable organic materials as they are mostly made of vegetable or animal fibres. The very small amount of textile remains found in many ancient contexts may not allow in-depth archaeological studies, compared to more durable mineral materials; (2) Historically, textiles used to wrap other artefacts (ceramics, metal objects, etc.) have been regarded as of lesser value than the wrapped artefacts themselves. For this reason, textile remnants have often been cleared to reveal the surfaces of ancient objects before exhibition or during conservation. However, archaeological textiles constitute an important material record of ancient human activities such as clothing, cloth manufacturing and funerary practices [102, 270]. The material archaeological record holds valuable witnesses of the development of the techniques and of the production of textile in early civilizations [17, 271]. The two main uses of textiles in Antiquity were similar to nowadays, i.e. for clothing and as container [269, 3]. Textiles displayed symbolic value allowing identifying social status in societies [272, 273, 3]. They were offered as gifts for diplomatic purposes and used as exchange goods [22, 23]. In many archaeological contexts, textile remains exceptionally preserved in a 'mineralized' form provide the only or the main source of knowledge on ancient textiles [5, 111, 129]. Mineralized textile remains can be found even in contexts of mild climate of moderate moisture and oxygenation [137]. They are found very close or in direct contact to corroded metal artefacts. The mineralisation process preserves the microscopic morphologies of textiles at macroscopic and often microscopic levels, thus allowing the identification of the fibres from characteristic morphological features and the detailed description of the weaving patterns [274, 3, 42]. Although deeply chemically transformed, mineralized fibres can still bear identifiable molecular biosignatures. To our knowledge, the oldest samples on which exceptional

preservation of molecular biosignatures was shown through detailed chemical analysis date from 3000 BC in protein-based fibres using proteomics [275] and from the late 1500 AD in cellulose-based fibres using Fourier-transform infrared spectroscopy [1].

5.2 Experimental section

5.2.1 Archaeological samples

A set of mineralized textiles on ancient copper artefacts from the sites of Gonur-Depe (Central Asia, current Turkmenistan), Nausharo (Indus valley, current Baluchistan, Pakistan) and Tello (ancient Mesopotamia, current Iraq) was studied here, for details refer to Sections 3.1 in 3).

5.2.2 Methods

A methodology based on conventional techniques (FT-IR, SEM-EDS/EBSD, etc.) and non-invasive synchrotron methods (µCT, photoluminescence imaging and µED-XRD) was implemented, for experimental setups refer to Section 3.2 in 3 and Appendix A.

5.3 Results and interpretation

The observation and the physico-chemical information obtained on the artefacts from each site (summarized in Table 5.1) are detailed below.

5.3.1 Textile fragment from Gonur-Depe

The textile appears very soft. Visual observation of the textile fragment Gonur 2380-1 (Figs. 3.2A and 5.1A) shows an homogeneous beige colour. The edges of the textile are loose and irregular. The weave used is a simple and balanced plain tabby of ca. 20 yarns per centimetre in each direction, as clearly identifiable in 3D digital microscopy. The Z-

Table 5.1: Summary of observation on mineralized textile remains and corroded copper-base substrates of each artefact. Symbols of + and - indicate degrees of flexibility and fragility, * means unidentified.

	Artefact	Gonur 2380	NS 95015002	AO 27703	AO 14506	AO 77	AO 76
Textile	Ø fibre (µm)	15	12-15	*	25	15	15
	Twisting mode	Z	Z	S and Z	S	S/ZZ	S/ZZ (x direction) Z (y direction)
	Ø yarn (µm)	200-400	150-250	*	350-350	300-500	300-500
	Weaving mode	Plain tabby	Plain tabby	*	Plain tabby	Plain tabby	Plain tabby
	Colour	Beige	Beige	Beige-brown-grey	Green	Green and beige	Green and beige
	Flexibility	++	+	-	-	-	-
	Fragility	-	+	++	++	++	++
	Presence of organic remnants	Yes	Yes	*	Yes	Yes	Yes
	Presence of major inorganic elements	Cu, Si and Al	Cu and Si	*	*	*	*
Main corrosion products of metal substrate (from external to internal layers)		*	Copper silicates; Atacamite; Nantokite; Cuprite	*	Copper silicates; Atacamite; Cuprite	Atacamite and malachite; Cuprite	Atacamite and malachite; Cuprite

twist yarns partly unwind while some fibres are detached from each other. The diameter of the altered yarns varies from 200 to 400 µm. The yarns do not show any gloss. Light microscopy shows dispersed green minerals attached to fibres surfaces of ca 15–20 µm in diameter (arrows, Fig. 5.1B), which were not further characterized. The diameter of the fibres is ca. 15 µm (Fig. 5.1C). We selected several individual fibres for closer examination (Fig. 5.1B). A central inner channel is observed in the fibre that may correspond to its former lumen (arrow 1, Fig. 5.1D). Fibre "dislocations", typical of bast fibres, are observed (arrows in Fig. 5.1C, arrows 2 and 3 in Fig. 5.1D). Very interestingly, FT-IR spectroscopy on cross-sections of extracted fibres shows many absorption bands characteristic of organics (Fig. 5.2). Most of these bands are in correspondence with modes observed in cellulosic materials (Table 5.2). The spectra show an intense and broad feature in the 3500–3100 cm^{-1} range corresponding to O–H stretches. Two peaked features at 3339 cm^{-1} and 3284 cm^{-1} are attributed to hydroxyl groups in adsorbed water or minerals. The two bands at 2896 cm^{-1} and 2870 cm^{-1} correspond to C–$H_{2/3}$ stretches. The very-low intensity band observed on one of the cross-sections at 1725 cm^{-1} is attributed to C=O stretching either from preserved hemicellulose or oxidised organic compounds (S.I. Fig. S1). The broad band at 1615 cm^{-1} is attributed to H–O–H bending modes of absorbed water. The four fine bands at ca. 1540, 1523, 1456 and 1420 cm^{-1}, variable in relative intensities and in a region were cellulosic materials show no characteristic

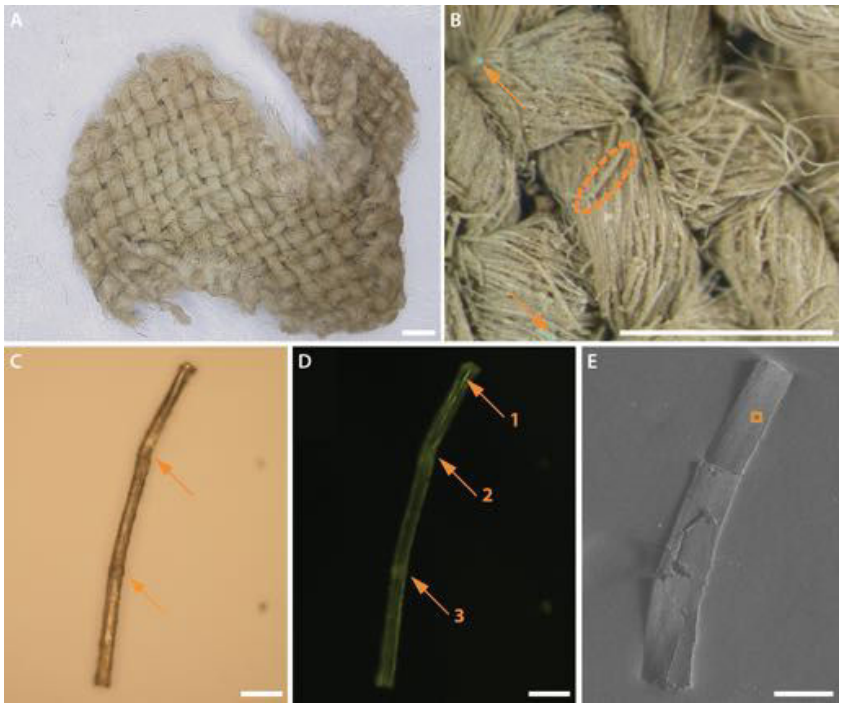

Figure 5.1: Textile fragment Gonur 2380-1 from the artefact Gonur 2380. A, Digital microscopy reconstruction of the sample surface. B, Close up on Z-twist yarns and green minerals indicated by arrows. An extracted individual fibre is shown in orange circle. Scale bars in A and B: 1 mm. C–D, Longitudinal view of the selected fibre in B using bright field (C) and fluorescence mode (D) microscopy. E, SEM-BSE imaging of the same fibre squashed. The orange square indicates zone for EDS analysis. Scale bars in C, D and E: 50 µm.

feature, may correspond to CO_3^{2-} in metal complexes. All the bands identified in the fingerprint region (1200–900 cm^{-1}) agree well with the characteristic absorption features of cellulose. In particular, the band at 1162 cm^{-1} attributed to asymmetric stretching of the glycosidic linkages C – O – C between glucose monomers appears as intense as in the reference flax. An individual fibre was further studied through SEM. Images obtained in BSE (back-scattered electrons) mode show a relatively homogeneous signal intensity, indicative of a rather homogeneous chemical composition (Fig. 5.1E). SEM-EDS analyses were performed in selected areas. Data collected at the surface of the fibre, at a place where no green minerals are attached, indicate an overwhelming organic composition (domination of signals from oxygen and carbon; orange square in Fig. 5.1E). Significant amounts of copper are identified, estimated at ca 15%wt. Minor elements widely encountered in soils are also found (Si, Al, Fe, Ca, Mg, K and Cl). Phosphorus is also present in rather significant proportion, as often encountered in anthropic or funerary settings [279]. No analysis of the metal support (i.e. the corroded copper ladder) could be performed.

5.3.2 Metal fragments from Nausharo

This more complex case of a fragmented artefact was studied through a large array of methods.

The textile appears still flexible. From visual observation, all the fragments NS 95015002-1,2,3,6-1 show identical external morphological features both for the mineralized textile (e.g., diameter, spinning and weaving, colour, flexibility, etc.) and for the corroded copper plate (e.g., colour, thickness, etc.). Textile remains cover both sides of each sample (Fig. 5.3A). Superficial yarns lay outside of the corrosion layer covering the artefact, while those in contact are either partly or totally embedded within the corrosion layer. The weave used is a simple plain tabby (ca. 23 yarns per centimetre). Z-twist yarns of a diameter of ca. 150–250 µm, elliptical in shape, are well identifiable

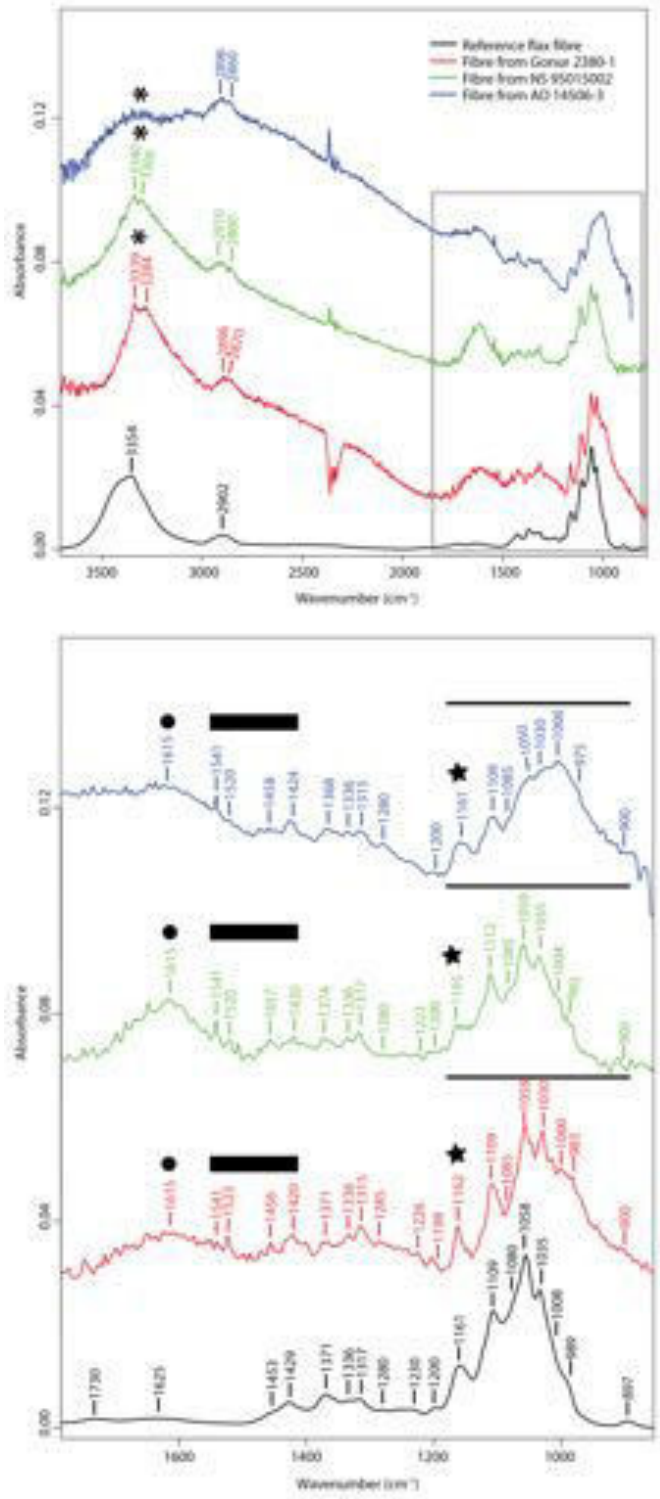

Figure 5.2: FT-IR spectra of mineralized fibres and of a reference flax fibre. The spectra have been vertically shifted for clarity. *: Absorption bands of O – H stretching. •: Absorption band of H – O – H bending. ■: Absorption bands of CO_3^{2-} asymmetric stretching. ⋆: Absorption band of C – O – C asymmetric stretching. –: Absorption bands in the fingerprint region.

(Fig. 5.3B). This feature is confirmed by our µCT observations. External yarns have an overall vitreous glossy appearance and a beige exterior colour, appearing to cover each individual exterior fibre. A localized beige encrustation is present which covers the surface of several yarns. Green globular particles are attached to the fibres surfaces, quite monodisperse in size. Yarns embedded more deeply in the external corrosion layer appear in various hues of green. µCT shows that each yarn contains typically ca. 200 fibres, separated by ca. 6 µm (Fig. 5.4C). The elongated shape of individual fibres in longitudinal view (arrow 1, Fig. 5.4C) and their round shape in cross-sectional view allow distinguishing easily the fibres from the corrosion products (arrows 2 and 3, Fig. 5.4C). Light microscopy on the sample surface and µCT show that the diameter of individual fibres typically varies from 12 to 15 µm. The resolution attainable in µCT is insufficient to evaluate further this size distribution. SEM-BSE imaging performed on a sample surface and a cross-section that includes the full stratigraphy shows three states of fibre surfaces: (i) some fibres are embedded within a compact matrix of corrosion products (Fig. 5.5E), (ii) other appear isolated and covered by minerals (arrow 4, Fig. 5.6C, diameters of minerals: ca. 2–3 µm), (iii) some fibres show a "clean" surface (arrow 2, Fig. 5.6C). The lumen of some fibres is identifiable on cross sectional view (arrow 3, Fig. 5.6C) while it is closed in other fibres (arrow 1, Fig. 5.6C). A significant contrast is observed in photoluminescence both between fibres and within individual fibres (Fig. 5.7C). Among the three bands studied (412–438 nm, 535–607 nm, 850–1020 nm), our data show that most fibres luminesce mainly in the 535–607 nm range (zone 2, Fig. 5.7C) while some have an intense luminescence signal resulting from emissions both in the range 412–438 and 850–1020 nm (zone 1, Fig. 5.7C). Interestingly, the contour and the lumen of fibres which bulk luminesces mostly in the 535–607 nm range (arrow 2, Fig. 5.7D) appear to luminesce in the 412–438 and 850–1020 nm ranges (arrows 1 and 3, Fig. 5.7D). FT-IR absorption features in fibres from artefact NS 95015002 appear at similar wavenumbers than in the modern flax fibre and in fibres from sample Gonur 2380-1 (Fig. 5.2, S.I.

Figure 5.3: Microscopic observation of sample NS 95015002-1. A, Binocular microscopy of one of the sample surfaces. B, Z-twist yarns and green globular particles attached to the fibres surface. Scale bars: 1 mm.

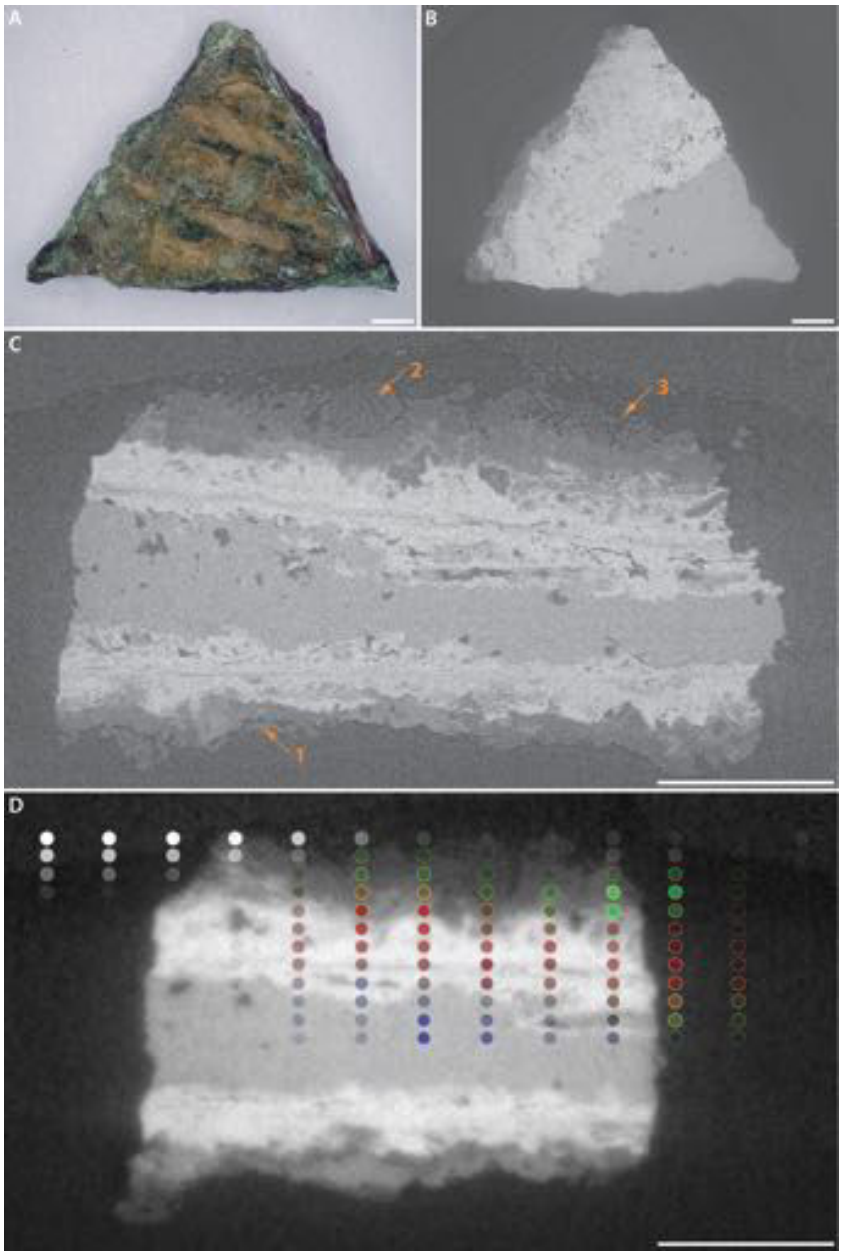

Figure 5.4: µCT and XRD imaging of sample NS 95015002-6-1. A, Digital microscopy reconstruction of the sample surface. B, Reconstructed tomographic slice of the sample in an inner plane oriented as in A. C, Reconstructed tomographic slice of the sample in a perpendicular plane to B. D, Reconstructed tomographic slice selected for in-situ XRD experiment based on a set of points analyzed. Red: cuprite (Cu_2O); Green: atacamite ($Cu_2(OH)_3Cl$); Blue: nantokite (CuCl); White: polymer that covers the sample. Scale bars: 500 µm.

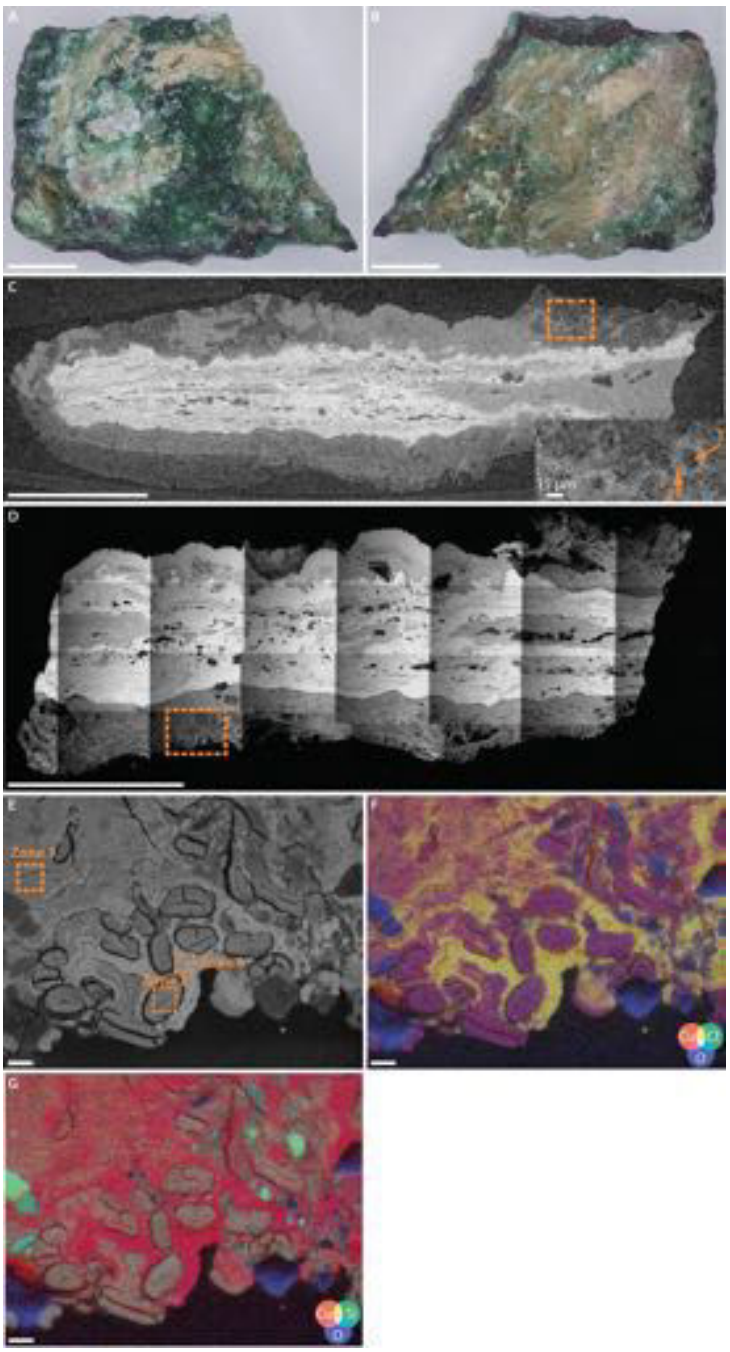

Figure 5.5: µCT and SEM imaging of sample NS 95015002-2. A, Digital microscopy reconstruction of the sample surface. B, Digital microscopy reconstruction of the opposite sample surface. C, Tomographic slice showing the distribution of corrosion products and cross sections of fibres in an inner plane perpendicular to the sample surface shown in A. D, SEM-BSE imaging of a real cross section. Scale bars in A–D: 500 µm. E, SEM-BSE imaging of fibres and mineral encrustation indicated in the orange rectangle in C. The three orange rectangles indicate zones for EDS analysis. F and G, False color elemental maps E established from SEM-EDS analysis. Scale bars in E–G: 10 µm.

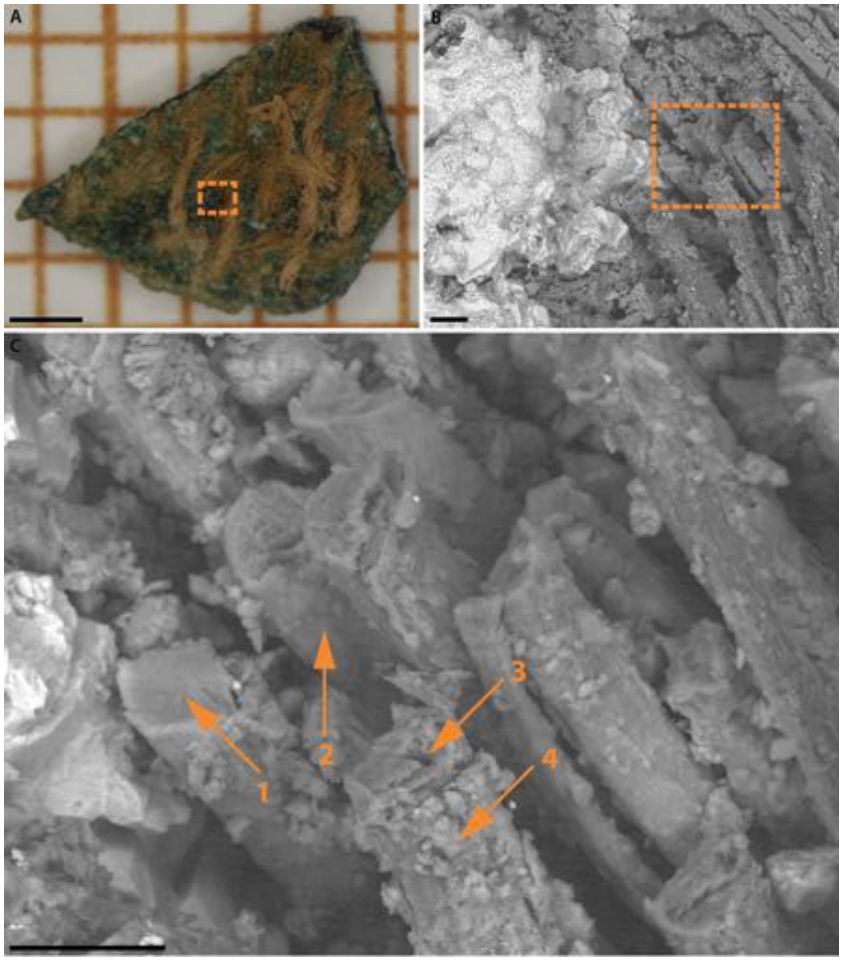

Figure 5.6: SEM imaging of textile remains covering sample NS 95015002-3. A, Digital microscopy reconstruction of the sample surface. Scale bar in A: 1 mm. B, SEM-BSE imaging of the orange rectangle area in A. C, SEM-BSE imaging of individual fibres from the orange rectangle area in B. Scale bars in B and C: 20 µm.

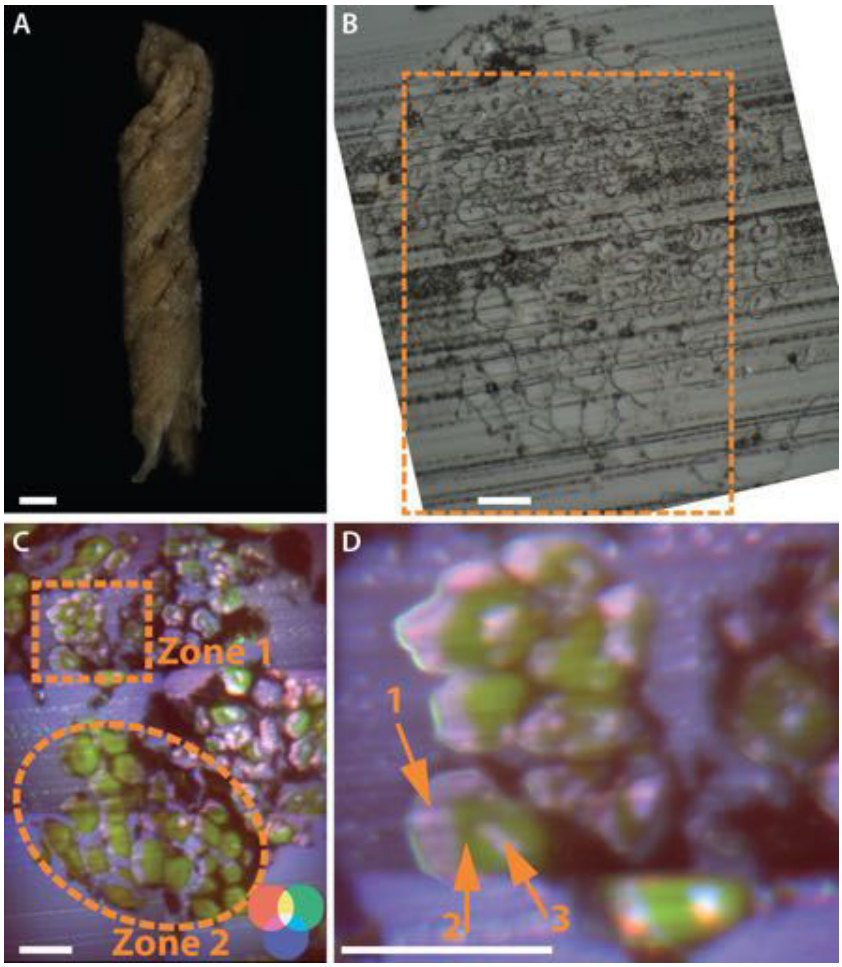

Figure 5.7: Photoluminescence micro-imaging of an individual yarn detached from the artefact NS 95015002. A, Longitudinal view of the yarn using dark field microscope. Scale bar: 100 µm. B, Cross sectional view of the yarn using bright field microscope. The yarn is embedded in epoxy resin then cut and polished. The orange rectangle indicates area selected for photoluminescence micro-imaging. C, Photoluminescence micro-imaging of the individual yarn. The excitation wavelength was set to 280 nm. Colour scale: Red 850–1020 nm; Green 535–607 nm; Blue 412–438 nm. D, Photoluminescence contrast within and between fibres. Scale bars in B, C and D: 20 µm.

Fig. 1 and Table 5.2). In particular, the broad band in the high wavenumber region (3400–2800 cm^{-1}) and the narrow bands in the fingerprint region (1200–900 cm^{-1}) agree well with the characteristic absorption features identified in cellulosic materials. Variations in band intensity will be interpreted later in the Discussion. Absorption bands at 1541, 1520, 1457 and 1420 cm^{-1} are attributed to carbonate in metallic complexes. In µCT, fibres show limited attenuation of X-rays (corresponding to a low electron density) compared to minerals in the corrosion layers (orange rectangle, Fig. 5.5C). However, this attenuation appears heterogeneous within and among individual fibres (arrows 1 and 2, Fig. 5.5C) in the studied artefact NS 95015002. SEM-EDS spectrum from the center of an altered fibre (zone 2, Fig. 5.5E) highlights Cu, Si and O as major elements in an elemental ratio of 1:1:4, as well as minor concentrations of Cl, Al, Ca and S. A zone of a crosss-section comprising a few fibres was analyzed with EBSD (refers to Chapter 4). Interestingly, no diffraction signal was observed, indicating most probably the amorphous nature of the compounds present in the fibres, despite their high mineral content. The surface of the corroded metal substrate is green. A red-brown layer is observed below this green surface, as seen at the broken edge of samples. The stratigraphy of the substrate itself has been studied in two samples. It shows very comparable features as in the sample that the previous description of the metal substrate of sample NS 95015002-2, detailed in Chapter 4 [197] (Fig. 5.5C and 5.4C). The inner part of corroded metal substrate consists of two layers: a highly absorbing flat plate that is associated with a Cu(I) phase (typically cuprous oxide Cu_2O) and, a relative lower attenuation zone composed of copper (I) chloride [197]. The external corrosion crust contains two low-attenuation compounds. These correspond to less absorbing Cu(II) corrosion products (copper hydroxide containing chlorine and copper silicates as well as a minor presence of copper carbonate) that form outside the sample surface.

5.3.3 Artefacts from Tello

Axe blade AO 27703

Textile remains are observed on both sides of the artefact. They appear very fragmentary and show an overall beige-brown-grey colour (Fig. 3.4D and Fig. 5.8D). These remains are not flexible and fragile. Parallel traces in the form of orange-brown stripes suggesting a probable restoration treatment (ex. usage of a crusher to remove the crust) are observed on the right of the Fig. 5.8A (arrow 1). A reddish inner layer (arrows 2, 3 and 4) is visible. Arcuate recesses on the contour of the artefact, which probably indicate past use for its corresponding function (ex. chopping), are present (arrows 1 and 2, Fig. 5.8B). Grey-beige encrustation forming a relatively flat zone (arrow 4) and cross-shaped zone are identifiable (arrow 3). A relatively large zone of external green minerals is clearly visible (arrow, Fig. 5.8C).

Textile fragment AO 14506-3 and vase AO 14506

The isolated textile fragment AO 14506-3 is very fragile and shows a relatively homogeneous green colour (Fig. 5.9A). The weave used is a simple plain tabby. S-twist yarns of a diameter of ca. 300–350 µm are identified (arrow, Fig. 5.9C), this observation is confirmed by µCT imaging. Yarns show an overall vitreous glossy appearance (Fig. 5.9A). Grey-beige compounds, probably from soil, are present and are attached to the surfaces of several yarns (arrow, Fig. 5.9D). µCT shows that each yarn contains typically ca. 150 fibres, separated each by ca. 5 µm (Fig. 5.9E–G). Even though conventional µCT attains its resolution limit, our data resolve the longitudinal forms of yarns (orange broken lines, Fig. 5.9E) and the ovoid cross sections of most individual fibres in the yarn (orange circles). Light microscopy examination of the sample surface and µCT imaging show that the diameter of individual fibres is ca. 25 µm (Fig. 5.9F and G). FT-IR measurements carried out on (thicker, between 6 and 8 µm) sections of an individual

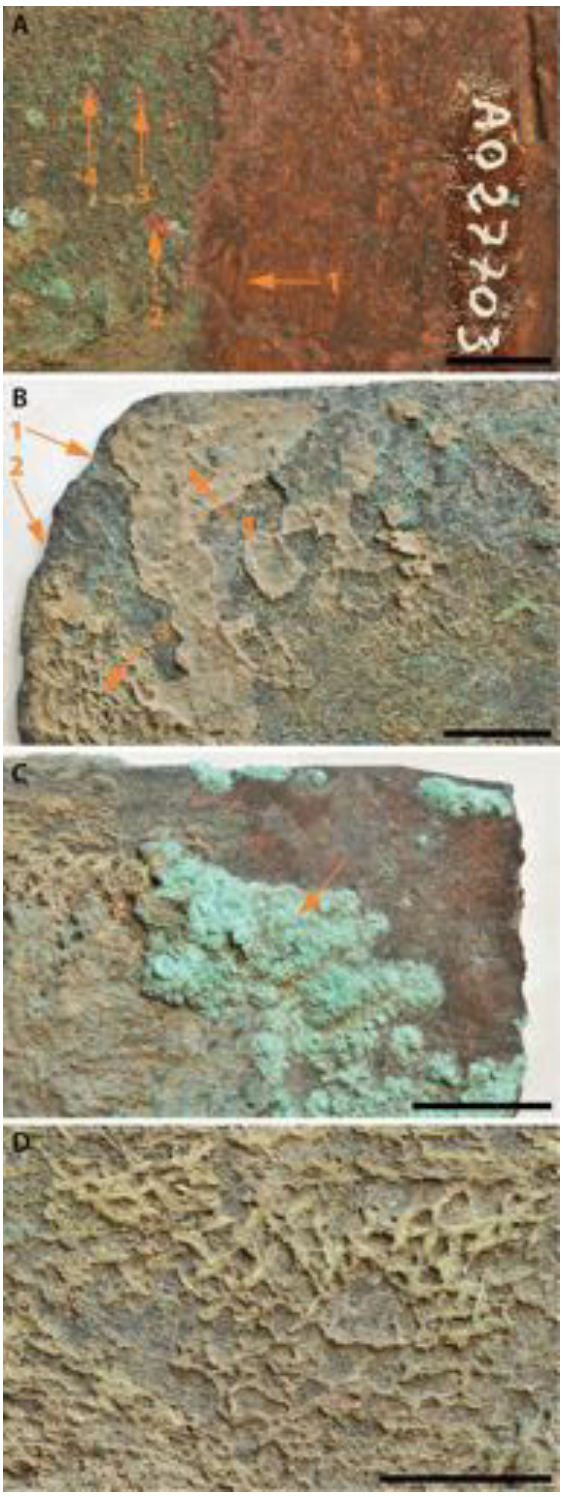

Figure 5.8: Visual observation of the axe blade AO 27703. A, Parallel strip-shaped traces in orange-brown (on the right) and trace of an internal reddish layer (on the left). B, The arc-shaped sunken parts on the contour and grey-beige encrustation forming relatively flat and cross-shaped zones. C, External green minerals. D, Very fragile and mineralized textile remains showing beige-brown-grey colour. Scale bars: 1 cm.

fibre reveal some features in common with data from the reference flax fibre (Fig. 5.2 and Table 5.2). The O–H stretch region shows almost no signal. In the fingerprint region below 1200 cm^{-1}, the absorption bands appear to be broader and lower in intensity, with a large signal background. In µCT, fibres appear less attenuated in average than soil minerals, yet with considerable variability attributed to chemical contrasts. Fibres close to the outer limits of yarns have a significantly greater attenuation than those in the middle of the yarns (e.g., orange broken line, Fig. 5.9G1). For instance, the cross section of a selected fibre (orange circle, Fig. 5.9F1) displays a very low-absorbing centre (arrow 2) together with a contrasting high attenuation periphery (arrow 1), while the cross section of another fibre appears more homogeneous, made of the relatively higher attenuation zone but without a low-absorbing centre with the spatial resolution attained in µCT (Fig. 5.9G2). In Chapter 4, a fragment of the metallic vase substrate without mineralized textiles on its surface (AO 14506-1b) is briefly described, which gives an overview of its chemical composition and stratigraphy [197]. The substrate is composed of quasi pure copper and is corroded to its core without remaining metallic copper. As, Pb and Ag are detected as main impurities. From the outer surfaces to the core, the corrosion structure consists of external green copper deposits – Cl-containing copper hydroxide (atacamite), copper silicates and, a small amount of copper carbonate – and internal copper (I) oxide and copper chloride. The original shape of the artefact could be identified from the observation of clearly identifiable original surfaces (i.e. lines delineating the limits of the original artefact) [197].

Foundation pegs AO 76 and AO 77

The foundation peg AO 77 (Fig. 3.4E) is almost entirely covered with mineralized textile remains. The heavily transformed textile remains are now stiff and fragile. They show green and beige exterior colour (arrows 2 and 1, respectively, Fig. 5.10A). The weave used is a simple plain tabby (ca. 20 yarns per centimetre). S/2Z-twist (arrow 1,

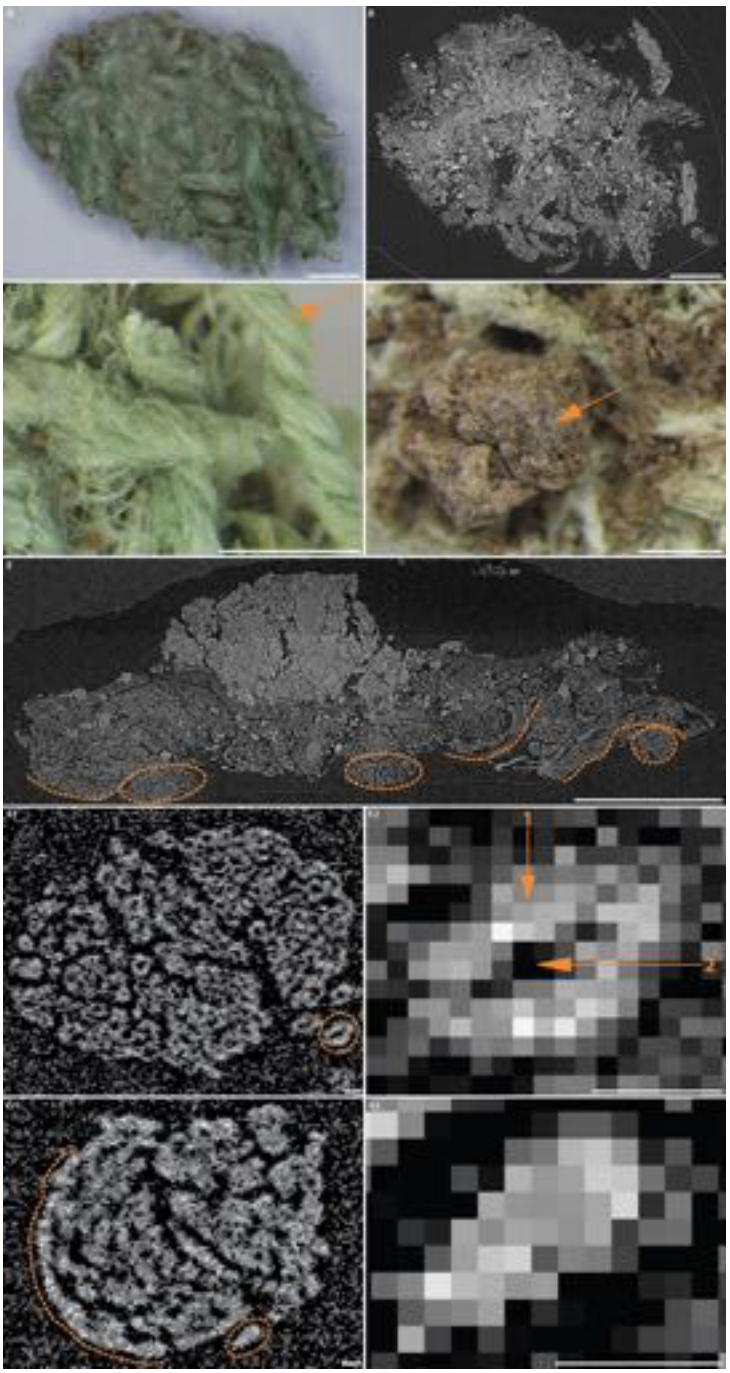

Figure 5.9: Microscopic investigation and µCT imaging of textile fragment AO 14506-3. A, Digital microscopy reconstruction of the sample surface. B, Reconstructed tomographic slice of the sample in an inner plane oriented as in A. C, Yarns in S-twist in green colour. D, Grey-beige compounds from soil attached to the surface of yarns. E, Reconstructed tomographic slice of the sample in a perpendicular plane to B. Scale bars in A–E: 1 mm. F1 and F2, "Hollow" fibres showing variation in grey levels with F2 a close-up of the fibre highlighted by the orange circle in F1. G1 and G2, "Infilled" fibres showing variation in grey levels with G2 a close-up of the fibre highlighted by the orange circle in G1. All the reconstructed tomographic slices are in adjusted in same brightness and contrast. Scale bars in F1–G2: 15 µm.

Fig. 5.10B) and Z-twist (arrow 2) yarns are both observed (Fig. 5.10E). The average diameter of individual yarn is ca. 300–500 µm. Yarns have an overall vitreous glossy appearance. Light microscopy examination of fibres cross-sections shows the characteristic features of flax fibres (polygonal shape, see discussion in Thomas et al., 2015 [73]). The diameter of the fibres is of about 15 µm (arrows, Fig. 5.10C). Mineralized textile remains covering the surface of foundation peg AO 76 show striking similarities (colour, fragility, average diameter of yarn and fibre, weaving, etc.) to those at the surface of AO 77 [37]. Nevertheless, the twisting of yarns attached to AO 76 is S/2Z in both directions (x and y). Under the textile, filamentous structures are visible in the dark green areas of the corroded pegs. These unidentified "filaments" form a regular pattern of parallel lines (diam.: 100–150 µm) and appear thicker on the arms or on the feet of the figure (arrows in Fig. 5.10D). The metal substrate is covered with external green mineral deposits on a locally visible red-brown layer (Fig. 5.10A and D). The analysis of the metal core of artefact AO 76 was performed by ICP-AES [280, 199]. The data identifies almost pure copper (≈98%wt) with As, Ni and S as minor elements (1.0, 0.5 and 0.7%wt, respectively).

5.4 Conclusion

The physico-chemical studies on mineralized fibres from three archaeological sites show an exceptional preservation of these precious material record for ancient civilizations. The combination of synchrotron-based 3D imaging techniques and conventional 2D approaches employed in this work revealed as promising methodology of investigation of ancient mineralized fibres in close contact to corroded copper-base artefacts.

Figure 5.10: Textile remains on foundation peg AO 77. A, Top of the foundation peg showing textile remains in green and beige. Scale bar: 1 cm. B, Microscopy observation of textiles located at the bottom of the beard of the man represented on the foundation peg. Scale bar: 1 mm. C, Cross sectional view of fibres in microsocpy. Scale bar: 10 µm. D, "Filaments" on the right arm of the man. Scale bar: 1 cm. (A–D are reused from A. Thomas et al., 2015 [73].) E, Twisting modes of fibres (adapted from C. Breniquet 2008 [26]).

Table 5.2: Attribution of absorption features in mineralized fibres and reference flax fibre, using data in Refs [1, 66, 276, 277, 68, 278].

Band position of reference flax fibre cm^{-1}	**Band position of fibre from Gonur 2380-1 cm^{-1}**	**Band position of fibre from NS 95015002 cm^{-1}**	**Band position of fibre from AO 14506-3 cm^{-1}**	**Assignment**
3400–3300	3339, 3284	3340, 3306	3300–3400	O–H stretching
2902	2896, 2870	2910, 2860	2896, 2860	CH and C–$H_{2/3}$ stretching
1730	–	–	–	unconjugated C=O stretching (hemicellulose)
1625	1615	1615	1615	H–O–H bending
–	1541	1541	1541	CO_3^{2-} asymmetric stretching
–	1523	1520	1520	CO_3^{2-} asymmetric stretching
1453	1456	1457	1458	C–H, CH_2 and C–OH bending, C=C stretching, CO_3^{2-} asymmetric stretching
1429	1420	1420	1424	CH_2 and O–C–H in-plane bending, CO_3^{2-} asymmetric stretching
1371	1371	1374	1368	C–H in-plane bending
1336	1336	1336	1336	O–H and C–H wagging
1317	1315	1317	1315	O–H and C–H wagging
1280	1285	1280	1280	C–O stretching, C–H and O–H wagging
1230	1226	1223	–	C–O stretching, C–H and O–H wagging
1200	1198	1200	1200	C–O–C symmetric stretching, C–H and O–H wagging
1161	1162	1165	1161	C–O–C asymmetric stretching
1109	1109	1112	1109	C–O–C asymmetric stretching and C–C stretching
1080	1085	1085	1085	C–O stretching
1058	1058	1059	1050	C–O stretching
1035	1030	1035	1035	C–O and C–OH stretching and bending, C–C stretching, aromatic C–H bending
1008	1000	1004	1006	C–O stretching
989	983	983	975	C–O stretching
897	900	900	900	CH_2 rocking

6

Discussion on the preservation of mineralized flax textiles

This chapter discusses the data acquired on the artefacts and samples in Chapter 5, which allow them to be presented in their socio-historical context and to study the exceptional preservation of organic remnants in the fibres. The relationship between substrate corrosion and mineralization is further interrogated. Additional insight on the relationship between local taphonomy and the local environmental information is provided for the three archaeological sites.

Contents

6.1 Socio-historical contexts

The use of flax may date back to the Upper Palaeolithic dated to 30,000 BC from excavation of several clay deposits [16]. The commonly cultivated flax used for textile production (*Linum usitatissimum*) is an annual plant [281]. Flax fibres are extracted from the wood core (i.e. bast) of the flax stem, which is surrounded by the stem of flax [62]. Flax fibres are strong and soft but show low elasticity, which make them particularly suited for fabric production [282]. As precious material record, the exceptionally preserved archaeological textile remains studied in this work provide insight into the corresponding cultural and social as well as economic contexts.

Textile fragments belonging to artefact Gonur 2380 (current Turkmenistan) are composed of flax fibres based on chemical dyeing examination [184]. Their origin is a question worth thinking about. As a main archaeological site in Turkmenistan of an enormous size, Gonur-Depe has yielded various artefacts from ceramics to metals. Other than those collected from the grave 2380, any contemporary analogous textile fragment in similar weaving mode (or even any evidence such as textile impression) was previously found in this region. It is not unrealistic that these textile fragments were of local manufacture. The development of textile production and twisting or weaving techniques there may be promoted from the ancient East Mediterranean and North Mesopotamian civilizations because of the outpost geographic position of Gonur-Depe. Although there is no discovery or evidence of ancient loom, many spindle whorls made by clay or stone have been found over the site [184]. Since some imported Egyptian-style artefacts have been excavated in Margush sites, in particular in Gonur-Depe, and ancient Egyptians heavily used flax fibres for weaving from pre-Dynastic period, an Egyptian import may also be purposed. However, due to cultural reason, S-spinning was the most commonly adopted mode for yarns and not limited to the use of flax fibres for Egyptian textiles [74]. Another origin of these textile fragments could be related to a possible importation from the

archaeological site Susa (current Iran). As the closest archaeological relative to Gonur-Depe site, Susa is an important center of Ancient Near East located at the Eastern border of ancient Mesopotamia and has already yielded archaeological textile remains in similar spinning mode dated to the 4th mill. BC [119]. Textile remains of artefact Gonur 2380 are considered to have originally wrapped the small corroded copper ladder (Fig. 3.2C) [184]. Since the type of object like ladder has a meaning of high social status [187], the use of textiles wrapping metallic artefact before buried underground may evoke the rites related to the burial practice of the deceased.

In the Indus valley, cotton fibres were the most commonly used during the 3rd ro 2nd mill. BC, but fibres from wool and plants (possibly jute or hemp) were also existed [43]. Discovery of flax in the form of carbonized seeds was already demonstrated in Nausharo [42, 283] although the presence of flax fibre remains from this site has never been reported before. Since the original form of artefact NS 95015002 (current Pakistan) is unknown, it is difficult to determine the purpose related to the use of textile on the object. According to the textile impression found on the interior of numerous faience vessels excavated at Harappa, Vats has reported the use of textiles during the practice of making faience bottles [58]. However, as textile remains are present at both sides of NS 95015002, it is very likely that these textiles were used as wrapping material.

In ancient Mesopotamia, the major production of textiles is thought to come from wool [26]. However, the significant amount of archaeological mineralized flax textile excavated suggests that the use of flax from local textile production must also have been common. Originating from vegetable and non-animal source, flax fibres might be considered as synonym of purity and were used for the highly symbolic artefacts such as foundation pegs [73]. However, the role of textiles preserved on artefacts from Tello (current Iraq) is another question still in doubt [37, 73]. For artefact AO 77, as nudity is synonymous with weakness in Mesopotamia, the divine and royal statues might be dressed according to archaeological text records [284, 285]. Textiles can be in such case

regarded as 'cloth' of artefacts for a decorative purpose similar to the presence of pearls in burial [286]. The fine shape of lumen of fibres on AO 77 indicate the high quality of flax (Fig. 5.10C) and the fineness of yarns can imply a well controlled processing steps of raw plant fibres (retting, scutching, combing) [73]. In addition, the textiles fit well the shape of artefact without deformation, which suggests that their production was of sufficient good quality or at least fibres were very flexible to match the shape of artefact. The flexibility of textiles could also be related to a probable application of liquid products. In some cases, use of a product applied to the reverse of textiles laid on the surface of copper-base artefact might help metal preservation, as nowadays metals including weapons are wrapped by greased fabric [73, 287]. The filament-like structures on AO 77 (Fig. 5.10D) can be remains of another organic material either from cellulosic textiles or animal origin such as leather, which were applied independently on artefact before textiles of flax fibres. In this case, hypothesis of the use of two separate textile layers might be purposed [37, 73]. These filaments can also be traces of a coating material or a fragrance oil intentionally used to the textiles [288] or to artefact itself [289]. For example, Neo-Babylonian rulers enjoined their successors to respect and anoint the burial deposits such as foundation pegs they would find. It suggests that this practice may have been in use in earlier times during Neo-Sumerian period [290]. The head and the peg carry more textile remains while there is very few textiles on the front of thighs and the back of peg, which might be explained by the difficult access to these parts for dressing. Nevertheless, this can support the hypothesis of simple wrapping or containing purpose of textiles to protect the precious artefacts (vase, tools, weapons etc.) [291, 292, 77] like cases of artefacts AO 14506 and AO 27703.

Based on what has been discussed above, the two main uses of textiles on artefacts in ancient times contributed to clothing and container, either for decorative or protective purposes. It also underlines the importance of possible economical trade between Mesopotamia and Egypt as a full part of a large historical and political context.

6.2 Exceptional preservation of organic compounds

An important result obtained on mineralized fibres from all three archaeological sites is the preservation of organic compounds, even in the most altered case of Tello. µCT data shows low-density areas within individual flax fibres from Nausharo and Tello. This suggests the presence of low-attenuating organic compounds within the mineralized fibres for all three samples. However, it is difficult to decorrelate µCT data from the lumen from those of the flax cell walls, as well as those from the flax cell walls from those of the encasing matrix, because the characteristics of interest are in the spatial range 2–3 µm, which is in the order of magnitude of our voxel size.

Achaeological Fibres from Gonur-Depe have a similar colour to modern fibres and a remarkably preserved flexibility, whereas the beige fibres from Nausharo have a moderate flexibility and fibres from Tello appear of a green colour and show almost no flexibility. The fibres in these three cases show an increase in the degree of mineralization.

The absorption bands in the FT-IR spectrum of the reference flax fibre are identified from the bibliographic data (Fig. 5.2 and Refs. [1, 66, 276, 277, 68, 278]). O–H and C–H stretching of the cellulose molecule is observed in the high wavenumber region (3400–2850 cm^{-1}). The two bands in the region of 1750–1600 cm^{-1} correspond to C=C stretching of hemicellulose and H–O–H bending of the absorbed water. The bands in the fingerprint region below 1500 cm^{-1} are mainly attributed to C–O and C–O–C stretching of cellulose molecule. The lignin in flax fibre has bands at 1592 cm^{-1} and 1506 cm^{-1} associated with C=C stretching in the aromatic rings. These bands are not observed in the FT-IR spectra of reference and mineralized fibres. It is possible that due to the relative thin thickness of the cross sections of fibres, the amount of lignin (vibrators) may be insufficient to be detected.

Between the reference flax fibre and the sample from Gonur-Depe, the main differences are as follows: (1) appearance of two additional bands in the O–H region (3400–

3300 cm^{-1}) and four bands in the 1540–1420 cm^{-1} region. The bands at 3339 cm^{-1} and 3284 cm^{-1} could result from the formation of new bonds with malachite after degradation of the cellulose molecules, as reported in the work of H. L. Chen et al [1, 139]. This result is consistent with the four fine bands (ca. 1540, 1523, 1456 and 1420 cm^{-1}) attributed to CO_3^{2-} vibration, which indicate the very probable presence of malachite also identified in corroded copper substrates. These mineral bands are present in all archaeological spectra, (2) an increase in the intensity of the complex broad band extending from 1700 to 1550 cm^{-1} at ca. 1615 cm^{-1} which shows the vibration of the absorbed (bound) water [276]. Water is a good solvent for cellulose, hemicellulose and lignin contributing to the formation of energetically favourable intermolecular hydrogen bonds, its absorption into the fibres could cause them to swell. Water absorption is strongly controlled by the crystallinity of the polymers. Amorphous areas of cellulose can trap more water molecules and swell more easily than crystalline ones [293]. The increase in the band intensity indicates that the amorphous areas are more important in mineralized fibres than in modern fibre. The shift of this band in mineralized fibres to energies lower than the reference fibre could be explained by oxidation processes involving the appearance of new functional groups with C=O bond [294].

Between the samples from Gonur-Depe and from Nausharo, the main differences are: (1) a significant decrease in intensity of the band at 1165 cm^{-1} related to the C–O–C stretching without major shift at 4 cm^{-1} resolution. Such a decrease in peak intensity could result from the hydrolysis of cellulose molecules [85] as shown in the equation 6.1 (R1 and R2 represent monomer units of α-D-glucose), resulting in a decrease in the C–O–C bonds of cellulose molecules and a more degraded state of fibres from Nausharo,

$$R_1{-}C{-}O{-}C{-}R_2 + H_2O \rightleftharpoons R_1{-}C{-}OH + R_2{-}C{-}OH \tag{6.1}$$

(2) a significant increase in band intensity at ca. 1615 cm^{-1}. This could be due to both

the less crystalline (more disordered) and more oxidized state of the celluose within fibres from Nausharo.

Between the samples from Nausharo and from Tello, the main differences are: (1) a remarkable decrease in band intensity in the O–H region (3400–3300 cm^{-1}) with almost no signal. Cellulose can ionize and provide cellulosate anions (equation 2.1 in Subsection 2.3.2 in Chapter 2) [148] during hydrolytic degradation. Cellulosate can react with copper ions induced during the corrosion processes to form new chemical bonds (relation 2.2 in Subsection 2.3.2 in Chapter 2) [6], leading to the disappearance of O–H bands in the high wavenumber region and inducing a more mineralized state of fibres from Tello, (2) a significant decrease in intensity of the band at ca. 1615 cm^{-1}. This observation is in agreement with the low amount of water present in fibres from Tello, which could be explained by the extreme stiffness of the polymeric matrix of the fibres due to mineralization that prevents their swelling. As the mineralization states of fibres from Tello is the most advanced among the corpus studied within this work, the higher amount of inorganic ions present in / around fibres from Tello could combine with the hydroxyl and carboxyl groups of cellulose, resulting in a decrease in the available groups to form hydrogen bonds with water. (3) a very significant broadening of the bands in the fingerprint region (1200–900 cm^{-1}). The hydrolytic degradation of the fibres mentioned above causes the polysaccharidic chains to break [86], leading to a decrease of the steric constraints within the supramolecular packing of the cellulose molecule. This result could facilitate oxidation of the hydroxyl groups into aldehyde, carboxylic acid or carbonyl groups [70]. The possible presence of these groups can thus generate a broadening of the bands in this low wavenumber region. The broadening could also be attributed to the possible presence of inorganic materials in fibres from Tello, such as silicate species, whose main bands are shown in this region due to the valence vibrations of Si–O at ca. 1020 cm^{-1} [183].

Increasing alteration is observed from the modern flax fibre to the samples from

Gonur-Depe, Nausharo and Tello, that may tentatively provide a clearer idea of the mineralization process.

The FT-IR spectra of mineralized fibres consistently show infrared absorption features encountered in reference cellulosic fibres. Nevertheless, it does not imply, *stricto sensu*, that cellulose molecules are completely preserved. Hydrolytic degradation and oxidation of cellulose molecules can cause the breakage of glycosidic bonds, leading to the formation of cellobioase (a disaccharide $C_{12}H_{22}O_{11}$) [85] and oxycellulose [88, 89], respectively. The functional groups detected in mineralized fibres may come from these fraction of cellulose. The identification of cellulose-like organic remnants in mineralized fibres indicates that a favourable context (i.e. contact with a metal artefact in a burial environment) can explain the exceptional preservation of the materials. This peculiar context can also contribute to the preservation of proteinaceous fibres (e.g. hair, wool, silk, etc.) [137, 126, 141].

6.3 Mineralization and corrosion

The particularities of these remarkably preserved textiles are linked to the presence of copper substrate and burial contexts. Thus, the phenomenon of mineralization involves the consideration of the global system "copper metal–textile fibre–archaeological environment".

Burial environment plays an important role in providing the necessary aerobic (oxygen) and moist (water) conditions for copper corrosion and fibre mineralization. For sample Gonur 2380-1 excavated from Gonur-Depe, the soils contained sand and clay [186]. Based on soil deposits identified on corroded metals (µCT and EDS data) from Nausharo and Tello, the significant presence of Si and Al as well as a small amount of other elements detected (such as Ca and K), indicate an overall burial context consisting of sandy silty soils and clay. These results are consistent with the information that all artefacts

were initially deposited in a relatively closed environment that could later have been filled by the soils [197, 165]. These soils, whose pH is often close to neutral, are generally classified as slightly or moderately aggressive media if their content of anionic species (chloride and sulphate) is low. Typical cases of archaeological soil investigation in this region was recently reported by O. Oudbashi 2018 based on soil analysis carried out at two Mesopotamian archaeological sites [245]. A major difference is found when comparing corroded artefacts from the two sites in Nausharo and Tello. A higher content of Cl-containing species is detected in Nausharo samples. The site of Nausharo therefore corresponds to a more saline environment and also more aggressive context for metal objects than the site of Tello. In fact, even if it remains difficult to precisely define the initial archaeological contexts, information revealed by metal corrosion can provide important additional information.

Previous analyses reported for the metal core of the four artefacts from Tello (AO 27703, AO 14506, AO 77 and AO 76) indicate that they are composed of an almot pure copper (≈98–100%wt). As, Pb, Sn, Ag, Sb, Fe and Ni are present as minor elements [295]. µCT analysis of fragment of artefact from Nausharo showed that the substrate is also composed of quasi pure copper and is corroded to its core without remaining metallic copper [197]. As is detected as main impurity. It has been demonstrated for artefacts from Nausharo and Tello that the copper substrate has a similar corrosion morphology marked by a multi-layer structure including [197]: (1) soil deposits, (2) a green outer layer consisting mainly of copper hydroxyl species (atacamite $Cu_2(OH)_3Cl$ and a small amount of malachite $Cu_2(OH)_2CO_3$) and silicate containing species, (3) a brown-reddish copper oxide (Cu_2O) which replaces the complete original metal volume. This characteristic corresponds well to the corrosion structure found on ancient copper artefacts [166, 296, 176]. In addition, it should be noted that although the external deposits of green copper have some roughness, the corrosion morphology is relatively uniform and shows very few localized attacks. This must be attributed to

moderate aggressive environments relatively homogeneous over time, unlike the typical case of ancient copper subjected to seasonal fluctuations under aggressive and corrosive conditions [174, 175]. As these are unalloyed copper artefacts, the impact of alloying elements such as tin in bronze should not be considered. It should also be noted that the corrosion behaviour of bronze is mainly related to a decuprification process inducing preferential dissolution of copper [164, 165]. Thus, for ancient copper-base alloys, the corrosion process (deposition and soil dissolution) involved in textile mineralization should be considered similarly to those found for copper objects.

Characterization performed on samples from Nausharo and Tello (NS 95015002-2 and AO 14506-1b, respectively) shows that the original surfaces of the metal artefacts are preserved, even if both copper plates are completely corroded [197]. For sample NS 95015002-2, an internal enrichment marked with Cl is identified. Thus, even if the textiles had been preserved, the corrosion deposits were not sufficiently protective over time to block the corrosion process until the metal was completely oxidized. Considering the corrosion of bronze as reference, this case of sample NS 95015002-2 corresponds to an intermediate state between *Type I* corrosion (with preservation of the original surfaces) and *Type II* corrosion (with internal chloride enrichment) [165, 164]. In addition, the calculated ratio between the amount of initial copper and the amount of copper remaining in the corroded artefacts is close to 100% for these two samples, suggesting that a very small amount of copper has been dissolved in the surrounding environment or in mineralized fibres. These results are in accordance with a likely low humidity ("atmospheric") initial context in which the textiles on the metal artefact were placed. This could mean that all artefacts were initially deposited in a relatively closed environment before being buried by the silty soils [197, 165]. These results also suggest that the corrosion of copper in contact with textile fibres occurred without significant dissolution and leaching of copper ions in the soil. Some specific corrosion characteristics of the substrate should also be highlighted, which could take into account the exceptional preservation

of textiles depending on the archaeological contexts and corrosive environments. For artefact AO 27703 from Tello, grey-beige encrustation related to soil sediments forming cross-shaped zone is observed. This can be attributed to the fact that the yarns are no longer present (arrows 3, Fig. 5.8B) and only earthy materials are observed as usually found on buried archaeological artefacts [165]. In addition, the earthy encrustation is very uniform and compact on the flat areas (arrows 4), which corresponds well to the homogeneous burial conditions of this artefact.

Based on data obtained (µCT, FT-IR, SEM-EDS/EBSD) of samples from Nausharo and Tello (NS 95015002-2, NS 95015002-6-1 and AO 14506-3), similar mineralization cases are identified. The internal zone at very low attenuation (arrow 2, Fig. 5.9F2; arrow 1, Fig. 5.5C) should be attributed to the 'hollow' lumen of fibres. The external zone showing higher attenuation (arrow 1, Fig. 5.9F2; arrow 2, Fig. 5.5C) corresponds to preserved organic remnants and substituted inorganic compounds as described in studies of H.L. Chen [1, 139, 6] and C. Moulhérat [3]. 'Filled' lumen is also observed that may suggest infilling of inorganic compounds. These results are consistent with SEM-BSE (arrows 1–4, Fig. 5.6D; Fig. 5.5E) and photoluminescence imaging (zones 1 and 2, Fig. 5.7C). The glossy appearance of fibres should be resulted from the presence of mineral encrustation (Fig. 5.3B and Fig. 5.9C). The EDS analysis showed that Cu, Si and O are the main chemical elements present in the fibres of the sample NS 95015002-2. Cu / Si atomic ratios range from ca. 1 to 1.4, indicating the formation of copper silicates (e.g. dioptase $CuSiO_2(OH)_2$). The identification of the precise chemical composition of the phases present in mineralized fibres requires further study using higher resolution techniques.

As a result of the movement of soil water that has served as a transport medium and has a high chemical content of organic compounds, Si-containing anions have penetrated into the fibres and combined with Cu cations potentially to form hydrated or hydroxy copper silicates. Such behaviour has been observed in the outermost layer of

bronze patina [165, 164], although no precise identification of Si-Cu-O compounds is achieved mainly due to their amorphous nature. However, the action of natural silicic acid (H_4SiO_4) or other species such as dissolved silica orthosilicate anions ($Si(OH)_3O^-$) could play a major role over time. It could reasonably be assumed that these species can form polymeric silicic acid of complex structure in the presence of copper cations. Thus, the mechanism of formation of these compounds could be considered as a sol-gel process that remains to be clarified. A typical example is the cross-section of sample NS 95015002-2 shown in Fig. 5.5D–G, in which fibres containing mainly Cu-Si-O elements as mentioned above, are enclosed by encrustation consisting mainly of copper silicates and copper hydroxychloride (atacamite here). Atacamite is located on the outer part of the encrustation and does not fill the fibres. It should be noted that the similar Cu/Si ratios are identified in mineralized fibres and the external encrustation. Thus, it appears that different stages occured during the mineralization processes of fibres, including a first step related to the precipitation (polymerization) of cupric silicate species, followed in a second step by the formation of copper hydroxychloride. This appears related to a sequential influence on archaeological burial conditions rather than a different chemical affinity between the organic molecules in fibres and soil anions, since hydroxychloride-mineralized fibres are also observed as described in R. D. Gillard et al., 1994 [137] in mineralized wool fibres. However, in mineralized cellulosic fibres, malachite is usually found as substituted compound [1, 137]. Thus here this could be appropriate for a possible confined initial environment (ex. sandy soil) of these artefacts followed by a progressive contact with the beloved slit to an evolution of the archaeological context over time. For the other mineralized fibres of sample Gonur 2380-1, which were not in direct contact with copper metal, the green minerals present (arrows, Fig. 5.1B) might also be attributed to copper silicates based on EDS data. Here, the mineralization is observed because the textile fibres were found very close to the copper ladder (Fig. 3.2C). Thus, even in this case, the role of copper ion leaching in the archaeological environment

remains a fundamental parameter for fibre mineralization.

The hypothesis of mineralization mechanisms can be briefly constructed as follows [1, 139, 6, 3]: (1) the copper-based metal oxidizes in a moist environment and produces copper ions, (2) at the same time, the degradation of the fibres continues leading to the opening of the fibres structure, (3) the copper ions (Cu^{2+}) diffuse into moistened fibres and combine with other local anions of the environmental contexts forming stable compounds (e. g. $Si-O^-$ species); the copper ions also agglomerate on fibre surfaces to generate a mineral incrustation consisting mainly of hydroxylated species. The preservation of fibres depends not only on the rate of fibres degradation but also on the rate of copper corrosion. The mechanisms can show a slight micro-scale differences depending on the variability of the state of fibres mineralization. If fibres degradation occurs faster than copper corrosion, the original chemical composition of the fibres will not be preserved, resulting in negative mineralization with fibres imprints [129, 137]. On the contrary, the case of positive mineralization indicates a slower rate of fibres degradation than copper corrosion [1]. Cases of superficial and partial mineralization of the fibres are also observed [3], suggesting a balance between the rate of fibres degradation and copper corrosion.

6.4 Conclusion

Fibres were used as decorative (clothing) or protective (wrapping material) purposes in ancient times. The preservation of organic compounds even in very mineralized fibres is confirmed and variability of mineralization states of fibres is observed. The chemical composition of mineralized fibres and their mineral encrustation allow to propose potential steps in terms of mineralization mechanisms and compare the burial contexts among three sites. These results lead to stress the focus on mineralized fibres to obtain a better understanding of their preservation, which will be helpful to explore the textile

manufacturing and corresponding techniques in antiquity. Further studies at higher resolution are required to analyze fibres degradation and, differences among mineralization states potentially caused by variability of micro-environment and of corrosion processes.

Conclusion and perspectives

Artefacts studied in this PhD were excavated from three main archaeological sites, Tello (current Iraq), Nausharo (current Pakistan) and Gonur-Depe (Turkmenistan). Archaeological textiles have been dated to ca. 3000-1800 BC and were found in direct or very close contact with corroded copper-base artefacts. Textiles exhibit different colours and flexibilities that reflect distinct preservation states. Their exceptional preservation over millennia is linked to the presence of metal artefacts, as the so-called "mineralization" phenomenon. Mineralized textiles provide important additional resource with respect to the study of archaeological textiles, which rarely survive in burial contexts due to their organic nature. Analysis of ancient textiles help to understand not only the development of textile manufacturing in early history, but also the role of textiles in burial practices as clothing or container. The main objectives of this thesis consist of:

- developing a methodology including synchrotron-based imaging techniques and complementary traditional approaches at multi spatial resolution,
- verifying organic remnants and inorganic ions present in mineralized fibres,
- studying corrosion products of copper attached to, or in the vicinity of mineralized textiles,
- proposing hypothesis about mineralization mechanisms of mineralized textiles re-

lated to copper corrosion processes,

- exploring environmental information as influencing factors involved in mineralization and corrosion processes.

The micro-structures of mineralized textiles are revealed by µCT and SEM imaging. In cross-sectional view, fibres from Nausharo with opened and closed lumen are both observed. Inorganic compounds mainly originating from copper corrosion not only cover the outside surfaces of fibres as mineral encrustation, but also penetrate fibres as substitution. These observations are consistent with those shown in longitudinal view of fibres. The heterogeneity of chemical composition is indicated by photoluminescence imaging, suggesting a presence of organic compounds in fibres and inorganic compounds on the periphery of fibres. EDS analysis confirm that the mineral encrustation of fibres mainly consist of Cu, O and Si while mineral infilling in fibres contain Cu, O and Cl. Based on atomic ratios, the potential compounds are dioptase ($CuSiO_2(OH)_2$) and atacamite ($Cu_2(OH)_3Cl$), respectively. Fibres from Tello show similar outside mineral encrustation and internal infiltration. However, only a very small amount of inorganic compounds containing Cu, O and Si is detected at surface of fibres from Gonur-Depe. According to FT-IR results, the preservation of organic remnants showing typical cellulosic absorption features is found in fibres from all the three archaeological sites through comparison with reference modern flax fibres.

The corrosion layers identified are very comparable in corroded copper-base samples from Tello and Nausharo based on results obtained from µCT coupled with ED-XRD, SEM-EDS/EBSD, Raman and FT-IR spectroscopy as well as XAS spectra. In addition to observing internal 3D structure of sample without any sample preparation, the semi-quantitative µCT provides great potential related to phases identification. According to analysis of a purpose-made metal standard, a calibration curve between grey levels in CT images and corresponding theoretical linear attenuation coefficients (μ_{Th})

of metals is established. This curve allows comparing calculated experimental linear attenuation coefficients (μ_{Exp}) of phases present in samples with their μ_{Th}, leading to attribution of each phase without damaging the form of samples. A relative thick layer of cuprite (Cu_2O) locates at the core of samples. External corrosion layers contain copper silicates (e.g. chrysocolla $Cu_{1.75}Al_{0.25}H_{1.75}(Si_2O_5)(OH)_4 \cdot 0.25\,(H_2O)$ and dioptase), atacamite and a small amount of malachite ($Cu_2(OH)_2CO_3$). A layer of nantokite (CuCl) is clearly present in samples from Nausharo. Some impurities of Pb and Ag particles are detected in a sample from Tello. However, the presence of nantokite is not demonstrated in the real cross-section of sample from Nausharo through Raman and FT-IR analysis, a possible reason is that this compound is unstable and converted rapidly to atacamite when contact humid atmosphere. This point shows a significant advantage of µCT as in-situ technique to ensure presence of unstable compounds inside samples. Other than corrosion features commonly encountered in corroded copper-base samples such as holes in various size, the original surfaces are observed both in samples from two sites but the structure of those in samples from Nausharo reveal more irregular, suggesting a probable *Type II* corrosion mechanism of samples from Nausharo and *Type I* of sample from Tello.

Based on morphological observation and chemical composition, textile from Tello, Nausharo and Gonur-Depe show decreasing mineralization degrees. Fibres from Tello display very mineralized degree, from which distinct mineralization states are distinguished mainly including partial mineralization, i.e. a co-existence of original organic remnants in fibres and minerals in the interior and exterior of fibres. Similar mineralization states are identified in textiles from Nausharo that show a moderately mineralized degree. Fibres from Gonur-Depe exhibit a less mineralized degree and a possible superficial mineralization state, in which organic compounds are relatively well preserved in fibres and minerals attached to fibres surfaces are detected as minor compounds. These differences could be due to the distance between textiles and corrosion products of copper, as textiles from Tello and Nausharo covered metal artefacts while textiles from

Gonur-Depe studied in this thesis were not in direct contact with the metal artefact. The mineralization state depends on rates of fibres degradation and copper corrosion. If fibres degrade rapidly than copper corrosion, organic compounds would not be preserved; in contrast, the chemical composition of fibres can be partially or even completely preserved. In an aerobic and humid burial context, as fibres are hydroscopic material, ions from copper corrosion and soil can diffuse into fibres forming minerals as fibre degradation gives opened access in amorphous regions. In addition, ions can aggregate on surfaces of fibres forming mineral encrustation. The difference between minerals formed inside and outside of fibres might be linked to size of inorganic ions, that is, it is difficult to penetrate in fibres for bigger ions like Cl^- while small ions like Si^{4+} can have an easier access moving into fibres.

The identification of chemical composition of corrosion products and fibres leads to better understanding of environmental information of three archaeological sites. For example, the presence of Si as major element and Al as minor one is detected in all samples, implying the soil of three sites contain mostly sand and some clays. The nantokite layer identified in samples from Nausharo suggest a more saline environment there. The three archaeological sites display comparable features of typical burial context, from which the presence of oxygen and water are indispensable factors for fibres degradation and copper corrosion as well as transport media of ions.

This thesis opens several perspectives. The spatial resolution obtainable from the set of techniques used are limited to the micro-scale, preventing a precise confirmation of chemical composition of mineralized fibres. Techniques of higher resolution such as nano-IR and scanning transmission electron microscopy (STEM) will be expected to obtain clear spatial distribution of organic and inorganic compounds inside and outside of fibres, which ensure a better understanding of fibres degradation and pathway of growth of minerals in fibres and on fibres surfaces. The variability of mineralization states in the same sample is another issue worth investigating with respect to the relation with

variability of micro-environment surrounding sample.

Focus is given to flax-copper system in this work but the proposed methodology would be suitable for other systems also showing complicated heterogeneity, such as cotton-copper system. In addition, mineralization of non-cellulosic fibres like wool or silk due to the contact with iron-base artefacts deserves to be studied taking account to results of this thesis as reference.

A

Supplementary analytical methods

In this appendix, principles of several techniques in Chapter 3 and other supplementary analytical methods used are described.

Photoluminescence UV–Visible spectroscopy

Principle

Photoluminescence is the emission process of photons following the absorption by a compound of ultraviolet, visible or near infra-red radiation. The emission of photons is based on the existence of discrete electronic levels or continuous energy bands within the electronic structure of organic or inorganic compounds. The excitation process can be the result of absorption of a single photon (one-photon absorption) or several photons. For returning to a fundamental stable state, that is, to the minimal energy of the chemical phases, the excess energy can be dissipated radiately, by the emission of a photon of energy less than or equal to that of the incident photon.

The term photoluminescence includes two distinct phenomena, phosphorescence and fluorescence. The distinction is revealed in the nature of the electronic levels involved.

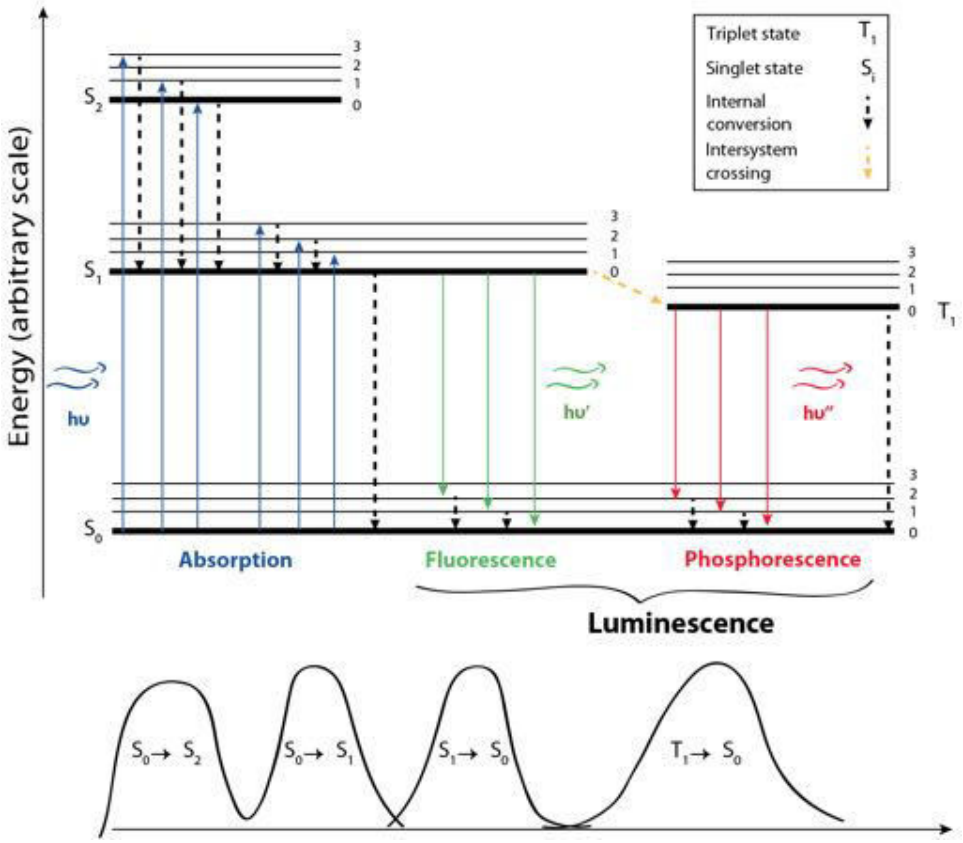

Figure A.1: Scheme of Perrin-Jablonski (modified from B. Valeur 2001 [297])

According to the scheme of Perrin-Jablonski (Figure A.1) [297], three stages are present during the photoluminescence process with different characteristic durations. Following the absorption of a photon, an electron of a stable ground state orbit (S_0) can be excited to an unoccupied orbital thus leading to an electronic state of higher energy (around 10^{-15}s). The electron is then in a vibrational level associated with a singlet electronic state (S_1). The transition of the electron to the lowest vibrational level of the first excited electronic state is by vibrational relaxation (around 10^{-12}s to 10^{-10}s). This transition results in energy loss of the electron without photon emission. During the de-excitation process, the electron can directly return to the ground state S_0 (fluorescence), or first to a vibrational level associated with this state T_1 before the subsequent decadence to S_0 (phosphorescence). Several possible energetic transitions, radiative or non-radiative during the process of de-excitation, are shown in the figure. The emitted light is related to the specific electronic transitions involved, therefore the luminescence spectrum may give chemical information on the detected samples.

Fourier-transform infrared spectroscopy (FT-IR)

Principle

IR is based on the interaction radiation-material during which energy is absorbed by a molecular, ionic or radical group. The energy of a molecule consists of a kinetic part of translation related to the temperature, and another part which represents the sum of several terms involving energies of different transitions:

- Rotation of molecule around an axis passing through the centre of inertia $\Delta E_r \sim 10^{-3}$ eV;
- Vibrations of atoms around their equilibrium position $\Delta E_v \sim 10^{-1}$ eV;
- Electron energy $\Delta E_e \sim 1$ eV.

According to the model of a harmonic oscillator, a molecule can be seen as a system consisting of two balls (atoms) of masses m_A and m_B linked by a spring (connection) with a spring constant k more or less high whose vibrations appear at determined frequencies ν. These vibration frequencies depend on the interatomic forces, the mass of the atoms as well as the lengths and the angles of connections. They are described by the following relation:

$$\sigma = \frac{1}{2\pi c}\sqrt{\frac{k}{\mu}} \tag{A.1}$$

with σ the wave number in cm^{-1} associated with the vibration frequency ν of the connection by $\sigma = \frac{\mu}{c}$, c is the speed of light in vacuum in $m{\cdot}s^{-1}$, k is the spring constant of the bond in $N{\cdot}m^{-1}$ and μ the reduced mass of the system equalling $\frac{m_A \cdot m_B}{m_A + m_B}$ in kg.

Dipole moment variations associated with link vibrations create a periodic electromagnetic field that absorbs electromagnetic radiation of the same frequency. Since the force constant of a given bond is independent of the nature of molecule, the characteristic frequencies make it possible to analyse the structure of the molecule. The group frequencies are classified as stretching or bending vibrations depending on whether the movement of atomic nucleus is related to the lengths or the binding angles. For example the modes of vibration of CH_2 molecule are shown in the Figure A.2 [298]. In addition, all other possible vibration of the molecule can be described as a superposition of these modes.

To describe the absorption of the sample at characteristic vibration frequencies, the following quantities are defined:

- The transmittance $T = \frac{I}{I_0}$ expressed in %;
- The absorbance $A = \log\frac{1}{T} = \log\frac{I_0}{I}$.

with I_0 and I the intensity (without unit) of the incident and transmitted beam,

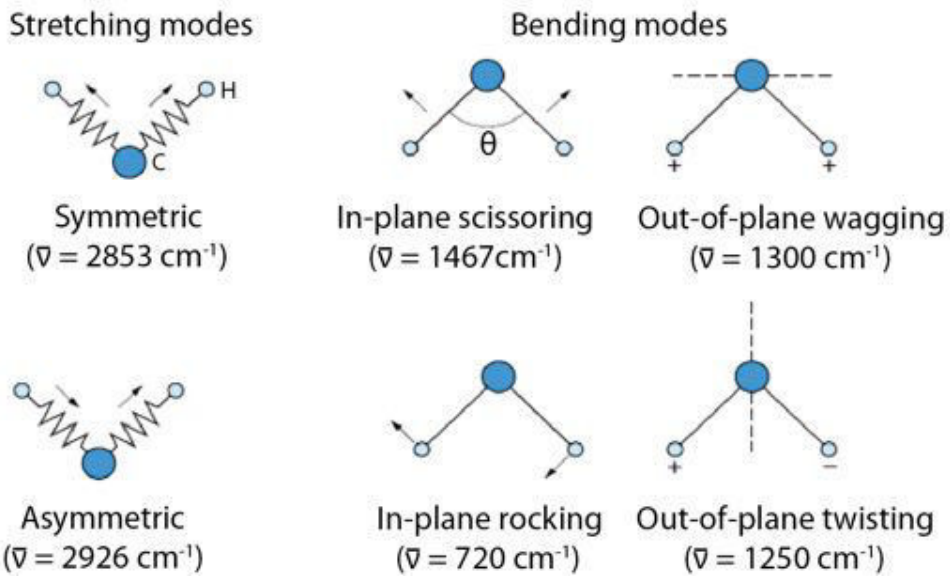

Figure A.2: Modes of vibration of CH_2 molecule (modified from M. Dalibart 2000 [298]).

respectively. Thus, the spectra obtained are represented by the transmittance or the absorbance of sample as a function of the wave numbers corresponding to the energies of IR range.

Contrary to IR spectroscopy which is dispersive, the principle of FT-IR is to generate an interferogram using a Michelson interferometer. The spectrum is obtained via its Fourier transform. The advantage of this technique is that it provides spectra with high resolution and accuracy in a short time with a good signal-to-noise ratio.

In practice, the IR electromagnetic radiation emitted by the source is divided into two beams F1 and F2 through a separating blade (Figure A.3). The beam F1 is reflected by a fixed mirror M1, and the beam F2 is reflected by a moving mirror M2. The combination of these two beams gives rise to an interference of the two waves which is constructive or destructive depending on the position of the moving mirror, and then the corresponding analysed interferogram can be obtained.

A FT-IR spectrophotometer can be coupled with an optical microscope, which represents an important tool for studying organic materials. FT-IR spectroscopic data can

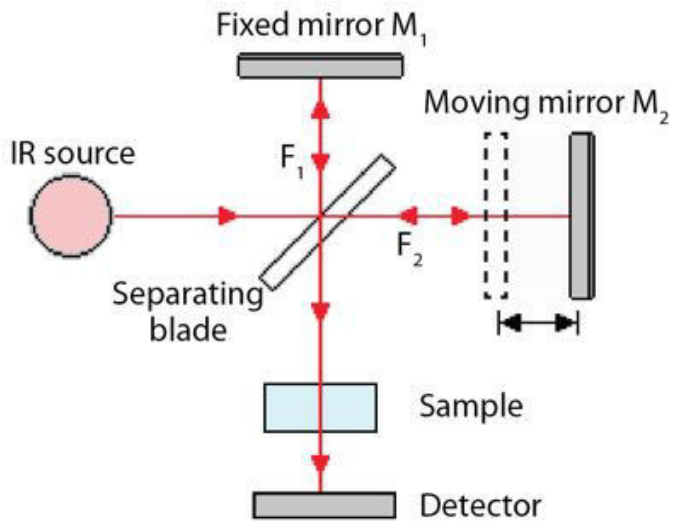

Figure A.3: Simplified presentation of Michelson interferometer.

be obtained with several different detectors including:

- The thermic Deuterated TriGlycide Sulfate detector (DTGS) that is sensitive to heat due to photons absorption.
- The Mercury Cadmium Telluride detector (MCT) that reacts mainly with photons for giving a fast response because of the photoconductivity property.
- The Focal Plane Array detector (FPA) which can be used to obtain hyper-spectral images. It allows to collect images on the functional groups by integrating the intensities of characteristic absorption bands within a selected sample area for a chemical map.

All detectors can be used for collecting punctual spectra in transmission or reflection mode.

FT-IR in transmission mode

Based on the Beer-Lambert law, the transmission mode is generally used during conventional FT-IR spectroscopic analysis. Several IR-transparent windows composed by NaCl

or ZnS can be served as sample support thanks to their IR-transparency properties [299]. In addition, the micro-compression cell made by two anvil diamond windows is often used for analysing reactive, opaque, hard or rubbery samples and ancient materials. Diamond has some absorption bands from 2500 to 1800 cm^{-1} so that a background should be collected to remove these analytical interferences. It requires only a small amount of sample thus allows to avoid any embedding process. However, the sample may suffer distortion during the compression in the anvil cell, particularly when heterogeneous samples are considered [300].

FT-IR in reflection mode

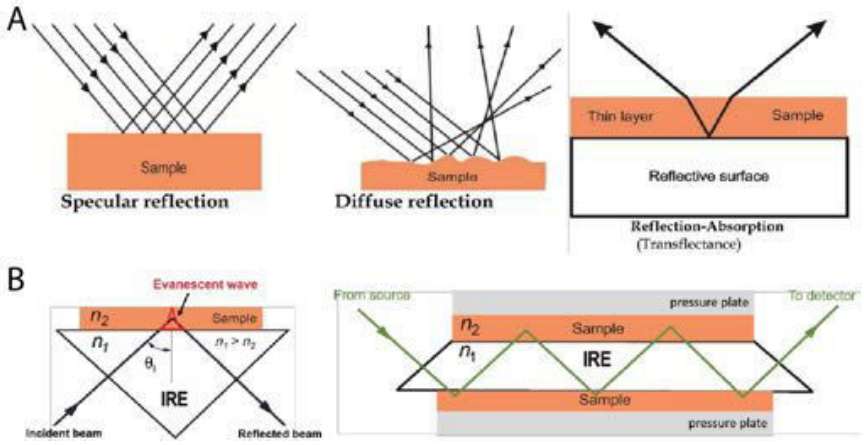

Figure A.4: Various detection modes for FT-IR analysis in reflection (modified from Z. M. Khoshhesab 2012 [301]). A, Three approaches for external reflection. B, The internal reflection based on ATR.

For samples that are not suitable to be analysed in transmission mode, the reflection method is developed and can be extended to a non-destructive approach. Two kinds of reflection techniques are existed, external and internal reflection. The external reflection techniques include (Figure A.4A):

- Specular reflection that mainly used when sample surface is mirror-like. In this case, the sample is normally embedded in resin for subsequent polishing. This

technique provides spectra appearing as derivate-like transmitted bands, for quantitative analysis, Kramers-Kroning Transform is applicable to convert spectra into absorption ones for obtaining a direct relationship between intensity and concentration as the result extracted from transmission method [298].

- Diffuse reflection that generally performed when sample surface is rough so that the incident IR beam is reflected in all directions. Samples are normally analysed in the form of pellets obtained by pressing the powered sample with an IR-transparent medium such as KBr or KCl. Samples can also be simply placed onto specific windows mentioned above [302] During analysis, Diffuse Reflectance Infrared Fourier Transform Spectroscopy (DRIFTS) device eliminates the strong specular reflected radiation in order to avoid spectra distortions. However, in this arrangement, absorption intensity is not directly proportional to the matter concentration of the absorbing species and the Kubelka-Munk transform is thus necessary for quantitative data processing [298].

- Reflection-absorption approach that occurs when the incident IR beam is reflected by a mirror surface attached under a thin layer of sample. It permits to exploit the part of the incident beam that is specularly reflected by the upper surface of sample and also the part that penetrates into the layer. Here, the radiation is reflected by the mirror surface of sample support passing twice through the upper surface of the sample layer. The resulting spectrum, similar to the transmitted ones, has reflectance intensities increased as compared to the signal deriving from the normal transmission mode [303].

The Internal Reflection Spectroscopy (IRS) is based on the Total Attenuated Reflection (ATR) phenomenon (Figure A.4B). It occurs when the incident IR beam passes from a high-refractive-index material, namely the Internal Reflection Element (IRE) with index n_1, into a closer lower-refractive-index material (the sample with index n_2).

IREs are also called ATR crystals, the most commonly used are Germanium (Ge) and Zinc Selenide (ZnSe) because of the high refractive index and great resistivity to etching, respectively. The incident radiation is partially reflected and refracted at the interface. If the incident angle θ_i increases, the portion of the reflected radiation becomes greater and the refracted one decreases. When the critical angle θ_c is reached, the incident beam will be completely specularly reflected at the interface leading to total internal reflection. This phenomenon is accompanied by formation of an "evanescent wave"that penetrates for a short distance into the sample. The sample absorbing the radiation provides a spectrum very similar to that obtained in the transmission mode. Therefore, ATR can be performed in place of the conventional transmission method on a large set of different samples for example opaque materials and even liquid [301].

Scanning electron microscopy (SEM)

Principle

During SEM analysis, a thin beam of electrons whose energy can vary from a few hundreds eV to 40 keV is focused on the sample surface. The scans can be produced on selected area through the movement of beam by parallel lines. Under the impact of this electron beam, various electron–matter interactions result in the emission of different signals. These are collected to form an image of the surface of the artefact to be observed, or to carry out a chemical analysis of the same surface.

The main signals emitted in SEM are shown in Figure A.5 with the corresponding irradiated area in the electron-matter interaction volume. The three signals generally collected are:

- The Secondary Electrons (SE) that have an energy of 0 to 50 eV showing essentially the topographic contrast and morphological information.

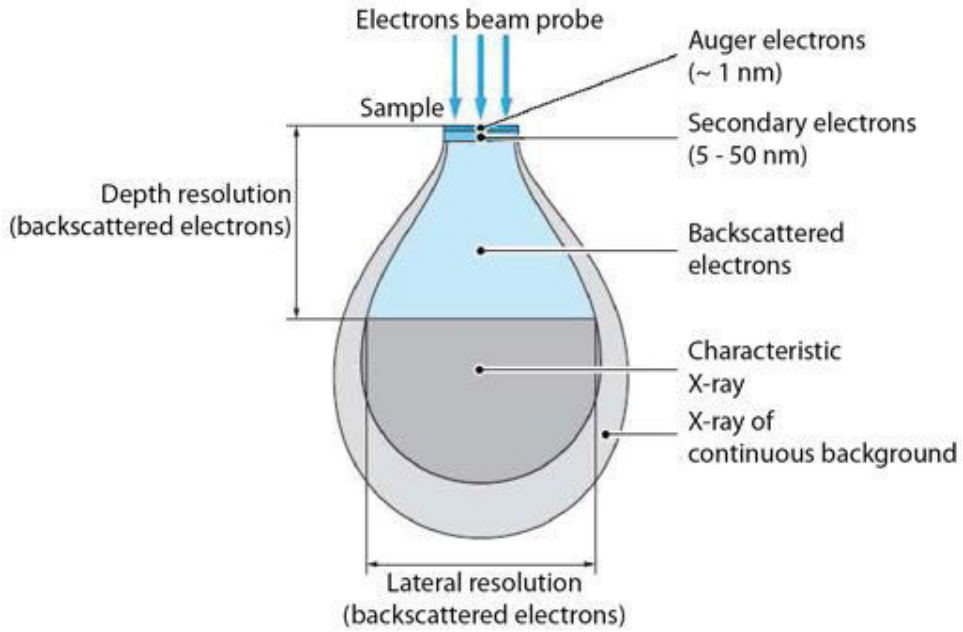

Figure A.5: Principal signals obtained during SEM analysis. (modified from C. Plummer 2001 [304]).

- The Backscattered Electrons (BSE) emitted with a high energy close to that of the incident eletron beam providing topographic and/or chemical contrast based on atomic number.

- The characteristic X-ray of elements existed in the sample for a chemical analysis when coupled with an energy dispersive detector (EDX).

Apart from this, the diffraction of backscattered electrons (EBSD) is also used in our studies. This technique can provide information on the crystal orientation of the grains (Figure A.6). The principle is similar to that of X-ray diffraction, except that here the sample is illuminated with an incidence angle of 20°(the sample is inclined 70°with respect to the horizontal when the beam is vertical) under an electron beam. The beam interacts with the surface of sample and produces backscattered electrons in all spatial directions. The electrons diffract on the inter-planar plane hkl according to the Bragg condition. The constructive interferences form two symmetrical cones with

respect to the plane hkl. The intersection between the cone and the detector, equipped with a phosphorescent screen, forms lines slightly curved and symmetrical in related to the trace of the plane hkl that called Kikuchi lines. The space between the pair of lines for a given plane is a function of the distance between sample and detector and the interplanar distance d_{hkl}. The diffraction pattern is composed of the set of Kikuchi lines that diffract on the grain. When the Kikuchi lines are sufficiently contrasted, the automatic indexation makes it possible to differentiate the mineral phases and their orientation. The quality of the Kikuchi lines depends greatly on the surface preparation of the sample.

The EBSD detector is equipped with four forward scatter detectors (FSD), two topographically sensitive and two others for compositional detection.

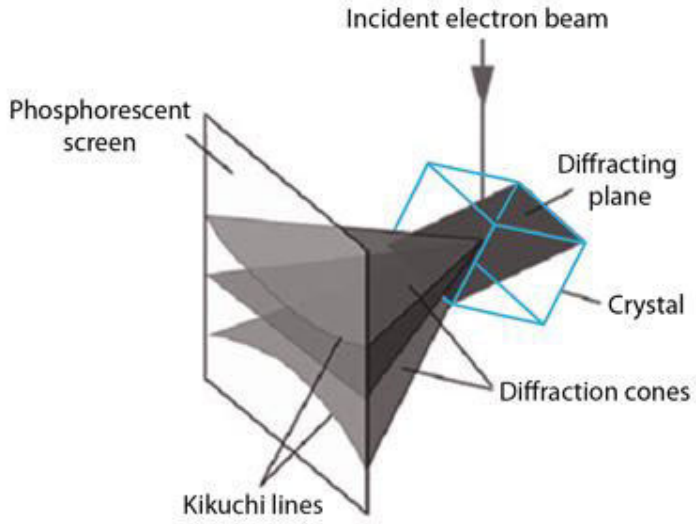

Figure A.6: Principle of formation of Kikuchi diagrams. (modified from T. Baudin 2001 [305]).

Raman spectroscopy

Principle

Raman spectroscopy analyses the dynamics of atoms through the tensor coupling between a monochromatic light and the polarizability variation of chemical bonds, i.e. the deformation of the electron cloud during the motion of atoms [306]. This method explores the physical phenomenon according to which a medium slightly modifies the frequency of the light passing through the medium. This frequency shift corresponds to an exchange of energy between the light beam and the medium and gives information on the substrate itself [307, 308].

When a monochromatic light beam produced by a continuous laser of frequency υ_0 is focused on the sample to be analysed, the energy E_0 of the incident radiation is defined by the following relation :

$$E_0 = h\upsilon_0 = h\frac{c}{\lambda_0} \tag{A.2}$$

with h: Planck's constant (6.63×10^{-34} J·s), υ_0: frequency of incident radiation, c: speed of light in the vacuum (3×10^{8} m/s) and λ_0: wavelength of the incident radiation.

The incident beam are largely transmitted, reflected or absorbed and a much smaller fraction is scattered resulting to that [242]:

- a part of the incident photons is diffused at the same frequency υ_0 as the incident radiation, which is called in this case elastic or Rayleigh scattering;
- a very small amount of the incident photons is diffused with a change of frequency. This effect is called inelastic or Raman scattering and represents about 1 Raman photon for 10^8 incident photons (in order of magnitude).

The Figure A.7 illustrates the Rayleigh and Raman scattering mechanisms. If the frequency υ_0-υ of the scattered photon is less than that of the incident photon (υ_0),

there is a gain of vibrational energy for the molecule (and energy loss for the photon) corresponding to Stokes line. In contrast, if the incident photon is scattered at a frequency $\upsilon_0+\upsilon$, there is a loss of vibrational energy for the molecule (and energy gain for the photon) that corresponds to the anti-Stokes line.

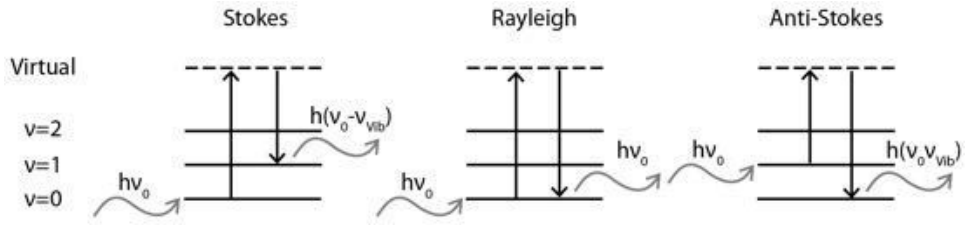

Figure A.7: Raman and Rayleigh diffusion mechanisms (in case of $\upsilon_0 \gg \upsilon_{\mathrm{Vib}}$).

X-ray absorption spectroscopy (XAS)

XAS provides information on the oxidation state of an absorbing atom and its local coordination. This technique is applicable to all elements and can be used for different types of samples, regardless of their physical form (solid, liquid, etc.) and quantity.

Principle

For this purpose, the element of interest is subjected to the X-radiation. These X-rays can be potentially absorbed by the material according to the photoelectric effect. When the energy of incident X-ray equals the binding energy between a core electron and the K, L or M layer, this electron can be ejected and then a gap is created in the electron distribution on the electronic layers, leaving thus the atom in an excited state. To stabilize the system, the excited atom relaxes by reorganization of the electron cloud to fill the gap according to a process of X-ray fluorescence or Auger electron emission (Figure A.8A).

Like the principle of absorption tomography, the absorption of X-radiation is analysed by the study of the linear absorption coefficient μ defined by Lambert-Beer law (3.2).

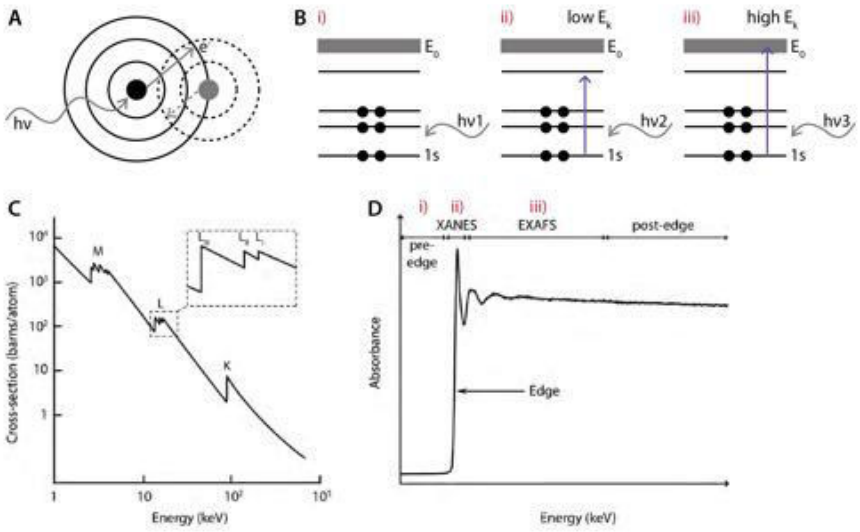

Figure A.8: The principle of XAS. A, Physical principle. B, The three physical processes corresponding to a XAS spectrum: i. pre-edge ii. XANES iii. EXAFS. C, Schematic representation of K, L and M edges (modified from B. Teo 1986 [309]). D, Typical K-edge XAS spectrum, the region of pre-edge, XANES, EXAFS and post-edge corresponds respectively to the three cases of B (modified from B. Teo 1986 [309]).

The XAS analysis aims to measure the energy dependence of μ around and after the absorption edge of the element of interest, μ can be determined according two modes:

- in transmission (Figure A.9A): the absorption is calculated directly by the transmitted radiation, that is:

$$\mu(E) * x = -\ln(I/I_0) \tag{A.3}$$

- in fluorescence (Figure A.8B): it measures, as a function of the energy of the incident photons, the intensity of the fluorescence photons emitted during the process of radiative decay while filling the hole at the core of atom. In this case, μ is determined by a formula of the type μ(E) $\propto I_f/I_0$ with I_f representing the intensity of fluorescence

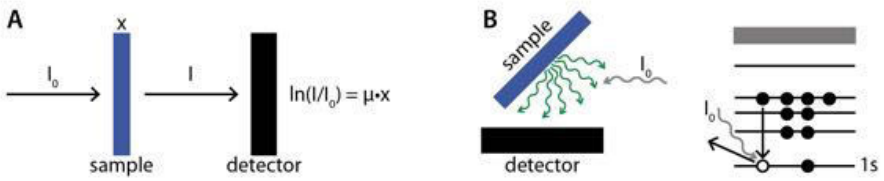

Figure A.9: Two modes of the detection of XAS signal. A, Transmission mode. B, Fluorescence mode.

XANES (X-ray Absorption Near-Edge Structure)

The analysis of XANES corresponds to the region of the X-ray absorption spectrum around the absorption edge of the element of interest up to 100 eV. The study of this region of interest provides information on the oxidation state of the element of interest and its local coordination geometry around, the molecular orbitals as well as the multiple diffusion of the photoelectron generated by the neighbouring atoms (Figure A.8B, C and D).

EXAFS (Extended X-Ray Absorption Fine Structure)

The analysis of EXAFS corresponds thus to the region of the X-ray absorption spectrum after the absorption edge of the element of interest, from 100 eV of post-edge to the end of the spectrum. It consists of oscillations resulted from the interference between the wave associated with the emitted photoelectron and the wave of the photoelectron backscattered by the neighbouring atoms of the absorbing element. The result of EXAFS offers information on the number and the nature of the neighbouring elements around the absorbing element, as well as the distance between them (Figure A.8B, C and D).

The signal of EXAFS is represented by the function χ(E), defined by the formula:

$$\chi(E) = [\mu(E) - \mu_0(E)]/\Delta\mu_0(E_0) \tag{A.4}$$

μ(E): the absorption coefficient of the element surrounded by its neighbours

μ_0(E): the absorption coefficient of the isolated element

$\Delta\mu_0(E_0)$: the jump to the absorption edge of the element

Experimental setup at DIFFABS beamline

The analysis of X-ray absorption were performed at beamline DIFFABS (DIFFraction ABSorption, 3-23 keV range), which is placed on a bending magnet in SOLEIL Synchrotron. The goal is therefore to optimize the maximum photon flux, the beam stability, the minimum beam size, the best monochromatization and the tunable energy of the beam during the acquisition of X-ray absorption spectrum. Besides, X-ray diffraction (XRD) and X-ray fluorescence (XRF) can be combined simultaneously with XAS at the beamline. The field of study ranges from geology, mineralogy, and materials science to catalysis and magnetism. The beamline consists of a Si(111) double-crystal monochromator for a normal beam size around 300 x 300 µm2, and an additional Kirkpatrick-Baez (KB) mirror enabling to focus the beam into micro mode for example 9 x 4 μm^2 in our studies (Figure A.10A and D).

The main analysed regions are the broken side or polished cross section (in resin) of corroded copper-based fragments and mineralized threads. As the corrosion products are clearly layered in these regions, the samples were placed nearly horizontally on nylon screws to avoid confused signals of adjacent layers resulted from the beam spreading. Samples and reference compounds were nextly mounted on a xyz plate oriented at 45°with respect to the incident beam and to the detector (Figure A.10B and C).

All the XAS spectra were obtained at room temperature. Since the samples are mainly composed by copper, the energy scans at the Cu K edge (electron binding energy: 8993 eV) were carried out ranging from 8900 to 9500 eV. Energy step sizes were 2 eV between 8900 and 8958 keV, 1 eV between 8960 and 8970 eV, 0.5 eV between 8970.5 and 9030 eV, 1 eV between 9031 and 9100 eV, 2 eV between 9102 and 9150 eV, and 2eV between 9152 and 9500 eV. Different counting times have been used per energy step

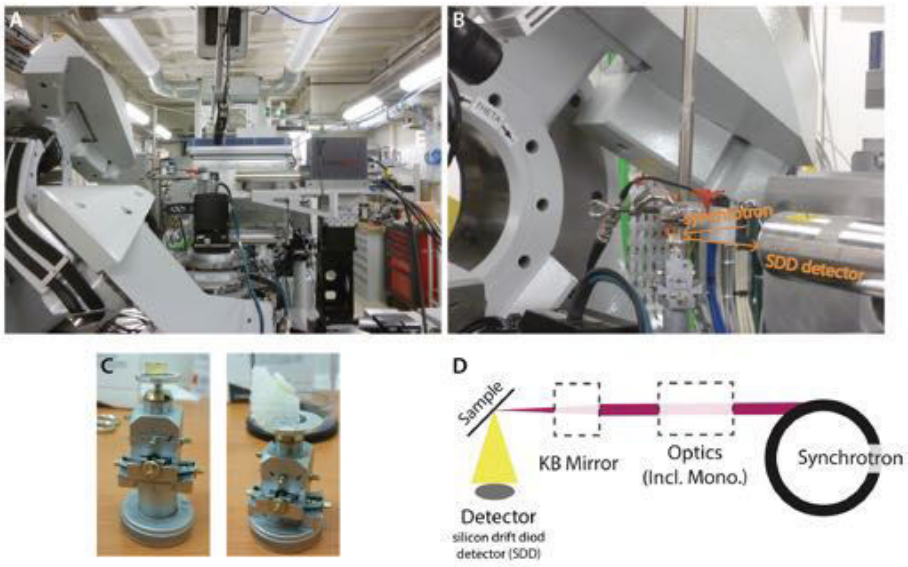

Figure A.10: XRF analysis at the DIFFABS beamline (SOLEIL synchrotron, France). A, Experimental hutch. B, The path of incident synchrotron radiation, the placement of sample and the detection of fluorescence signal. C, Sample fixed on nylon screw. D, Schematic setup of the experiment (reused from P. Guériau 2014 [310]).

and two or three spectra have been cumulated at each point. The speciation maps, corresponding to the regions of pre-edge, edge, major EXAFS oscillations and post-edge, have been additionally recorded through several successive XRF maps conducted at different excitation energies.

In the case of the study of archaeological corroded copper-based samples, the detection in fluorescence mode was opted to obtain a better sensitivity and, according to the Lambert-Beer law, to avoid the total attenuation of incident X-ray while passing through the dense samples. In the fluorescence mode, the silicon drift diode detector (SDD) is placed perpendicularly to the X-ray path at the height of sample.

Data processing of XAS spectrum

Concerning the data processing of XAS, many softwares exist today but the most commonly used are the programs Athena-Artemis [311], Winxas [312] and MAX [313]. In

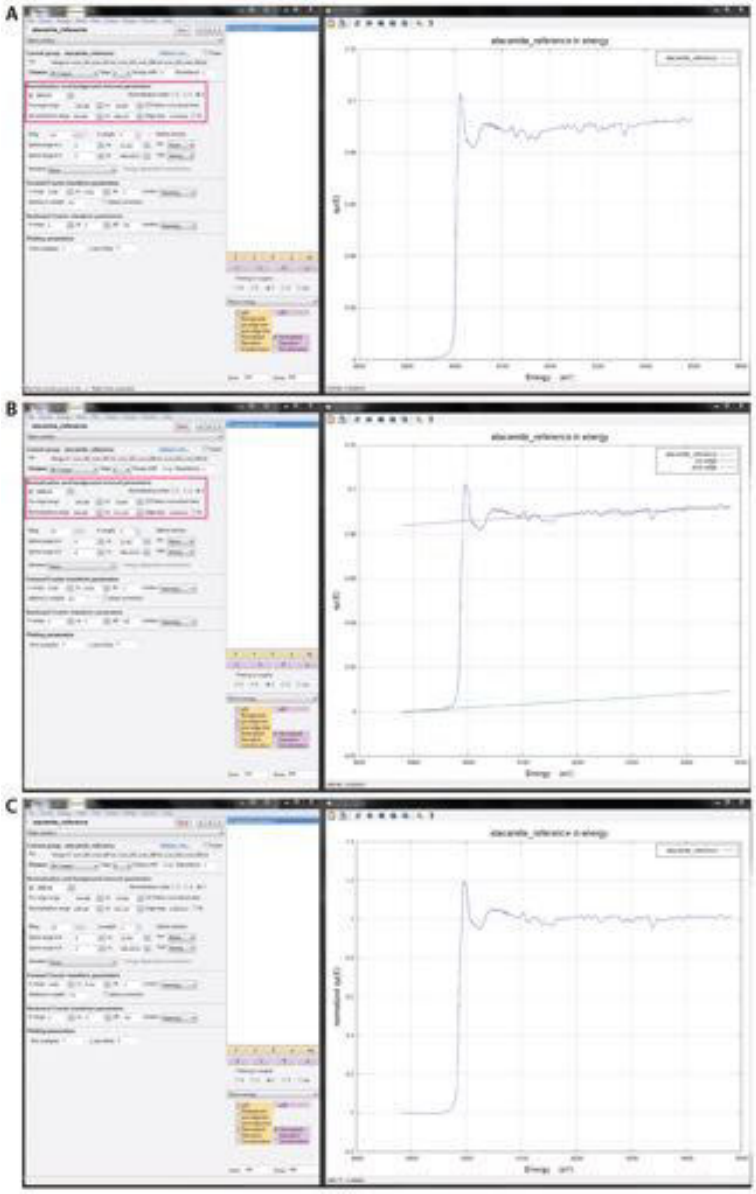

Figure A.11: Main steps of the data processing of XAS spectrum of atacamite ($Cu_2(OH)_3Cl$, reference compound) using ATHENA software. A, Original spectrum. B, Treatment of spectrum including energy calibration, adjustment of pre-edge and post-edge line, as well as the normalization. C, Processed spectrum with $\mu = 1$.

this project, we mainly worked with Athena-Artemis, the group of programs developed by Bruce Raval et al [311].

For XANES, qualitative information can be obtained by comparison with reference compounds without excessive treatment after acquisition. The process takes the following steps in the order indicated (Figure A.11A, B and C):

- Calibration (Figure A.11B) It means involving a given value of energy (E) with each point of the observed spectrum μ(E) by assigning a theoretical value. For example a copper foil was used in our studies and the position of the first point of inflexion at K edge of copper must be theoretically measured at 8979 eV.

- Correction of instrumental effects That is the elimination of the outliers (very far from the average). Two methods are usable for the correction: the first is simply to "mark and erase"to trace the spectrum again, while the second is the use of an algorithm that identifies and overestimates these points by giving a tolerance and a range of energy to finally retrace the spectrum.

- Normalization (Figure A.11C) The difference between μ(E) and μ_0(E) is divided by an estimate of μ_0(E). The spectra of XANES are standardized in several steps, which are useful to compensate the variations of samples in thickness or concentration.

  - Subtraction before and after the edge: The elimination of the continuous absorption background is obtained by normalizing the spectral region before the edge by using a polynomial function and subtracting it from the spectrum. The area before the edge is set thus to zero and the spectrum is straightened horizontally.

  - Subtraction after the edge: It is the modelling by a horizontal line which makes it possible to normalize the whole spectrum so that the equation of

this straight line is reduced to $\mu = 1$ (Figure A.11C).

The processing protocol applied to EXAFS spectra is carried out according to the following steps:

- Once the normalization is done (as for the XANES analysis), an interpolation is performed to the k space.
- Subtraction of the weak background to generate χ(k)
- The use of Fourier transform to obtain the amplitude of each layer and the determination of a parametric model using the data of theoretical crystallographic standards. The Fourier transform makes it possible to go from the k(Å-1) space to that of the distances R(Å) [314].
- Signal simulation: The structure parameters (σ, r and N) are obtained using the expression of χ(k) and the atomic parameters such as F(k) and Φ(k) calculated from the model system. The aim is to verify that the local structure of the compound corresponds well to the data of the literature.

Athena allows processing the experimental spectra up to the Fourier transform of signal of EXAFS. Then, with the help of Artemis, the modulations of experimental signal of EXAFS can be adjusted, by using the least squares, to a theoretical signal calculated for a cluster of atoms whose spatial arrangement is calculated using the module Atomes [311]. To generate the theoretical signal of EXAFS, the software Artemis uses the amplitude and phase functions calculated by the FeFF program [315, 316].

X-ray fluorescence (XRF)

As a very useful technique for qualitative and quantitative elemental analysis of materials, XRF is non-destructive, multi-elemental and fast. Based on a focused X-ray

radiation, this method has a high spatial resolution and low detection limits, providing information on very small samples and analysis of trace elements.

Principle

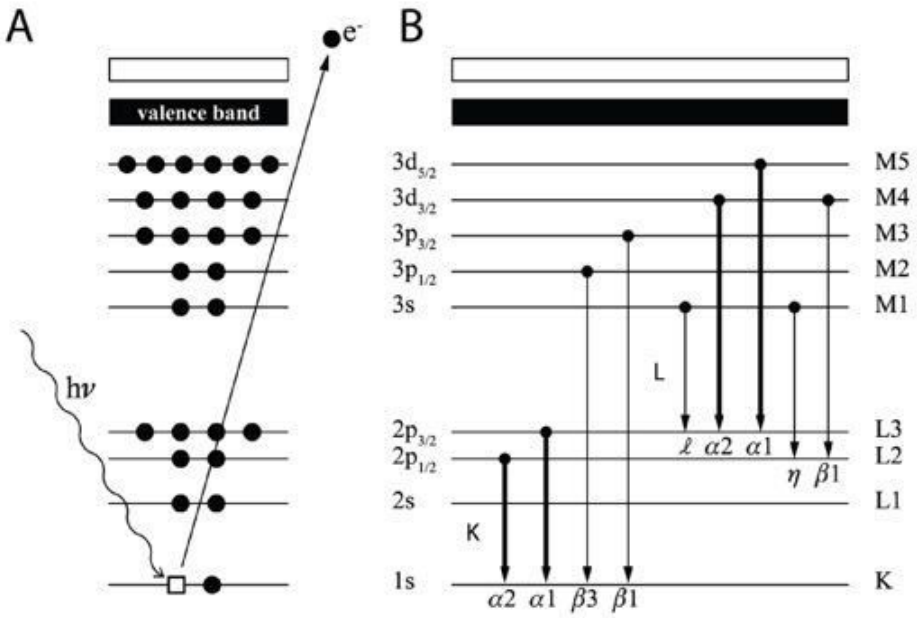

Figure A.12: Physical principle of XRF (modified from Bertrand et al., 2012a [201]). A, Schematic representation of the photo-excitation process. B, Subsequent X-ray fluorescence transitions. Main emission lines are shown in bold.

Fluorescence is a physical phenomenon obtained as a result of the photoelectric effect, that is, the atoms become radiation emitters after absorbing themselves an incident photon. According to the Figure A.12A and B, when a substance is irradiated with an X-ray beam of determined energy, it absorbs or attenuates the beam (by different interactions) and behaves in turn as an X-ray source. The spectral analysis of this new radiation makes it possible to distinguish the scattered radiation and, the fluorescence radiation itself that forms a spectrum of characteristic lines of the substance [317].

Experimental setup

The X-ray synchrotron microfluorescence (µXRF) presented here was also carried out at the DIFFABS beamline in SOLEIL Synchrotron. The beam size (9 x 4 μm^2), experimental setup and the fixing of samples are described at the part of XAS analysis. XRF maps and spectra were collected at excitation energy of 18 keV or 9.5 keV. The exposure time per pixel was set at 5 ms suing a continuous acquisition mode called Flyscan. The resolution of the XRF maps is $9\mu m^2$.

Data processing

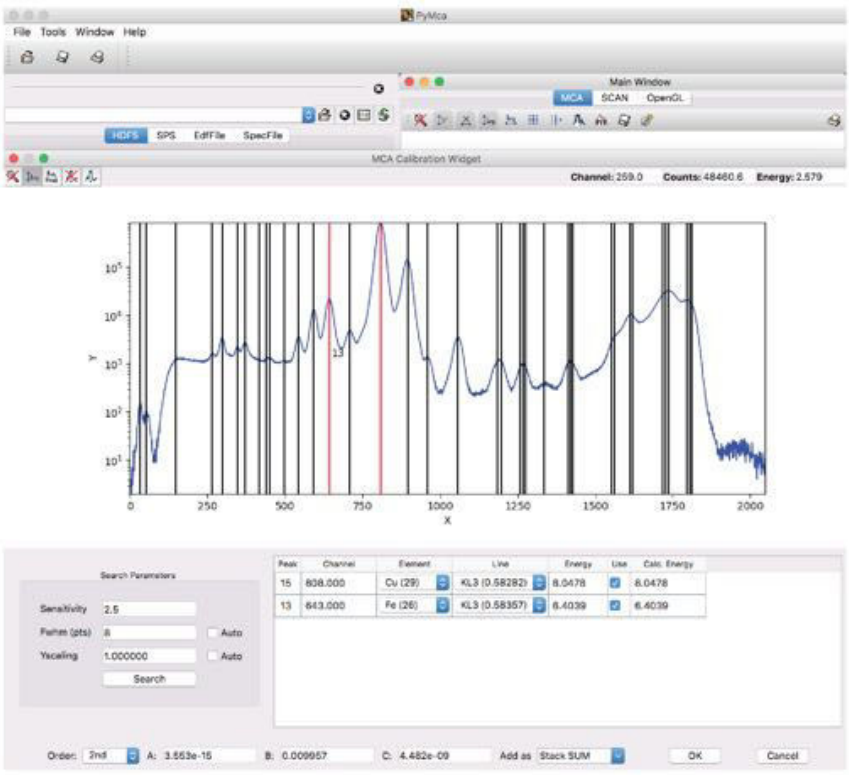

Figure A.13: Calibration of channel to energy using Cu and Fe using PyMCA software.

XRF data were processed using a non-linear least squares fitting routine PyMCA developed at ESRF [318]. This software allows us to firstly calibrate the detector (re-

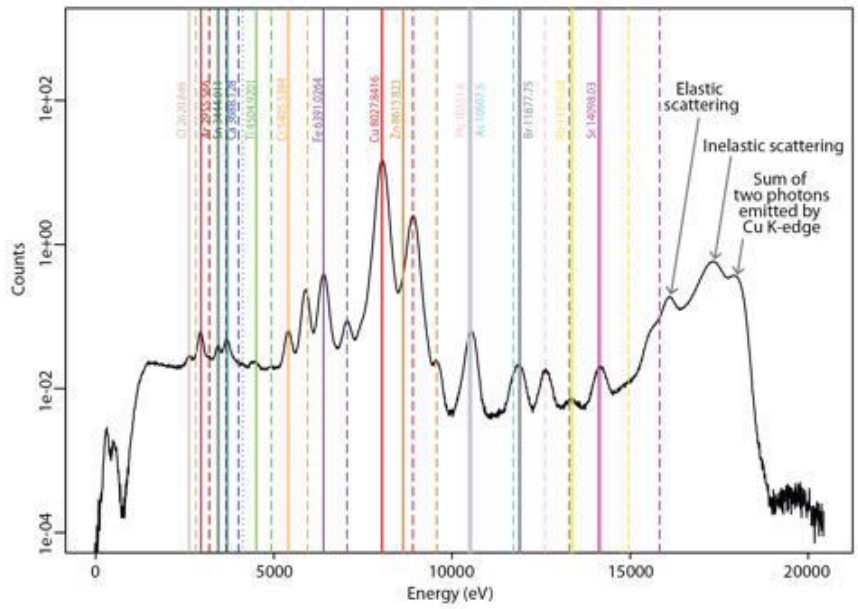

Figure A.14: Identification of elements of the mean XRF spectrum (incident energy at 18 keV) obtained from the polished section of sample NS 95015002–1.

lationship between the channel number and energy), through the precise knowledge of the fluorescence energy of certain elements present in the sample (e.g. Cu and Fe in our studies, Figure A.13). The peak identification (qualitative treatment) can be achieved by comparing its experimental data with that of the reference element (Figure A.14). Then, the XRF elemental maps can then be produced through two main approaches:

- The simpler (and much quicker) consist in extracting integrated intensities in selected spectral regions of interest (ROI) corresponding to a targeted emission line, i.e. the intensity of a selected peak. This is basically used at beamlines to follow live the scan progression. It works pretty well, and is often sufficient, for elements that are the main contributors to the XRF spectra and are not hampered by other elements dominating the signal (Figure A.15A and C).

- When emission lines of different elements overlap and the user is interested in a minor contributor to the XRF spectrum, a full spectral decomposition is needed

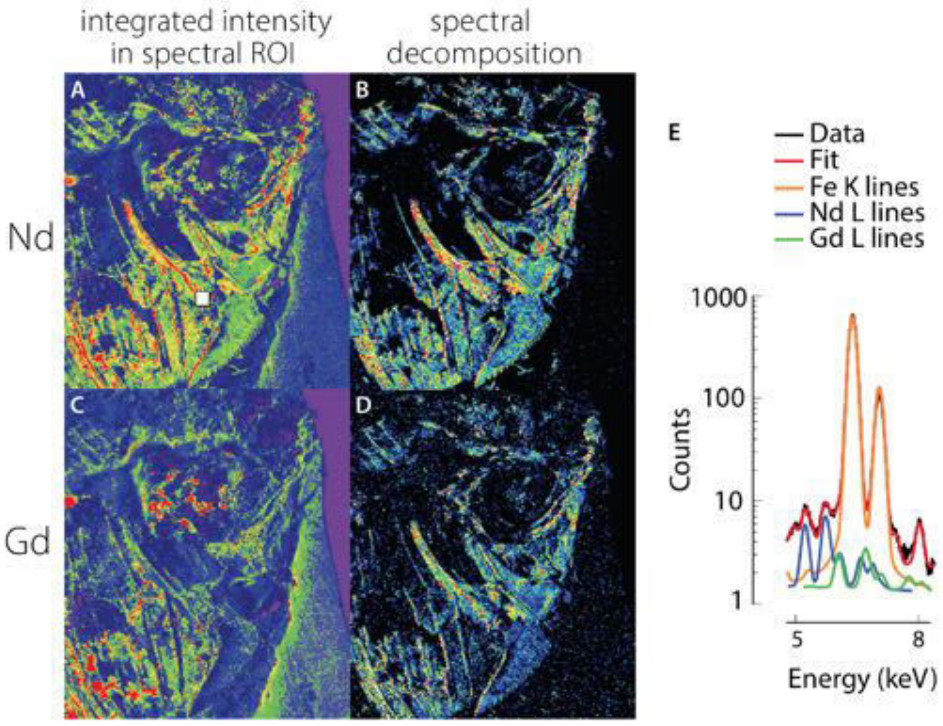

Figure A.15: Example of the elemental map generated for Nd and Gd using two approches from a sample of fossil (reused from P. Guériau et al., 2014 [319]). A and B, The distribution of Nd produced respectively by extracting the integrated intensity of ROI from the selected spectrum and spectral decomposition. C and D, The distribution of Gd produced respectively by extracting the integrated intensity of ROI from the selected spectrum and spectral decomposition. E, A part of the selected XRF spectrum (black) and fit line (red) from the 9×9 pixels white square area in A for the main contributors (Fe, Nd and Gd).

(Figure A.15B and D). Due to their alteration history, ancient materials are highly heterogeneous and therefore often include "the whole periodic table". While the production of elemental maps using integrated intensities in ROIs take a few seconds, a full spectral deconvolution of a megapixel map requires several days of computing. This approach can be quantitative simultaneously [319].

Once the energy calibration and peak identification are done, the peak intensity can provide the elemental concentrations. Using PyMCA, the concentration can be estimated by the fundamental parameter method or matrix composition method after determining the incident intensity and detector efficiency [320].

X-ray diffraction (XRD)

XRD is one of the most widely used methods for characterizing the phases present in metallic materials. Indeed, it allows to determine the crystallographic nature of phases and their crystalline parameters, as well as the possible states of stress and crystallographic textures. The principle of this technique is based on the measurement of the inter-reticular distances with respect to the different families of crystalline planes [321].

According to the photon emitting source used for the diffraction experiments, the analyzed volume is different. The diffraction analysis performed in laboratory using generally X-ray tubes as photon generators, in this case only a thin thickness on the surface of sample is irradiated. This can be explained by the low energy of the beam produced depending on the material of anticathode, for example the energy obtained with an anticathode of copper is 8 keV so that the penetration power of photons remains limited.

In order to perform diffraction experiment inside the sample volume, the sample preparation (cutting and polishing) is necessary for the layer-by-layer analysis. In addi-

tion, due to the low X-ray flux delivered by the X-ray tube, the time required to acquire a diffractogram is relatively high (approximately one hour), thus limiting the possibility of in situ monitoring of the kinetics of transformations (often fast).

When the diffraction technique is combined with synchrotron radiation, it has many advantages compared with that used in laboratory. Firstly, synchrotron source makes it possible to obtain photon beams with a wide range of energy from a few eV to 100 keV. It permits to perform measurements on the surface of sample with the low energies but also in the sample volume with high energies. When working with a high-energy radiation (of the order of 90 keV), it is possible to perform X-ray diffraction analysis on solid samples. The information obtained is therefore representative of the whole volume of sample and the experiment is thus non-destructive. The second characteristic of synchrotron radiation is the high brightness of the radiation delivered (of the order of 10^{12} photon/s). This makes it possible to considerably reduce the acquisition time to obtain a diffractogram. Finally, it allows performing the in situ analysis because of the high temporal stability of the synchrotron X-ray beam.

Principle

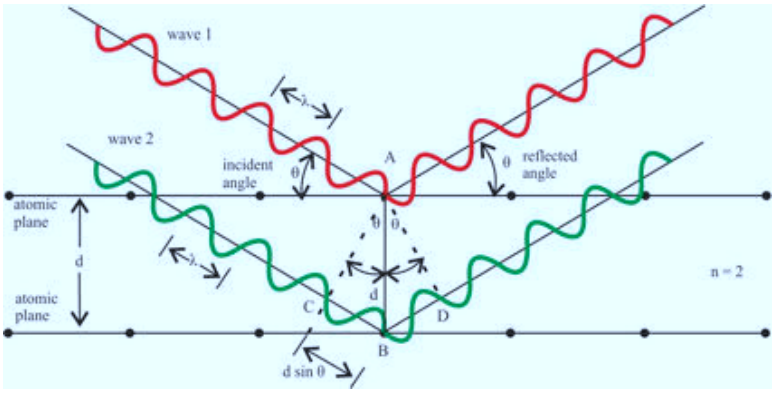

Figure A.16: Schematic representation of Bragg's law.

A crystal is a periodic stack of atoms, when it is irradiated by an X-ray beam,

each atom of the crystal diffuses a wave, which propagates (diffracts) in all directions according to Bragg's law (Figure A.16):

$$2d \sin\theta = n\lambda \tag{A.5}$$

d: inter-reticular distance of planes $\{hkl\}$

n: a positive interger called diffraction order (n=1)

θ: incident beam angle

λ: wavelength of the beam

Based on the angle of sample with respect to the X-rays, the diffracted lights have different positions, so that the distances between the planes and their orientation can be determined. According to the Bragg law, each peak can be then assigned to an imaginary atomic plane that designated by Miller index ($\{hkl\}$). It is therefore possible to associate the attributed index with the diffraction peak.

Another information that can be obtained by XRD is the dimension of the crystallites on the normal direction to the planes $\{hkl\}$. It can be determined by the Scherrer relation from the width at half height of the diffracted peak $\{hkl\}$:

$$L_{hkl} = \frac{K \cdot \lambda}{\beta \cdot \cos\theta} \tag{A.6}$$

L: the average size of the crystals in the normal direction to the planes $\{hkl\}$

K: a constant based on the crystallite form

β: the width at half height of the diffracted peak that measured on the scale 2θ in textdegree and then multiplied by $\pi/180$

Theoretically, the value of the width at mid-height of the diffracted peak in the {001} plane gives indication to the average number of sheets N per crystallite via the relation:

$$N = \frac{L_{001}}{d_{001}} \tag{A.7}$$

However, the direct application of Scherrer's formula is not simple because of several causes like the broadening of the diffracted peak (instrumental aberrations, folding of sheets...).

When the X-ray diffraction technique is associated with synchrotron radiation, experiments can be performed under different conditions, including angle-dispersive XRD (ADXRD or ADX) and energy-dispersive XRD (EDXRD or EDX).

Angle-dispersive XRD (ADXRD or ADX)

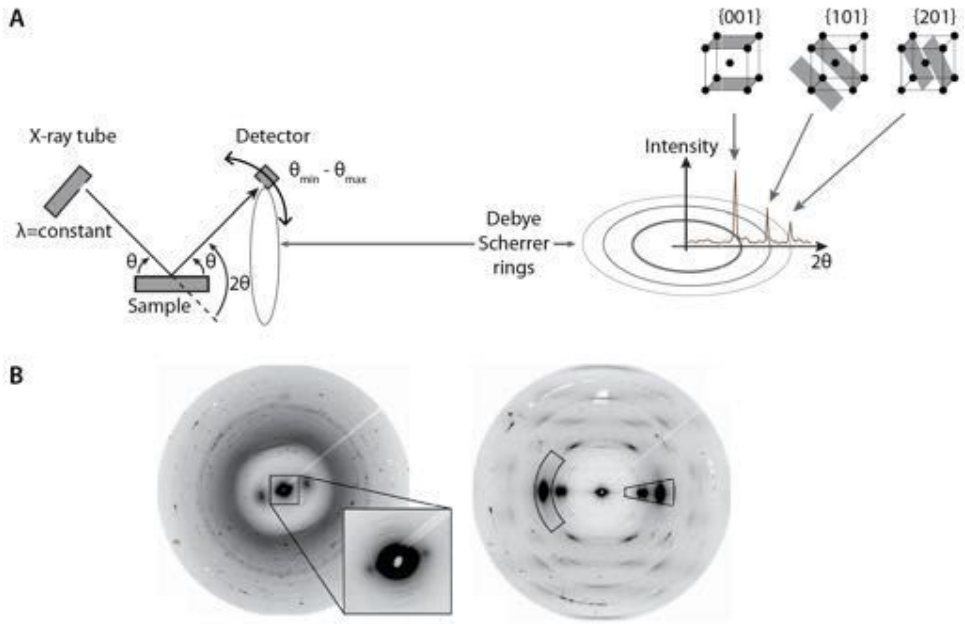

Figure A.17: Simplified presentation of ADXRD (modified from M. Müller et al., 2006 [322]). A, Principle of an ADXRD diffractometer. B, Diffraction diagrams (Debye Scherrer rings) of archaeological fibre of wool (left) and flax (right).

The most common method is to send a monochromatic X-ray beam onto the sample that fixed on a goniometer (Figure A.17A). The diffracted beam is then collected through a detector (usually flat-panel detector). The raw results of such experiments are, in the case of polycrystalline materials, the Debye Scherrer rings. An example is shown in the Figure A.17B. Each of these rings is composed of a set of spots and corresponds to the

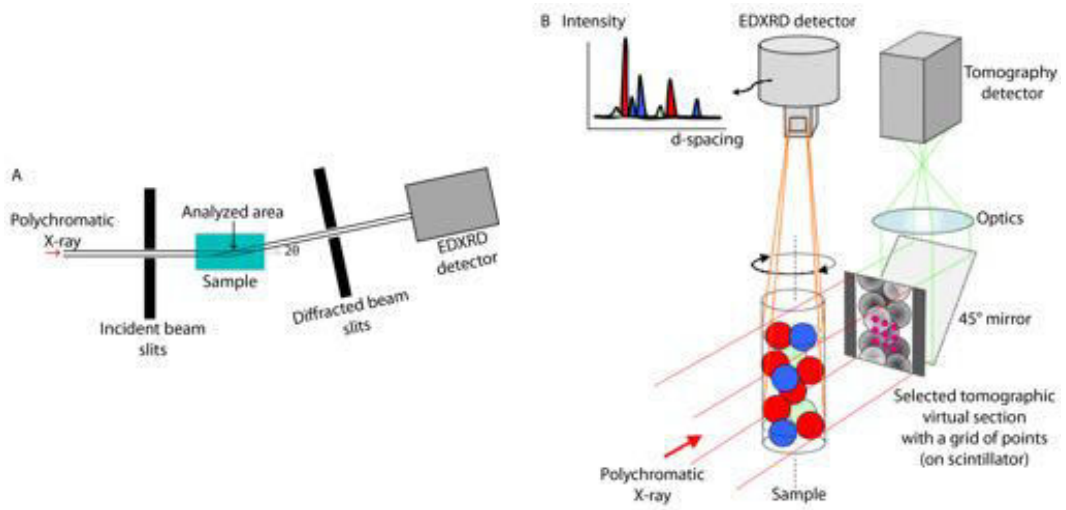

Figure A.18: Simplified presentation of EDXRD technique (© A. King). A, The principle of EDXRD. B, Coupling of EDXRD and FIT.

diffraction of a set of grains of the same orientation (i.e. a coherent diffraction domain). The analysis of these images is generally conducted after integration of the intensity of the rings. The result obtained corresponds to the diffractogram in the classical format that give the diffracted intensity (I) as a function of the diffraction angle (2θ).However, the rather long time of acquisition and necessity of high spatial accessibility of ADXRD limit sometimes its application.

Energy-dispersive XRD (EDXRD or EDX) coupled with fast tomography

It is nevertheless important to note that during a diffraction experiment, the X-ray beam is not always monochromatic. In fact, for a micro-diffraction experiment, also called "micro Laue", the X-ray beam can be polychromatic (Figure A.18A). With this technique that usually operated at a fixed angle (2θ) [323], the collimated white beam scans the ROIs of sample in x, y with its movement. At each x, y position, the monocrystalline grain is illuminated by the photon and gives rise to a Laue diffraction pattern (set of spots) that is recorded by an energy-dispersive detector (EDD). According to the Plank's equation $\lambda = 12.398/\varepsilon$, where λ in [Å] and ε in [keV], the Bragg's law can be transformed

to:

$$\varepsilon = \frac{6.199}{d \cdot \sin\theta} \tag{A.8}$$

Thus, for a given energy (or wavelength), a set of d values can be obtained at a fixed angle. The measured energy distribution of the scattered X-rays reveals distinct peaks, providing the useful information for structural analysis of polychromatic materials.

In our studies, the EDXRD was combined with fast imaging tomography (FIT) for the first time to characterize the corrosion phases of copper for a specially selected section inside the sample (Figure A.18B). Once the tomography experiment is finished, one can access to the spatial distribution of the phases inside the sample to selected a virtual section that contains almost all the observed compounds. Then, a set of point can be taken to perform the following EDXRD analysis.

Experimental setup

ADXRD experiment in laboratory GEMaC

The preliminary ADXRD analysis were carried out in laboratory GEMaC with a BRUCKER D5000 X-ray Diffractometer on one small ancient corroded copper-based fragment (NS 95015002-2, Figure A.19A and B). The tension was at 40 kV and current at 30 mA. The Cu-Kα1 radiation was selected with a wavelength $\lambda = 0.154059$ nm (Figure A.19C). The diffraction patterns were recorded for 2θ angles between 10°and 80°, the step size was 0.02°with a counting time of 50s.

ADXRD experiment at DIFFABS beamline

ADXRD measurements on embedded fibres from Tello and Nausharo in transmission coupled with XRF and XAS were performed at DIFFABS beamline using a micro-beam of 9×7 μm^2 at 9.5 keV. The detailed experimental setup and fixing of sample are

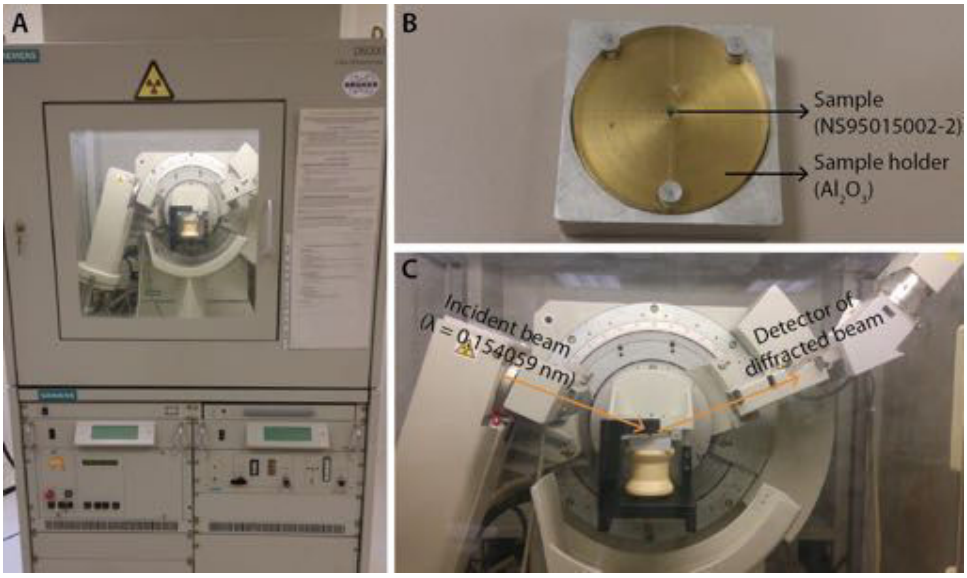

Figure A.19: Experimental setup of ADXRD in GEMaC. A, The diffractometer. B, The detected sample and its holder. C, The path of incident and diffracted beam.

Figure A.20: Experimental setup of ADXRD at DIFFABS beamline.

shown in the section XAS. A two dimensional detector called XPAD using pixel hybrid technology was mounted on a 6 circles diffractometer to collect the diffracted signal. The set of the movement of sample position (xyz and χ, Δ, Ω, κ) and two additional axes of the detector (μ and γ) were controlled and adjusted according to the signal strength via computer outside the experimental cabin (Figure A.20).

EDXRD experiment at PSICHE beamline

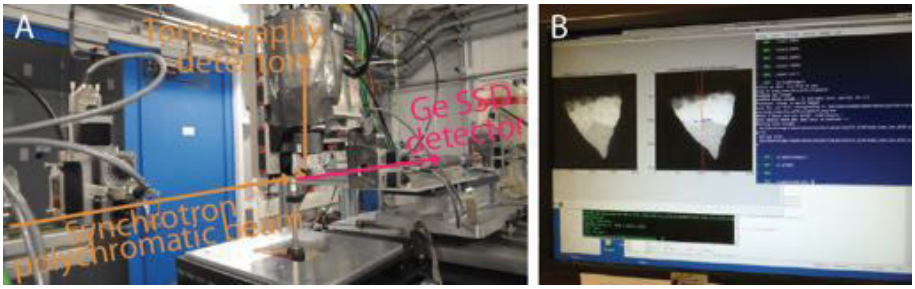

Figure A.21: Experimental setup of EDXRD at PSICHE beamline. A, The path of incident and diffracted beam for XRD, as well as the transmitted photons for tomography. B, The selection of detected area from a tomography virtual section inside the reconstructed data volume.

ED-XRD analysis coupled with fast µCT were carried out at the PSICHE beamline on two samples, AO 14506-3 and NS 95015002-6 of the artefacts AO 14506 and NS 95015002, respectively (Figure A.21). A white beam (polychromatic) spectrum ranging from 25 to 100 keV was used and the incident beam size was defined to 50×50 µm^2 by slits. The diffracted signals were measured using a Ge solid-state detector. The 2θ angle defined by output slits was at 12.5°.

Data processing

After a circular integration of all the Debye Scherrer rings [324], the classical diffractograms (I = f(2θ)) obtained from the ADXRD analysis were processed by software MATCH!. After several pre-treatment steps (elimination of background, automatic

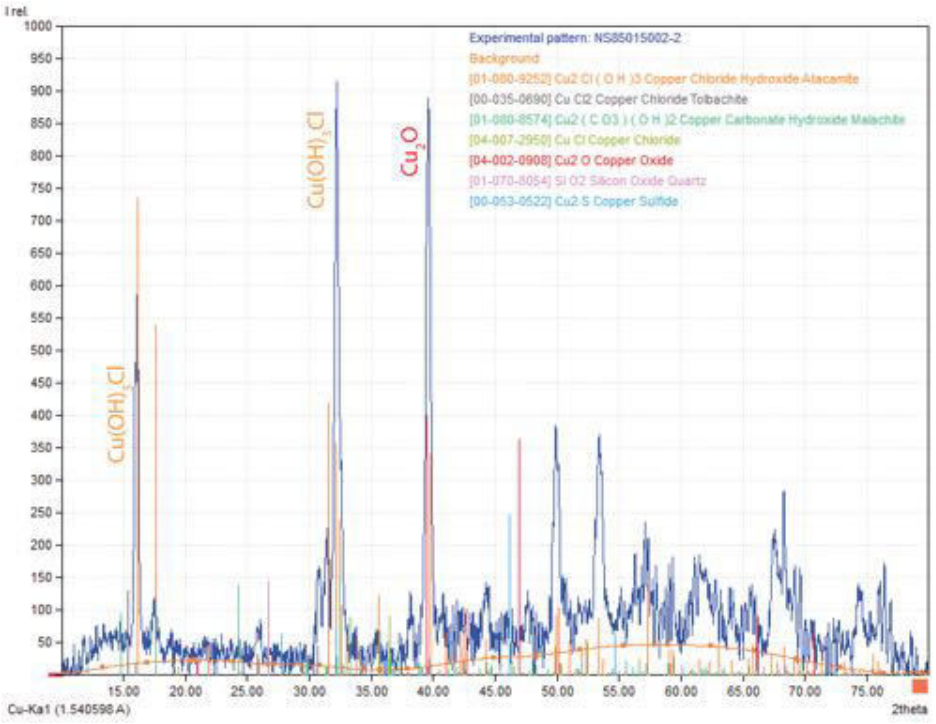

Figure A.22: Phase identification by MATCH!.

smoothing), it compares the experimental diffraction patterns of the sample to a database containing reference patterns and gives a match index in order to identify the phases which are present (Figure A.22). In addition, all the diffractograms obtained during the experiments were calibrated to the corresponding reference (LaB_6 and the powder of Si, respectively at GEMaC and DIFFABS), aiming at correcting potential errors such as centring error.

The data of EDXRD analysis at PSICHE were treated by Andrew King (beamline scientist). After the collection of all diffractograms, the intensity variations (I = f(d–spacing)) can help to identify peaks belonging to the same phase and eventually to confirm its composition in comparison with reference data (Figure A.23).

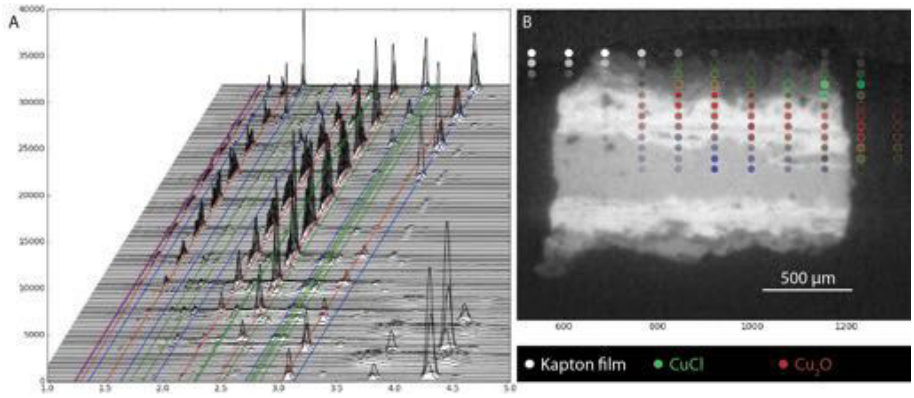

Figure A.23: Phase identification from EDXRD analysis. A, Collection of the diagrams corresponding to all selected points in the tomography section. B, Phase attribution in the selected tomography section (from the reconstruction volume of sample NS 95015002–6) after comparison with reference data.

Additional imaging techniques

Several complementary imaging tools were also used mainly for obtaining images of full samples and selected ROIs.

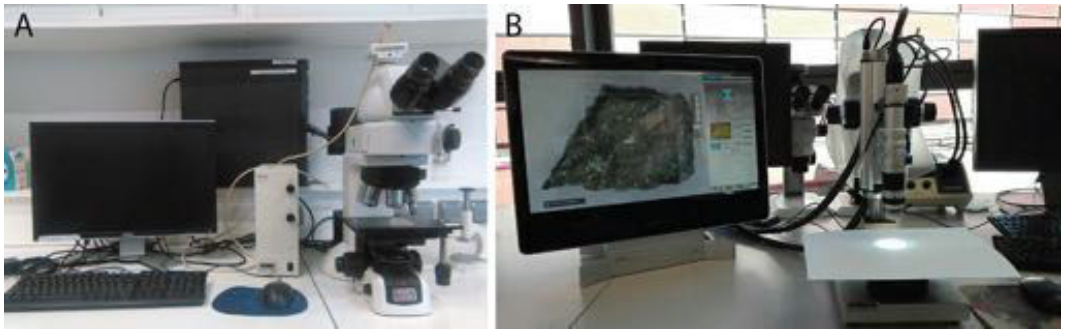

Figure A.24: Additional imaging methods. A, Digital microscope at Musée du Quai Branly–Jacques Chirac. B, Light microscope at IPANEMA.

Macrophotography

Macro photographs were collected through a photography camera (Nikon D300) coupled with a macro lens (Nikon AF-S Micro NIKKOR 60 mm; Focal 6.3 mm; exposure time

1/60; ISO 400) and a white of reference (STN-0005) was used in advance to correct chromatic aberration.

Light microscopy

Samples were also studied in detail using a light microscope (NIKON Eclipse LV100) equipped with a halogen source for the dark-field images, and a mercury source (INTENS ELIGHT C-HGFI) for the bright-field images, and coupled with a camera (NIKON Digital Sight DS-Fi1, 2560x1920 pixels). Images were collected in reflection mode using auto-white and manual exposure with suitable acquisition time. Collection of the images was performed by using the NIS–Elements software (Nikon) (Figure A.24A).

Digital microscopy

A digital microscope (Hirox, KH-8700) was used to collect images of all the samples at Musée du Quai Branly – Jacques Chirac, which coupled with a CCD camera allowing thus the high-quality resolution of 1600x1200 pixel^2 (HxV) (Figure A.24B).

B

Scientific productions during this thesis

Publication

J. Li, P. Guériau, M. Bellato, A. King, L. Robbiola, M. Thoury, M. Baillon, C. Fossé, S. X. Cohen, C. Moulhérat, A. Thomas, P. Galtier, L. Bertrand. Synchrotron-based phase mapping in corroded metals: insights from early copper-base artifacts. *Analytical Chemistry*, DOI: 10.1021/acs.analchem.8b02744, vol. 91, no. 3, pp. 1815–1825, 2019.

Conferences

Oral presentations

- **J. Li**, P. Guériau, M. Bellato, A. King, L. Robbiola, M. Thoury, C. Moulhérat, A. Thomas, P. Galtier, L. Bertrand. Exceptional preservation of archaeological textiles from Mesopotamian and Indus sites: Prospects from synchrotron X-ray micro-tomography. *GMPCA*, Rennes, France, April 2017.

- **J. Li**, P. Guériau, M. Bellato, A. King, L. Robbiola, M. Thoury, C. Moulhérat, A. Thomas, P. Galtier, L. Bertrand. Study of exceptional preservation of archae-

ological flax fabric from Mesopotamian and Indus areas using synchrotron X-ray micro-tomography. *Etude de documents graphiques*, Paris, France, January 2017.

- **J. Li**, P. Guériau, M. Bellato, A. King, L. Robbiola, M. Thoury, C. Moulhérat, A. Thomas, P. Galtier, L. Bertrand. Exceptional preservation of archaeological textiles from Mesopotamian and Indus sites: Why and how?, *Silk Road Youth Forum*, Xi'an, China, December 2016.

Posters

- **J. Li**, P. Guériau, M. Bellato, A. King, L. Robbiola, M. Thoury, M. Baillon, C. Fossé, S. X. Cohen, C. Moulhérat, A. Thomas, P. Galtier, L. Bertrand. Synchrotron-based phase mapping in corroded metals: insights from early copper-base artifacts. *Scientific Symposium Frontiers in Heritage Science*, Paris, France, February 2019.

- **J. Li**, P. Guériau, M. Bellato, A. King, L. Robbiola, M. Thoury, C. Moulhérat, A. Thomas, P. Galtier, L. Bertrand. Exceptional preservation of cellulosic textiles from Nausharo archaeological site (III mill. BC): Prospects from application of synchrotron X-ray micro-tomography. *Journée de l'école doctorale INTERFACES (ED 573)*, Versailles, France, December 2016.

Bibliography

[1] H.-L. Chen, *Microstructures of mineralized cellulosic fibers*. PhD thesis, The Ohio State University, 1995. xiii, xiv, xvii, xviii, 3, 25, 26, 27, 46, 48, 54, 55, 57, 58, 61, 63, 64, 65, 74, 76, 77, 78, 79, 83, 85, 184, 202, 207, 208, 213, 214, 215, 300, 301, 302, 308

[2] L. Sibley and K. Jakes, "Textile fabric pseudomorphs, a fossilized form of textile evidence," *Clothing and Textiles Research Journal*, vol. 1, no. 1, pp. 24–30, 1982. xiii, xvii, 54

[3] C. Moulherat, *Archéologie des textiles protohistoriques: exemple de la Gaule celtique*. PhD thesis, Paris 1, 2001. xiii, xvii, 4, 5, 6, 23, 24, 28, 30, 31, 35, 36, 46, 48, 49, 50, 55, 56, 57, 61, 62, 74, 75, 183, 213, 215, 300, 301, 302

[4] K. Anheuser and M. Roumeliotou, "Characterisation of mineralised archaeological textile fibres through chemical staining," *The Conservator*, vol. 27, no. 1, pp. 23–33, 2003. xiii, xvii, 76

[5] L. Biek, *Archaeology and the microscope: the scientific examination of archaeological evidence*. Praeger, 1963. xiv, xviii, 52, 59, 183

[6] H.-L. Chen, K. A. Jakes, and D. W. Foreman, "Preservation of archaeological textiles through fibre mineralization," *Journal of Archaeological Science*, vol. 25,

no. 10, pp. 1015–1021, 1998. xiv, xviii, 54, 55, 57, 61, 64, 65, 79, 87, 88, 209, 213, 215, 302

[7] L. Hurcombe, *Archaeological artefacts as material culture*. Routledge, 2014. 3, 4

[8] S. Landi, *Textile conservator's manual*. Routledge, 2012. 3, 41

[9] Merriam-Webster Dictionary, "Definition of textile." 3

[10] The Textile Museum, "An Introduction to Textile Terms." 3

[11] Merriam-Webster Dictionary, "Definition of fabric." 3

[12] Online Etymology Dictionary, "Etymology of fabric." 3

[13] Merriam-Webster Dictionary, "Definition of cloth." 3

[14] Online Etymology Dictionary, "Etymology of cloth." 3

[15] M. Balter, "Clothes make the (hu) man," 2009. 3

[16] E. Kvavadze, O. Bar-Yosef, A. Belfer-Cohen, E. Boaretto, N. Jakeli, Z. Matskevich, and T. Meshveliani, "30,000-year-old wild flax fibers," *Science*, vol. 325, no. 5946, pp. 1359–1359, 2009. 4, 204

[17] D. T. Jenkins and D. T. Jenkins, *The Cambridge history of western textiles*, vol. 1. Cambridge university press, 2003. 4, 6, 7, 8, 11, 12, 183, 299

[18] W. Fung and J. M. Hardcastle, *Textiles in automotive engineering*, vol. 13. Woodhead Publishing, 2000. 4

[19] W. Hufenbach, R. Böhm, M. Thieme, A. Winkler, E. Mäder, J. Rausch, and M. Schade, "Polypropylene/glass fibre 3D-textile reinforced composites for automotive applications," *Materials & Design*, vol. 32, no. 3, pp. 1468–1476, 2011. 4

[20] J. G. Ellis, “Textile surgical implants,” 1999. US Patent 5. 4

[21] E. López-Maya, C. Montoro, L. M. Rodríguez-Albelo, S. D. Aznar Cervantes, A. A. Lozano-Pérez, J. L. Cenís, E. Barea, and J. A. Navarro, “Textile/metal–organic-framework composites as self-detoxifying filters for chemical-warfare agents,” *Angewandte Chemie International Edition*, vol. 54, no. 23, pp. 6790–6794, 2015. 4

[22] M.-L. Nosch, H. Koefoed, and E. A. Strand, *Textile Production and Consumption in the Ancient Near East: archaeology, epigraphy, iconography*, vol. 12. Oxbow Books, 2013. 4, 5, 6, 8, 9, 183, 299

[23] M. Pirazzoli-t’Serstevens, *The Han Civilization of China*. Phaidon, 1982. 4, 183

[24] G. P. Shams, *Some minor textiles in antiquity*. Paul Åströms förlag, 1987. 4

[25] L. D’orazio, E. Martuscelli, G. Orsello, F. Riva, G. Scala, and A. Taglialatela, “Nature, origin and technology of natural fibres of textile artefacts recovered in the ancient cities around Vesuvius,” *Journal of archaeological science*, vol. 27, no. 9, pp. 745–754, 2000. 5

[26] C. Breniquet, *Essai sur le tissage en Mésopotamie: Des premières communautés sédentaires au milieu du IIIe millénaire avant J.-C.* Paris: De Boccard, 2008. 5, 8, 10, 31, 32, 33, 201, 205, 300

[27] W. J. READE and D. T. Potts, “New evidence for late third millennium linen from Tell Abraq, Umm al-Qaiwain, UAE,” *Paléorient*, vol. 19, no. 19, pp. 99–106, 1993. 5

[28] C. Breniquet, “Que savons-nous exactement du kaunakès mésopotamien?,” *Revue d’assyriologie et d’archéologie orientale*, vol. 110, no. 1, pp. 1–22, 2016. 6, 7, 33

[29] E. A. Strand, "The textile chaîne opératoire: using a multidisciplinary approach to textile archaeology with a focus on the Ancient Near East," *Paléorient*, pp. 21–40, 2012. 6, 28

[30] E. de Sarzec, L. Heuzey, A. Amiaud, and F. Thureau-Dangin, *Découvertes en Chaldée*. Ministère de l'Instruction publique et des Beaux-Arts, 1884–1912. 7, 51, 99, 100, 101, 102, 103

[31] S. Lloyd, *The art of the ancient Near East*, vol. 96. Praeger, 1961. 8, 299

[32] A. L. Oppenheim, *Ancient Mesopotamia: portrait of a dead civilization*. University of Chicago Press, 2013. 7

[33] F. Joannès, "L'itinéraire des Dix-Mille en Mésopotamie et l'apport des sources cunéiformes," *Pallas*, pp. 173–199, 1995. 7

[34] J. A. Black, G. Cunningham, J. Ebeling, E. Flückiger-Hawker, E. Robson, J. Taylor, and G. Zólyomi, "The electronic text corpus of Sumerian literature," *URL: http://www-etcsl. orient. ox. ac. uk/. Oxford*, 1998. 10, 299

[35] H. Helbaek *et al.*, "The paleoethnobotany of the Near East and Europe," *The paleoethnobotany of the Near East and Europe.*, no. 31, 1960. 8, 10

[36] W. Van Zeist, H. Bakker, *et al.*, "Evidence for linseed cultivation before 6000 BC," *Journal of Archaeological Science*, vol. 2, no. 3, pp. 215–219, 1975. 10

[37] A. Thomas, "Restes textiles sur un clou de fondation de Gudea. Étude préliminaire," *Paléorient*, vol. 38, no. 1, pp. 151–159, 2012. 11, 55, 76, 77, 102, 103, 200, 205, 206

[38] H. Crawford, *The sumerian world*. Routledge, 2013. 11

[39] J. McIntosh, *The ancient Indus Valley: new perspectives*. Abc-Clio, 2008. 13, 299

[40] M. Wheeler and R. E. M. Wheeler, *Civilizations of the Indus Valley and beyond*. Thames, 1966. 12, 13

[41] A. H. Dani and B. Thapar, "The Indus Civilization," *History of civilizations of Central Asia*, vol. 1, 1992. 13

[42] C. Moulherat, M. Tengberg, J.-F. Haquet, and B. Mille, "First evidence of cotton at Neolithic Mehrgarh, Pakistan: analysis of mineralized fibres from a copper bead," *Journal of Archaeological Science*, vol. 29, no. 12, pp. 1393–1401, 2002. 14, 16, 183, 205, 299

[43] J. Kenoyer, "Ancient textiles of the Indus Valley region," *Tana Bana: the woven soul of Pakistan*, pp. 18–31, 2004. 13, 15, 16, 18, 19, 205

[44] J. M. Kenoyer, *Ancient cities of the Indus Valley civilization*. American Institute of Pakistan Studies, 1998. 13

[45] M. Thoury, B. Mille, T. Séverin-Fabiani, L. Robbiola, M. Refregiers, J.-F. Jarrige, and L. Bertrand, "High spatial dynamics-photoluminescence imaging reveals the metallurgy of the earliest lost-wax cast object," *Nature communications*, vol. 7, p. 13356, 2016. 15, 73, 103, 143, 144, 150

[46] A. Samzun and P. Sellier, "First anthropological and cultural evidence for the funerary practices of the Chalcolithic population of Mehrgarh, Pakistan," *South Asian Archaeology*, pp. 91–119, 1983. 15

[47] R. Janaway and R. Coningham, "A review of archaeological textile evidence from South Asia," *South Asian Studies*, vol. 11, no. 1, pp. 157–174, 1995. 15

[48] J.-F. Jarrige and R. H. Meadow, "The antecedents of civilization in the Indus Valley," *Scientific American*, vol. 243, no. 2, pp. 122–137, 1980. 15, 16, 299

[49] J. M. Kenoyer and R. H. Meadow, "The Ravi phase: A new cultural manifestation at Harappa," *South Asian Archaeology*, vol. 1, pp. 55–76, 1997. 16, 300

[50] L. Costantini, "The beginning of agriculture in the Kachi Plain: the evidence of Mehrgarh," *South Asian Archaeology*, pp. 29–33, 1981. 15, 16

[51] M. Tengberg, "Crop husbandry at Miri Qalat Makran, SW Pakistan (4000–2000 bc)," *Vegetation History and Archaeobotany*, vol. 8, no. 1-2, pp. 3–12, 1999. 16

[52] J.-F. Jarrige, "Du néolithique à la civilisation de l'Inde ancienne: contribution des recherches archéologiques dans le nord-ouest du sous-continent indo-pakistanais," *Arts asiatiques*, pp. 5–30, 1995. 16

[53] C. Jarrige, "The figurines from Nausharo, period I and their further developments," *South Asian Archaeology*, vol. 1995, pp. 33–43, 1997. 16

[54] R. P. Wright, D. L. Lentz, H. F. Beaubien, and C. K. Kimbrough, "New evidence for jute (Corchorus capsularis L.) in the Indus civilization," *Archaeological and Anthropological Sciences*, vol. 4, no. 2, pp. 137–143, 2012. 17, 19

[55] I. L. Good, J. M. Kenoyer, and R. H. Meadow, "New evidence for early silk in the Indus civilization," *Archaeometry*, vol. 51, no. 3, pp. 457–466, 2009. 17, 19

[56] S. L. Huntington and J. C. Huntington, *The Art of Ancient India: Buddhist, Hindu, Jain*. Weatherhill, 1985. 18, 19

[57] J.-F. Jarrige, "Les fouilles de Nausharo au Balochistan pakistanais et leur contribution à l'étude de la civilisation de l'Indus," *Comptes rendus des séances de l'Académie des Inscriptions et Belles-Lettres*, vol. 140, no. 3, pp. 821–878, 1996. 19, 97, 98

[58] M. S. Vats, *Excavations at Harappa*. New Delhi: Munshiram Manoharlal, 1940. 19, 205

[59] D. Chandramohan and K. Marimuthu, "A review on natural fibers," *International Journal of Research and Reviews in Applied Sciences*, vol. 8, no. 2, pp. 194–206, 2011. 20, 21, 28, 41, 300

[60] H. M. Appleyard, *Guide to the identification of animal fibres*. Wool Industries Research Association, 1960. 20, 52

[61] F. Anton, "Artificial thread and method of producing same," Jan. 16 1940. US Patent 2,187,306. 20

[62] S. Kalia, B. Kaith, and I. Kaur, *Cellulose fibers: bio-and nano-polymer composites: green chemistry and technology*. Springer, 2011. 21, 22, 23, 27, 28, 29, 204, 300, 307

[63] M. S. Smole, S. Hribernik, K. S. Kleinschek, and T. Kreže, "Plant fibres for textile and technical applications," in *Advances in agrophysical research*, InTech, 2013. 21, 25, 30

[64] T. A. Gorshkova, S. E. Wyatt, V. V. Salnikov, D. M. Gibeaut, M. R. Ibragimov, V. V. Lozovaya, and N. C. Carpita, "Cell-wall polysaccharides of developing flax plants," *Plant Physiology*, vol. 110, no. 3, pp. 721–729, 1996. 21

[65] G. Siqueira, J. Bras, and A. Dufresne, "Luffa cylindrica as a lignocellulosic source of fiber, microfibrillated cellulose and cellulose nanocrystals," *BioResources*, vol. 5, no. 2, pp. 727–740, 2010. 23

[66] P. Garside and P. Wyeth, "Identification of cellulosic fibres by FTIR spectroscopy-thread and single fibre analysis by attenuated total reflectance," *Studies in Conservation*, vol. 48, no. 4, pp. 269–275, 2003. 25, 202, 207, 300, 308

[67] H. Edwards and M. Falk, "Investigation of the degradation products of archaeological linens by raman spectroscopy," *Applied spectroscopy*, vol. 51, no. 8, pp. 1134–1138, 1997. 25

[68] M. Fan, D. Dai, and B. Huang, "Fourier transform infrared spectroscopy for natural fibres," in *Fourier transform-materials analysis*, InTech, 2012. 26, 27, 85, 202, 207, 308

[69] H. Edwards, D. Farwell, and D. Webster, "FT Raman microscopy of untreated natural plant fibres," *Spectrochimica Acta Part A: Molecular and Biomolecular Spectroscopy*, vol. 53, no. 13, pp. 2383–2392, 1997. 26, 27

[70] C. J. Knill and J. F. Kennedy, "Degradation of cellulose under alkaline conditions," *Carbohydrate Polymers*, vol. 51, no. 3, pp. 281–300, 2003. 26, 27, 43, 209

[71] S. Eichhorn, C. Baillie, N. Zafeiropoulos, L. Mwaikambo, M. Ansell, and A. Dufresne, "Review-Current international research into cellulosic fibers and composites," *J. Mat. Sci.*, vol. 36, pp. 19–26, 2002. 27

[72] L. J. Gibson, "The hierarchical structure and mechanics of plant materials," *Journal of the Royal Society Interface*, pp. 341–351, 2012. 27

[73] A. Thomas and C. Moulhérat, "Les fondations mésopotamiennes, conservatoire pour l'étude des textiles," *Techne*, vol. 41, pp. 8–18, 2015. 28, 55, 76, 77, 102, 103, 200, 201, 205, 206

[74] R. Hall, *Egyptian textiles*, vol. 4. Osprey Publishing, 1986. 28, 204

[75] M. M. Le Fustec and M. le Fustec, *Technologie des matières et industries textiles*. Eyrolles, 1962. 29, 30, 300

[76] C. Bergfjord and B. Holst, "A procedure for identifying textile bast fibres using microscopy: Flax, nettle/ramie, hemp and jute," *Ultramicroscopy*, vol. 110, no. 9, pp. 1192–1197, 2010. 32, 76

[77] A. Garcia-Ventura, "Neo-Sumerian textile wrappings. revisiting some foundation figurines from Nippur," *Zeitschrift für Orient Archäologie*, vol. 1, pp. 246–254, 2008. 32, 33, 206

[78] Z. C. Koren, "The colors and dyes on ancient textiles in Israel," *Colors from Nature: Natural Colors in Ancient Times, Eretz-Israel Museum, Tel-Aviv*, pp. 15–31, 1993. 32

[79] A. K. Samanta and P. Agarwal, "Application of natural dyes on textiles," *Indian Journal of Fibre & Textile Research*, vol. 34, pp. 384–399, December 2009. 34

[80] D. Cardon, *Le monde des teintures naturelles*. Paris: Belin Sciences, 2003. 34

[81] D. Klemm, B. Philpp, T. Heinze, U. Heinze, W. Wagenknecht, *et al.*, *Comprehensive cellulose chemistry. Volume 1: Fundamentals and analytical methods*. Wiley-VCH Verlag GmbH, 1998. 41

[82] E. E. Peacock, "The biodeterioration of textile fibres in wet archaeological contexts with implications for conservation choices," *Intrecci vegetali e fibre tessili da ambiente umido: analisi conservazione e restauro: Atti (Trento, 28–30 maggio 2003), Incontri di Restauro*, vol. 4, pp. 46–61, 2005. 41, 46

[83] D. N. Saheb, J. Jog, *et al.*, "Natural fiber polymer composites: a review," *Advances in polymer technology*, vol. 18, no. 4, pp. 351–363, 1999. 41, 46

[84] W. S. Mok, M. J. Antal Jr, and G. Varhegyi, "Productive and parasitic pathways in dilute acid-catalyzed hydrolysis of cellulose," *Industrial & Engineering chemistry research*, vol. 31, no. 1, pp. 94–100, 1992. 41

[85] M. Sevilla and A. B. Fuertes, "The production of carbon materials by hydrothermal carbonization of cellulose," *Carbon*, vol. 47, no. 9, pp. 2281–2289, 2009. 41, 208, 210

[86] L.-t. Fan, M. M. Gharpuray, and Y.-H. Lee, "Nature of cellulosic material," in *Cellulose hydrolysis*, pp. 5–20, Springer, 1987. 42, 43, 209, 301

[87] J. Kolar, "Mechanism of autoxidative degradation of cellulose," *Restaurator*, vol. 18, no. 4, pp. 163–176, 1997. 43

[88] K. A. Jakes and L. R. Sibley, "Survival of cellulosic fibres in the archaeological context," *Science and Archaeology*, no. 25, pp. 31–38, 1983. 43, 45, 46, 210

[89] M. Strlič and J. Kolar, *Ageing and stabilisation of paper*. National and university library Ljubljana, 2005. 43, 210

[90] J. Le Roux, *Modification des fibres cellulosiques amélioration des propriétés hydrophiles des pates bisulfites*. PhD thesis, Université Bordeaux I, 2003. 43, 301

[91] J. Kolar, M. Strlic, G. Novak, and B. Pihlar, "Aging and stabilization of alkaline paper," *J Pulp Pap Sci*, vol. 24, no. 3, pp. 89–94, 1998. 44

[92] V. S. Šelih, M. Strlič, J. Kolar, and B. Pihlar, "The role of transition metals in oxidative degradation of cellulose," *Polymer Degradation and Stability*, vol. 92, no. 8, pp. 1476–1481, 2007. 44, 65

[93] M. Van der Zee, J. Stoutjesdijk, P. Van der Heijden, and D. De Wit, "Structure-biodegradation relationships of polymeric materials. 1. Effect of degree of oxidation on biodegradability of carbohydrate polymers," *Journal of environmental polymer degradation*, vol. 3, no. 4, pp. 235–242, 1995. 44

[94] M. Falkiewicz-Dulik, K. Janda, and G. Wypych, *Handbook of Material Biodegradation, Biodeterioration, and Biostablization*. Elsevier, 2015. 44

[95] K. Arshad, M. Skrifvars, V. Vivod, J. Valh, and B. Voncina, "Biodegradation of natural textile materials in soil," *Tekstilec*, vol. 57, no. 2, pp. 118–132, 2014. 44, 46, 47, 301

[96] G. Zaikov *et al.*, *Biodegradation and Durability of Materials under the Effect of Microorganisms*. CRC Press, 2014. 44, 45

[97] B. Gutarowska, K. Pietrzak, W. Machnowski, and J. M. Milczarek, "Historical textiles–a review of microbial deterioration analysis and disinfection methods," *Textile Research Journal*, vol. 87, no. 19, pp. 2388–2406, 2017. 44

[98] R. Siu, "Mechanism of microbiological decomposition of cellulose," *Textile Research Journal*, vol. 20, no. 5, pp. 281–288, 1950. 45

[99] A. Desai and S. Pandey, "Microbial degradation of cellulosic textiles," *J Sci Indus Res*, 1971. 45

[100] S. S. Block, *Disinfection, sterilization, and preservation*. Lippincott Williams & Wilkins, 2001. 45

[101] J. Szostak-Kotowa, "Biodeterioration of textiles," *International biodeterioration & biodegradation*, vol. 53, no. 3, pp. 165–170, 2004. 46

[102] I. Good, "Archaeological textiles: a review of current research," *Annual Review of Anthropology*, vol. 30, no. 1, pp. 209–226, 2001. 46, 61, 183

[103] E. Barber, "Bronze Age cloth and clothing of the Tarim Basin: The Kroran (Loulan) and Qumul (Hami) Evidence," *Institute for the Study of Man in collaboration with University of Pennsylvania Museum Publications*, pp. 647–655, 1999. 48, 49

[104] R. Thomas, M. Tengberg, C. Moulhérat, V. Marcon, and R. Besenval, "Analysis of a protohistoric net from Shahi Tump, Baluchistan (Pakistan)," *Archaeological and Anthropological Sciences*, vol. 4, no. 1, pp. 15–23, 2012. 48, 49, 50

[105] M. E. King, "Analytical methods and prehistoric textiles," *American Antiquity*, vol. 43, no. 1, pp. 89–96, 1978. 49, 53

[106] S. I. Rudenko, "Frozen tombs of Siberia: The Pazyryk burials of Iron Age Horsemen," *MW Thompson, London*, 1970. 49

[107] N. Polosmak and H.-P. Francfort, "Un nouveau kourgane à «tombe gelée» de l'Altaï (rapport préliminaire)," *Arts asiatiques*, vol. 46, no. 46, pp. 5–20, 1991. 49

[108] N. Polosmak and F. Van Noten, "Les scythes de l'Altaï," *La Recherche*, no. 276, pp. 524–530, 1995. 49

[109] V. Jenssen, "La conservation de matériaux organiques gorgés d'eau:«Notre honte cachée»," *Museum International (Edition Francaise)*, vol. 35, no. 1, pp. 15–21, 1983. 49

[110] K. Schlabow, *Textilfunde der Eisenzeit in Norddeutschland*, vol. 15. Göttinger Schriften zur vor-und Frühgeschichte, 1976. 49

[111] K. A. Jakes and L. R. Sibley, "An examination of the phenomenon of textile fabric pseudomorphism," in *Archaeological chemistry-III*, pp. 403–424, American Chemical Society, 1984. 49, 54, 183

[112] A. R. David, "Mummification," *Ancient Egyptian materials and technology*, p. 372, 2000. 49

[113] *Fibre damage in archaeological textiles*, (York), The Conference Textile for the Archaeological Conservator, UKIC Archaeological Section, 1988. 50

[114] H.-J. Hundt, "Vorgeschichtliche Gewebe aus dem Hallstätter Salzberg," *Jahrbuch des Römisch-Germanischen Zentralmuseums Mainz*, vol. 6, pp. 66–100, 1959. 50

[115] H. Masurel, "Les vestiges textiles retrouvés dans l'embarcation," *Origini*, vol. 11, pp. 381–414, 1982. 50

[116] M. Gleba and J. M. Turfa, "Digging for archaeological textiles in museums:'New' finds in the University of Pennsylvania Museum of archaeology and anthropology," in *Proceedings of the 9th North European Symposium for Archaeological Textiles, NESAT IX—18–21 Mai*, pp. 35–40, 2005. 50

[117] M. civico archeologico delle acque (Chianciano Terme) and G. Paolucci, *Museo civico archeologico delle acque di Chianciano Terme*. Protagon editori toscani, 1997. 50

[118] H. De Genouillac, P. A, G. R, W. H, G. M, P. P, and L. J, *Fouilles de Telloh: Epoques présargoniques*. Académie des Inscriptions et Belles-Lettres, 1934. 51, 99, 102

[119] M. Lecaisne, "Note sur les tissues recouvrant des hache en cuivre," *Memoires de la Mission archeologique en Iran*, vol. 8, p. 163, 1912. 51, 205

[120] R. Pfister, "Les textiles à Suse," *Memoires de la Mission archeologique en Iran*, vol. 29, pp. 192–94, 1943. 51

[121] V. Sylwan, *Silk from the Yin dynasty*. Stockholm: Museum of Far Eastern Antiquities, 1937. 51

[122] V. Sylwan *et al.*, "Investigation of silk from Edsen-gol and Lop-nor," in *Sino-Swedish Expedition (1927-1935).*, 1949. 51

[123] A. Whitford, *Textile fibers used in eastern aboriginal North America*, vol. 38. New York: American Museum of Natural History, 1941. 52

[124] F. Church, "An analysis of textile fragments from three Ohio Hopewell sites," *Ohio Archaeologist*, vol. 33, no. 1, pp. 10–15, 1983. 52

[125] D. L. Carroll, "An etruscan textile in Newark," *American Journal of Archaeology*, vol. 77, no. 3, pp. 334–336, 1973. 52

[126] J. Vollmer, "Textile pseudomorphs on Chinese bronzes," in *Archaeological textiles: Irene Emery Roundtable on Museum Textiles*, (Washington), pp. 170–174, Textile Museum, 1974. 53, 56, 210

[127] R. Janaway, "Textile fibre characteristics preserved by metal corrosion: the potential of SEM studies," *The Conservator*, vol. 7, no. 1, pp. 48–52, 1983. 53

[128] R. Janaway, "Dust to dust: the preservation of textile materials in metal artifact corrosion products with reference to inhumation graves," *Science and archaeology*, vol. 27, pp. 29–34, 1985. 53

[129] R. C. Janaway, "The preservation of organic materials in association with metal artefacts deposited in inhumation graves," in *Death, decay and reconstruction: approaches to archaeology and forensic science*, pp. 127–148, Manchester University Press, 1987. 53, 61, 75, 183, 215

[130] R. Janaway, "Corrosion preserved textile evidence: mechanism, bias and interpretation," *Occasional Papers*, vol. 8, pp. 21–29, 1989. 53

[131] K. A. Jakes and J. Howard, "Formation of textile fabric pseudomorphs," in *Proceedings of the 24th International Archaeometry Symposium. JS Olin and M. J. Blackman*, pp. 165–77, 1968. 54

[132] K. A. Jakes and A. Angel, "Determination of elemental distribution in ancient fibers," *Advances in chemistry series*, 1989. 54

[133] K. Jakes and J. Howard III, "Conservation and characterization of historical paper and textile materials," *Advances in Chemistry*, no. 212, pp. 277–287, 1986. 54, 59, 60, 61, 301

[134] L. R. Sibley and K. A. Jakes, "Etowah textile remains and cultural context: a model for inference," *Clothing and Textiles Research Journal*, vol. 7, no. 2, pp. 37–45, 1989. 54

[135] L. R. Sibley, K. A. Jakes, and C. Song, "Fiber and yarn processing by prehistoric people of North America: examples from Etowah," *Ars Textrina*, vol. 11, pp. 191–209, 1989. 54

[136] E. J. Tiedemann and K. A. Jakes, "An exploration of prehistoric spinning technology: spinning efficiency and technology transition," *Archaeometry*, vol. 48, no. 2, pp. 293–307, 2006. 54

[137] R. D. Gillard, S. Hardman, R. Thomas, and D. Watkinson, "The mineralization of fibres in burial environments," *Studies in Conservation*, vol. 39, no. 2, pp. 132–140, 1994. 54, 61, 74, 87, 183, 210, 214, 215

[138] R. Gillard and S. Hardman, "Investigation of fiber mineralization using Fourier transform infrared microscopy," in *Archaeological Chemistry*, vol. 625, ch. 14, pp. 173–186, ACS Symposium Series, 1996. 54, 61

[139] H.-L. Chen, K. A. Jakes, and D. W. Foreman, "SEM, EDS, and FTIR examination of archeological mineralized plant fibers," *Textile Res. J.*, vol. 66, no. 4, pp. 219–224, 1996. 54, 55, 78, 79, 83, 84, 85, 86, 208, 213, 215, 302, 307

[140] L. Bertrand, *Approche structurale et bioinorganique de la conservation de fibres kératinisées archéologiques*. PhD thesis, Paris 6, 2002. 55, 75

[141] L. Bertrand, A. Vichi, J. Doucet, P. Walter, and P. Blanchard, "The fate of archaeological keratin fibres in a temperate burial context: microtaphonomy study of hairs from Marie de Bretagne (15th c., Orléans, France)," *Journal of Archaeological Science*, vol. 42, pp. 487–499, 2014. 55, 210

[142] L. G. Berry, B. H. Mason, *et al.*, *Mineralogy, concepts, descriptions, determinations*. W H Freeman & Co, 1959. 55

[143] C. Keepax, "Scanning electron microscopy of wood replaced by iron corrosion products," *Journal of Archaeological Science*, vol. 2, no. 2, pp. 145–150, 1975. 55

[144] H. Chen, D. Foreman, and K. A. Jakes, "X-ray diffractometric analyses of microstructure of mineralized plant fibers," in *Archaeological Chemistry*, vol. 625, ch. 15, pp. 187–201, ACS Symposium Series, 1996. 55, 79, 80, 81, 82, 86, 302, 307

[145] C. A. Arnold, *An introduction to paleobotany*. Read Books Ltd, 2013. 59

[146] S. Cook, S. T. Brooks, and H. Ezra-Cohn, "The process of fossilization," *Southwestern Journal of Anthropology*, vol. 17, no. 4, pp. 355–364, 1961. 59

[147] J. Aspland, "The application of anions to nonionic fibers: Cellulodc fibers and their sorption of anions," *Textile Chemist and Colorist*, vol. 23, pp. 31–39, 1991. 64

[148] J. Aspland, "Reactive dyes and their application," *Textile Chemist and Colorist*, vol. 24, no. 5, pp. 31–36, 1992. 64, 209

[149] M. Radivojević, T. Rehren, S. Farid, E. Pernicka, and D. Camurcuoğlu, "Repealing the çatalhöyük extractive metallurgy: The green, the fire and the 'slag'," *Journal of Archaeological Science*, vol. 86, pp. 101–122, 2017. 65, 143

[150] B. W. Roberts and C. P. Thornton, *Archaeometallurgy in global perspective: methods and syntheses*. Springer, 2014. 65, 143

[151] D. A. Scott, *Copper and bronze in art: corrosion, colorants, conservation*. Getty publications, 2002. 65, 66, 68, 69, 73, 143, 144, 168, 175

[152] M. Pourbaix, "Atlas of electrochemical equilibria in aqueous solutions," *NACEmTX*, 1974. 66, 67, 301

[153] D. Rice, P. Peterson, E. B. Rigby, P. Phipps, R. Cappell, and R. Tremoureux, "Atmospheric corrosion of copper and silver," *Journal of the Electrochemical Society*, vol. 128, no. 2, pp. 275–284, 1981. 66

[154] H. Leidheiser Jr, *The corrosion of copper, tin and their alloys*. Krieger Pub Co, 1971. 66

[155] H. H. Schmitt, *Equilibrium diagrams for minerals at low temperature and pressure*. University of California, 1962. 67, 301

[156] H. Strandberg and L.-G. Johansson, "Some aspects of the atmospheric corrosion of copper in the presence of sodium chloride," *Journal of the Electrochemical Society*, vol. 145, no. 4, pp. 1093–1100, 1998. 66

[157] K. Mizuno, M. Izaki, K. Murase, T. Shinagawa, M. Chigane, M. Inaba, A. Tasaka, and Y. Awakura, "Structural and electrical characterizations of electrodeposited p-type semiconductor Cu2O films," *Journal of The Electrochemical Society*, vol. 152, no. 4, pp. C179–C182, 2005. 66

[158] C. Leygraf, I. O. Wallinder, J. Tidblad, and T. Graedel, *Atmospheric corrosion*. John Wiley & Sons, 2016. 68, 70, 301

[159] J. Shaerkey and S. Lewin, "Conditions governing the formation of atacamite and paratacamite," *American Mineralogist: Journal of Earth and Planetary Materials*, vol. 56, no. 1-2, pp. 179–192, 1971. 68, 168

[160] T. Graedel, "Copper patinas formed in the atmosphere—II. A qualitative assessment of mechanisms," *Corrosion Science*, vol. 27, no. 7, pp. 721–740, 1987. 69

[161] M. Billiau and C. Drapier, "La tenue à la corrosion perforante du cuivre dans les installations d'eaux sanitaires-Mécanismes et progrès récents," *Matériaux & Techniques*, vol. 71, no. 1-2, pp. 11–15, 1983. 69, 301

[162] L. Robbiola and L.-P. Hurtel, "New contribution to the study of corrosion mechanisms of outdoor bronzes: characterization of the corroding surfaces of Rodin's bronzes," *Mémoires et Etudes scientifiques Revue de Métallurgie*, vol. 88, no. 12, pp. 809–823, 1991. 70

[163] L. Robbiola and L.-P. Hurtel, "Standard nature of the passive layers of buried archaeological bronze-The example of two Roman half-length portraits," in *METAL 95: International conference on metals conservation*, pp. 109–117, James and James Science Publisher, London, 1995. 70

[164] L. Robbiola, J.-M. Blengino, and C. Fiaud, "Morphology and mechanisms of formation of natural patinas on archaeological Cu–Sn alloys," *Corrosion Science*, vol. 40, no. 12, pp. 2083–2111, 1998. 70, 71, 72, 73, 144, 160, 212, 214

[165] L. Robbiola and R. Portier, "A global approach to the authentication of ancient bronzes based on the characterization of the alloy–patina–environment system," *Journal of Cultural Heritage*, vol. 7, no. 1, pp. 1–12, 2006. 70, 71, 72, 73, 144, 175, 211, 212, 213, 214

[166] R. Bertholon, L. Robbiola, and N. Lacoudre, "Corrosion du rouleau de cuivre de Qumrân et localisation de la surface originelle," in *Conférence internationale sur la conservation des métaux*, pp. 125–135, 1998. 70, 148, 168, 174, 175, 211

[167] M. Aucouturier, M. Keddam, L. Robbiola, and H. Takenouti, "Les patines des alliages de cuivre: processus naturel ou oeuvre de l'homme?," *Techne*, vol. 18, 2003. 71, 72

[168] P. Piccardo, B. Mille, and L. Robbiola, "Tin and copper oxides in corroded archaeological bronzes," *European federation of corrosion publications*, vol. 48, p. 239, 2007. 71, 72, 73, 144

[169] L. Soto, J. Franey, T. Graedel, and G. Kammlott, "On the corrosion resistance of certain ancient Chinese bronze artifacts," *Corrosion Science*, vol. 23, no. 3, pp. 241–250, 1983. 71

[170] L. Robbiola, *Caractérisation de l'altération de bronzes archéologiques enfouis à partir d'un corpus d'objets de l'age du Bronze. Mécanismes de corrosion.* PhD thesis, Université Pierre et Marie Curie-Paris VI, 1990. 72, 307

[171] I. De Ryck, A. Adriaens, and F. Adams, "An overview of Mesopotamian bronze metallurgy during the 3rd millennium BC," *Journal of Cultural Heritage*, vol. 6, no. 3, pp. 261–268, 2005. 73, 143, 144

[172] O. Oudbashi, S. M. Emami, and P. Davami, "Bronze in archaeology: a review of the archaeometallurgy of bronze in ancient Iran," in *Copper alloys-early applications and current performance-enhancing processes*, London: InTech, 2012. 73, 143, 144

[173] D. A. Scott, "A review of copper chlorides and related salts in bronze corrosion and as painting pigments," *Studies in Conservation*, vol. 45, no. 1, pp. 39–53, 2000. 73, 143, 144, 168

[174] D. A. Scott, "Periodic corrosion phenomena in bronze antiquities," *Studies in Conservation*, vol. 30, no. 2, pp. 49–57, 1985. 73, 143, 144, 168, 212

[175] I. De Ryck, A. Adriaens, E. Pantos, and F. Adams, "A comparison of microbeam techniques for the analysis of corroded ancient bronze objects," *Analyst*, vol. 128, no. 8, pp. 1104–1109, 2003. 73, 143, 144, 160, 168, 212

[176] O. Oudbashi, "Multianalytical study of corrosion layers in some archaeological copper alloy artefacts," *Surface and Interface Analysis*, vol. 47, no. 13, pp. 1133–1147, 2015. 73, 143, 144, 150, 168, 211

[177] A. Doménech-Carbó, M. T. Doménech-Carbó, J. Redondo-Marugán, L. Osete-Cortina, and M. V. Vivancos-Ramón, "Electrochemical characterization of corrosion products in leaded bronze sculptures considering ohmic drop effects on Tafel analysis," *Electroanalysis*, vol. 28, no. 4, pp. 833–845, 2016. 73, 144

[178] C. P. Thornton, C. Lamberg-Karlovsky, M. Liezers, and S. M. Young, "On pins and needles: tracing the evolution of copper-base alloying at Tepe Yahya, Iran, via ICP-MS analysis of common-place items," *Journal of Archaeological Science*, vol. 29, no. 12, pp. 1451–1460, 2002. 73, 144

[179] V. Hayez, J. Guillaume, A. Hubin, and H. Terryn, "Micro-Raman spectroscopy for the study of corrosion products on copper alloys: setting up of a reference database and studying works of art," *Journal of Raman Spectroscopy*, vol. 35, no. 8-9, pp. 732–738, 2004. 73, 144

[180] M. Schreiner and M. Grasserbauer, "Microanalysis of art objects: Objectives, methods and resultsmikroanalyse von kunstwerken: Aufgaben, methoden und ergebnisse," *Fresenius' Zeitschrift für analytische Chemie*, vol. 322, no. 2, pp. 181–193, 1985. 74, 302

[181] M. Goodway, "Fiber identification in practice," *Journal of the American Institute for Conservation*, vol. 26, no. 1, pp. 27–44, 1987. 76

[182] M.-C. Gay and R. Monrocq, "Identification des fibres textiles naturelles par examen microscopique," *Annale du Laboratoire de recherche des Musée de France*, vol. 8, no. 70, pp. 16–22, 1972. 76

[183] D. Buti, F. Rosi, B. Brunetti, and C. Miliani, "In-situ identification of copper-based green pigments on paintings and manuscripts by reflection FTIR," *Analytical and bioanalytical chemistry*, vol. 405, no. 8, pp. 2699–2711, 2013. 85, 165, 166, 170, 209

[184] V. I. Sarianidi and I. Sarianidi, *Necropolis of Gonur*. Kapon, 2007. 94, 95, 96, 204, 205

[185] D. T. Potts, "An Umm an-Nar-type compartmented soft-stone vessel from Gonur Depe, Turkmenistan," *Arabian archaeology and epigraphy*, vol. 19, no. 2, pp. 168–181, 2008. 94

[186] N. Miller, "Preliminary archaeobotanical results from the 1989 excavation at the central Asian site of Gonur Depe, Turkmenistan," *Information Bulletin, International Association for the Study of the Cultures of Central Asia*, vol. 19, pp. 149–163, 1993. 94, 210

[187] M. Lurker, P. A. Clayton, and B. Cummings, *The gods and symbols of ancient Egypt: An illustrated dictionary*. Thames and Hudson, 1980. 96, 205

[188] A. Bouquillon, B. B. de Saizieu, and A. Duval, "Glazed steatite beads from Merhgarh and Nausharo," *Material Issues in Art and Archaeology*, pp. 4–352, 1995. 97, 98

[189] S. Méry, P. Anderson, M.-L. Inizan, M. Lechevallier, and J. Pelegrin, "A pottery workshop with flint tools on blades knapped with copper at Nausharo (Indus civilisation, ca. 2500 BC)," *Journal of Archaeological science*, vol. 34, no. 7, pp. 1098–1116, 2007. 97

[190] Q. Gonzague, "The pottery sequence from 2700 to 2400 BC at Nausharo, Baluchistan," in *Annales Academiae Scientiarum Fennicae. Series B*, vol. 273, pp. 629–644, Suomalainen tiedeakatemia, 1993. 97

[191] C. Jarrige, "Une tête d'éléphant en terre cuite de Nausharo (Pakistan)," *Arts asiatiques*, vol. 47, pp. 132–136, 1992. 97

[192] G. Cros, L. Heuzey, and F. Thureau-Dangin, *Nouvelles fouilles de Tello*. Ministère de l'Instruction publique et des Beaux-Arts et de l'Académie des Inscriptions et Belles-Lettres (Fondation Eugène Piot), 1910. 99

[193] H. De Genouillac and R. Ghirshman, *Fouilles de Telloh: Epoques d'UR IIIe Dynastie et de Larsa*. Académie des Inscriptions et Belles-Lettres, 1936. 99, 101

[194] A. Parrot, *Tello: vingt campagnes de fouilles (1877-1933)*. Musée du Louvre, 1948. 99, 101

[195] P. Sanlaville, "Considérations sur l'évolution de la basse Mésopotamie au cours des derniers millénaires," *Paléorient*, pp. 5–27, 1989. 101

[196] J. Pournelle, *Deltaic Landscapes and the Evolution of Early Mesopotamian Civilization: Marshland of Cities*. PhD thesis, PhD. Thesis, University of California, San Diego, 2003, 314p, 2003. 101

[197] J. Li, P. Gueriau, M. Bellato, A. King, L. Robbiola, M. Thoury, M. Baillon, C. Fossé, S. X. Cohen, C. Moulherat, A. Thomas, P. Galtier, and L. Bertrand, "Synchrotron-based phase mapping in corroded metals: insights from early copper-base artefacts," *Analytical chemistry*, vol. 91, no. 3, pp. 1815–1825, 2019. 102, 195, 198, 211, 212

[198] F. Tallon, *Métallurgie susienne I: de la fondation de Suse au XVIIIe siècle avant J.-C.*, vol. 1. Paris: Editions de la Réunion des musées nationaux, 1987. 102

[199] B. David, "Analyse élémentaire d'un clou de fondation. Alliage cuivreux IIIe millénaire av Jc, Tello, Mésopotamie," Tech. Rep. R22681, C2RMF, 2013. 103, 200

[200] M. Berthelot, *Introduction à l'étude de la chimie, des anciens et du moyen âge*. G. Steinheil, 1889. 103

[201] L. Bertrand, M. Cotte, M. Stampanoni, M. Thoury, F. Marone, and S. Schöder, "Development and trends in synchrotron studies of ancient and historical materials," *Physics Reports*, vol. 519, no. 2, pp. 51–96, 2012. 105, 107, 116, 243, 306

[202] L. Bertrand, L. Robinet, M. Thoury, K. Janssens, S. X. Cohen, and S. Schöder, "Cultural heritage and archaeology materials studied by synchrotron spectroscopy and imaging," *Applied Physics A*, vol. 106, no. 2, pp. 377–396, 2012. 105

[203] P. Willmott, *An introduction to synchrotron radiation: techniques and applications*. John Wiley & Sons, 2011. 105

[204] G. N. Hounsfield, "Computerized transverse axial scanning (tomography): Part 1. Description of system," *The British journal of radiology*, vol. 46, no. 552, pp. 1016–1022, 1973. 107, 108, 303

[205] J. Baruchel, J.-Y. Buffiere, and E. Maire, *X-ray tomography in material science*. Paris: HERMES Science Publications, 2000. 107, 108, 109, 112, 113, 114, 116, 117, 123, 153, 303

[206] J. Banhart, *Advanced tomographic methods in materials research and engineering*, vol. 66. Oxford University Press, 2008. 107, 108, 109, 117

[207] G. Jean Louis and T. Christian, *Tomographie à rayons X*. Ed. Techniques Ingénieur, 2002. 107, 109, 121, 124

[208] G. T. Herman, *Fundamentals of computerized tomography: image reconstruction from projections*. Springer Science & Business Media, 2009. 108, 117

[209] U. Bonse and F. Busch, "X-ray computed microtomography (μct) using synchrotron radiation (SR)," *Progress in biophysics and molecular biology*, vol. 65, no. 1-2, pp. 133–169, 1996. 109

[210] J. L. Gerstenmayer and C. Thiery, *Tomographie à rayons X*. Ed. Techniques Ingénieur, 2002. 113, 177

[211] S. Mayo, T. Davis, T. Gureyev, P. Miller, D. Paganin, A. Pogany, A. Stevenson, and S. Wilkins, "X-ray phase-contrast microscopy and microtomography," *Optics Express*, vol. 11, no. 19, pp. 2289–2302, 2003. 113

[212] F. Jian, "Phase contrast computed tomography," in *Computed Tomography-Clinical Applications*, InTech, 2012. 113

[213] T. Jensen, "Refraction and scattering based x-ray imaging," *University of Copenhagen*, 2010. 113, 114, 303

[214] T. Davis, D. Gao, T. Gureyev, A. Stevenson, and S. Wilkins, "Phase-contrast imaging of weakly absorbing materials using hard X-rays," *Nature*, vol. 373, no. 6515, p. 595, 1995. 113

[215] U. Bonse and M. Hart, "An x-ray interferometer," *Applied Physics Letters*, vol. 6, no. 8, pp. 155–156, 1965. 114

[216] A. Momose, "Demonstration of phase-contrast X-ray computed tomography using an X-ray interferometer," *Nuclear Instruments and Methods in Physics Research Section A: Accelerators, Spectrometers, Detectors and Associated Equipment*, vol. 352, no. 3, pp. 622–628, 1995. 114

[217] A. Momose, T. Takeda, Y. Itai, and K. Hirano, "Phase–contrast X–ray computed tomography for observing biological soft tissues," *Nature medicine*, vol. 2, no. 4, pp. 473–475, 1996. 114

[218] D. Chapman, W. Thomlinson, R. Johnston, D. Washburn, E. Pisano, N. Gmür, Z. Zhong, R. Menk, F. Arfelli, and D. Sayers, "Diffraction enhanced x-ray imaging," *Physics in Medicine & Biology*, vol. 42, no. 11, p. 2015, 1997. 114

[219] A. Snigirev, I. Snigireva, V. Kohn, S. Kuznetsov, and I. Schelokov, "On the possibilities of x-ray phase contrast microimaging by coherent high-energy synchrotron radiation," *Review of scientific instruments*, vol. 66, no. 12, pp. 5486–5492, 1995. 114

[220] J. F. Clauser, "Ultrahigh resolution interferometric x-ray imaging," 1998. US Patent 5. 114

[221] P. Cloetens, W. Ludwig, J. Baruchel, J.-P. Guigay, P. Pernot-Rejmánková, M. Salomé-Pateyron, M. Schlenker, J.-Y. Buffière, E. Maire, and G. Peix, "Hard x-ray phase imaging using simple propagation of a coherent synchrotron radiation beam," *Journal of Physics D: Applied Physics*, vol. 32, no. 10A, p. A145, 1999. 114

[222] M. Bech, *X-ray imaging with a grating interferometer*. PhD thesis, Museum Tusculanum, 2009. 115, 303

[223] P. Cloetens, W. Ludwig, J. Baruchel, D. Van Dyck, J. Van Landuyt, J. Guigay, and M. Schlenker, "Holotomography: Quantitative phase tomography with micrometer resolution using hard synchrotron radiation x rays," *Applied physics letters*, vol. 75, no. 19, pp. 2912–2914, 1999. 114

[224] M. Heethoff and P. Cloetens, "A comparison of synchrotron x-ray phase contrast tomography and holotomography for non-invasive investigations of the internal anatomy of mites," *Soil organisms*, vol. 80, no. 2, pp. 205–215, 2008. 115

[225] D. Paganin, S. Mayo, T. E. Gureyev, P. R. Miller, and S. W. Wilkins, "Simultaneous phase and amplitude extraction from a single defocused image of a homoge-

neous object," *Journal of microscopy*, vol. 206, no. 1, pp. 33–40, 2002. 115, 117, 303

[226] P. Paleo and A. Mirone, "Efficient implementation of a local tomography reconstruction algorithm," *Advanced structural and chemical imaging*, vol. 3, no. 1, p. 5, 2017. 115

[227] S. Zhao, K. Yang, and X. Yang, "Reconstruction from truncated projections using mixed extrapolations of exponential and quadratic functions," *Journal of X-ray Science and Technology*, vol. 19, no. 2, pp. 155–172, 2011. 117

[228] A. Faridani, K. A. Buglione, P. Huabsomboon, O. D. Iancu, J. McGrath, *et al.*, "Introduction to local tomography," *Contemporary Mathematics*, vol. 278, pp. 29–48, 2001. 117

[229] E. A. Rashed and H. Kudo, "Recent advances in interior tomography (mathematical programming in the 21st century: Algorithms and modeling)," 京都大学数理解析研究所, no. 1676, pp. 145–156, 2010. 118, 303

[230] A. Mirone, E. Brun, E. Gouillart, P. Tafforeau, and J. Kieffer, "The PyHST2 hybrid distributed code for high speed tomographic reconstruction with iterative reconstruction and a priori knowledge capabilities," *Nuclear Instruments and Methods in Physics Research Section B: Beam Interactions with Materials and Atoms*, vol. 324, pp. 41–48, 2014. 119, 128

[231] S. Stock, "Recent advances in X-ray microtomography applied to materials," *International Materials Reviews*, vol. 53, no. 3, pp. 129–181, 2008. 120

[232] S. W. Smith *et al.*, *The scientist and engineer's guide to digital signal processing*. California Technical Pub. San Diego, 1997. 121, 122, 303

[233] S. R. Deans, *The Radon transform and some of its applications*. Courier Corporation, 2007. 121, 124

[234] P. W. Hawkes, B. Kazan, and T. Mulvey, *Advances in imaging and electron physics*, vol. 126. Academic press, 2003. 121

[235] M. Liebling, "Computerized Tomography," 2018. 124, 303

[236] R. A. Brooks and G. Di Chiro, "Beam hardening in x-ray reconstructive tomography," *Physics in medicine and biology*, vol. 21, no. 3, p. 390, 1976. 126

[237] C. A. Schneider, W. S. Rasband, and K. W. Eliceiri, "NIH image to imagej: 25 years of image analysis," *Nature methods*, vol. 9, no. 7, pp. 671–675, 2012. 128

[238] A. Jablonski, "Efficiency of anti-Stokes fluorescence in dyes," *Nature*, vol. 131, no. 839-840, p. 21, 1933. 128

[239] L. Bertrand, M. Réfrégiers, B. Berrie, J.-P. Échard, and M. Thoury, "A multiscalar photoluminescence approach to discriminate among semiconducting historical zinc white pigments," *Analyst*, vol. 138, no. 16, pp. 4463–4469, 2013. 129

[240] T. Séverin-Fabiani, *Imagerie de photoluminescence synchrotron pour l'étude de matériaux anciens semi-conducteurs*. PhD thesis, Université Paris-Saclay, 2016. 132, 304

[241] S. Preibisch, S. Saalfeld, and P. Tomancak, "Globally optimal stitching of tiled 3D microscopic image acquisitions," *Bioinformatics*, vol. 25, no. 11, pp. 1463–1465, 2009. 132

[242] R. Loudon, "The Raman effect in crystals," *Advances in Physics*, vol. 13, no. 52, pp. 423–482, 1964. 137, 234

[243] B. S. Ottaway and B. Roberts, "The emergence of metalworking," *Prehistoric Europe: theory and practice*, pp. 193–225, 2008. 143

[244] M. Radivojević, T. Rehren, E. Pernicka, D. Šljivar, M. Brauns, and D. Borić, "On the origins of extractive metallurgy: new evidence from Europe," *Journal of Archaeological Science*, vol. 37, no. 11, pp. 2775–2787, 2010. 143

[245] O. Oudbashi, "A methodological approach to estimate soil corrosivity for archaeological copper alloy artefacts," *Heritage Science*, vol. 6, no. 1, p. 2, 2018. 143, 168, 211

[246] L. Robbiola, I. Queixalos, L.-P. Hurtel, M. Pernot, and C. Volfovsky, "Etude de la corrosion de bronzes archeologiques du Fort-Harrouard: alteration externeet mecanisme d'alteration stratifiee," *Studies in Conservation*, vol. 33, no. 4, pp. 205–215, 1988. 143, 168

[247] L. I. McCann, K. Trentelman, T. Possley, and B. Golding, "Corrosion of ancient Chinese bronze money trees studied by Raman microscopy," *Journal of Raman spectroscopy*, vol. 30, no. 2, pp. 121–132, 1999. 144

[248] "National Institute of Standards and Technology." https://physics.nist.gov/PhysRefData/FFast/html/form.html, 1997. 146

[249] P. J. Linstrom and W. G. Mallard, "NIST chemistry webbook," 2001. 146

[250] D. Barthelmy, "Mineralogy database," *Online at http://webmin eral. com*, 2004. 146

[251] C. Chantler, K. Olsen, R. Dragoset, A. Kishore, S. Kotochigova, and D. Zucker, "X-ray form factor, attenuation, and scattering tables," 2005. 146

[252] J. Fox and S. Weisberg, *An R companion to applied regression*. Sage Publications, 2011. 147

[253] T. R. D. C. Team, *R: A language and environment for statistical computing*. R Foundation for Statistic Computing, 1999–2013. 147

[254] O. Oudbashi and P. Davami, "Metallography and microstructure interpretation of some archaeological tin bronze vessels from Iran," *Materials Characterization*, vol. 97, pp. 74–82, 2014. 148, 168

[255] G. Masi, J. Esvan, C. Josse, C. Chiavari, E. Bernardi, C. Martini, M. Bignozzi, N. Gartner, T. Kosec, and L. Robbiola, "Characterization of typical patinas simulating bronze corrosion in outdoor conditions," *Materials Chemistry and Physics*, vol. 200, pp. 308–321, 2017. 148

[256] R. Bertholon, *La limite de la surface d'origine des objets métalliques archéologiques. Caractérisation, localisation et approche des mécanismes de conservation.* PhD thesis, Université Panthéon-Sorbonne-Paris I, 2000. 150, 172

[257] V. Lucey, "Developments leading to the present understanding of the mechanism of pitting corrosion of copper," *British Corrosion Journal*, vol. 7, no. 1, pp. 36–41, 1972. 150

[258] D. Swinehart, "The Beer-Lambert law," *Journal of chemical education*, vol. 39, no. 7, p. 333, 1962. 152

[259] K. Heinrich, "X-ray optics and microanalysis," in *Proceedings of the 4th Conference on X-ray Optics and Microanalysis*, p. 159, 1966. 152

[260] A. Tsuchiyama, K. Uesugi, T. Nakano, and S. Ikeda, "Quantitative evaluation of attenuation contrast of X-ray computed tomography images using monochromatized beams," *American Mineralogist*, vol. 90, no. 1, pp. 132–142, 2005. 152, 178

[261] J. Konieczny, K. Labisz, K. Głowik-Łazarczyk, J. Ćwiek, and Ł. Wierzbicki, "Microstructure of archaeological 17th century cast copper alloys," *Archives of Foundry Engineering*, vol. 17, no. 2, pp. 190–196, 2017. 161

[262] J. Sharkey and S. Lewin, "Thermochemical properties of the copper (II) hydroxychlorides," *Thermochimica Acta*, vol. 3, no. 3, pp. 189–201, 1972. 166

[263] I. L. Soroka, A. Shchukarev, M. Jonsson, N. V. Tarakina, and P. A. Korzhavyi, "Cuprous hydroxide in a solid form: does it exist?," *Dalton Transactions*, vol. 42, no. 26, pp. 9585–9594, 2013. 170

[264] S. Réguer, P. e. Dillmann, and F. Mirambet, "Buried iron archaeological artefacts: corrosion mechanisms related to the presence of Cl-containing phases," *Corrosion Science*, vol. 49, no. 6, pp. 2726–2744, 2007. 177

[265] R. H. Bossi and J. M. Nelson, "X-ray computed tomography standards," tech. rep., Air Force Weapons Lab Kirtland Afb Nm Civil Engineering Div, 1994. 177

[266] R. T. Mull, "Mass estimates by computed tomography: physical density from CT numbers," *American journal of roentgenology*, vol. 143, no. 5, pp. 1101–1104, 1984. 177

[267] J. H. Fromm, I. Sautter, D. Matthies, J. Kremer, P. Schumacher, and C. Ganter, "Xylem water content and wood density in spruce and oak trees detected by high-resolution computed tomography," *Plant Physiology*, vol. 127, no. 2, pp. 416–425, 2001. 177

[268] I. Sinka, S. Burch, J. Tweed, and J. Cunningham, "Measurement of density variations in tablets using X-ray computed tomography," *International Journal of Pharmaceutics*, vol. 271, no. 1, pp. 215–224, 2004. 177

[269] P. R. S. Moorey, *Ancient Mesopotamian materials and industries: the archaeological evidence*. Eisenbrauns, 1999. 183

[270] D. T. Potts, *A companion to the archaeology of the ancient Near East*. Wiley Black Well, 2012. 183

[271] E. A. Strand, K. M. Frei, M. Gleba, U. Mannering, M.-L. Nosch, and I. Skals, "Old textiles–new possibilities," *European Journal of Archaeology*, vol. 13, no. 2, pp. 149–173, 2010. 183

[272] M. Sotton, *Tissu et vêtement: 5000 ans de Savoir-Faire*. Musée archéologique du Val d'Oise, 1986. 183

[273] J. Colombel and R. a. Tang, *Trésor de la Cité interdite : art de vivre des empreurs de Chine*. Palace Museum, 1992. 183

[274] M. T. Ordoñez and L. Welters, "Textiles from the seventeenth-century privy at the Cross Street Back Lot site," *Historical Archaeology*, vol. 32, no. 3, pp. 81–90, 1998. 183

[275] C. Solazzo, P. W. Rogers, L. Weber, H. F. Beaubien, J. Wilson, and M. Collins, "Species identification by peptide mass fingerprinting (pmf) in fibre products preserved by association with copper-alloy artefacts," *Journal of Archaeological Science*, vol. 49, pp. 524–535, 2014. 184

[276] N. Zafeiropoulos, P. Vickers, C. Baillie, and J. Watts, "An experimental investigation of modified and unmodified flax fibres with XPS, ToF-SIMS and ATR-FTIR," *Journal of Materials Science*, vol. 38, no. 19, pp. 3903–3914, 2003. 202, 207, 208, 308

[277] D. Dai and M. Fan, "Characteristic and performance of elementary hemp fibre," *Materials Sciences and Applications*, vol. 1, no. 06, p. 336, 2010. 202, 207, 308

[278] P. Garside and P. Wyeth, "Identification of cellulosic fibres by FTIR spectroscopy differentiation of flax and hemp by polarized ATR FTIR," *Studies in Conservation*, vol. 51, no. 3, pp. 205–211, 2006. 202, 207, 308

[279] L. Majgier, O. Rahmonov, and R. Bednarek, "Features of abandoned cemetery soils on sandy substrates in Northern Poland," *Eurasian soil science*, vol. 47, no. 6, pp. 621–629, 2014. 187

[280] D. Bourgarit and B. Mille, "The elemental analysis of ancient copper-based artefacts by inductively-coupled-plasma atomic-emission spectrometry: an optimized methodology reveals some secrets of the Vix crater," *Measurement Science and Technology*, vol. 14, no. 9, p. 1538, 2003. 200

[281] O. Muravenko, N. Bolsheva, O. Y. Yurkevich, I. Nosova, O. Rachinskaya, T. Samatadze, and A. Zelenin, "Karyogenomics of species of the genus Linum L.," *Russian Journal of Genetics*, vol. 46, no. 10, pp. 1182–1185, 2010. 204

[282] L. Yan, N. Chouw, and K. Jayaraman, "Flax fibre and its composites–A review," *Composites Part B: Engineering*, vol. 56, pp. 296–317, 2014. 204

[283] L. Costantini, "Harappan agriculture in Pakistan: the evidence of Nausharo," *South Asian Archaeology*, pp. 321–332, 1987. 205

[284] A. L. Oppenheim, "The golden garments of the gods," *Journal of Near Eastern Studies*, vol. 8, no. 3, pp. 172–193, 1949. 205

[285] I. J. Winter, "'idols of the King': Royal images as recipients of ritual action in ancient Mesopotamia," *Journal of Ritual Studies*, pp. 13–42, 1992. 205

[286] R. S. Ellis, *Foundation deposits in ancient Mesopotamia*. Yale University Press, 1968. 206

[287] E. Cano, D. M. Bastidas, V. Argyropoulos, S. Fajardo, A. Siatou, J. Bastidas, and C. Degrigny, "Electrochemical characterization of organic coatings for protection of historic steel artefacts," *Journal of Solid State Electrochemistry*, vol. 14, no. 3, p. 453, 2010. 206

[288] M. Van de Mieroop, *Sumerian administrative documents from the reigns of Išbi-Erra and Šū-Ilišu*. Yale University Press, 1987. 206

[289] D. O. Edzard, *Gudea and his Dynasty*, vol. 1. University of Toronto Press, 1997. 206

[290] G. Goossens, "Les recherches historiques à l'époque Néo-Babylonienne," *Revue d'Assyriologie et d'archéologie orientale*, vol. 42, no. 3/4, pp. 149–159, 1948. 206

[291] E. D. Van Buren, *Foundation figurines and offerings*. Hans Schoetz & Co., 1931. 206

[292] H. de Genouillac and F. Thureau-Dangin, *Inventaire des Tablettes de Tello conservées au Musée Impérial Ottoman: Textes de l'époque d'Agadé et de l'époque d'Ur*, vol. 2. Leroux, 1910. 206

[293] K. Awa, H. Shinzawa, and Y. Ozaki, "An effect of cellulose crystallinity on the moisture absorbability of a pharmaceutical tablet studied by near-infrared spectroscopy," *Applied spectroscopy*, vol. 68, no. 6, pp. 625–632, 2014. 208

[294] S. Coseri, G. Biliuta, L. F. Zemljič, J. S. Srndovic, P. T. Larsson, S. Strnad, T. Kreže, A. Naderi, and T. Lindström, "One-shot carboxylation of microcrystalline cellulose in the presence of nitroxyl radicals and sodium periodate," *Rsc Advances*, vol. 5, no. 104, pp. 85889–85897, 2015. 208

[295] H. Hauptmann and E. Pernicka, "Die metallindustrie Mesopotamiens von den Anfängen bis zum 2," *Jahrtausend v. Chr. Orient-Archäologie*, vol. 3, 2004. 211

[296] I. De Ryck, E. Pantos, and A. Adriaens, "Near eastern ancient bronze objects from Tell Beydar (NE-Syria): insights into their corrosion," *Europhysics News*, vol. 38, no. 5, pp. 29–33, 2007. 211

[297] B. Valeur and M. N. Berberan-Santos, *Molecular fluorescence: principles and applications*. John Wiley & Sons, 2001. 224, 225, 305

[298] M. Dalibart and S. Servant, "Spectroscopie dans l'infrarouge.," *Techniques de l'Ingénieur*, vol. 80, pp. 77–7–8, 2000. 226, 227, 230, 305

[299] E. Pouyet, A. Lluveras-Tenorio, A. Nevin, D. Saviello, F. Sette, and M. Cotte, "Preparation of thin-sections of painting fragments: classical and innovative strategies," *Analytica chimica acta*, vol. 822, pp. 51–59, 2014. 229

[300] J. van der Weerd, R. M. Heeren, and J. J. Boon, "Preparation methods and accessories for the infrared spectroscopic analysis of multi-layer paint films," *Studies in conservation*, vol. 49, no. 3, pp. 193–210, 2004. 229

[301] Z. M. Khoshhesab, "Reflectance IR spectroscopy," in *Infrared Spectroscopy-Materials Science, Engineering and Technology*, InTech, 2012. 229, 231, 305

[302] M. R. Derrick, D. Stulik, and J. M. Landry, *Infrared spectroscopy in conservation science*. Getty Publications, 2000. 230

[303] E. M. M. Joseph, *Application of FTIR microscopy to cultural heritage materials*. PhD thesis, Università di Bologna, 2009. 230

[304] C. J. G. Plummer, *Caractérisation des polymères par microscopie électronique*. Ed. Techniques Ingénieur, 2001. 232, 305

[305] T. BAUDIN, "Analyse EBSD-Principe et cartographies d'orientations," *Techniques de l'Ingénieur*, 2010. 233, 305

[306] G. Turrell and J. Corset, *Raman microscopy: developments and applications*. Academic Press, 1996. 234

[307] P. Colomban, "The on-site/remote Raman analysis with mobile instruments: a review of drawbacks and success in cultural heritage studies and other associated fields," *Journal of RAMAN spectroscopy*, vol. 43, no. 11, pp. 1529–1535, 2012. 234

[308] P. Colomban and J. Corset, "Foreword to the special issue on Raman (micro) spectrometry and materials science," *Journal of Raman Spectroscopy*, vol. 30, no. 10, pp. 863–866, 1999. 234

[309] B. Teo, "Exafs: Basic principles and data analysis," *Inorganic Chemistry Concepts*, vol. 9, p. 1, 1986. 236

[310] P. Guériau, *La faune continentale d'arthropodes aquatiques du Famennien (Dévonien supérieur) de Strud, Belgique : taxonomie, paléoécologie et taphonomie par imagerie 2D synchrotron.* PhD thesis, Museum National d'Histoire Naturelle, 2014. 239

[311] B. Ravel and M. Newville, "ATHENA, ARTEMIS, HEPHAESTUS: data analysis for X-ray absorption spectroscopy using ifeffit," *Journal of synchrotron radiation*, vol. 12, no. 4, pp. 537–541, 2005. 239, 241, 242

[312] T. Ressler, "Winxas: a program for X-ray absorption spectroscopy data analysis under MS-Windows," *Journal of synchrotron radiation*, vol. 5, no. 2, pp. 118–122, 1998. 239

[313] A. Michalowicz, ""EXAFS pour le MAC": A new version of an EXAFS data analysis code for the Macintosh," *Le Journal de Physique IV*, vol. 7, no. C2, pp. C2–235, 1997. 239

[314] B. Ravel, "ATHENA user's guide," *Athena IFFEFIT*, 2009. 242

[315] M. Newville, "IFEFFIT: interactive XAFS analysis and FEFF fitting," *Journal of synchrotron radiation*, vol. 8, no. 2, pp. 322–324, 2001. 242

[316] J. J. Rehr and R. C. Albers, "Theoretical approaches to x-ray absorption fine structure," *Reviews of modern physics*, vol. 72, no. 3, p. 621, 2000. 242

[317] B. Cagnac and J. C. Pebay-Peyroula, *Physique atomique: introduction à la physique quantique et structure de l'édifice atomique*, vol. 1. Dunod, 1971. 243

[318] V. Solé and E. Papillon, "PyMCA: X-ray spectra visualization and analysis in Python," in *NOBUGS 2004 conference, Paul Scherrer Institute, Villigen PSI, Switzerland*, 2004. 244

[319] P. Gueriau, C. Mocuta, D. B. Dutheil, S. X. Cohen, D. Thiaudière, S. Charbonnier, G. Clément, L. Bertrand, O. Consortium, *et al.*, "Trace elemental imaging of rare earth elements discriminates tissues at microscale in flat fossils," *PloS one*, vol. 9, no. 1, p. e86946, 2014. 246, 247, 306

[320] V. Solé, E. Papillon, M. Cotte, P. Walter, and J. Susini, "A multiplatform code for the analysis of energy-dispersive X-ray fluorescence spectra," *Spectrochimica Acta Part B: Atomic Spectroscopy*, vol. 62, no. 1, pp. 63–68, 2007. 247

[321] B. C. Giessen and G. E. Gordon, "X-ray diffraction: new high-speed technique based on X-ray spectrography," *Science*, vol. 159, no. 3818, pp. 973–975, 1968. 247

[322] M. Müller, B. Murphy, M. Burghammer, I. Snigireva, C. Riekel, J. Gunneweg, and E. Pantos, "Identification of single archaeological textile fibres from the cave of letters using synchrotron radiation microbeam diffraction and microfluorescence," *Applied Physics A: Materials Science & Processing*, vol. 83, no. 2, pp. 183–188, 2006. 250, 306

[323] E. Laine and I. Lähteenmäki, "The energy dispersive X-ray diffraction method," *Journal of Materials Science*, vol. 15, pp. 269–278, 1980. 251

[324] A. Taylor and H. Sinclair, "On the determination of lattice parameters by the Debye-Scherrer method," *Proceedings of the Physical Society*, vol. 57, no. 2, p. 126, 1945. 254

List of Figures

List of Tables